BIO-INSPIRED IRON COMPLEXES FEATURING SECONDARY COORDINATION SPHERE INTERACTIONS: LIGAND DESIGN STRATEGIES AND DIOXYGEN REACTIVITY

BY

ZACHARY GORDON

DISSERTATION

Submitted in partial fulfillment of the requirements
for the degree of Doctor of Philosophy in Chemistry
in the Graduate College of the
University of Illinois at Urbana-Champaign, 2018

Urbana, Illinois

Doctoral Committee:

Assistant Professor Alison R. Fout, Chair
Professor Gregory S. Girolami
Professor Kenneth S. Suslick
Professor Wilfred A. van der Donk

ABSTRACT

The activation of dioxygen plays an important role in processes ranging from biological oxidation to energy storage and utilization. In Nature, metalloenzymes use complex architectures to promote these multi-electron and multi-proton reactions using first-row transition metal centers. Many enzymes rely on well-place hydrogen bonding networks in the secondary coordination sphere and protein superstructure to facilitate favorable reactivity at the metal center. These non-covalent interactions can contribute to the overall reactivity in a number ways including fine-tuning metal ligand interactions, supporting reactive intermediates, and controlling the movement of protons and electrons in the active site. Interested in modeling these interactions and promoting oxygen activation with bio-inspired iron complexes, our research group has designed new ligand frameworks featuring dynamic secondary coordination sphere interactions. The work reported herein describes the synthesis and derivatization of several ligand scaffolds and application of their iron complexes to O_2 activation.

Early work focused on the synthesis and metallation of a dipodal ligand framework capable of tautomerization from a pyrrole-imine to an azafulvene-amine upon metallation. Dative coordination of this ligand with iron(II) salts demonstrated the success of this approach, resulting in ligand tautomerization upon metallation, placing hydrogen bond donating amino groups in the secondary coordination sphere. Coordination of ancillary redox active fragments further demonstrated the flexible coordination modes of this complex, resulting in a change from a meridional to facial geometry of the ligand. Binding and dioxygenation of *ortho*-phenylene moieties is also described, mimicking the reactivity of ring-cleaving dioxygenase enzymes.

Systematic modification of the related tripodal ligand was then carried out to examine the influence changes in the primary and secondary coordination spheres had on the properties of the iron complexes. Detailed analysis of the iron(II)-hydroxo and iron(III)-oxo complexes suggested that the ligands' conjugated π-system results in delocalization of electron density across the ligand, as demonstrated by similar changes upon modification of either coordination sphere. However, structural analysis of the hydrogen bond donor-acceptor distances in the secondary coordination sphere indicated that the identity of the ligand capping group could be used to tune the strength of these interactions. Additional studies with these derivatives highlighted an additional role of the capping groups in determining the reactivity of the iron complexes. Switching from a bulky cyclohexyl ligand derivative to less sterically demanding aryl variants resulted in the formation of new dimeric species not previously accessible and altered the reactivity of the iron(II) complexes towards water.

Having examined several different types of ligand dynamics, later work focused on applying this framework in O_2 activation. Treatment of the iron(II)-triflate complex was found to result in formation of a terminal iron(III)-oxo complex. Further investigation of this reaction resulted in the identification of an iron(III)-hydroxo intermediate as well as a bridging iron(III)-oxo species derived from off-pathway decomposition. Electrochemical analysis of these complexes, and several control compounds, provided further insight, suggesting that dynamics in the ligand's secondary coordination sphere play an important role in the dioxygen activation process.

Finally, the design of ligand frameworks seeking to incorporate hydroxy groups in the secondary coordination sphere is described. These ligands are based on elaboration of the commercially available chelate, tris(2-aminoethyl)amine (tren). Several generations of the framework are described and metallated using late first-row transition metals.

ACKNOWLEDGEMENTS

and helped me through all the stress along the way. My sister, Alexis, has always been so supportive throughout grad school, especially as a long distance training partner as we both tried distance running for the first time. And finally my parents Joanne and Bruce, I could not have made it here without your boundless generosity. You've always been the first line of encouragement and praise, even when you have no idea what I'm actually working on at the time, which meant more during graduate school than ever before.

All of these people have been essential to my graduate experience at Illinois and I am extremely grateful for their support throughout my PhD studies.

TABLE OF CONTENTS

CHAPTER 1: O₂ BINDING AND ACTIVATION PROCESSES FACILITATED BY SECONDARY COORDINATION SPHERE INTERACTIONS

1.1 Motivation for bio-inspired approaches to the development of O₂ activation catalysts

The activation of O_2 plays a critical role in a number of important transformations in biology, industrial oxidation processes, and energy storage and utilization.[1-6] Given the wide array of applications, the development of catalytic systems capable of efficiently carrying out this reaction has received considerable attention. These fields are often dominated by precious metals, such as platinum-based catalysts used in the oxygen reduction reaction in proton-exchange membrane (PEM) fuel cells.[5,6] Nature, however, has developed metalloenzymes capable of carrying out the four-electron reduction of dioxygen using abundant first-row transition metals, including iron.[1,2] These enzymes often use amino acid residues beyond the primary coordination sphere to achieve multi-electron transformations with base metals and promote favorable reactivity at the metal center. These carefully placed hydrogen-bonding networks in the secondary coordination sphere and extended protein superstructure can facilitate the desired O_2 activation in a number of ways, including: i) tuning the interaction of the primary coordination sphere ligands with the metal center; ii) increasing selectivity and binding affinity for O_2; iii) stabilizing reactive species; and iv) shuttling protons to and from the active site. Additional roles of secondary coordination sphere interactions specific to dioxygen activation have been previously reviewed by Borovik.[7]

While the study of biological O_2 activation processes has produced many important insights into the roles of hydrogen bonding interactions in this reaction,[1,2] there are several drawbacks to working with these enzymes directly. In addition to the difficulties inherent to characterizing such complex macromolecular species, many relevant intermediates are short-lived and highly unstable, further complicating detailed analysis of their properties and reactivity. Accordingly, significant work has been directed toward applying these design principles in synthetic model systems.[7-10] As the field rapidly expands, a number of research groups have developed ligand frameworks that mimic many of the secondary coordination sphere interactions described above for biological systems. Each role will be examined below, providing representative examples from biological systems and related model complexes. While the focus will be on O_2 binding and activation, additional examples will draw on related metal oxygen-bound species and O–O cleavage processes where relevant.

1.2 Tuning the interaction of primary coordination sphere ligands with the metal center

1.2.1 Biological examples

Hydrogen bonding networks in the second sphere often play an important role in fine-tuning the primary coordination sphere donor set. This effect is especially prominent in heme-based enzymes, where hydrogen bonding to the axial heme ligand influences the donor strength of metal-bound residues. It has

long been understood that these subtle interactions can play a major role in controlling heme-based enzymes' reactivity towards dioxygen.[11] For example, the extent of hydrogen bonding at the proximal histidine in peroxidases and globins has been shown to contribute significantly to the metal center's redox potential. In peroxidases this metal-bound histidine hydrogen bonds with a nearby aspartic acid residue, increasing the anionic character of the proximal ligand, compared to globins where the hydrogen bonding partner is a peptide carbonyl group (Figure 1.1).[12] Mutation studies carried out by

Figure 1.1 Hydrogen bonding to proximal histidine in peroxidases (left) and globins (right).

Goodin et al. have further demonstrated that even minor changes in this hydrogen bond angle can significantly alter the donor strength of the proximal histidine.[13]
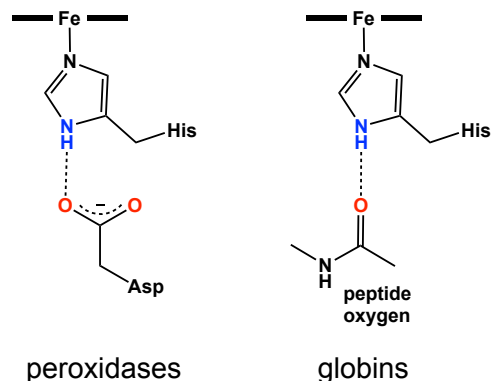
Work by Green and coworkers has shown the importance of related interactions for cysteine-ligated heme enzymes, where once again second sphere interactions are intimately involved in regulating the donor strength of the axial ligand (Figure 1.2).[14] In comparing the hydrogen bonding environments in the "cys-pocket" surrounding the thiolate ligands in chloroperoxidase (CPO) and cytochrome P450 Green and coworkers found that while P450 contained three potential hydrogen bond donors, only one of these residues was within the sum of the van der Waals radii, oriented at an angle of 130°, far removed from the ideal 180°. CPO however had two hydrogen bond interactions of this strength or greater, displaying a 172° angle for the stronger of the two interactions. The weaker donation to the thiolate in P450 results in a shorter Fe–S bond by ~0.1 Å and thus stronger electron donation to the metal center. These electronic differences between the two enzymes correlate to their C–H bond activation abilities, once again high-

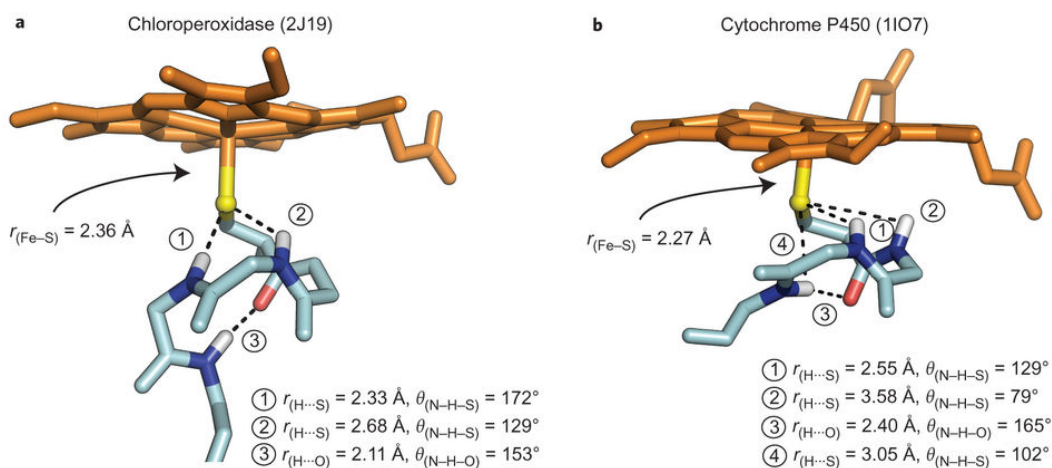
Figure 1.2 Hydrogen-bonding metrics and Fe–S distances from the crystal structures of (a) ferric CPO (2J19) and (b) ferric CYP119A1 (1IO7). The hydrogen-bonding metrics for CYP119A1 are typical of P450s. Protein Data Bank accession codes for each structure are given in parentheses. Reprinted from reference 14 by permission from Macmillan Publishers Ltd: Nature Chemistry, copyright 2015.

2

lighting the importance of the secondary coordination sphere interactions in controlling reactivity.

Hydrogen bonding often plays an important role in regulating primary sphere interactions in non-heme Fe(II) enzymes as well. O_2 activation in these enzymes frequently occurs at iron center ligated by a 2-His-1-carboxylate facial triad.[2,15] These enzymes have evolved specific mechanisms for regulating the coordination number at iron as a means of suppressing unproductive side reactions. In addition to the coordinated binding of cofactors or redox-activate substrates, certain subclasses of these non-heme enzymes regulate the binding of O_2 through secondary sphere interactions. Solomon has shown that hydrogen bonding between the triad carboxylate and nearby residues play an important role in maintaining monodentate coordination of the carboxylate, providing an open coordination site for binding of dioxygen.[16] Computational studies from his group examining the five-coordinate form of factor inhibiting hypoxia-inducible factor (FIH-1), an α-ketoglutarate(αKG)-dependent dioxygenase, indicated that in the absence of this hydrogen bond from Arg238 the carboxylate would bind in a bidentate fashion (Figure 1.3).[17] The importance of this residue was previously established in site-directed mutagenesis where a R238M mutant of FIH-1 showed minimal activity.[18] This mode of promoting monodentate binding of the triad carboxylate through hydrogen bonding to protein residues was found to be a general motif used in many additional non-heme iron(II) enzymes that require binding of a cofactor or substrate, including the larger family of αKG-dependent and extradiol dioxygenases.[16,17] These interactions once again highlight the role secondary coordination sphere residues can play in tuning the donor abilities of the metal-bound ligands in the primary sphere.

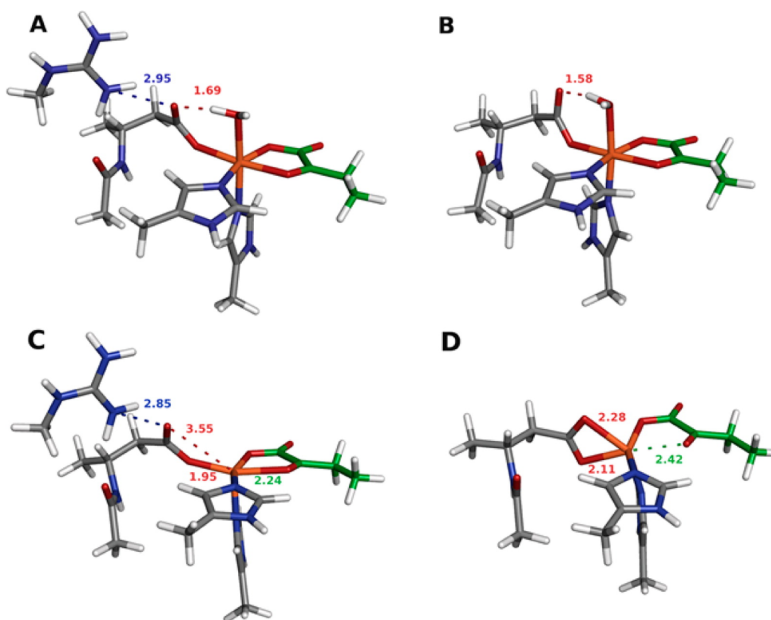**Figure 1.3** DFT optimized structures of FIH, showing the effects of Arg238 displacement on 6C ((A) and (B)) and 5C (C) and (D)) forms. Arg238-facial triad carboxylate heavy atom distance in blue, facial triad carboxylate O−Fe^{II} and O−H distances in red, and αKG carbonyl O−Fe^{II} distance in green. All distances are measured in Å. Reprinted with permission from reference 17. Copyright 2013 American Chemical Society.

3

1.2.2 Model systems

   Synthetic heme systems have been developed to model these hydrogen-bonding interactions and examine their effects on the properties of their metal complexes. In an early model system, a series of arylthiolate ligands with 0-2 hydrogen bonds to the sulfur were synthesized and bound to ferric hemes. It was shown that the introduction of hydrogen bond donors resulted in elongation of the Fe–S bond by 0.03-0.06 Å, effectively modeling the role of the second sphere in the heme-based enzymes described above. This bond elongation was correlated with reduced donor strength of the axial ligand as demonstrated by a shift in the $Fe^{III/II}$ redox couple to more positive potentials by 0.16-0.33 V (Figure 1.4).[19-21] A related series of iron porphyrin complexes containing tethered alkylthiolate axial donors were used to study these
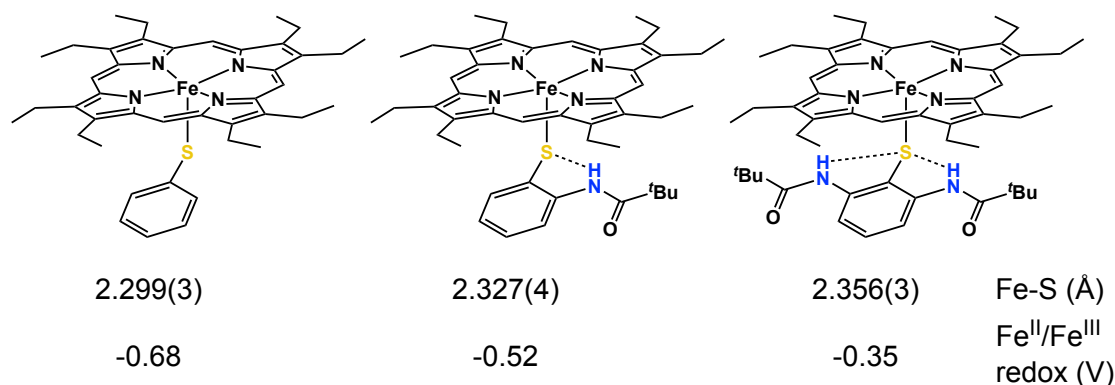

2.299(3)	2.327(4)	2.356(3)	Fe-S (Å)
-0.68	-0.52	-0.35	Fe^{II}/Fe^{III} redox (V)

Figure 1.4 Tuning axial thiolate donor strength through hydrogen bonding interactions.[19]

effects with thiolate ligands that more closely mimicked the cysteine donors found in cytochrome P-450. While hydrogen bonding was once again correlated with a positive shift in the $Fe^{III/II}$ redox couple (of ~0.1 V), the increased donor strength of the alkylthiolate, compared to the arylthiolates, resulted in electronic differences that cause shortening of the Fe–S bond.[22] Hydrogen bonding to the thiolate donor was also shown to impact the oxygenase activity, relative to the non-hydrogen bonding derivatives, as shown by competitive oxidation of a mixture of cyclooctane and cyclooctene. A decrease in the ratio of hydroxylation to epoxidation products indicated the increased preference for electrophilic pathways when secondary sphere interactions were present.

   Model systems have also been developed to examine the role of hydrogen bonding in controlling the binding mode of potentially chelating ligands, as described for non-heme iron dioxygenases above. Work by Berreau in modeling the non-heme enzyme acireductone dioxygenase (ARD) has effectively demonstrated the role of hydrogen bonding in determining ligand coordination modes.[23] The reactivity described with these complexes demonstrated that carboxylate ligands' binding mode were heavily influenced by the presence of hydrogen bond donors. Addition of water to nickel complexes with a κ_2-bound carboxylate ligand resulted in the formation of nickel(II)-aqua complexes with a then monodentate carboxylate hydrogen bonding with the aqua ligand (Scheme 1.1).[24] While the dioxygenase reactivity cata-

lyzed by these nickel complexes does not require formation of metal oxygen species, as are involved in the other enzymes discussed, it provides an interesting example of hydrogen bonding controlling ligand binding modes, which has been demonstrated to play an important role is controlling enzymatic activity in other non-heme dioxygenases.
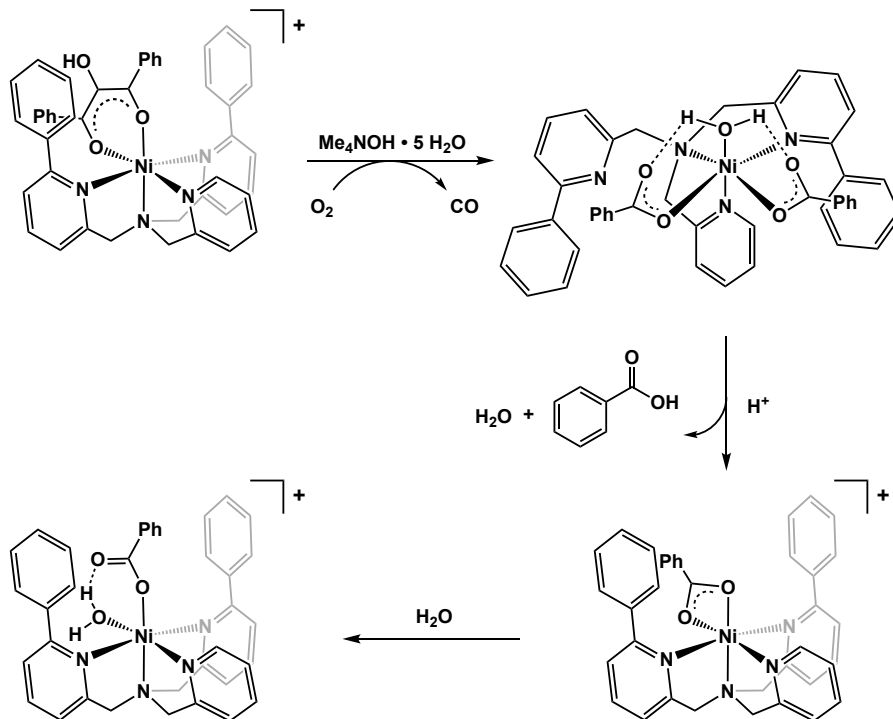
Scheme 1.1 Hydrogen bonding control over carboxylate binding modes.[21]

1.3 Increasing selectivity and binding affinity for O_2

1.3.1 Biological examples

Along with other methods, secondary coordination sphere interactions allow biological systems to differentiate between similar molecules, such as O_2 and CO, increasing the selectivity for their target ligand.[25] In globins, heme-based proteins responsible for O_2 storage and transport, a highly-conserved distal histidine contributes significantly to the observed affinity for O_2 over CO.[26] Initial studies identified two potential roles for this histidine in promoting preferential binding of O_2: i) disfavoring CO binding, through steric hindrance of the preferred linear binding mode, and ii) increasing

Figure 1.5 Stabilization of oxyMb by interaction of the bound O_2 with a distal histidine.

the binding affinity for O_2 through hydrogen bonding. While early structural data from X-ray crystallography studies of CO bound myoglobin (MbCO) showed a significantly bent Fe–CO geometry,[27] more recent higher-resolution structures have shown nearly-linear binding where the steric hindrance is avoided by distortions in the helices that bind the heme.[28-30] These results have led many to argue increased O_2-
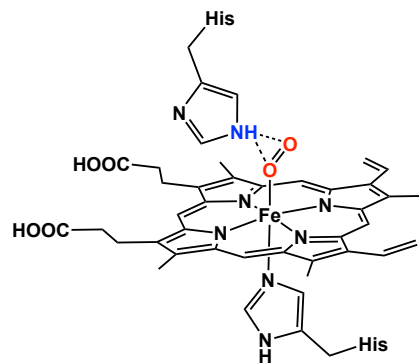
binding affinity is more likely to influence the observed selectivity. Springer et al. estimated that the hydrogen bond formed between the histidine and the bound oxygen results in a ~1000-fold increase in the O_2-binding affinity, supporting this hypothesis (Figure 1.5).[26,31] Mutation studies have provided further evidence, showing decreased oxygen affinity when the distal histidine is replaced with other amino acid residues.

Hydrogen bonding has been shown to play a similar role in O_2 sensing by the FixL class of heme proteins. Binding studies with *Bradyrhizobium japonicum* FixL (BjFixL) have shown that hydrogen bonding once again plays a critical role in controlling the selectivity for O_2 over NO and CO. Binding of all three ligands increases the planarity of the heme, howev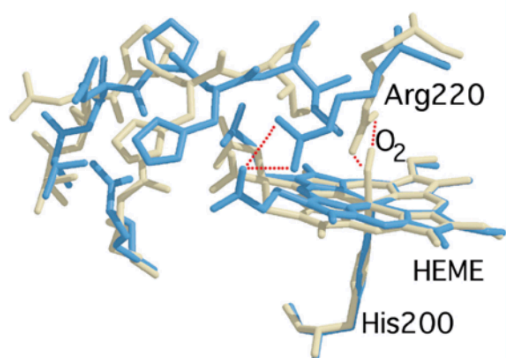er data from X-ray crystallography has demonstrated that the oxy-BjFixL undergoes an additional conformational change, while the NO- and CO-bound structures do not.[32-34] Upon binding, O_2 forms a hydrogen bonding interaction with an arginine residue, Arg220 (Figure 1.6). This interaction draws the residue into the heme pocket, giving a structural shift in the heme relative to the NO- and CO-BjFixL structures where this residue remains in a salt bridge with heme propionate 7, as is observed in the met and deoxy forms. Thus this hydrogen bond from Arg220 is understood to effectively discriminate between O_2 and related ligands by both increasing its binding affinity and facilitating a conformational change that is not induced with other less polar ligands such as NO and CO.

Figure 1.6 Comparison of the structure of FG loop and conformation of Arg220 in the unliganded "on" (blue) and liganded "off" (tan) state. Reprinted from reference 25 with permission of Springer. Copyright 2002 SBIC.

1.3.2 Model systems

Work by Naruta and co-workers demonstrated that similar principles could be used to discriminate between CO and O_2 in model heme systems.[35,36] Hydroxyl-functionalized binaphthyl flanking groups were attached to porphyrin complexes to allow the placement of hydrogen bond donors within the heme's binding pocket. Ligand binding studies demonstrated that the family of complexes all form weak CO adducts, while strongly binding O_2. Determination of the kinetic binding constants for the ferrous CO complex demonstrated that this weak binding is not the result of steric constraints, as the on rate was comparable to other unhindered porphyrin systems, if not higher. However, the dissociate rate was significantly higher than related systems, indicating a strong destabilization of the bound CO. This unfavorable binding was probed spectroscopically and ultimately attributed to the interactions between CO and the lone pairs of the hydroxyl groups.[37] This strong electrostatic interaction suppresses back-bonding from the iron center into the CO π^* orbital, resulting in weak binding of the CO ligand and accordingly its high dissociation rate (Figure 1.7).

The oxy-form of these complexes are stabilized by hydrogen bonding between the bound O_2 molecule and one of the hydroxyl groups in the heme's secondary coordination sphere (Figure 1.7). Substitution of the hydroxyl groups for methoxy analogs indicated that the increased O_2 affinities were not inherent to the binaphthyl-appended porphyrins, but were unique to the hydrogen bond donating variants.[35] Furthermore, vibrational spectroscopy experiments offered direct evidence of the hydrogen bonding interaction in the Fe–O_2 and O–O stretching modes.[36,38] This combination of destabilizing CO binding, while favoring the O_2 adducts resulted in the model systems' exceptional ability to discriminate between the two potential ligands through interactions of the bound ligands with the secondary coordination sphere.
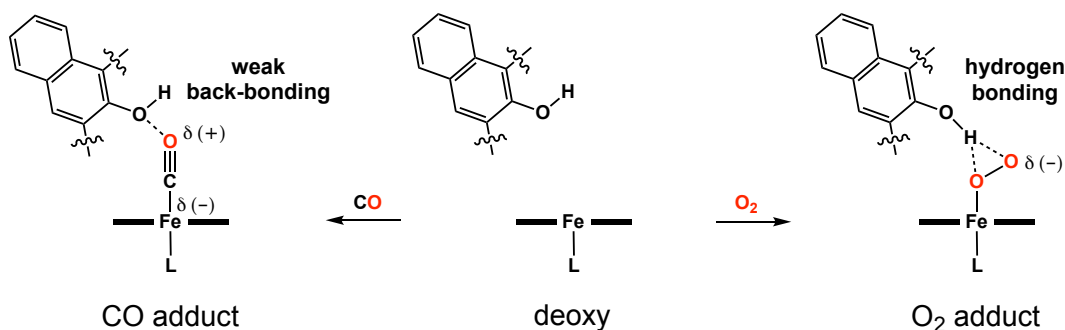

Figure 1.7 Interaction of appended hydroxyl groups with heme-bound ligands providing for discrimination between CO and O_2 binding at the iron center.[36]

1.4 Stabilizing reactive species

1.4.1 Biological examples

In addition to increasing the stability of O_2 adducts in globins, as described in the previous section, hydrogen bonding can play an important role in supporting reactive iron-oxygen intermediates during catalysis. These secondary sphere interactions have been invoked as a possible mechanism for discriminating between hydroxylation and halogenation pathways in the non-heme iron halogenase, WelO5.[39] The enzyme is a member of the αKG-dependent halogenase family of enzymes, which utilize O_2 and the αKG co-substrate to access a *cis*-halo-oxo-iron(IV) intermediate.[40-43] This reactive iron-oxo species abstracts a hydrogen atom from the substrate immediately prior to transfer of the halogen. To achieve the desired halogenation, these enzymes have evolved mechanisms to suppress the competing hydroxylation pathway where the substrate radical couples with the hydroxo ligand generated upon H-atom abstraction.

Previous work with a related halogenase, SyrB2, highlighted the importance of substrate orientation in differentiating between halogenation and hydroxylation based on proximity of the target carbon to the respective ligands.[43-45] However, structural data obtained for substrate-bound WelO5 indicated that a ligand rearrangement must occur to position the target carbon (C13) away from the oxo ligand. Refinement of the NO-bound state was also examined as a stable mimic for oxygen binding; this structure suggested that the proposed ligand rearrangement occurred after O_2,[39] unlike SyrB2 where NO is bound in a position consistent with the *cis*-halo-oxo-iron(IV) species' selectivity in halogenation.[45] Boal and coworkers high-

light the potential role of a second sphere residue, Ser189, in promoting this isomerization by forming a hydrogen bond with the resulting iron-oxo ligand (Scheme 1.2). This hypothesis was supported by site-directed mutagenesis data showing that removal of this hydrogen bond results in significantly decreased selectivity in the rebound step for the S189A mutant.[39] These studies provide an intriguing example of stabilizing a reactive iron-oxo fragment through secondary sphere interactions, underscoring the ability of these hydrogen-bonding networks to facilitate selective reactivity in enzymes.
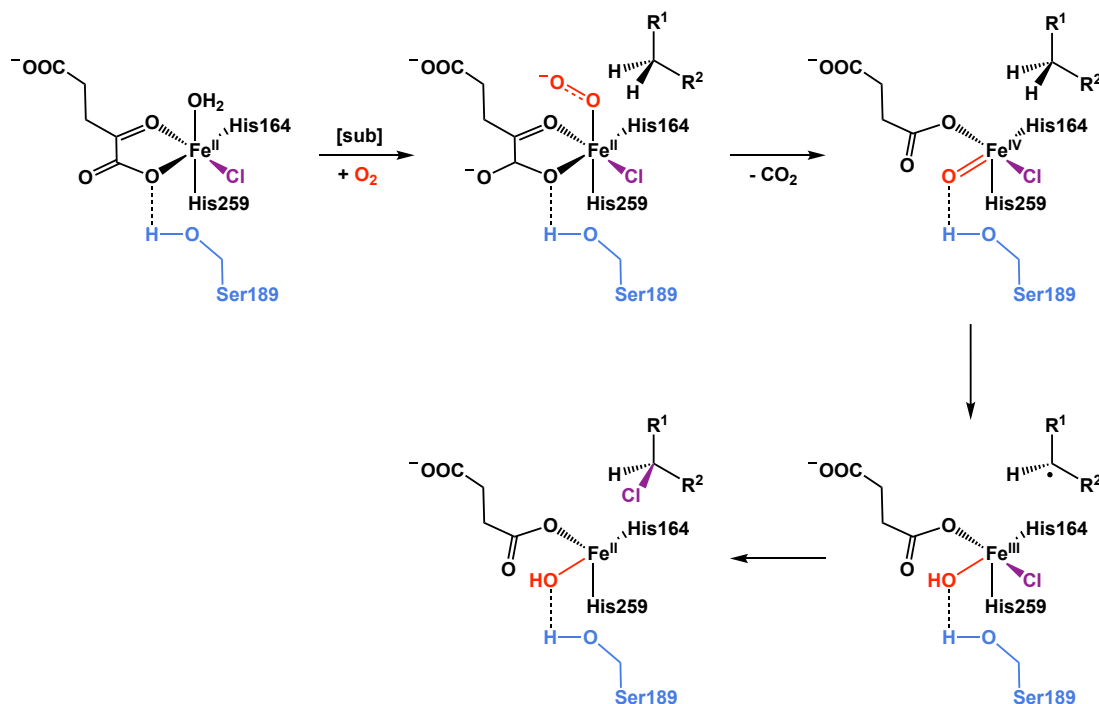
Scheme 1.2 Proposed mechanism for halogenation in WelO5, including the role of hydrogen bonding from Ser189 to promote geometric rearrangement of the critical *cis*-halo-oxo-iron(IV) intermediate.[39]

1.4.2 Model systems

Hydrogen bonding interactions have proven particularly useful in the study of model complexes containing reactive metal oxygen bonds. One of the earliest structurally characterized manganese-dioxygen complexes displayed a single hydrogen bond from a pyrazole donor to the side-on peroxo ligand, as reported by Kitajima. Although infrared spectroscopy and structural data revealed the presence of this hydrogen bonding interaction to be temperature- and solvent-dependent, it provided one of the first examples of second sphere stabilization of reactive species in a synthetic system.[46] Since then, a number of tripodal ligands featuring hydrogen bond donors have been developed to trap reactive species, popularized in part by Masuda's use of polypyridyl frameworks. In an early demonstration of these designs, the ligand framework was used to isolate a Cu^{II}-hydroperoxo complex.[47] Work by Borovik and co-workers extended these design principles to O_2 activation by bio-inspired transition metal complexes. Using a tripodal urea framework, they reported the first terminal Fe(III)-oxo complex, where the oxo ligand is

supported by interactions with each of the three hydrogen bond donors in the secondary sphere.[48] The isolation of this product from O_2 activation highlighted the ability of the secondary coordination sphere to support unusual, and often reactive species.
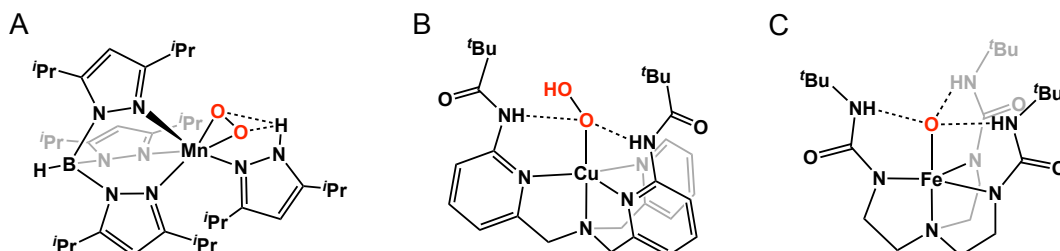

Figure 1.8 First-row transition metal complexes featuring hydrogen bonding to bound peroxo and oxo ligands; (A) $Mn^{III}O_2$,[46] (B) $Cu^{II}OOH$,[47] (C) $Fe^{III}O$.[48]

Expanding upon this work, Borovik developed a series of related ligands with 0-3 hydrogen-bond donors to study the effects of variations in the hydrogen bonding network on the reactivity of the metal complexes. Upon metallation with cobalt, it was shown that the binding and activation of O_2 was correlated to the number of hydrogen bond donors.[49] While the Co^{II} complexes with two and three urea groups both reacted with stoichiometric amounts of dioxygen, the derivative with only one hydrogen bond donor required treatment with excess O_2 to promote conversion (Scheme 1.3). Furthermore, the complex with no appended donor groups showed no reactivity towards dioxygen under any of the conditions studied. A similar trend was observed in the stability of the $Co^{III}OH$ products, where the rate of decay was negatively correlated to the number of hydrogen bond donors in the secondary coordination sphere. Thus, these ligands demonstrated the role of the secondary coordination sphere is accessing and stabilizing reactive species. Importantly, these design principles have been successfully applied to active catalysts for O_2 reduc-
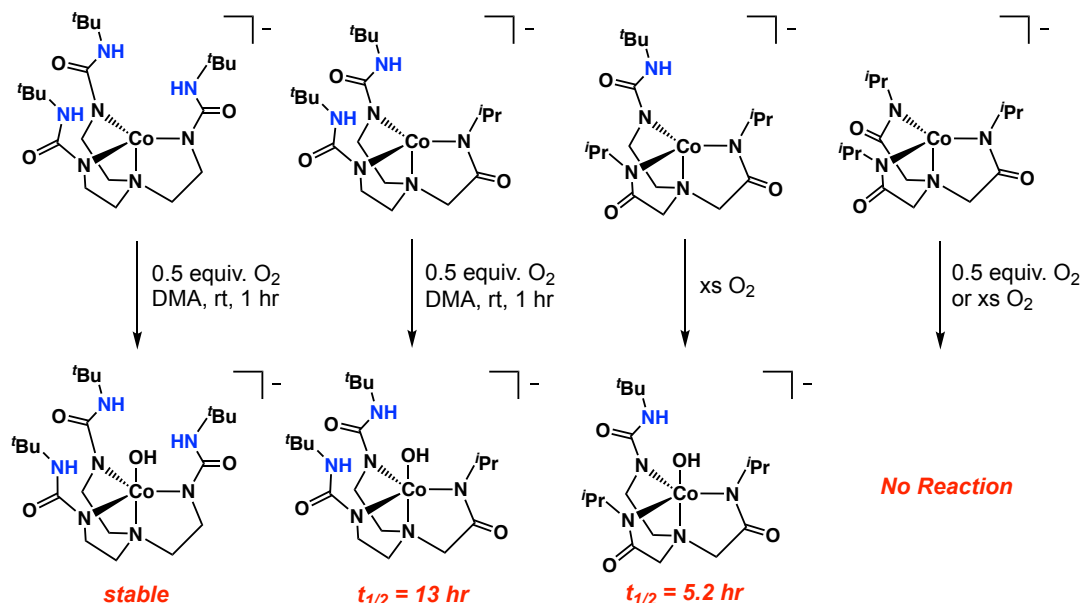

Scheme 1.3 Dioxygen reactivity of a series of Co(II) complexes featuring 0-3 hydrogen bond donors in the secondary coordination sphere.[49]

tion, effectively stabilizing intermediates for detection, while maintaining the desired catalytic activity.[50]

1.5 Shuttling protons to and from the active sites

1.5.1 Biological examples

Another important role of the protein superstructure in enzymes is to facilitate the controlled movement of protons in the active site. Perhaps the best-established example of this structure-function relationship is provided by cytochrome P450.[51-53] Activation of O_2 in this family of enzymes is regulated by efficient protonation during O–O bond cleavage, facilitated by a hydrogen-bonding chain of amino acid residues and associated water molecules. Two nearby residues, Thr252 and Asp251, play key roles in the controlled protonation of the Fe^{III}-peroxo species at the distal oxygen (Scheme 1.4).[54,55] Site-directed muta-

1st protonation   2nd protonation
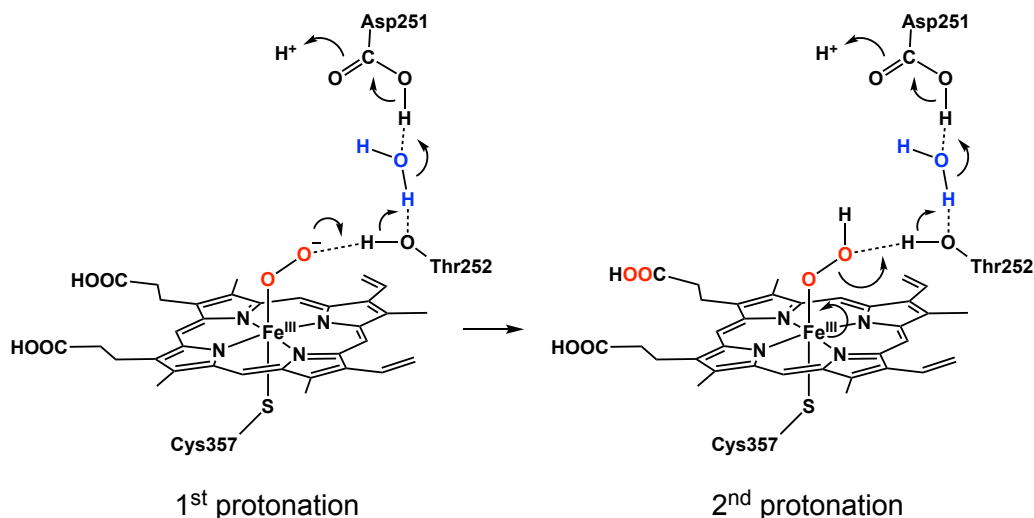
Scheme 1.4 Protonation of a Fe^{III}-peroxo intermediate in cytochrome P450 immediately prior to O–O bond cleav-

genesis in P450$_{cam}$ demonstrated the essential role of this pathway. Replacing the highly conserved Thr252 with other residues typically results in production of hydrogen peroxide in large excess instead of the desired substrate hydroxylation, likely due to uncontrolled protonation of the bound O_2 ligand by additional solvent introduced by the mutation. Mutations at Asp251 have also been demonstrated to dramatically increase the accessibility of the active site to bulk water by disrupting the hydrogen bonding network present in the wild-type enzyme, underscoring the importance of the interaction between Thr252 and Asp251 in productive enzymatic activity.[56]

Secondary sphere residues in extradiol dioxygenases play a similar role in controlling the movement of protons within the enzymes' active site. Lipscomb and coworkers have investigated the function of a conserved histidine (His200) in promoting the reactivity of homoprotocatechuate 2,3-dioxygenase (FeHPCD).[57] An important step in the catalytic cycle of the enzyme involves proton transfer from substrate to bound O_2, which was proposed to be facilitated by His200 based on its ideal positioning in structural analyses. The involvement of His200 in this manner was supported by a series of point mutations. Substitution with residues incapable of such proton transfer was found to dramatically decreased the en-

zyme's turnover frequency by 3- to 30-fold depending on the mutant. Reactivity with a non-native substrate, 4-nitrocatechol (4NC), gave further evidence for the essential role of His200, as only the wild type FeHPCD was capable of converting this electron deficient substrate to its ring cleavage product. Given that the 4-nitrocatechol binds in the fully deprotonated state, unlike the native substrate that binds in the monoprotonated form, Lipscomb and coworkers attribute the wild type enzyme's reactivity with 4NC to His200's ability to facilitate proton transfer from a hydrogen-bonding network that connects bulk solvent to the active site through this residue (Figure 1.9). When mutants incapable of this transfer are introduced, limiting the accessibility of external protons to the active site, reactivity towards the non-native substrate is lost. Similar proton transfer pathways have been proposed for salicylate 1,2-dioxygenase, a
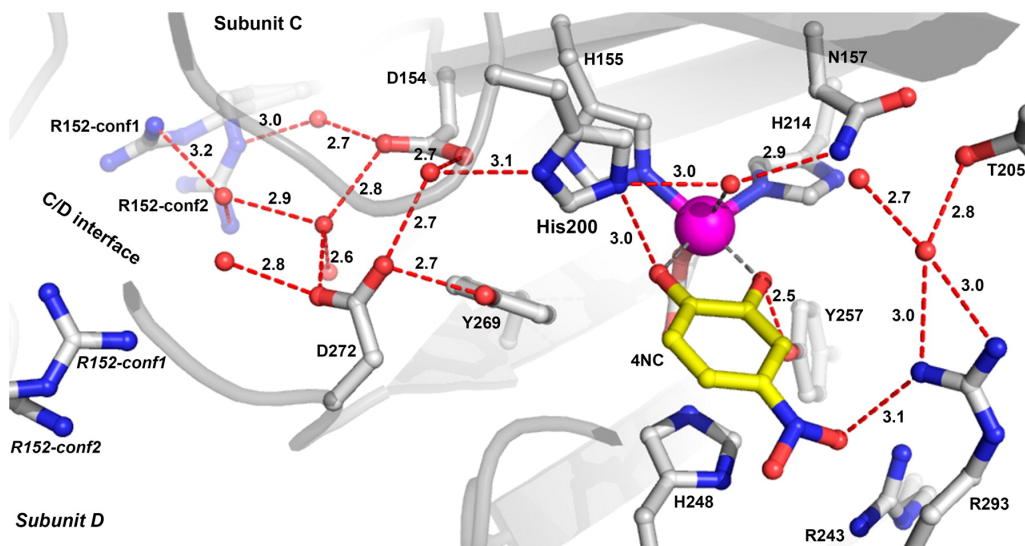

Figure 1.9 Proton-transfer pathway in the active sites of the FeHPCD in complex with 4NC (PDB entry 4GHH, subunit C). Atom color code: gray, carbon (enzyme); yellow, carbon (substrate); blue, nitrogen; red, oxygen; purple, iron. Red dashed lines show hydrogen bonds (reported in Å). Gray dashed lines indicate bonds or potential bonds to iron (Å). Reprinted with permission from reference 57. Copyright 2015 American Chemical Society.

related non-heme iron enzyme, further highlighting the importance of the secondary coordination sphere in facilitating controlled proton movement within the active site.[58-60]

1.5.2 Model systems

Inspired by these interactions, Nocera designed a series of Hangman porphyrins containing a pendant proton relay attached at one of the four *meso*-positions. After an initial report demonstrating the ability of the appended functionality to position a water molecule near the metal center (Figure 1.10),[61] these modified porphyrins (and related corrole derivatives) were shown to increase the selectivity in O–O bond cleavage processes.[62] Comparison of the carboxylic acid hangman porphyrin with both methyl ester hangman
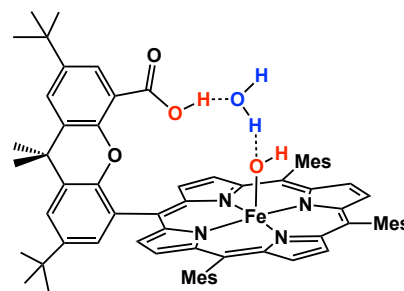

Figure 1.10 Hydrogen bonding interactions in Nocera's Fe(III)-OH Hangman porphyrin.[61]

and tetramesityl derivatives demonstrated that the pendant acid functionality disfavors one electron homolytic O–O bond cleavage, directing reactivity towards the two electron heterolytic pathway, similarly to secondary sphere residues in cytochrome P450 and related heme enzymes.[63] The pK_a of the pendant acidic functionality was also demonstrated to play an important role in discriminating between these two pathways.[64] The pendant acidic functionality in these hangman systems was shown to increase the selectivity in oxygen reduction by cobalt catalysts, where the percent of O_2 converted to H_2O was improved by 15-20% compared to the parent porphyrins and corroles.[65,66]

Mayer has used similar design principles, positioning carboxylic acid and pyridyl-based proton relays along the periphery of iron-porphyrin catalysts.[67,68] Comparison of the selectivity in oxygen reduction for inward- and outward-facing functionalities suggested careful positioning of pendant proton relays may be important to the reactivity in both cases (Figure 1.11). While later work with these catalysts demonstrated that choice of electrochemical medium led to larger differences in selectivity than catalyst modifications did, the inward-facing proton functionalities still resulted in higher selectivity for H_2O production in each
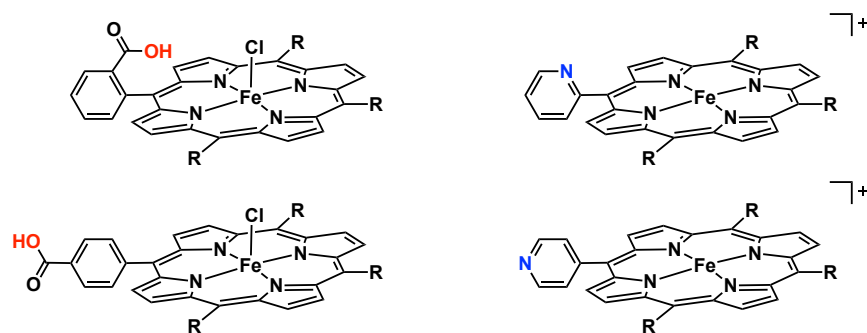

Figure 1.11 Electrocatalysts featuring pendant acid and base functionalities as potential proton transfer relays.

of the mediums used.[69] Mayer and co-workers have recently expanded upon this work, outlining a number of design criteria for developing non-heme ligands with pendant acid/base functionalities for small molecule activation.[70] Their report highlights the difficulty associated with applying these principles to non-heme systems for O_2 reduction chemistry, as selective protonation of the pendant functionality is often a challenge.

1.6 Development of new non-heme ligand frameworks with dynamic secondary sphere interactions

As the number of and complexity of model systems for dioxygen activation has expanded, researchers have been able to effectively emulate several key functions of the secondary coordination sphere and extended protein superstructure in metalloenzymes. These hydrogen bonding networks have been demonstrated to tune the interaction of primary coordination sphere ligands with the metal center, increase selectivity and binding affinity for O_2, and stabilize reactive species in model systems. However, the use of these appended groups as proton relays remains underexplored. Although Nocera, Mayer, and others

have demonstrated the utility of such relays in promoting selective dioxygen reduction with heme catalysts, translating these design principles to non-heme architectures remains an outstanding challenge.

Given the difficulties associated with selective protonation of appended acid/base functionalities, our research group has sought to incorporate dynamic secondary coordination sphere interactions via ligand tautomerization. Several frameworks have been developed containing pyrrole-imine moieties, elaborating on work by Love and co-workers.[71-73] These groups were targeted for their ability to tautomerize between pyrrole-imine and azafulvene-amine forms (Figure 1.12). When a first row transition metal is bound in the pocket formed by the pyrroles, and an additional apical nitrogen donor, the appended groups in the second sphere can switch between hydrogen bond acceptors (in the pyrrole-imine form) and donors (in the azafulvene-amine form) depending on i) the metallation route, ii) the nature of axially bound substrate, and iii) the oxidation state of the metal center.
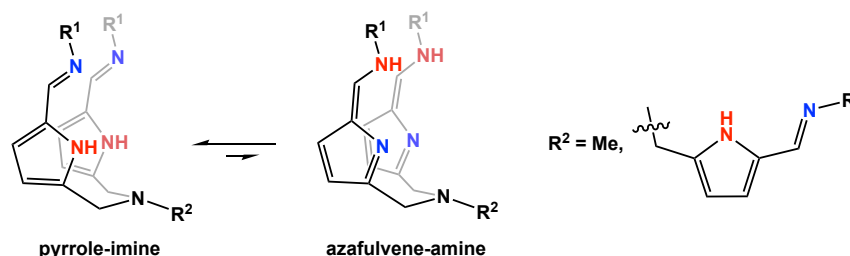

Figure 1.12 Ligand frameworks featuring dynamic second sphere interactions based on tautomerization of the pyrrole-imine ligand arms.

This thesis describes the following: 1) the development of a dipodal ligand framework based on the design principles outlined above and its use as a model for non-heme dioxygenases; 2) the derivatization of an analogous tripodal system, where primary and secondary coordination sphere modifications were pursued and their roles in determining the metal complexes' properties were examined; and 3) the application of the tripodal iron system in dioxygen activation. Finally, early work exploring the design and metallation of phenoxy-appended ligand architectures will be discussed.

1.7 References

(1)   Poulos, T. L. Heme Enzyme Structure and Function. *Chem. Rev.* **2014**, *114* (7), 3919–3962.
(2)   Solomon, E. I.; Goudarzi, S.; Sutherlin, K. D. O_2 Activation by Non-Heme Iron Enzymes. *Biochemistry* **2016**, *55* (46), 6363–6374.
(3)   Punniyamurthy, T.; Velusamy, S.; Iqbal, J. Recent Advances in Transition Metal Catalyzed Oxidation of Organic Substrates with Molecular Oxygen. *Chem. Rev.* **2005**, *105* (6), 2329–2364.
(4)   Shi, Z.; Zhang, C.; Tang, C.; Jiao, N. Recent Advances in Transition-Metal Catalyzed Reactions Using Molecular Oxygen as the Oxidant. *Chem. Soc. Rev.* **2012**, *41* (8), 3381–50.
(5)   Chen, Z.; Higgins, D.; Yu, A.; Zhang, L.; Zhang, J. A Review on Non-Precious Metal Electrocatalysts for PEM Fuel Cells. *Energy Environ. Sci.* **2011**, *4* (9), 3167–26.
(6)   Banham, D.; Ye, S.; Pei, K.; Ozaki, J.-I.; Kishimoto, T.; Imashiro, Y. A Review of the Stability and Durability of Non-Precious Metal Catalysts for the Oxygen Reduction Reaction in Proton Exchange Membrane Fuel Cells. *J. Power Sources* **2015**, *285* (C), 334–348.
(7)   Shook, R. L.; Borovik, A. S. Role of the Secondary Coordination Sphere in Metal-Mediated Di-

oxygen Activation. *Inorg. Chem.* **2010**, *49* (8), 3646–3660.

(8)   Sahu, S.; Goldberg, D. P. Activation of Dioxygen by Iron and Manganese Complexes: a Heme and Nonheme Perspective. *J. Am. Chem. Soc.* **2016**, *138* (36), 11410–11428.

(9)   Baglia, R. A.; Zaragoza, J. P. T.; Goldberg, D. P. Biomimetic Reactivity of Oxygen-Derived Manganese and Iron Porphyrinoid Complexes. *Chem. Rev.* **2017**, acs.chemrev.7b00180–33.

(10)   Fiedler, A. T.; Fischer, A. A. Oxygen Activation by Mononuclear Mn, Co, and Ni Centers in Biology and Synthetic Complexes. *J. Biol. Inorg. Chem.* **2016**, 1–18.

(11)   Dawson, J. H. Probing Structure-Function Relations in Heme-Containing Oxygenases and Peroxidases. *Science* **1988**, *240* (4851), 433–439.

(12)   Poulos, T. L. The Role of the Proximal Ligand in Heme Enzymes. *J. Biol. Inorg. Chem.* **1996**, *1* (4), 356–359.

(13)   Goodin, D. B.; McRee, D. E. The Asp-His-Fe Triad of Cytochrome *C* Peroxidase Controls the Reduction Potential, Electronic Structure, and Coupling of the Tryptophan Free Radical to the Heme. *Biochemistry* **1993**, *32* (13), 3313–3324.

(14)   Krest, C. M.; Silakov, A.; Rittle, J.; Yosca, T. H.; Onderko, E. L.; Calixto, J. C.; Green, M. T. Significantly Shorter Fe-S Bond in Cytochrome P450-I Is Consistent with Greater Reactivity Relative to Chloroperoxidase. *Nat. Chem.* **2015**, 1–7.

(15)   Kal, S.; Que, L., Jr. Dioxygen Activation by Nonheme Iron Enzymes with the 2-His-1-Carboxylate Facial Triad That Generate High-Valent Oxoiron Oxidants. *J. Biol. Inorg. Chem.* **2017**, 1–27.

(16)   Light, K. M.; Hangasky, J. A.; Knapp, M. J.; Solomon, E. I. First- and Second-Sphere Contributions to Fe(II) Site Activation by Cosubstrate Binding in Non-Heme Fe Enzymes. *Dalton Trans.* **2014**, *43* (4), 1505–1508.

(17)   Light, K. M.; Hangasky, J. A.; Knapp, M. J.; Solomon, E. I. Spectroscopic Studies of the Mononuclear Non-Heme Fe[II] Enzyme FIH: Second-Sphere Contributions to Reactivity. *J. Am. Chem. Soc.* **2013**, *135* (26), 9665–9674.

(18)   Saban, E.; Chen, Y.-H.; A Hangasky, J.; Y Taabazuing, C.; Holmes, B. E.; Knapp, M. J. The Second Coordination Sphere of FIH Controls Hydroxylation. *Biochemistry* **2011**, *50* (21), 4733–4740.

(19)   Ueyama, N.; Nishikawa, N.; Yamada, Y.; Okamura, T.-A.; Nakamura, A. Cytochrome P-450 Model (Porphinato)(Thiolato)Iron(III) Complexes with Single and Double NH⋯S Hydrogen Bonds at the Thiolate Site. *J. Am. Chem. Soc.* **1996**, *118* (50), 12826–12827.

(20)   Ueyama, N.; Nishikawa, N.; Yamada, Y.; Okamura, T.-A.; Oka, S.; Sakurai, H.; Nakamura, A. Synthesis and Properties of Octaethylporphinato(Arenethiolato)Iron(III) Complexes with Intramolecular NH⋯S Hydrogen Bond: Chemical Function of the Hydrogen Bond. *Inorg. Chem.* **1998**, *37* (10), 2415–2421.

(21)   Dey, A.; Okamura, T.-A.; Ueyama, N.; Hedman, B.; Hodgson, K. O.; Solomon, E. I. Sulfur K-Edge XAS and DFT Calculations on P450 Model Complexes: Effects of Hydrogen Bonding on Electronic Structure and Redox Potentials. *J. Am. Chem. Soc.* **2005**, *127* (34), 12046–12053.

(22)   Suzuki, N.; Higuchi, T.; Urano, Y.; Kikuchi, K.; Uekusa, H.; Ohashi, Y.; Uchida, T.; Kitagawa, T.; Nagano, T. Novel Iron Porphyrin−Alkanethiolate Complex with Intramolecular NH⋯S Hydrogen Bond: Synthesis, Spectroscopy, and Reactivity. *J. Am. Chem. Soc.* **1999**, *121* (49), 11571–11572.

(23)   Szajna, E.; Arif, A. M.; Berreau, L. M. Aliphatic Carbon−Carbon Bond Cleavage Reactivity of a Mononuclear Ni(II) Cis-*B*-Keto−Enolate Complex in the Presence of Base and O_2: A Model Reaction for Acireductone Dioxygenase (ARD). *J. Am. Chem. Soc.* **2005**, *127* (49), 17186–17187.

(24)   Szajna-Fuller, E.; Chambers, B. M.; Arif, A. M.; Berreau, L. M. Carboxylate Coordination Chemistry of a Mononuclear Ni(II) Center in a Hydrophobic or Hydrogen Bond Donor Secondary Environment: Relevance to Acireductone Dioxygenase. *Inorg. Chem.* **2007**, *46* (14), 5486–5498.

(25)   Jain, R.; Chan, M. Mechanisms of Ligand Discrimination by Heme Proteins. *J. Biol. Inorg. Chem.* **2003**, *8* (1-2), 1–11.

(26)   Springer, B. A.; Sligar, S. G.; Olson, J. S.; Phillips, G. N., Jr. Mechanisms of Ligand Recognition in Myoglobin. *Chem. Rev.* **1994**, *94* (3), 699–714.

(27)   Kuriyan, J.; Wilz, S.; Karplus, M.; Petsko, G. A. X-Ray Structure and Refinement of Carbon-Monoxy (Fe II)-Myoglobin at 1.5 Å Resolution. *J. Mol. Biol.* **1986**, *192* (1), 133–154.

(28)   Lim, M.; Jackson, T. A.; Anfinrud, P. A. Binding of CO to Myoglobin From a Heme Pocket Docking Site to Form Nearly Linear Fe-CO. *Science* **1995**, *269* (5226), 962–966.

(29)   Kachalova, G. S.; Popov, A. N.; Bartunik, H. D. A Steric Mechanism for Inhibition of CO Binding to Heme Proteins. *Science* **1999**, *284* (5413), 473–476.

(30)   Vojtěchovský, J.; Chu, K.; Berendzen, J.; Sweet, R. M.; Schlichting, I. Crystal Structures of Myoglobin-Ligand Complexes at Near-Atomic Resolution. *Biophys. J.* **1999**, *77*, 2153–2174.

(31)   Springer, B. A.; Egeberg, K. D.; Sligar, S. G.; Rohlfs, R. J.; Mathews, A. J.; Olson, J. S. Discrimination Between Oxygen and Carbon Monoxide and Inhibition of Autooxidation by Myoglobin. Site-Directed Mutagenesis of the Distal Histidine. *J. Biol. Chem.* **1989**, *264* (6), 3057–3060.

(32)   Gong, W.; Hao, B.; Mansy, S. S.; Gonzalez, G.; Gilles-Gonzalez, M. A.; Chan, M. K. Structure of a Biological Oxygen Sensor: a New Mechanism for Heme-Driven Signal Transduction. *Proc. Natl. Acad. Sci. USA* **1998**, *95* (26), 15177–15182.

(33)   Gong, W.; Hao, B.; Chan, M. K. New Mechanistic Insights From Structural Studies of the Oxygen-Sensing Domain of *Bradyrhizobium Japonicum* FixL. *Biochemistry* **2000**, *39* (14), 3955–3962.

(34)   Hao, B.; Isaza, C.; Arndt, J.; Soltis, M.; Chan, M. K. Structure-Based Mechanism of O_2 Sensing and Ligand Discrimination by the FixL Heme Domain of *Bradyrhizobium Japonicum*. *Biochemistry* **2002**, *41* (43), 12952–12958.

(35)   Kossanyi, A.; Tani, F.; Nakamura, N.; Naruta, Y. Properties of a Binaphthyl-Bridged Porphyrin-Iron Complex Bearing Hydroxy Groups Inside Its Cavity. *Chem. Eur. J.* **2001**, *7* (13), 2862–2872.

(36)   Tani, F.; Matsu-ura, M.; Ariyama, K.; Setoyama, T.; Shimada, T.; Kobayashi, S.; Hayashi, T.; Matsuo, T.; Hisaeda, Y.; Naruta, Y. Iron Twin-Coronet Porphyrins as Models of Myoglobin and Hemoglobin: Amphibious Electrostatic Effects of Overhanging Hydroxyl Groups for Successful CO/O_2 Discrimination. *Chem. Eur. J.* **2003**, *9* (4), 862–870.

(37)   Matsu-ura, M.; Tani, F.; Naruta, Y. Formation and Characterization of Carbon Monoxide Adducts of Iron "Twin Coronet" Porphyrins. Extremely Low CO Affinity and a Strong Negative Polar Effect on Bound CO. *J. Am. Chem. Soc.* **2002**, *124* (9), 1941–1950.

(38)   Matsu-ura, M.; Tani, F.; Nakayama, S.; Nakamura, N.; Naruta, Y. Hydrogen-Bonded Dioxygen Adduct of an Iron Porphyrin with an Alkanethiolate Ligand: an Elaborate Model of Cytochrome P450. *Angew. Chem. Int. Ed.* **2000**, *39* (11), 1989–1991.

(39)   Mitchell, A. J.; Zhu, Q.; Maggiolo, A. O.; Ananth, N. R.; Hillwig, M. L.; Liu, X.; Boal, A. K. Structural Basis for Halogenation by Iron- and 2-Oxo-Glutarate-Dependent Enzyme WelO5. *Nat. Chem. Biol.* **2016**, *12* (8), 636–640.

(40)   Blasiak, L. C.; Vaillancourt, F. H.; Walsh, C. T.; Drennan, C. L. Crystal Structure of the Non-Haem Iron Halogenase SyrB2 in Syringomycin Biosynthesis. *Nature* **2006**, *440* (7082), 368–371.

(41)   Wong, C.; Fujimori, D. G.; Walsh, C. T.; Drennan, C. L. Structural Analysis of an Open Active Site Conformation of Nonheme Iron Halogenase CytC3. *J. Am. Chem. Soc.* **2009**, *131* (13), 4872–4879.

(42)   Khare, D.; Wang, B.; Gu, L.; Razelun, J.; Sherman, D. H.; Gerwick, W. H.; Håkansson, K.; Smith, J. L. Conformational Switch Triggered by Alpha-Ketoglutarate in a Halogenase of Curacin a Biosynthesis. *Proc. Natl. Acad. Sci. U.S.A.* **2010**, *107* (32), 14099–14104.

(43)   Wong, S. D.; Srnec, M.; Matthews, M. L.; Liu, L. V.; Kwak, Y.; Park, K.; Bell, C. B., III; Alp,

15

E. E.; Zhao, J.; Yoda, Y.; Kitao, S.; Seto, M.; Krebs, C.; Bollinger, J. M.; Solomon, E. I. Elucidation of the Fe(IV)=O Intermediate in the Catalytic Cycle of the Halogenase SyrB2. *Nature* **2013**, *499* (7458), 320–323.

(44)   Matthews, M. L.; Neumann, C. S.; Miles, L. A.; Grove, T. L.; Booker, S. J.; Krebs, C.; Walsh, C. T.; Bollinger, J. M. Substrate Positioning Controls the Partition Between Halogenation and Hydroxylation in the Aliphatic Halogenase, SyrB2. *Proc. Natl. Acad. Sci. U.S.A.* **2009**, *106* (42), 17723–17728.

(45)   Martinie, R. J.; Livada, J.; Chang, W.-C.; Green, M. T.; Krebs, C.; Bollinger, J. M., Jr.; Silakov, A. Experimental Correlation of Substrate Position with Reaction Outcome in the Aliphatic Halogenase, SyrB2. *J. Am. Chem. Soc.* **2015**, *137* (21), 6912–6919.

(46)   Kitajima, N.; Komatsuzaki, H.; Hikichi, S.; Osawa, M.; Moro-oka, Y. A Monomeric Side-on Peroxo Manganese(III) Complex: $Mn(O_2)(3,5-iPr_2pzH)(HB(3,5-iPr_2Pz)_3)$. *J. Am. Chem. Soc.* **1994**, *116* (25), 11596–11597.

(47)   Wada, A.; Harata, M.; Hasegawa, K.; Jitsukawa, K.; Masuda, H.; Mukai, M.; Kitagawa, T.; Einaga, H. Structural and Spectroscopic Characterization of a Mononuclear Hydroperoxo–Copper(II) Complex with Tripodal Pyridylamine Ligands. *Angew. Chem. Int. Ed.* **1998**, *37* (6), 798–799.

(48)   MacBeth, C. E.; Golombek, A. P.; Young, V. G.; Yang, C.; Kuczera, K.; Hendrich, M. P.; Borovik, A. S. O_2 Activation by Nonheme Iron Complexes: a Monomeric Fe(III)-Oxo Complex Derived From O_2. *Science* **2000**, *289* (5481), 938–941.

(49)   Lucas, R. L.; Zart, M. K.; Mukherjee, J.; Sorrell, T. N.; Powell, D. R.; Borovik, A. S. A Modular Approach Toward Regulating the Secondary Coordination Sphere of Metal Ions: Differential Dioxygen Activation Assisted by Intramolecular Hydrogen Bonds. *J. Am. Chem. Soc.* **2006**, *128* (48), 15476–15489.

(50)   Shook, R. L.; Peterson, S. M.; Greaves, J.; Moore, C.; Rheingold, A. L.; Borovik, A. S. Catalytic Reduction of Dioxygen to Water with a Monomeric Manganese Complex at Room Temperature. *J. Am. Chem. Soc.* **2011**, *133* (15), 5810–5817.

(51)   Meunier, B.; de Visser, S. P.; Shaik, S. Mechanism of Oxidation Reactions Catalyzed by Cytochrome P450 Enzymes. *Chem. Rev.* **2004**, *104* (9), 3947–3980.

(52)   Denisov, I. G.; Makris, T. M.; Sligar, S. G.; Schlichting, I. Structure and Chemistry of Cytochrome P450. *Chem. Rev.* **2005**, *105* (6), 2253–2278.

(53)   Shaik, S.; Cohen, S.; Wang, Y.; Chen, H.; Kumar, D.; Thiel, W. P450 Enzymes: Their Structure, Reactivity, and Selectivity—Modeled by QM/MM Calculations. *Chem. Rev.* **2010**, *110* (2), 949–1017.

(54)   Raag, R.; Martinis, S. A.; Sligar, S. G.; Poulos, T. L. Crystal Structure of the Cytochrome P-450$_{Cam}$ Active Site Mutant Thr252Ala. *Biochemistry* **1991**, *30* (48), 11420–11429.

(55)   Gerber, N. C.; Sligar, S. G. Catalytic Mechanism of Cytochrome P-450: Evidence for a Distal Charge Relay. *J. Am. Chem. Soc.* **1992**, *114* (22), 8742–8743.

(56)   Vidakovic, M.; Sligar, S. G.; Li, H.; Poulos, T. L. Understanding the Role of the Essential Asp251 in Cytochrome P450cam Using Site-Directed Mutagenesis, Crystallography, and Kinetic Solvent Isotope Effect. *Biochemistry* **1998**, *37* (26), 9211–9219.

(57)   Kovaleva, E. G.; Rogers, M. S.; Lipscomb, J. D. Structural Basis for Substrate and Oxygen Activation in Homoprotocatechuate 2,3-Dioxygenase: Roles of Conserved Active Site Histidine 200. *Biochemistry* **2015**, *54* (34), 5329–5339.

(58)   Ferraroni, M.; Steimer, L.; Matera, I.; Bürger, S.; Scozzafava, A.; Stolz, A.; Briganti, F. The Generation of a 1-Hydroxy-2-Naphthoate 1,2-Dioxygenase by Single Point Mutations of Salicylate 1,2-Dioxygenase - Rational Design of Mutants and the Crystal Structures of the A85H and W104Y Variants. *J. Struct. Biol.* **2012**, *180* (3), 563–571.

(59)   Eppinger, E.; Ferraroni, M.; Bürger, S.; Steimer, L.; Peng, G.; Briganti, F.; Stolz, A. Function of Different Amino Acid Residues in the Reaction Mechanism of Gentisate 1,2-Dioxygenases Deduced From the Analysis of Mutants of the Salicylate 1,2-Dioxygenase From *Pseudaminobacter*

Salicylatoxidans. *Biochim. Biophys. Acta, Proteins Proteomics* **2015**, *1854* (PA), 1425–1437.

(60) Dong, G.; Ryde, U. O$_2$ Activation in Salicylate 1,2-Dioxygenase: a QM/MM Study Reveals the Role of His162. *Inorg. Chem.* **2016**, *55* (22), 11727–11735.

(61) Yeh, C.-Y.; Chang, C. J.; Nocera, D. G. "Hangman" Porphyrins for the Assembly of a Model Heme Water Channel. *J. Am. Chem. Soc.* **2001**, *123* (7), 1513–1514.

(62) Rosenthal, J.; Nocera, D. G. Role of Proton-Coupled Electron Transfer in O–O Bond Activation. *Acc. Chem. Res.* **2007**, *40* (7), 543–553.

(63) Soper, J. D.; Kryatov, S. V.; Rybak-Akimova, E. V.; Nocera, D. G. Proton-Directed Redox Control of O−O Bond Activation by Heme Hydroperoxidase Models. *J. Am. Chem. Soc.* **2007**, *129* (16), 5069–5075.

(64) Chng, L. L.; Chang, C. J.; Nocera, D. G. Catalytic O−O Activation Chemistry Mediated by Iron Hangman Porphyrins with a Wide Range of Proton-Donating Abilities. *Org. Lett.* **2003**, *5* (14), 2421–2424.

(65) McGuire, R., Jr; Dogutan, D. K.; Teets, T. S.; Suntivich, J.; Shao-Horn, Y.; Nocera, D. G. Oxygen Reduction Reactivity of Cobalt(II) Hangman Porphyrins. *Chem. Sci.* **2010**, *1* (3), 411–414.

(66) Dogutan, D. K.; Stoian, S. A.; McGuire, R., Jr; Schwalbe, M.; Teets, T. S.; Nocera, D. G. Hangman Corroles: Efficient Synthesis and Oxygen Reaction Chemistry. *J. Am. Chem. Soc.* **2011**, *133* (1), 131–140.

(67) Carver, C. T.; Matson, B. D.; Mayer, J. M. Electrocatalytic Oxygen Reduction by Iron Tetra-Arylporphyrins Bearing Pendant Proton Relays. *J. Am. Chem. Soc.* **2012**, *134* (12), 5444–5447.

(68) Matson, B. D.; Carver, C. T.; Ruden, Von, A.; Yang, J. Y.; Raugei, S.; Mayer, J. M. Distant Protonated Pyridine Groups in Water-Soluble Iron Porphyrin Electrocatalysts Promote Selective Oxygen Reduction to Water. *Chem. Commun.* **2012**, *48* (90), 11100–11103.

(69) Rigsby, M. L.; Wasylenko, D. J.; Pegis, M. L.; Mayer, J. M. Medium Effects Are as Important as Catalyst Design for Selectivity in Electrocatalytic Oxygen Reduction by Iron-Porphyrin Complexes. *J. Am. Chem. Soc.* **2015**, *137* (13), 4296–4299.

(70) Blacquiere, J. M.; Pegis, M. L.; Raugei, S.; Kaminsky, W.; Forget, A.; Cook, S. A.; Taguchi, T.; Mayer, J. M. Synthesis and Reactivity of Tripodal Complexes Containing Pendant Bases. *Inorg. Chem.* **2014**, *53* (17), 9242–9253.

(71) Reid, S. D.; Blake, A. J.; K ckenberger, W.; Wilson, C.; Love, J. B. Double-Stranded, [4 + 4] Helicates of Fe(II) and Mn(II) Supported by an Extended Dipyrrolide Ligand. *Dalton Trans.* **2003**, No. 23, 4387–4388.

(72) Reid, S. D.; Wilson, C.; Blake, A. J.; Love, J. B. Tautomerisation and Hydrogen-Bonding Interactions in Four-Coordinate Metal Halide and Azide Complexes of N-Donor-Extended Dipyrromethanes. *Dalton Trans.* **2010**, *39* (2), 418–425.

(73) Hart, J. S.; White, F. J.; Love, J. B. Donor-Extended Tripodal Pyrroles: Encapsulation, Metallation, and H-Bonded Tautomers. *Chem. Commun.* **2011**, *47* (20), 5711–5713.

CHAPTER 2: FLEXIBLE COORDINATION MODES OF A DIPODAL LIGAND FRAMEWORK FEATURING A SECONDARY COORDINATION SPHERE AND APPLICATION OF THE IRON(II) COMPLEXES IN *O*-PHENYLENE DIOXYGENASE REACTIVITY[†]

2.1 Introduction

Hydrogen bond donating/accepting ligands and redox active amino acids play a number of important roles in reactivity mediated by metalloenzymes.[1-6] These well-positioned hydrogen bonds or amino acids (e.g. tyrosine, tryptophan, and histidine) ease the electronic burden placed on the metal center during the activation of small molecules.[1-12] Taking a cue from Nature, we and others have designed ligand scaffolds that feature a secondary coordination sphere capable of tautomerizing to be either hydrogen bond donating or accepting depending on the metal-bound ancillary ligand and the oxidation state of the metal center.[13-18] An additional redox-active ligand may also be coordinated to the metal center to facilitate activation of substrates, such as dioxygen, while the secondary coordination sphere can stabilize the resulting reactive intermediates. The studies described in this report focus on the development of iron complexes featuring a dipodal platform with a hydrogen bond donating or accepting secondary coordination. Herein, we report a structurally diverse family of metal complexes with the dipodal ligand, $H_2[^{Me}N(pi^{Cy})_2]$, demonstrating the flexibility of this framework driven by its interactions with ancillary ligands. Metallation of the ligand with iron(II) salts and subsequent binding of redox active fragments (2,2′-bipyridine; 1,10-phenanthroline; 3,5-di-*tert*-butylcatechol; and 2-amino-4,6-di-*tert*-butylphenol) is described. Finally, reactivity of the iron(II) *ortho*-phenylene complexes towards dioxygen is explored.

2.2 Synthesis and metallation of the dipodal ligand

In an effort to synthesize sterically unencumbered dipodal ligand derivatives of the tripodal system recently reported by our group,[13] a platform with a single arm removed was designed based on the pyrrole-derived *N,N*-di(pyrrolyl-α-methyl)-*N*-methylamine (H$_2$dpma) reported previously by Odom and coworkers.[19] Installation of an aldehyde substituent in the 5 position of the pyrrole rings of H$_2$dmpa was accomplished by a Vilsmeier Haack Formylation.[20] Following workup, addition of an excess of cyclohexylamine in acetonitrile afforded the desired ligand, *N,N*-di(5-cyclohexylimmino-pyrrolyl-α-methyl)-*N*-methylamine, $H_2[^{Me}N(pi^{Cy})_2]$ (**1**) (Scheme 2.1).
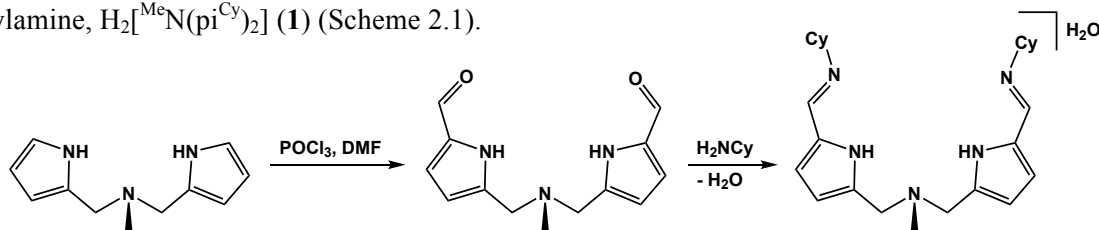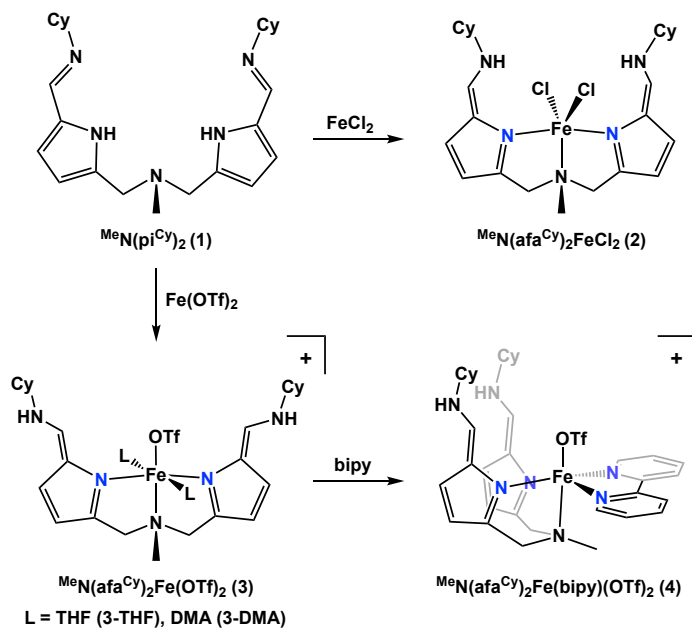

Scheme 2.1 Synthesis of the ligand hydrate, $H_2[^{Me}N(pi^{Cy})_2] \cdot H_2O$ (**1 · H₂O**).

† Portions of this chapter are reproduced from the following publication with permission from the authors. Matson, E. M.; Gordon, Z.; Lin, B.; Nilges, M. J.; Fout, A. R. *Dalton Trans.*, **2014**, *43*, 16992–16995.

Primarily interested in understanding the effects of the secondary coordination sphere provided by the pendant functional groups of the ligand framework, two pathways were pursued for metallation. The anionic coordination mode of the ligand was found to be undesirable, as attempts to synthesize mononuclear species by the addition of ligand in the presence of a variety of Lewis bases resulted in formation of a dimeric helicate species exclusively.[14] In analogy to the work of Love and co-workers, generation of the azafulvene derivative, $H_2[^{Me}N(afa^{Cy})_2]$, was attempted by addition of $H_2[^{Me}N(pi^{Cy})_2]$ to a THF slurry of $FeCl_2$, resulting in a gradual color change from tan to orange.[15] Following workup, analysis by ^1H NMR spectroscopy revealed the formation of a new paramagnetic product with 16 resonances ranging from −5.8 to 154.2 ppm and a spectrum which is consistent with C_s symmetry about the metal center in solution. The electronic absorption spectrum of **2** was relatively featureless, save for a strong band at 333 nm ($\varepsilon = 63100$ M^{-1} s^{-1}) assigned to the π–π* transition of the azafulvene ligand.

Characterization of the product by X-ray crystallography revealed a five-coordinate iron center in a distorted trigonal bipyramidal geometry, with the desired di(amino-azafulvene) ligand framework, $^{Me}N(afa^{Cy})_2FeCl_2$ (**2**) (Figure 2.1). The dipodal ligand is coordinated to the metal in an intriguing pseudoplanar fashion. This ligand coordination mode is exemplified by the N2–Fe1–N4 bond angle of 150.60(10)°, which deviates significantly from the N–Fe–N bond angles in the tripodal derivative (~115°).[13] The pendant amines of complex **2** extend outward from the primary coordi-

Scheme 2.2 Synthesis of iron(II) complexes **2-4**.

nation sphere of the metal center, engaging in hydrogen bonding with the coordinated chlorides. Characterization of **2** by Mössbauer spectroscopy revealed a high spin Fe(II) center with a symmetric ligand field environment ($\delta = 1.05$ mm s^{-1}; $\Delta E_Q = 3.14$ mm s^{-1}),[21] consistent with the measured μ_{eff} of 5.47(4) μ_B (Figure 2.2). The measured magnetic moment compares favorably with calculated values for high spin, Fe(II), $g = 2$ ion ($\mu_{calc} = 4.90$ μ_B), and similar species reported by Love and co-workers.[15]

To synthesize a variant of complex **2** with non-coordinating anions, the ligand was added to a THF solution of $Fe(OTf)_2(MeCN)_2$. An immediate color change from tan to yellow was observed. Crystallization of the product via vapor diffusion of diethyl ether into a solution of acetonitrile and THF (1 : 3) revealed an octahedral iron species, $^{Me}N(afa^{Cy})_2Fe(OTf)_2(THF)_2$ (**3-THF**) where the ligand framework and
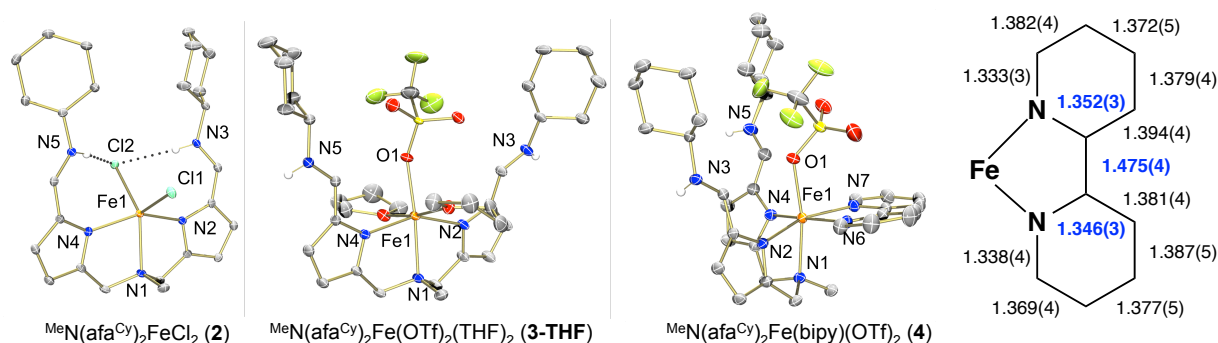
Figure 2.1 Molecular structures of complexes **2**–**4** shown with 50% probability ellipsoids. Selected hydrogen atoms, counter ions and solvent molecules have been removed for clarity. Diagram depicting bond lengths (Å) in the bipyridine ligand of complex **4** illustrating bond distances consistent with neutral coordination of the ligand (right).

one triflate anion occupy the equatorial plane with two THF molecules coordinated in the axial positions (Figure 2.1). In contrast to complex **2**, the pendant amines point away from the secondary coordination sphere of the complex, engaging in hydrogen bonding with the outer sphere triflate anion. Similar structural properties were observed when single crystals were grown from a mixture of benzene and dimethylacetamide (DMA) (10 : 1), where the bound THF solvent molecules were replaced by DMA. The molecular structure of **3-DMA** definitively depicts a distorted octahedral species, but the poor quality of the X-ray data prevents the discussion of any specific metrical parameters.

Characterization of complex **3**, crystallized from a THF–acetonitrile mixture, by Mössbauer spectroscopy revealed two species. The first is electronically similar to complex **2** (δ = 1.1 mm s^{-1}; ΔE_Q = 3 mm s^{-1}), suggesting a desolvated structure, and the second resembling an octahedral ligand environment for a high spin Fe(II) species with a nearly identical isomer shift, but dramatically decreased quadrupole splitting (δ = 1.09 mm s^{-1}; ΔE_Q = 1.02 mm s^{-1}) (Figure 2.2). The Mössbauer spectrum of **3-DMA** (δ = 1.14 mm s^{-1}; ΔE_Q = 1.49 mm s^{-1}) is consistent with the stringent octahedral ligand environment due to the coordination of the DMA solvent compared to the fluxionality of the solvent molecules in complex **3** (Figure 2.2).
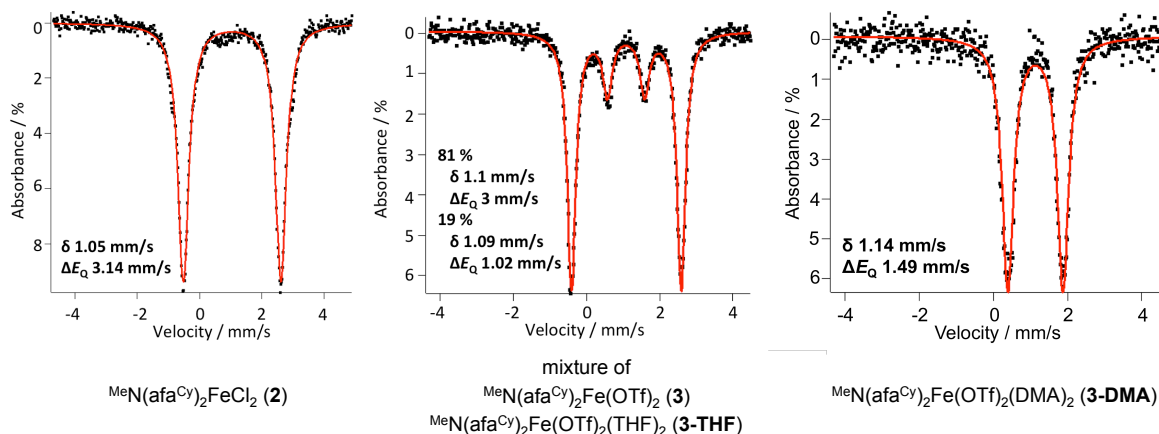

Figure 2.2 Mössbauer spectra of complexes **2** (left), **3(-THF)** (center), and **3-DMA** (right).

2.3 Binding of an ancillary redox-active fragment, 2,2'-bipyridine

Attempts to reduce complexes **2** and **3** (or **3-DMA**) resulted in decomposition of the metal species as evidenced by the observance of free ligand in the ^{1}H NMR spectrum. In an effort to elaborate on the electrochemical character of complexes **2** and **3**, and to prevent dimerization upon oxidation, the addition of a redox activity moiety was targeted. An equivalent of 2,2′-bipyridine was added as a solid to a solution of **3**. An immediate color change from yellow to magenta was noted, however, ^{1}H NMR spectroscopy depicted a similar spectrum to that of **3** with three resonances in the aryl region. Upon further analysis these signals were assigned to previously reported low spin $[Fe(bipy)_3]^{2+}$ complex.[22,23]

The Mössbauer spectrum of the product mixture depicts the presence of both an Fe(II) high spin species (δ = 1.08 mm s^{-1}, ΔE_Q = 2.64 mm s^{-1}) and an Fe(II) low spin impurity (δ = 0.35 mm s^{-1}, ΔE_Q = 0.30 mm s^{-1}).[21] This low spin species corresponds to the spectrum for $[Fe(bipy)_3]^{2+}$ reported previously (Figure 2.3).[22,23] The relative percentages of the two complexes extracted from Mössbauer data were consistent with integration values found using an internal standard by ^{1}H NMR spectroscopy. Additionally, the electronic absorption spectrum of the reaction mixture has two bands located at 294 nm (ε = 2800 M^{-1} cm^{-1}) and 518 nm (ε = 230 M^{-1} cm^{-1}), assigned to the π–π* and MLCT transitions of the $[Fe(bipy)_3]^{2+}$ impurity (Figure 2.3).[22,23] The absorption intensity matches appropriately when independently collected data for the tris bipyridine complex are scaled by its percentage in the mixture.

Figure 2.3 Mössbauer and electronic absorption spectra of complex **4**.

To elucidate the identity of the high spin component, structural analysis of a single crystal grown from a concentrated MeCN–Et$_2$O solution (1 : 1) was performed via X-ray crystallography. Refinement of the data revealed a new, facial coordination geometry of the ligand to the iron center, resulting in the formation of $^{Me}N(afa^{Cy})_2Fe(bipy)(OTf)_2$ (**4**) (Figure 2.1). Ligand reorganization yields a pseudooctahedral iron center with two azafulvene nitrogens and the nitrogen atoms of the bipyridine forming the equatorial plane; the apical nitrogen of the ligand framework and a triflate occupy the axial positions. Analysis of the structural data collected at 170 K revealed no bond perturbations that would be consistent with reduction of the bipyridine ligand, confirming the assignment of the oxidation state of **4** as Fe(II). This observation is consistent with the Mössbauer data collected on the mixture of products. Despite exhaustive attempts to separate the two species, isolation of complex **4** was not achieved.

Given the ability of 2,2′-bipyridine and related 2,2′-diimine ligands to support a radical anion, the re-duction chemistry of **4** (and the analogous complex of 1,10-phenanthroline) was explored. Treatment of the datively coordinated iron(II)-diimine complexes with potassium graphite (KC$_8$) resulted primarily in formation of the dimeric helicate species previously observed, as determined by ^{1}H NMR spectroscopy. Given the similar behavior observed in solution following binding of 2,2′-bipyridine in complex **4**, crys-tallographic characterization was attempted nonetheless to determine if the diimine ligand was reduced in this system (Scheme 2.3). Vapor diffusion of hexane into a solution of the material isolated from reac-

^{Me}N(afa^{Cy})$_2$FeBr$_2$ (2-Br) ^{Me}N(afa^{Cy})$_2$Fe(phen)Br$_2$ (5) ^{Me}N(pi^{Cy})$_2$Fe(phen)(H$_2$O) (6)
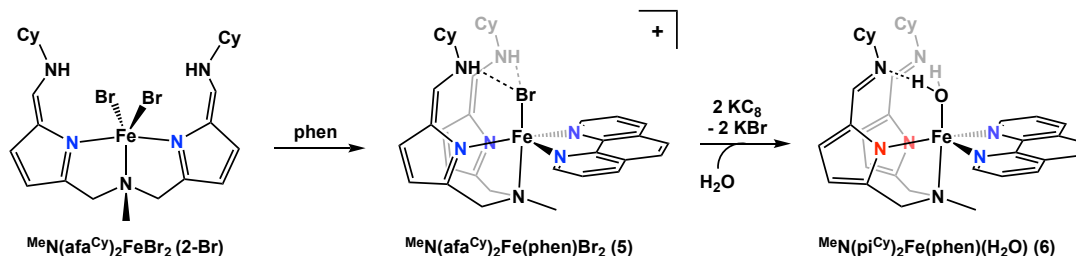
Scheme 2.3 Coordination of 1,10-phenanthroline, yielding complex **5,** and its subsequent reduction to **6**. As noted in the text, complexes **5** and **6** both represent a single component from a mixture of iron species present in solution.

tion of ^{Me}N(afa^{Cy})$_2$Fe(phen)Br$_2$ (**5**) with two equivalents of KC$_8$ yielded single crystals suitable for X-ray diffraction analysis. Refinement of the data resulted in a structural model consisting of an iron complex bound in an octahedral geometry with the azafulvene donors of the facially bound dipodal ligand and the phenanthroline nitrogens comprising the equatorial plane. The axial position is occupied by an aquo lig-and, resulting from adventitious water in the crystallization solvents, yielding ^{Me}N(pi^{Cy})$_2$Fe(phen)(H$_2$O) (**6**). The binding mode of the dipodal ligand was confirmed crystallographically by comparing bond lengths throughout the ligand arm with the datively coordination ligand in complex **4** (Figure 2.4). Ap-propriate elongations and contractions were noted throughout the pi-system, indicative of tautomerization to the pyrrole-imine binding mode in **6**. While ^{1}H NMR spectroscopy suggested this complex represents a minor component of the species present in solution, it demonstrated that ligand tautomerization could be used to access anionic coordination of the ligand when an appropriate ancillary fragment is bound.
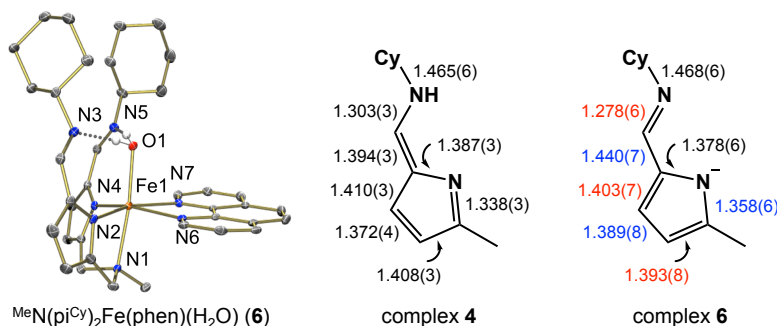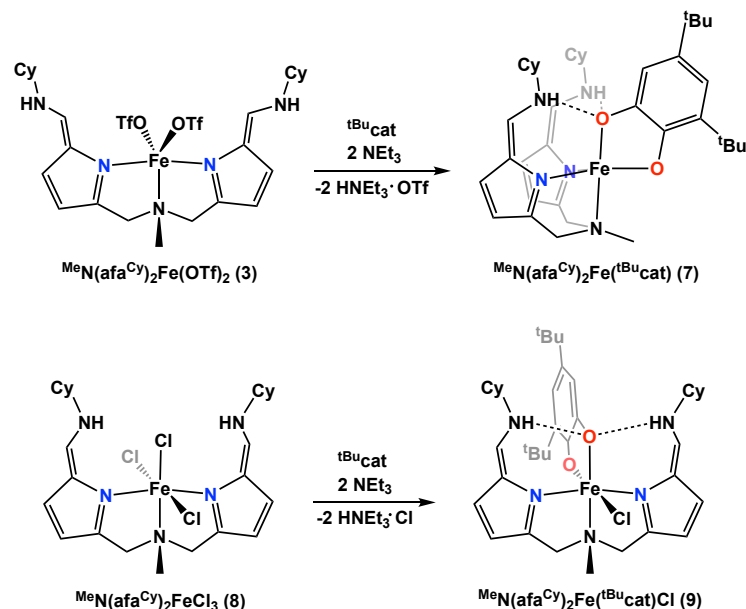

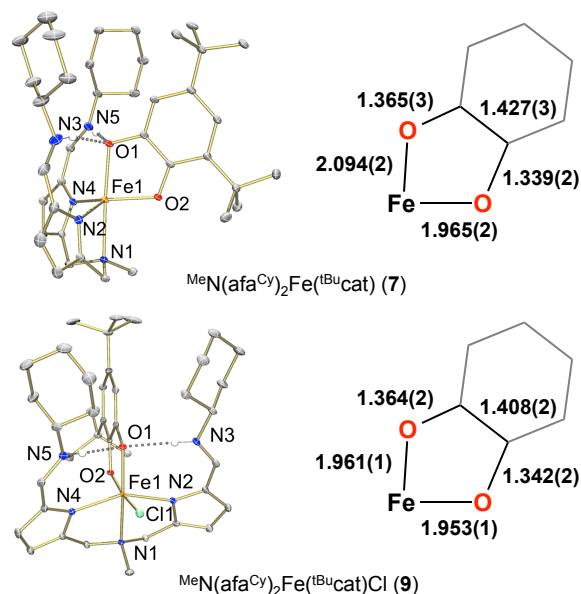^{Me}N(pi^{Cy})$_2$Fe(phen)(H$_2$O) (**6**)   complex **4**   complex **6**

Figure 2.4 Molecular structure of complex **6** shown with 50% probability ellipsoids. For clarity, only the aquo pro-tons are shown (left). Diagram depicting bond lengths (Å) in the ligand π-system for complexes **4** (center) and **6** (right). Bond contractions (red) and elongations (blue) in **6** are consistent with tautomerization from the dative, azafulvene coordination mode in **4** to anionic, pyrrole coordination in **6**.

22

2.4 Binding of *ortho*-substituted phenylene fragments

Given the ligand dissociation observed with diimine ligands, anionic coordination of catechol and other *o*-phenylene compounds was targeted to determine if hydrogen bonding in the second sphere would disfavor formation of the homoleptic complexes. Treatment of the datively coordinated iron(II) complex-

Scheme 2.4 Synthesis of the iron(II)- and iron(III)-catecholate complexes (**7** and **9** respectively).

es with 3,5-di-*tert*-butylcatechol (^{tBu}cat) and two equivalents of triethylamine resulted in the formation of a new paramagnetic species and the expected triethylammonium triflate byproduct, as confirmed by ^{1}H NMR spectroscopy. The same complex was accessible by reacting the catechol with the helicate iron(II)-complex, providing further evidence for deprotonation of the catechol to yield an iron(II)-catecholate complex. Crystallographic characterization of this species confirmed this assignment, revealing a trigonal bypramidal iron(II)-

complex with facial binding on the dipodal ligand, ^{Me}N(afa^{Cy})$_2$Fe(^{tBu}cat) (**7**). The axially bound oxygen atom of the catecholate fragment was engaged in hydrogen bonding with the amino donors in the second sphere. Bond lengths in the catechol fragment were examined to determine its oxidation state. Carbon-oxygen bond lengths of 1.365(3) and 1.339(2) Å were consistent with a catecholate binding mode, as significantly shorter lengths would be expected if the ligand were oxidized to yield a coordinated semiquinone (~1.29 Å).[24]

To determine if the oxidation state of the metal center changed the interaction of the catechol and dipodal ligands, analogous experiments were carried out starting from an iron(III)-chloride complex, ^{Me}N(afa^{Cy})$_2$FeCl$_3$ (**8**). Treatment of **8** with 3,5-di-*tert*-butylcatechol in the presence of two equivalents

Figure 2.5 Molecular structures of complexes **7** and **9** shown with 50% probability ellipsoids. For clarity, only the amino protons are shown (left). Diagram depicting bond lengths in the catecholate ligand (Å), confirming dianionic binding in both complexes (right).

of triethylamine resulted in a color change from dark brown to dark blue-green. The ^{1}H NMR spectrum for the crude material confirmed formation of triethylammonium chloride, once again consistent with deprotonation of the catechol fragment. Crystallographic characterization revealed the product to be the iron(III)-catecholate complex, ^{Me}N(afa^{Cy})$_2$Fe(^{tBu}cat)Cl (**9**). The iron center is bound in an octahedral geometry with the dipodal ligand bound meridionally, as in the starting material. The catechol fragment was hydrogen bonding with the amino groups in the second sphere, analogously to **7**. Analysis of the structural parameters confirmed the redox fragment was again bound in the reduced catecholate form, with C–O bond lengths of 1.364(2) and 1.342(2) Å.

Additional studies were carried out with 2-amino-4,6-di-*tert*-butylphenol (^{tBu}AP), another commonly studied redox active *o*-phenylene ligand. Unfortunately attempts to isolate discrete coordination complexes with this ligand were unsuccessful under a variety of conditions.

2.5 Oxidative ring cleavage reactivity of the iron(II) *ortho*-phenylene complexes

In Nature *o*-phenylene compounds are metabolized by nonheme dioxygenase enzymes via oxidative ring cleavage.[25] These enzymes are divided into two subclasses depending on whether the C–C bond cleaved during oxidation is between (intradiol) or adjacent to (extradiol) the ortho substituents (hydroxyl/amino). In extradiol dioxygenases the active site consists of an iron(II) center (or a manganese(II) center in a minority of enzymes) ligated by a 2-His-1-carboxylate facial triad. The mechanism of these enzymes is well understood (Scheme 2.5) and has been successfully reproduced by a variety of model complexes.[26-31] Despite evidence for the role of the secondary coordination sphere in facilitating substrate activation in these enzymes,[32,33] model systems that include hydrogen-bonding interactions are limited.[34]
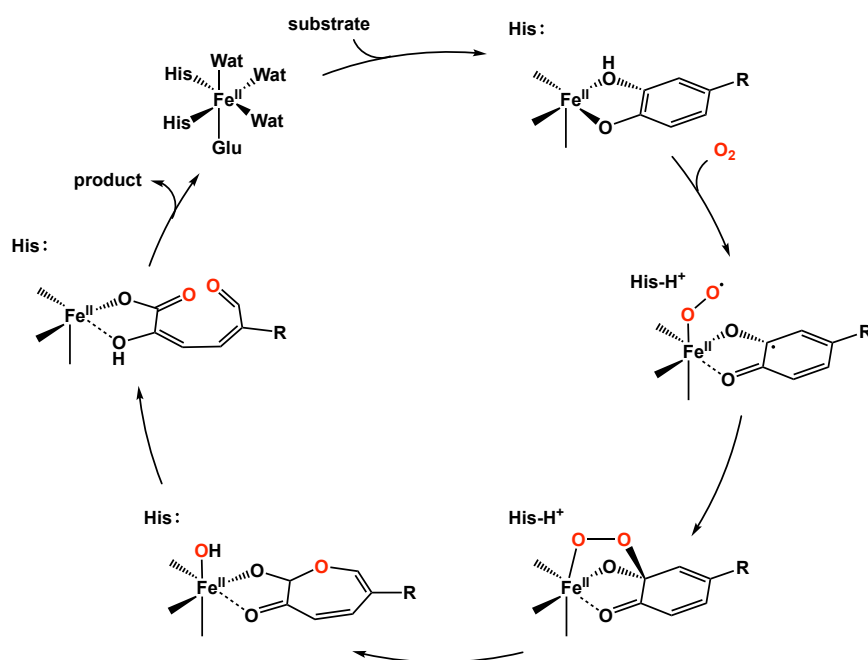
Scheme 2.5 The catalytic cycle proposed for extradiol ring-cleaving dioxygenases. See reference 27 for additional details and the related mechanism of intradiol dioxygenases.

Given the similarities between the facially bound $^{Me}N(pi^{Cy})_2$ ligand and the enzymes' active site, the dioxygenase activity of the iron(II) *o*-phenylene complexes described above was explored.

Although metallation of ^{tBu}AP did not yield well-behaved coordination complexes, the dioxygenase reactivity of the iron(II) species was briefly explored. A variety of oxidation conditions were examined. Most of these oxidations yielded a mixture of oxidized species with 4,6-di-*tert*-butyl-2*H*-pyran-2-one (derived from the hydrolysis of 4,6-di-*tert*-butyl-2*H*-pyran-2-imine during workup, product A) and 4,6-di-tert-butyl-2-picolinic acid (product B) as the major products (Scheme 2.6). Both of these products are derived from extradiol ring cleavage at the C1–C6 bond, mimicking the reactivity of 2-aminophenol dioxygenase (APD) enzymes.[34,35] External factors, such as choice of solvent and the equivalents of base added during coordination of the aminophenol, were found to place a significant role in determining the ratio of the two products. This variable reactivity was attributed to the mixture of species present in solution following coordination of ^{tBu}AP.
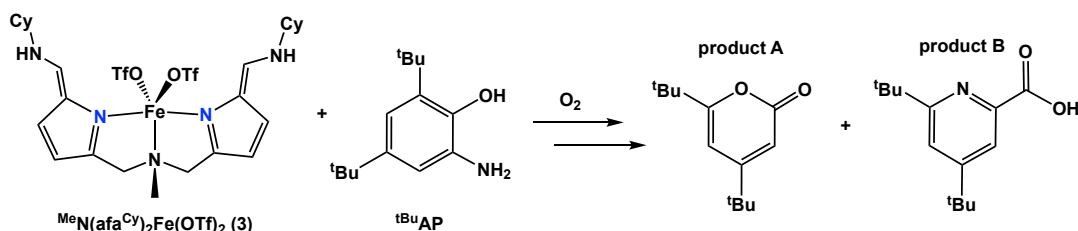
Scheme 2.6 2-Aminophenol dioxygenase (APD) reactivity observed with complex **3**. Both products are the result of extradiol cleavage (see references 34 and 35).

Oxidation of the iron(II)-catecholate complex (**7**) was also examined. Treatment of an acetonitrile solution of **7** with dioxygen resulted in a rapid color change from brown to dark green, consistent with the desired oxidation process. Although ^{1}H NMR spectroscopy analysis of the resulting mixture demonstrated significant demetallation of the $^{Me}N(pi^{Cy})_2$ ligand had occurred, formation of a new paramagnetic species was also observed. Single crystals of this complex were grown by slow evaporation of the ^{1}H NMR sample (CD$_3$CN). Refinement of the X-ray diffraction data revealed formation of a multimetallic cluster resulting from four iron centers bound across two $^{Me}N(pi^{Cy})_2$ ligands ([$^{Me}N(pi^{Cy})_2Fe(\mu$-OH)(μ-$^{tBu}RCO_2^-$)]$_2$(μ-O)$_2$, **10**; Figure 2.6). Each of the four iron centers is coordinated in trigonal bipyramidal geometry between the pyrrole and imine nitrogens of a single arm of the dipodal ligand framework.
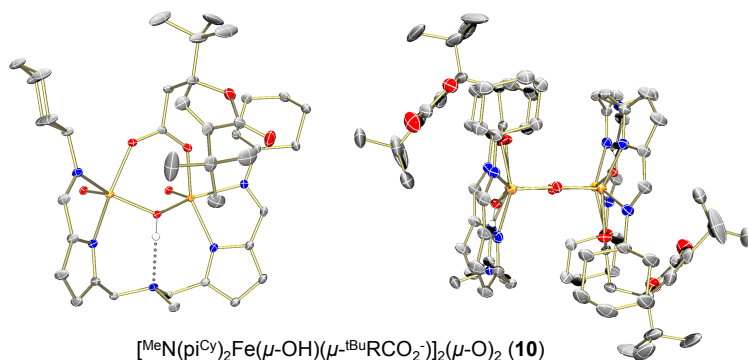

[$^{Me}N(pi^{Cy})_2Fe(\mu$-OH)(μ-$^{tBu}RCO_2^-$)]$_2$(μ-O)$_2$ (**10**)

Figure 2.6 Molecular structure of complex **10** shown with 50% probability ellipsoids. For clarity, only the hydroxo protons are shown. The bimetallic monomer and bridging oxo ligands are depicted (left) with a side-view of the completed dimer displayed from a perspective rotated by 90º (right).

The other arm of the ligand binds an additional iron center with a hydroxo and the carboxylate group of 3,5-di-*tert*-butyl-5-(carboxymethyl)-2-furanone (the intradiol oxidation product; abbreviated as $^{tBu}RCO_2^-$) bridging between the two metal centers. This two-iron unit dimerizes in a head-to-tail orientation with two bridging oxo ligands connecting the adjacent metal centers. Conversion of the 3,5-di-*tert*-butylcatecholate fragment in **7** to the ring contracted furanone observed in **10** once again demonstrated the competence of the $^{Me}N(pi^{Cy})_2$ ligand in promoting dioxygenase reactivity with *o*-phenylene redox active fragments (Scheme 2.7). However, the formation of another multimetallic species underscored the difficulties associated with coordinative flexibility of the tridentate $^{Me}N(pi^{Cy})_2$ ligand.
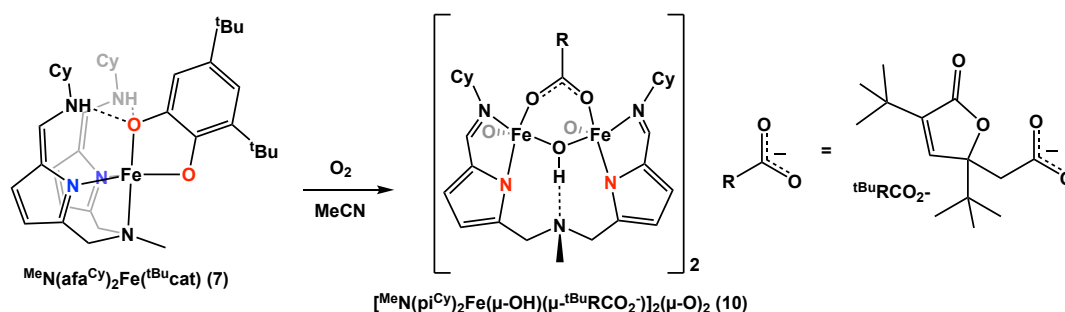
Scheme 2.7 Intradiol catechol dioxygenase reactivity observed with complex **7**, resulting in the formation of a multimetallic cluster (**10**) containing the ring-contracted furanone product.

2.6 Conclusion

A family of Fe(II) complexes of the dipodal, azafulvene-amine ligand framework has been synthesized via dative tautomerization of the newly synthesized $H_2[^{Me}N(pi^{Cy})_2]$ ligand. Structural characterization of $(^{Me}N(afa^{Cy})_2)FeX_2$ (X = Cl (**2**), OTf (**3**)) has revealed a trigonal bipyramidal geometry of the metal center, with a pseudo planar arrangement of the ligand framework. In the case of the triflate species, upon addition of strongly coordinating solvents, the metal center adopts an octahedral configuration, $[^{Me}N(afa^{Cy})_2Fe(OTf)(L)_2](OTf)$ (L = DMA or THF), where two solvent molecules displace a triflate anion. The structural diversity of the metal species is evident in the Mössbauer spectra in the case of complexes **2-3**. Binding of ancillary redox active fragments was then described, providing further evidence for the coordinative flexibility of the ligand framework.

Addition of an equivalent of 2,2′-bipyridine to **3**, resulted in the generation of a new complex, $^{Me}N(afa^{Cy})_2Fe(bipy)(OTf)_2$ (**4**). Although characterization of **4** demonstrated partial dissociation of the ligand occurred in solution to form the homoleptic $[Fe(bipy)_3](OTf)_2$ species, the intended heteroleptic complex was crystallographically characterized, revealing the facial coordination geometry of the dipodal ligand. Reduction of a related 1,10-phenanthroline complex, $^{Me}N(afa^{Cy})_2Fe(phen)Br_2$ (**5**), showed similar ligand dissociation in solution, yet the intended heteroleptic complex was successfully characterized once again via X-ray crystallography. Structural data for this complex demonstrated tautomerization of the ligand had occurred, affording access to the anionic binding mode of the ligand in the iron(II)-aquo com-

plex, $^{Me}N(pi^{Cy})_2Fe(phen)(H_2O)$ (**6**). Given the observation of homoleptic impurities in these reactions, additional studies were carried out using *o*-phenylene fragments where anionic coordination of the ancillary ligand could be targeted to disfavor its dissociation in solution.

Characterization of the iron(II)- and iron(III)-catecholate complexes (**7** and **9**) demonstrated the successful coordination of 3,5-di-*tert*-butylcatechol. In both cases the catechol was bound in the reduced, dianionic state and engaged in hydrogen bonding with the amino groups of the dipodal ligand. The reactivity of **7** towards O_2 was examined, demonstrating that the iron(II) complex served as a functional mimic for intradiol catechol dioxygenase enzymes. Although discrete coordination complexes were not isolated, the analogous 2-amino-4,6-di-*tert*-butylphenolate was successfully oxidized to give the extradiol ring cleavage products. Given the mixture of intradiol and extradiol cleavage products observed, as well as the variety of multimetllic species observed throughout this chapter, later work focused on the analogous tetradentate ligand framework, $N(_{X}pi^R)_3$.

2.7 Experimental section

General Considerations. All manipulations were carried out in the absence of water and dioxygen using standard Schlenk techniques, or in an MBraun inert atmosphere drybox under a dinitrogen atmosphere except where specified otherwise. All glassware was oven dried for a minimum of 8 h and cooled in an evacuated antechamber prior to use in the drybox. Solvents were dried and deoxygenated on a Glass Contour System (SG Water USA, Nashua, NH) and stored over 4 Å molecular sieves purchased from Strem following literature procedure prior to use. Chloroform-d_1, tetrahydrofuran-d_8, and acetontrile-d_3 were purchased from Cambridge Isotope Labs and were degassed and stored over 4 Å molecular sieves prior to use. 2,2'-bipyridine was purchased from Sigma Aldrich and recrystallized from diethyl ether under an inert atmosphere prior to use. Ferrous chloride and potassium carbonate were purchased from Strem and used as received. Cyclohexylamine was purchased from Acros and used as received. Dimethylformamide and sodium hydroxide were purchased from Fisher and used as received. $POCl_3$ and hydrochloride etherate (2.0 M) were purchased from Sigma Aldrich and used as received. Ferrous triflate was prepared according to literature procedures. Celite® 545 (J. T. Baker) was dried in a Schlenk flask for 24 h under dynamic vacuum while heating to at least 150 ºC prior to use in a drybox. NMR Spectra were recorded at room temperature on a Varian spectrometer operating at 400, 500 MHz (^{1}H NMR) and 126 MHz (^{13}C NMR) and referenced to the residual solvent resonance (δ in parts per million, and J in Hz).

Physical Measurements. Cyclic voltammetry was performed under nitrogen at room temperature using a CH Instruments CHI600D electrochemical analyzer with a glassy carbon working electrode, Pt wire counter electrode, and the pseudoreference electrode Ag wire. Zero-field, ^{57}Fe Mössbauer spectra were measured on a constant acceleration spectrometer (SEE Co, Minneapolis, MN) with a Janis SVT-100 cry-

ostat. Isomer shifts are quoted relative to α-Fe foil (< 25 μm thick) at room temperature. Samples were prepared using approximately 30 mg of sample suspended in paratone-N oil. Temperatures were controlled using a LakeShore 321 autotuning temperature controller. Temperature variations were no greater than ±10 K, and were generally within ±2 K. Data were analyzed using an in-house package in Igor Pro (Wavemetrics). Elemental analysis was performed by Complete Analysis Laboratories, Inc. in Parsippany, NJ and the University of Illinois at Urbana-Champaign School of Chemical Sciences Microanalysis Laboratory in Urbana, IL.

Preparation of H$_2$dpma. This preparation is a slight modification of the literature procedure.[19] In a 500 mL round bottom flask methylamine hydrochloride (6.81 g, 0.101 mol) and aqueous formaldehyde (37%, 16.35 g, 0.202 mol) were combined in 100 mL of absolute ethanol. The colorless solution was heated to 55 ºC. Once the methylamine hydrochloride was dissolved, pyrrole (13.49 g, 0.201 mol) was added drop-wise to the reaction. The resulting mixture was stirred at 55 ºC for 4 h; during this time the solution developed a red-brown color. After cooling the reaction to room temperature, volatiles were removed under reduced pressure to yield the crude product as a thick brown oil. This oil was then diluted with water (~100 mL), and basified by slow addition of anhydrous K$_2$CO$_3$. The product was extracted with chloroform (3 x 50 mL). Volatiles were again removed under reduced pressure, yielding the neutralized product as a thick 3 brown oil. This oil was triturated with a Et$_2$O/DCM mixture (10:1, 50 mL), resulting in an off-white powder (14.62 g, 0.077 mol, 77%). ^{1}H NMR was consistent with the formation of the desired product, despite minor differences from the published data. ^{1}H NMR (400 MHz, CDCl$_3$, 25 ºC): δ = 2.44 (3H, s, CH$_2$NCH_3), 4.16 (4H, s, CH_2NCH$_3$), 6.13 (2H, m, 3-C$_4H_3$N), 6.24 (2H, m, 4-C$_4H_3$N), 6.92 (2H, m, 5-C$_4H_3$N), 10.39 (2H, s, N(H)-pyrrole).

Preparation of H$_2$[^{Me}N(pi^{Cy})$_2$] · H$_2$O. In a 500 mL three-neck round bottom flask di(pyrrolyl-α-methyl)methylamine (H$_2$dpma) (3.8767 g, 0.021 mol) and DMF (9.50 mL, 0.12 mol) were combined in 10 mL of 1,2-dichloroethane. The dark brown solution was cooled to -10 °C. The flask was fitted with an addition funnel containing a solution of POCl$_3$ (9.50 mL, 0.10 mol) in 1,2-dichloroethane (20 mL), then purged with nitrogen for 5-10 minutes. The POCl$_3$ solution was added drop-wise over an hour with vigorous stirring. The mixture was removed from the ice bath and heated to 50 °C for one hour. The reaction mixture was allowed to cool to room temperature, before adding a saturated solution of aqueous sodium acetate (42 g, 0.51 mol). The contents were heated to 50 °C for two hours. After cooling the reaction to room temperature, the mixture was neutralized by slow addition of anhydrous Na$_2$CO$_3$, resulting in copious evolution of CO$_2$. The product was extracted with dichloromethane (3 x 150 mL). Volatiles were removed under reduced pressure to yield the proligand, H$_2$dpma^{CO}, as a dark brown oil. The oil was dissolved in approximately 250 mL dry acetonitrile. Cyclohexyamine (H$_2$NCy) (6.1061 g, 0.062 mol) was added dropwise and the mixture was stirred for 16 hours. The product, H$_2$[^{Me}N(pi ^{Cy})$_2$] · H$_2$O, precip-

itates from solution as a tan powder, which is isolated by filtration (6.8003 g, 0.016 mol, 78%). Analysis for $C_{25}H_{37}N_5 \cdot H_2O$: Calcd. C, 70.55; H, 9.24; N, 16.45. Found C, 70.19; H, 9.12; N, 15.99. ^{1}H NMR (500 MHz, CDCl$_3$, 25 °C): δ = 1.16 – 1.83 (m, 20 H, Cy-CH_2), 2.24 (s, 3H, NCH_3), 3.07 (tt, J = 10.9, 3.5 Hz, 2H, Cy-CH), 3.56 (s, 4H, NCH_2), 5.99 (d, J = 3.4 Hz, 2H, Ar-CH), 6.37 (d, J = 3.5 Hz, 2H, Ar-CH), 7.96 (s, 2H, imine-CH). ^{13}C NMR (101 MHz, C$_6$D$_6$, 25 °C): δ = 25.31 (Cy-C3,C5), 26.00 (Cy-C4), 35.20 (Cy-C2,C6), 42.05 (methyl-C), 54.71 (methylene-C), 69.09 (Cy-C1), 107.92 (pyr-C), 116.47 (pyr-C), 129.77 (pyr-C), 136.42 (pyr-C), 150.52 (imine-C).

Preparation of $H_2[^{Me}N(pi^{Cy})_2]$ (1). The water adduct of the ligand, $H_2[^{Me}N(pi^{Cy})_2] \cdot H_2O$, was dried in the glovebox under a dry, inert atmosphere. Ligand (4.1971 g, 9.86 mmol) was dissolved in a minimal amount of dry DCM (~20 mL), molecular sieves were added, then the solution was diluted with dry Et$_2$O (~80 mL). The solution was dried at room temperature over 48 h, then filtered to separate the sieves and a small amount of precipitate. Volatiles were removed in vacuo to yield the dried ligand $H_2[^{Me}N(pi^{Cy})_2]$ (3.5824 g, 8.79 mmol, 89%) Analysis for $C_{27}H_{35}N_5$: Calcd. C, 73.67; H, 9.15; N, 17.18. Found C, 73.54; H, 9.33; N, 16.95. ^{1}H NMR (500 MHz, CD$_3$CN, 25 ºC): δ = 1.24-1.29 (m, 2H, Cy-CH_2), 1.33-1.48 (m, 8H, Cy-CH_2), 1.63-1.70 (m, 6H, Cy-CH_2), 1.77-1.80 (m, 4H, Cy-CH_2), 2.04 (s, 3H, NCH_3), 3.09 (tt, J = 9.8, 4.1 Hz, 2H, Cy-CH), 3.49 (s, 4H, NCH_2), 6.00 (d, J = 3.2 Hz, 2H, Ar-CH), 6.31 (d, J = 3.2 Hz, 2H, Ar-CH), 8.03 (s, 2H, imine-CH), 9.50 (broad, 2H, pyrrole NH). ^{13}C NMR (126 MHz, C$_6$D$_6$, 25 °C): δ = 25.17 (Cy-C3,C5), 26.10 (Cy-C4), 35.31 (Cy-C2,C6), 41.55 (methyl-C), 53.95 (methylene-C), 69.43 (Cy-C1), 109.17 (pyr-C), 113.62 (pyr-C), 131.02 (pyr-C), 132.97 4 (pyr-C), 148.93 (imine-C).

Preparation of $^{Me}N(afa^{Cy})_2FeCl_2$ (2). A 20 mL scintillation vial was charged with FeCl$_2$ (0.013 g, 0.103 mmol) and approximately 3 mL of THF. In a separate vial, $H_2[^{Me}N(pi^{Cy})_2]$ (0.044 g, 0.108 mmol) was dissolved in 3 mL of THF and added drop wise with vigorous stirring to the previously prepared FeCl$_2$ slurry. Upon addition of the ligand, formation of an orange suspension was observed, with simultaneous dissolution of FeCl$_2$. After one hour, solvents were removed under reduced pressure and the remaining orange residue was washed with diethyl ether and dried in vacuo. The product, $^{Me}N(afa^{Cy})_2FeCl_2$, was isolated as an orange powder in high yields (>90 %). For analytically pure samples, **2** was crystallized by vapor diffusion of a THF/MeCN solution (3:1) with Et$_2$O (0.037 g, 0.070 mmol, 68%). Crystals suitable for X-ray analysis were grown from a solution of acetonitrile layered with diethyl ether. Analysis for $FeC_{25}H_{37}N_5Cl_2$: Calcd. C, 56.19; H, 6.98; N, 13.11. Found C, 56.00; H, 6.99; N, 12.86. ^{1}H NMR, (500 MHz, CD$_3$CN, 25 ºC) δ = -5.80, -3.73, -1.50, -1.34, -0.42, -0.79, 11.72, 42.49, 55.29, 138.54, 154.16.

Preparation of $^{Me}N(afa^{Cy})_2Fe(OTf)_2$ (3). A 20 mL scintillation vial was charged with Fe(OTf)$_2$(MeCN)$_2$ (0.043 g, 0.098 mmol) and approximately 3 mL of THF. In a separate vial, $H_2[^{Me}N(pi^{Cy})_2]$ (0.041 g, 0.101 mmol) was dissolved in 3 mL of THF and added drop wise with vigorous

stirring to the previously prepared Fe(OTf)$_2$ slurry. Upon addition of the ligand, an immediate color change to yellow was noted. The reaction mixture was stirred for an hour to ensure conversion. Solvents were removed in vacuo. The resulting yellow residue was washed with diethyl ether. The product was isolated as a yellow powder in high yields (>90%) and was used for subsequent experiments. For analytically pure samples, **3** was crystallized by vapor diffusion of a THF/MeCN solution (3:1) with Et$_2$O (0.052 g, 0.057 mmol, 58%). Crystals suitable for X-ray analysis were grown using the same conditions. Analysis for FeC$_{35}$H$_{53}$N$_5$O$_8$F$_6$S$_2$: Calcd. C, 46.41; H, 5.90; N, 7.73. Found C, 46.27; H, 5.84; N, 7.81.

Preparation of ^{Me}N(afa^{Cy})$_2$Fe(bipy)(OTf)$_2$ (4). A 20 mL scintillation vial was charged with ^{Me}N(afa^{Cy})$_2$Fe(OTf)$_2$ (0.090 g, 0.100 mmol) and approximately 3 mL of THF. An equivalent of 2,2'-bipyridine (0.016 g 0.102 mmol) was weighed by difference and added as a solid to the metal solution. Following addition of 2,2'-bipyridine, an immediate and striking color change to a dark red was noted. The mixture was stirred for 45 minutes to ensure complete conversion, after which time solvents were removed under reduced pressure. The product was isolated as a dark pink powder in high yields (>90%). Crystals of complex **4** suitable for X-ray analysis were grown from a concentrated MeCN/Et$_2$O solution (3:1) at -35 °C. Due to the instability of complex **4**, elemental analysis could not be obtained.

Preparation of ^{Me}N(pi^{Cy})$_2$Fe(phen)(H$_2$O) (6). ^{Me}N(afa^{Cy})$_2$Fe(phen)Br$_2$ was generated in situ as follows. FeBr$_2$ (28 mg, 0.13 mmol) and H$_2$[^{Me}N(pi^{Cy})$_2$] (53 mg, 0.13 mmol) were combined in THF (~20 mL). The reaction was stirred at room temperature until all of the solid FeBr$_2$ was consumed, yielding an orange solution over the course of ~30 min. An equivalent of 1,10-phenanthroline (25 mg 0.14 mmol) was weighed by difference and added as a solid to the solution resulting in a color change to maroon. The mixture was stirred for 30 minutes to ensure complete conversion, after which time the mixture was cooled to -35 ºC. KC$_8$ (37 mg, 0.27 mmol, 2 equiv) were added to the solution resulting in a rapid color change to give a dark yellow-green suspension. After stirring at room temperature for an additional hour, the reaction was filtered over a pad of Celite to remove the graphite byproduct. Crystals of complex **6** suitable for X-ray analysis were grown from a vapor diffusion of hexanes into a concentrated toluene solution. Due to the ligand dissociation observed in solution, as described in the text, further characterization of the complex was not pursued.

Preparation of ^{Me}N(afa^{Cy})$_2$Fe(^{tBu}cat) (7). ^{Me}N(afa^{Cy})$_2$Fe(OTf)$_2$ (**3**) was generated in situ from Fe(OTf)$_2$(MeCN)$_2$ (265 mg, 0.61 mmol) and H$_2$[^{Me}N(pi^{Cy})$_2$] (249 mg, 0.61 mmol) giving a suspension in THF (~10 mL). ^{tBu}cat (137 mg, 0.62 mmol) was added as a solid, followed by dropwise addition of NEt$_3$ (125 mg, 1.24 mmol, 2 equiv). A color change from yellow to brown was observed upon addition of base with complete dissolution of the solid material. Volatiles were removed in vacuo. Purified product was obtained by cooling a concentrated solution of the material in MeCN (~5 mL) to -35 ºC overnight. The

crystalline material was collected over a frit and washed with cold MeCN, yielding pure $^{Me}N(afa^{Cy})_2Fe(^{tBu}cat)$ (**7**) (298 mg, 0.44 mmol, 72%).

Preparation of $^{Me}N(afa^{Cy})_2Fe(^{tBu}cat)Cl$ (9). $^{Me}N(afa^{Cy})_2FeCl_3$ (**8**) was generated in situ from $FeCl_3$ (83 mg, 0.51 mmol) and $H_2[^{Me}N(pi^{Cy})_2]$ (210 mg, 0.52 mmol) in THF (~10 mL) giving a dark brown solution. After 1 h ^{tBu}cat (116 mg, 0.52 mmol) and NEt_3 (108 mg, 1.07 mmol, 2 equiv), resulting in an immediate color change from brown to dark blue-green. After stirring for an additional hour, the reaction was filtered to remove the $[HNEt_3]Cl$ precipitate. The filtrate was dried to yield the product, $^{Me}N(afa^{Cy})_2Fe(^{tBu}cat)Cl$ (**9**).

Oxidation of $^{Me}N(afa^{Cy})_2Fe(^{tBu}cat)$ (7). $^{Me}N(afa^{Cy})_2Fe(^{tBu}cat)$ (**7**) (24 mg, 0.035 mmol) was dissolved in MeCN (5 mL). The vial was sealed with a 14/20 septum and tape, and then removed from the glovebox. A standard balloon attached to a syringe barrel was filled with O_2 and injected through the septum with a needle. The atmosphere was purged with O_2, resulting in an immediate color change from brown to dark green. The mixture was stirred at room temperature for one hour to ensure completion. The reaction was degassed and dried under vacuum on a Schlenk line. The resulting residue was returned to the glovebox for purification. Crude material was redissolved in CD_3CN for NMR spectroscopy analysis. Slow evaporation of the NMR sample gave single crystals of suitable quality for X-ray analysis, revealing the product to be $[^{Me}N(pi^{Cy})_2Fe(\mu\text{-}OH)(\mu\text{-}^{tBu}RCO_2^-)]_2(\mu\text{-}O)_2$ (**10**).

2.8 References

(1) Etter, M. C. Encoding and Decoding Hydrogen-Bond Patterns of Organic Compounds. *Acc. Chem. Res.* **1990**, *23* (4), 120–126.

(2) Emsley, J. Very Strong Hydrogen Bonding. *Chem. Soc. Rev.* **1980**, *9* (1), 91–124.

(3) Perutz, M. F.; Fermi, G.; Luisi, B.; Shaanan, B.; Liddington, R. C. Stereochemistry of Cooperative Mechanisms in Hemoglobin. *Acc. Chem. Res.* **1987**, *20* (9), 309–321.

(4) Springer, B. A.; Sligar, S. G.; Olson, J. S.; Phillips, G. N., Jr. Mechanisms of Ligand Recognition in Myoglobin. *Chem. Rev.* **1994**, *94* (3), 699–714.

(5) Martinis, S. A.; Atkins, W. M.; Stayton, P. S.; Sligar, S. G. A Conserved Residue of Cytochrome P-450 Is Involved in Heme-Oxygen Stability and Activation. *J. Am. Chem. Soc.* **1989**, *111* (26), 9252–9253.

(6) Shook, R. L.; Borovik, A. S. Role of the Secondary Coordination Sphere in Metal-Mediated Dioxygen Activation. *Inorg. Chem.* **2010**, *49* (8), 3646–3660.

(7) Weinberg, D. R.; Gagliardi, C. J.; Hull, J. F.; Murphy, C. F.; Kent, C. A.; Westlake, B. C.; Paul, A.; Ess, D. H.; McCafferty, D. G.; Meyer, T. J. Proton-Coupled Electron Transfer. *Chem. Rev.* **2012**, *112* (7), 4016–4093.

(8) Huynh, M. H. V.; Meyer, T. J. Proton-Coupled Electron Transfer. *Chem. Rev.* **2007**, *107* (11), 5004–5064.

(9) Hoffman, B. M.; Dean, D. R.; Seefeldt, L. C. Climbing Nitrogenase: Toward a Mechanism of Enzymatic Nitrogen Fixation. *Acc. Chem. Res.* **2009**, *42* (5), 609–619.

(10) Hoffman, B. M.; Lukoyanov, D.; Dean, D. R.; Seefeldt, L. C. Nitrogenase: a Draft Mechanism. *Acc. Chem. Res.* **2013**, *46* (2), 587–595.

(11) Seefeldt, L. C.; Hoffman, B. M.; Dean, D. R. Mechanism of Mo-Dependent Nitrogenase. *Annu. Rev. Biochem.* **2009**, *78* (1), 701–722.

(12) Roubelakis, M. M.; Bediako, D. K.; Dogutan, D. K.; Nocera, D. G. Proton-Coupled Electron

Transfer Kinetics for the Hydrogen Evolution Reaction of Hangman Porphyrins. *Energy Environ. Sci.* **2012**, *5* (7), 7737–4.

(13)   Matson, E. M.; Bertke, J. A.; Fout, A. R. Isolation of Iron(II) Aqua and Hydroxyl Complexes Featuring a Tripodal H-Bond Donor and Acceptor Ligand. *Inorg. Chem.* **2014**, *53* (9), 4450–4458.

(14)   Reid, S. D.; Blake, A. J.; Wilson, C.; Love, J. B. Syntheses and Structures of Dinuclear Double-Stranded Helicates of Divalent Manganese, Iron, Cobalt, and Zinc. *Inorg. Chem.* **2006**, *45* (2), 636–643.

(15)   Reid, S. D.; Wilson, C.; Blake, A. J.; Love, J. B. Tautomerisation and Hydrogen-Bonding Interactions in Four-Coordinate Metal Halide and Azide Complexes of N-Donor-Extended Dipyrromethanes. *Dalton Trans.* **2010**, *39* (2), 418–425.

(16)   Park, Y. J.; Sickerman, N. S.; Ziller, J. W.; Borovik, A. S. Utilizing Tautomerization of 2-Amino-Oxazoline in Hydrogen Bonding Tripodal Ligands. *Chem. Commun.* **2010**, *46* (15), 2584–3.

(17)   Sickerman, N. S.; Park, Y. J.; Ng, G. K. Y.; Bates, J. E.; Hilkert, M.; Ziller, J. W.; Furche, F.; Borovik, A. S. Synthesis, Structure, and Physical Properties for a Series of Trigonal Bipyramidal MII–Cl Complexes with Intramolecular Hydrogen Bonds. *Dalton Trans.* **2012**, *41* (15), 4358–7.

(18)   Moore, C. M.; Quist, D. A.; Kampf, J. W.; Szymczak, N. K. A 3-Fold-Symmetric Ligand Based on 2-Hydroxypyridine: Regulation of Ligand Binding by Hydrogen Bonding. *Inorg. Chem.* **2014**, *53* (7), 3278–3280.

(19)   Harris, S. A.; Ciszewski, J. T.; Odom, A. L. Titanium H 1-Pyrrolyl Complexes: Electronic and Structural Characteristics Imposed by the N, N-Di(Pyrrolyl-A-Methyl)- N-Methylamine (Dpma) Ligand. *Inorg. Chem.* **2001**, *40* (9), 1987–1988.

(20)   Shan, W. G.; Shi, X. J.; Su, W. K. VILSMEIER-HAACK SYNTHESIS of AROMATIC ALDEHYDES USING Bis-(TRICHLOROMETHYL) CARBONATE and DIMETHYLFORMAMIDE. *Organic Preparations and Procedures International* **2004**, *36* (4), 337–340.

(21)   Sazama, G. T.; Betley, T. A. Multiple, Disparate Redox Pathways Exhibited by a Tris(Pyrrolido)Ethane Iron Complex. *Inorg. Chem.* **2014**, *53* (1), 269–281.

(22)   Sato, H.; Tominaga, T. Mössbauer Studies of the Thermal Decomposition of Tris(2,2′-Bipyridine)Iron(II) Chloride and the Structures of the Isomers of 2,2′-Bipyridineiron(II) Chloride. *Bull. Chem. Soc. Jpn.* **1976**, *49* (3), 697–700.

(23)   Braterman, P. S.; Song, J. I.; Peacock, R. D. Electronic Absorption Spectra of the Iron(II) Complexes of 2,2'-Bipyridine, 2,2'-Bipyrimidine, 1,10-Phenanthroline, and 2,2':6',2"-"Terpyridine and Their Reduction Products. *Inorg. Chem.* **1992**, *31* (4), 555–559.

(24)   Pierpont, C. G. Ligand Redox Activity and Mixed Valency in First-Row Transition-Metal Complexes Containing Tetrachlorocatecholate and Radical Tetrachlorosemiquinonate Ligands. *Inorg. Chem.* **2011**, *50* (20), 9766–9772.

(25)   Vaillancourt, F. H.; Bolin, J. T.; Eltis, L. D. The Ins and Outs of Ring-Cleaving Dioxygenases. *Crit. Rev. Biochem. Mol. Biol.* **2006**, *41* (4), 241–267.

(26)   Lipscomb, J. D. Mechanism of Extradiol Aromatic Ring-Cleaving Dioxygenases. *Current Opinion in Structural Biology* **2008**, *18* (6), 644–649.

(27)   Wang, Y.; Li, J.; Liu, A. Oxygen Activation by Mononuclear Nonheme Iron Dioxygenases Involved in the Degradation of Aromatics. *J. Biol. Inorg. Chem.* **2017**, *22* (2-3), 395–405.

(28)   Costas, M.; Mehn, M. P.; Jensen, M. P.; Que, L., Jr. Dioxygen Activation at Mononuclear Nonheme Iron Active Sites: Enzymes, Models, and Intermediates. *Chem. Rev.* **2004**, *104* (2), 939–986.

(29)   Fielding, A. J.; Lipscomb, J. D.; Que, L., Jr. A Two-Electron-Shell Game: Intermediates of the Extradiol-Cleaving Catechol Dioxygenases. *J. Biol. Inorg. Chem.* **2014**, *19* (4-5), 491–504.

(30)   Fiedler, A. T.; Fischer, A. A. Oxygen Activation by Mononuclear Mn, Co, and Ni Centers in Biology and Synthetic Complexes. *J. Biol. Inorg. Chem.* **2016**, 1–18.

(31)   Sahu, S.; Goldberg, D. P. Activation of Dioxygen by Iron and Manganese Complexes: a Heme and Nonheme Perspective. *J. Am. Chem. Soc.* **2016**, *138* (36), 11410–11428.

(32)   Mendel, S.; Arndt, A.; Bugg, T. D. H. Acid−Base Catalysis in the Extradiol Catechol Dioxygenase Reaction Mechanism: Site-Directed Mutagenesis of His-115 and His-179 in *Escherichia Coli* 2,3-Dihydroxyphenylpropionate 1,2-Dioxygenase (MhpB). *Biochemistry* **2004**, *43* (42), 13390–13396.

(33)   Kovaleva, E. G.; Rogers, M. S.; Lipscomb, J. D. Structural Basis for Substrate and Oxygen Activation in Homoprotocatechuate 2,3-Dioxygenase: Roles of Conserved Active Site Histidine 200. *Biochemistry* **2015**, *54* (34), 5329–5339.

(34)   Chatterjee, S.; Paine, T. K. Oxygenative Aromatic Ring Cleavage of 2-Aminophenol with Dioxygen Catalyzed by a Nonheme Iron Complex: Catalytic Functional Model of 2-Aminophenol Dioxygenases. *Inorg. Chem.* **2015**, *54* (4), 1720–1727.

(35)   Chakraborty, B.; Paine, T. K. Aromatic Ring Cleavage of 2-Amino-4-Tert-Butylphenol by a Nonheme Iron(II) Complex: Functional Model of 2-Aminophenol Dioxygenases. *Angew. Chem. Int. Ed.* **2013**, *52* (3), 920–924.

CHAPTER 3: TUNING THE FE(II/III) REDOX POTENTIAL IN NONHEME FE(II)−HYDROXO COMPLEXES THROUGH PRIMARY AND SECONDARY COORDINATION SPHERE MODIFICATIONS[†]

3.1 Introduction

The reactivity of metalloproteins is determined by primary, secondary, and extended coordination sphere interactions. Minor modifications within any of these spheres can alter the reactivity at the active site. These differences can afford a wide range of reactivity with a single metal cofactor. For example, heme-containing metalloproteins display a variety of interactions with dioxygen, from O_2 storage and transport by globins to O–O bond cleavage in cytochromes.[1-7] Although there are numerous interrelated factors that contribute to this differential reactivity, many studies have demonstrated the importance of tuning the heme electronics through non-covalent interactions with proximal residues.[8-12] Similar secondary coordination sphere interactions also play an important role in modulating the redox properties of many other metalloproteins.[13-15] Given the significant impact these subtle modifications can have, model systems have been developed to understand and rationally tune both the primary and secondary coordination spheres' influence on the reactivity of metal complexes.

Nam and Que have demonstrated that varying the axial ligand in non-heme iron complexes changes their electronic structures and reactivity.[16-19] Work from the Long and Chang groups has shown that altering the donor strength of a pyridine ligand framework can produce analogous differences in the metal complexes' properties.[20] Although a number of researchers have demonstrated the importance of the secondary coordination sphere in controlling the properties of metal complexes,[21-29] systematic alteration of these secondary sphere interactions remains less developed, likely due to the non-trivial nature of such modifications. Several ligand families have been developed specifically to study the impact of changing the number (and/or type) of pendant hydrogen-bond donors on the properties of their metal complexes.[30-32] Borovik has shown that these alterations in the secondary coordination sphere can contribute to significant differences in reactivity.[33-35] However, variations in the secondary coordination sphere often directly impact the primary coordination sphere through steric or electronic interactions, complicating the interpretation of the resulting changes in reactivity.[36,37]

Previously, we demonstrated the ability of our tripodal ligand platform, tris(5-cyclohexyliminopyrrol-2-ylmethyl)amine (N(pi^{Cy})$_3$), to tautomerize from the pyrrole-imine tautomer to the azafulvene-amine analog (N(afa^{Cy})$_3$), depending on the substrate bound to and oxidation state of the metal center.[38-40] Given the ligand's modular synthesis, modification of both the primary and secondary coordination spheres was tar-

geted. Herein, we describe new electronic derivatives of the ligand framework, $N(_xpi^R)_3$, and their metallation to the corresponding Fe(II)-hydroxo complexes ($N(_xpi^R)(_xafa^R)_2Fe(II)OH$). Chemical and electrochemical oxidation of these compounds is presented to examine the impact of the primary and secondary coordination sphere modifications. Combined spectroscopic, structural, and theoretical characterization of each derivative highlights the role of both coordination spheres in determining the electronic properties of the iron complexes. This work provides a method for rationally tuning the complexes' redox potential via facile ligand modification of the primary and/or secondary coordination sphere.

3.2 Electronic modification of the $N(_xpi^R)_3$ platform

Two potential points of modification on the $N(_xpi^R)_3$ ligand platform ($_xL^R$) were identified, with the goal of separately tuning the metal complexes' primary and secondary coordination spheres. The primary coordination sphere was tuned by altering the electronics of the pyrrole backbone, while the R-group capping the appended imine-functionality was changed to modify the hydrogen bonding properties of the secondary coordination sphere.
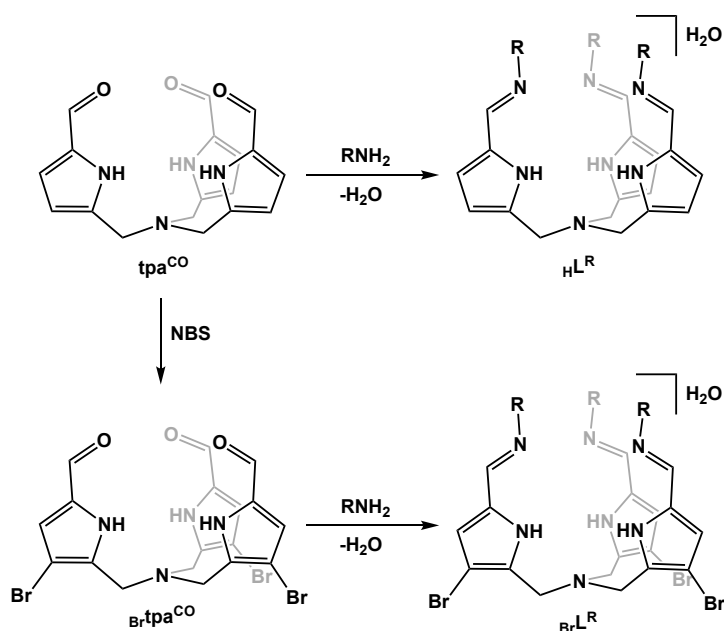
Scheme 3.1 Derivatization of the ligand platform, $N(_xpi^R)_3 \cdot H_2O$ (X = H, Br; R = Cy, Ph).

Initial work focused on the primary coordination sphere, turning to halogenation of the pyrrole moieties (Scheme 3.1). Previous work from the Betley group with dipyrrinato ligands demonstrated that this method can be used effectively to shift the redox potential of the subsequent iron complexes.[41] Bromination was achieved by treating a slurry of the formylated proligand, tpa^{CO}, with *N*-bromosuccinimide in cold THF (0 °C), giving a deep red-brown solution. The product was precipitated with cold water and collected over a fritted funnel to give the brominated product, $_{Br}$tpa^{CO}, in high yields (84%). Tribromination of the ligand was established by the presence of a single pyrrole C–*H* resonance at 7.06 ppm in the

^{1}H NMR spectrum. Finally, condensation with cyclohexylamine afforded the desired ligand, $N(_{Br}pi^{Cy})_3 \cdot$ H_2O ($_{Br}L^{Cy}$), in high yield (91%).

The secondary coordination sphere was modified by changing the amine used in the final condensation step of the ligand synthesis (Scheme 3.1). Aniline was targeted as an alternative capping group to provide electron-withdrawing groups in both coordination spheres as a point of comparison. Condensation with either the proteo (tpa^{CO}) or tribrominated ($_{Br}$tpa^{CO}) proligand, in the presence of catalytic formic acid, afforded the corresponding phenyl ligand, $N(_{X}pi^{Ph})_3 \cdot H_2O$, in good or high yield ($_{H}L^{Ph}$ – 68%; $_{Br}L^{Ph}$ – 82%). All three new ligand derivatives, $N(_{X}pi^{R})_3 \cdot H_2O$ ($_{X}L^{R}$), were fully characterized by ^{1}H NMR, ^{13}C NMR, electronic absorption, and infrared spectroscopies. Elemental analyses confirmed the isolation of ligand monohydrates ($N(_{X}pi^{R})_3 \cdot H_2O$) in each case, consistent with the previously reported $_{H}L^{Cy}$ derivative.

3.3 Synthesis of Fe(II)-hydroxo complexes

We have previously demonstrated that a number of Fe(II) complexes are accessible with this framework, depending on the method of metallation.[38] Having developed a series of electronically modified ligands, the corresponding Fe(II)-hydroxo complexes were targeted. The Fe(II)-OH molecules were chosen for their well-behaved cyclic voltammetry (see below), allowing straightforward comparison of redox potentials across the series.
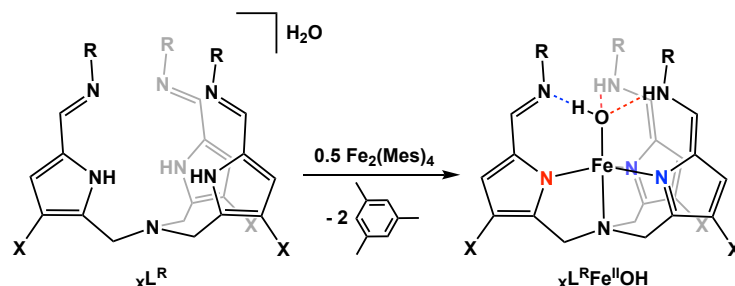
Scheme 3.2 Synthesis of Fe(II)−hydroxo complexes, $N(_{X}pi^{R})(_{X}afa^{R})_2Fe(II)OH$ ($_{X}L^{R}Fe^{II}OH$; X = H, Br; R = Cy, Ph).

The complexes were synthesized in analogy to the previous published proteo cyclohexyl variant, $N(pi^{Cy})(afa^{Cy})_2Fe(II)OH$ ($_{H}L^{Cy}Fe^{II}OH$) (Scheme 3.2).[38] Ligand was added to a cold (-35 °C) solution of dimesityliron(II) (Fe$_2$Mes$_4$) in THF, giving a dark red-orange solution. Reactions were stirred at room temperature for 24 hours to ensure complete conversion to the desired hydroxo complex. Solvent was evaporated *in vacuo* to give the crude product, which was then recrystallized to give the pure compound, $N(_{X}pi^{R})(_{X}afa^{R})_2Fe(II)OH$ ($_{X}L^{R}Fe^{II}OH$), in high yields ($_{Br}L^{Cy}Fe^{II}OH$ – 84%, $_{H}L^{Ph}Fe^{II}OH$ – 74%, $_{Br}L^{Ph}Fe^{II}OH$ – 70%). Solution magnetic moments, determined by Evans' method, were consistent with high spin, $S = 2$ iron(II) species ($\mu_{eff} = 5.14(1) – 5.58(10)\ \mu_B$).

^{1}H NMR spectra for these derivatives were consistent with C_3 symmetry in solution. The resonances could be reliably assigned based on integration and comparison across the series. The secondary sphere amino and hydroxo protons showed the greatest paramagnetic shift, giving a broad resonance at 190 (R =

Cy) or 200 ppm (R = Ph), depending on the capping group.   Mixed tautomer binding of the ligand was confirmed by infrared spectroscopy, as indicated by the presence of two distinct C=N stretches (pyrrole-imine <1630 cm^{-1}, azafulvene-amine >1630 cm^{-1}; see Table 3.1 for values). While both tautomers are observed in the solid-state and in solution by infrared spectroscopy, they are not resolved on the NMR timescale, suggesting dynamic exchange of the protons in the secondary sphere.

  The complexes were structurally characterized by X-ray crystallography (selected bond lengths and angles are given in Table 3.1). Each complex displayed a trigonal bipyramidal geometry, with the iron(II) center bound slightly above the trigonal plane created by the nitrogen donors of the ligand arms. Comparison of the primary coordination sphere bond lengths for these complexes, relative to the previous published $_H$L^{Cy}Fe^{II}OH structure, demonstrated two distinct trends: 1) elongation of the Fe–O bond, and 2) contraction of the Fe–N bond for the apical nitrogen donor. Interestingly, these trends show no differentiation between ligand modification in the primary and secondary coordination sphere, suggesting that the electron-withdrawing effects are delocalized across the ligand in both cases. Elongation of the Fe–O bond is potentially consistent with increased hydrogen bond donation from the secondary coordination sphere, resulting from decreased electron density at the pendant amino groups. This increased donation to the hydroxo ligand would decrease its anionic character, thus elongating the Fe–O bond. The weaker donation from the hydroxo to the iron center would allow for a stronger interaction with the apical nitrogen lone pair, resulting in the observed Fe–N contraction.

  To more directly assess the differences in hydrogen bonding interactions for the two capping groups, the distances between the donor and acceptor pairs were examined. It would be expected that the more electron donating nature of the cyclohexyl capping group, compared to phenyl analog, would provide a

Table 3.1 Selected structural parameters of $_x$L^{R}Fe^{II}OH and $_x$L^{R}Fe^{III}O complexes.^{a}

	$_x$L^{R}Fe^{II}OH				$_x$L^{R}Fe^{III}O		
	$_H$L$^{Cy\ b}$	$_{Br}$L^{Cy}	$_H$L^{Ph}	$_{Br}$L^{Ph}	$_H$L$^{Cy\ c}$	$_{Br}$L^{Cy}	$_H$L$^{Ph\ d}$
Fe–O	2.0339(12)	2.080(3)	2.0701(16)	2.0602(16)	1.808(1)	1.846(4)	1.8246(14)
Fe–N	2.2675(14)	2.238(3)	2.235(2)	2.2503(18)	2.3084(12)	2.243(4)	2.2473(16)
Fe–N$_{afa}$^{e}	2.1178(14)	2.104(4)	2.0959(19)	2.0933(19)	2.0467(12)	2.027(5)	2.0299(17)
Fe–N$_{pi}$	2.1020(14)	2.088(4)	2.0845(18)	2.0759(18)			
N$_{afa}$···O^e	2.608(2)	2.755(5)	2.671(3)	2.634(3)	2.6531(16)	2.710(5)	2.594(2)
N$_{pi}$···O	2.7939(19)	2.663(5)	2.623(2)	2.628(3)			
N$_{ave}$···O^f	2.670(2)	2.724(5)	2.655(3)	2.632(3)			
ν$_{C=N}$	1624, 1655	1627, 1653	1619, 1650	1618, 1646	1667	1670	1670

^{a}Bond lengths and distances are reported in Å, infrared stretching frequencies are given in cm^{-1}. ^{b}Structural data for $_H$L^{Cy}Fe^{II}OH are reproduced from reference 38. ^{c}Strucutral data for $_H$L^{Cy}Fe^{III}O are reproduced from reference 39. ^{d}Structural data reported for [$_H$L^{Ph}Fe^{III}O]BArF. ^{e}Values reported are an average of the two or three arms bound in the azafulvene-amine tautomer for that structure. ^{f}Values reported are an average of all three arms, including data for both tautomeric forms.

stronger hydrogen bond acceptor in the imino form and a weaker donor in the amino form. However, for the imino-hydroxo interactions the opposite trend is observed, as evidenced by the $N_{pi}\cdots O$ distances. The phenyl derivatives ($_X L^{Ph} Fe^{II} OH$) contain shorter $N_{pi}\cdots O$ distances (X=H, 2.623(2) Å; X=Br, 2.628(3) Å) than the cyclohexyl analogs ($_X L^{Cy} Fe^{II} OH$; X=H, 2.734(2) Å; X=Br 2.663(5) Å), suggesting the phenyl capping group results in stronger hydrogen bonding interactions than the cyclohexyl. The $N_{afa}\cdots O$ distances for the amino groups acting as hydrogen bond donors do not show any clear trend (Table 3.1); the cyclohexyl analogs show the shortest (X=H, 2.608(2) Å) and longest (X=Br, 2.755(5) Å) $N_{afa}\cdots O$ interactions of the four complexes.

$N(_{Br}pi^{Cy})(_{Br}afa^{Cy})_2Fe(II)OH$ $N(pi^{Ph})(afa^{Ph})_2Fe(II)OH$ $N(_{Br}pi^{Ph})(_{Br}afa^{Ph})_2Fe(II)OH$

$_{Br}L^{Cy}Fe^{II}OH$ $_H L^{Ph}Fe^{II}OH$ $_{Br}L^{Ph}Fe^{II}OH$
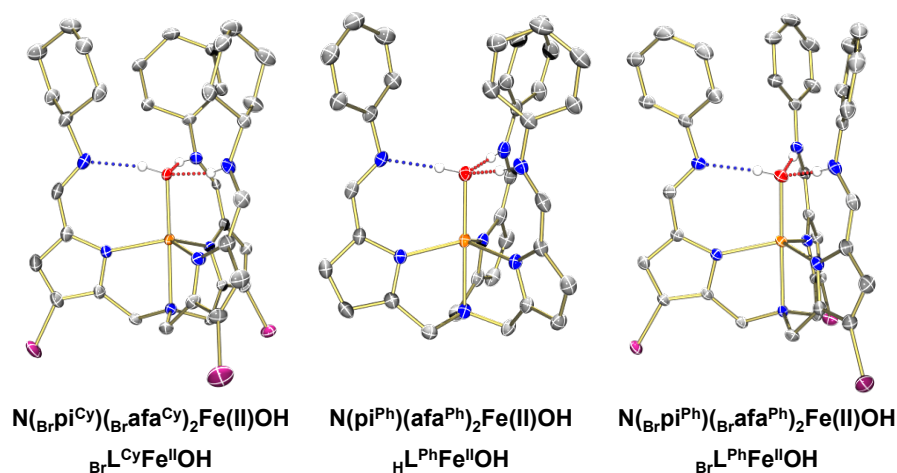
Figure 3.1 Molecular structures of $_{Br}L^{Cy}Fe^{II}OH$, $_H L^{Ph}Fe^{II}OH$, and $_{Br}L^{Ph}Fe^{II}OH$ shown with 50% probability ellipsoids. For clarity, only the hydroxo and amino protons are shown.

Given the dynamic exchange of these protons, the strength of the hydrogen bonding interactions may be better assessed using the average values, calculated for all three $N\cdots O$ distances regardless of tautomeric form. Both phenyl derivatives display slightly shorter $N_{ave}\cdots O$ distances than the cyclohexyl capped variants, consistent with stronger hydrogen bonding interactions overall, which is in agreement with the predicted trend for the amino hydrogen bond donors. Because two of the three ligand arms are bound in the azafulvene-amine tautomer for each of these structures, the donor strength would be expected to dominate the overall trend. This trend is also supported by the ^1H NMR data, where the hydroxo/amino proton in the secondary coordination sphere resonance is shifted 10 ppm downfield for the phenyl capping groups ($\delta = 200$ ppm), relative to the cyclohexyl variants ($\delta = 190$ ppm).

3.4 Establishing the redox chemistry of $_H L^{Cy}Fe^{II}OH$

The redox chemistry of the proteo cyclohexyl derivative was explored to establish a benchmark for comparison with the other derivatives. Cyclic voltammetry with $_H L^{Cy}Fe^{II}OH$ in a 1:1 THF/MeCN solvent mixture revealed a single reversible redox event centered at $E_{1/2} = -0.69$ V vs. $Fc^{0/+}$ (Figure 3.2). This event was tentatively assigned as a reversible Fe(II/III) couple. To confirm the assignment, we turned to chemical oxidation of $_H L^{Cy}Fe^{II}OH$ with one-electron oxidants such as ferrocenium triflate

(FcOTf) and silver triflate (AgOTf). Treatment of $_H\mathbf{L^{Cy}Fe^{II}OH}$ with either oxidant in DCM resulted in a change from light brown to dark brown. Following workup, the product was identified as the previously reported Fe(III)-oxo complex,[39] [N(afa^{Cy})$_3$Fe(III)O]OTf ($_H\mathbf{L^{Cy}Fe^{III}O}$), based on its ^{1}H NMR and infrared spectra (Scheme 3.3).
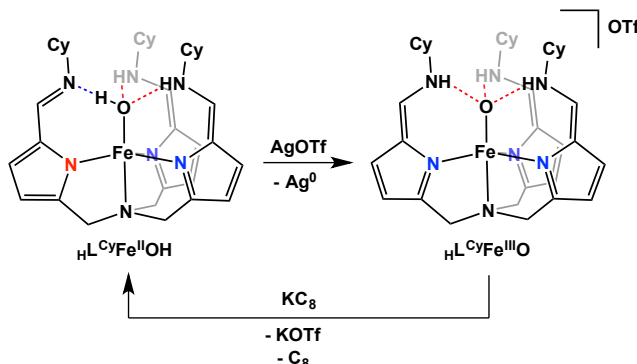
Scheme 3.3 Oxidation of $_H\mathbf{L^{Cy}Fe^{II}OH}$ to form $_H\mathbf{L^{Cy}Fe^{III}O}$, and the corresponding reduction to reform $_H\mathbf{L^{Cy}Fe^{II}OH}$.

Given the dearth of known terminal Fe(III)-oxo complexes, $_H\mathbf{L^{Cy}Fe^{III}O}$ was further characterized to confirm its spin state. The complex was experimentally confirmed to be high-spin, $S = 5/2$, using temperature dependent magnetic measurements (Figure 3.7). The room temperature χT value of 4.46 emu K mol^{-1} was slightly larger than the theoretical value 4.375 emu K mol^{-1} for the spin only magnetic moment (assuming a g value of 2.0), but is consistent with previously reported high-spin iron(III) complexes in related tris(pyrollyl-α-methyl)amine ligand frame-works.[42,43] Related C_3-symmetric, tetradentate ligands have been previously demonstrated to yield high-spin Fe(III)-oxo ($S=5/2$)[44] and Fe(IV)-oxo ($S=2$)[43,45,46] complexes.

While there is a formal proton transfer from the hydroxo moiety to the secondary coordination sphere upon oxidation, the framework has been designed to accommodate this proton movement via ligand tautomerization. Reduction of $_H\mathbf{L^{Cy}Fe^{III}O}$ by potassium graphite reforms the Fe(II)-hydroxo ($_H\mathbf{L^{Cy}Fe^{II}OH}$) in high yield (83%), indicating this intramolecular proton transfer is chemically reversible. These compounds were also determined to be electrochemically equivalent; analysis of either complex, or a 1:1 mixture of the two, gave indistinguishable cyclic voltammograms when collected under identical experimental conditions (Figure 3.17). Variable scan rate experiments further demonstrated that this Fe(II/III) redox event is electrochemically reversible, as determined by comparison of the peak-to-peak separations against a ferrocene standard (Figure 3.18). While the potential is more positive than the Fe(III/IV) redox couple reported for Borovik's Fe(III)-oxo complex ($E_{1/2}$ =-0.90 V),[46] $_H\mathbf{L^{Cy}Fe^{III}O}$ was found to be unreactive towards FcOTf (Figure 3.16), providing further support to assignment of this redox event as the Fe(II/III) couple in our system. We attribute the significant disparity in redox potentials to the electronic difference in the ligands; Borovik's urea ligand is trianionic, while the azafulvene binding mode in $_H\mathbf{L^{Cy}Fe^{III}O}$ provides a neutral donor set.

3.5 Comparing redox potentials across the series

After establishing the redox chemistry of $_H L^{Cy} Fe^{II} OH$, the newly synthesized derivatives ($_{Br} L^{Cy} Fe^{II} OH$, $_H L^{Ph} Fe^{II} OH$, and $_{Br} L^{Ph} Fe^{II} OH$) were examined to understand the impact of the ligand modifications. Each complex showed a single reversible redox event (Figure 3.2), assigned as the Fe(II/III) couple, in analogy to $_H L^{Cy} Fe^{II} OH$. The tribrominated analog, $_{Br} L^{Cy} Fe^{II} OH$, gave a Fe(II/III) couple at $E_{1/2}$ = −0.49 V vs. $Fc^{0/+}$, a positive shift of 200 mV. Intriguingly, changing the capping R-group from cyclohexyl to phenyl resulted in nearly the same shift in potential, with $_H L^{Ph} Fe^{II} OH$'s redox centered at $E_{1/2}$ = −0.51 V. Furthermore, the impact of these two ligand modifications was additive, with $_{Br} L^{Ph} Fe^{II} OH$ showing its Fe(II/III) couple at −0.29 V.
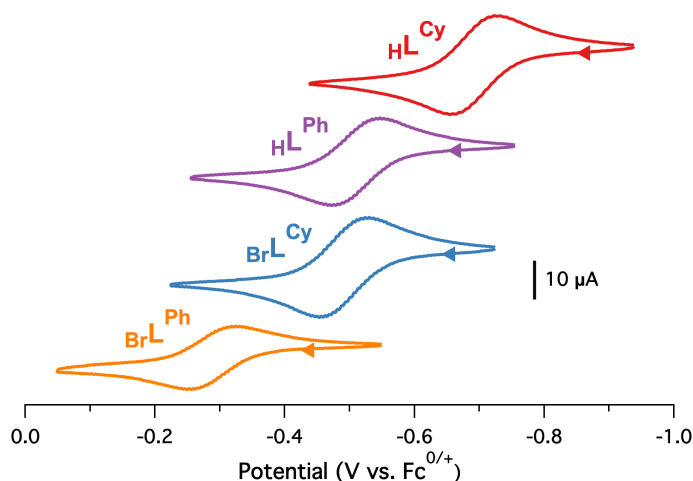
Figure 3.2 Cyclic voltammograms for the full series of iron(II) complexes, obtained for 1 mM solutions of the complex in a 1:1 THF/MeCN mixture with 0.1 M [$^n Bu_4 N$][PF_6] as supporting electrolyte (scan rate 0.1 V/sec).

Given our group's interest in small molecule activation with this framework,[39,40,47] understanding the impact of these ligand changes could allow intelligent tuning of the reactivity profile of our complexes through related ligand modifications. Accordingly, we sought to determine how changing the capping R-group shifted the redox potential. The phenyl ligand derivative was initially targeted as a means of tuning the strength of hydrogen bonding interactions in the secondary coordination sphere. Because structural data for the Fe(II)-OH complexes suggested the phenyl capped derivatives were stronger hydrogen bond donors, chemical oxidation of this variant was pursued to determine if this trend held true for the Fe(III)-O analogs. Treatment of $_H L^{Ph} Fe^{II} OH$ with AgOTf afforded an iron(III) species, which was isolated in high crystalline yield (77%). The product's ^1H NMR spectrum contained characteristic paramagnetic resonances at 61 and 79 ppm that closely resemble the spectral features observed for $_H L^{Cy} Fe^{III} O$. Further analysis by infrared spectroscopy revealed a single C=N stretch at 1667 cm^{-1}, indicating that all three arms of the ligand were bound as the azafulvene-amine tautomer and the complex is best described as an Fe(III)-oxo, [N(afa^{Ph})$_3$Fe(III)O]OTf ($_H L^{Ph} Fe^{III} O$).

To further examine the donor-acceptor interactions, the molecular structure of $_H\mathbf{L^{Ph}Fe^{III}O}$ was determined by X-ray diffraction studies. Attempts to crystallize the triflate salt did not yield diffraction quality crystals, so the tetrakis[3,5-bis(trifluoromethyl)phenyl]borate (BArF$_{24}$) variant, [N(afa^{Ph})$_3$Fe(III)O]BArF$_{24}$ ($[_H\mathbf{L^{Ph}Fe^{III}O}]\mathbf{BArF}$), was analyzed (Figure 3.3). Comparison of the primary coordination sphere bond lengths in $[_H\mathbf{L^{Ph}Fe^{III}O}]\mathbf{BArF}$ to those of $_H\mathbf{L^{Cy}Fe^{III}O}$ showed elongation of the Fe–O bond and contraction of the apical Fe–N bonds, analogous to the trends observed for the corresponding Fe(II)-OH species. The brominated cyclohexyl iron(III) complex, [N($_{Br}$afa^{Cy})$_3$Fe(III)O]OTf ($_{Br}\mathbf{L^{Cy}Fe^{III}O}$), was also synthesized and structurally characterized as an additional point of comparison (see Experimental Section for details). Once again the $_H\mathbf{L^{Ph}}$ and $_{Br}\mathbf{L^{Cy}}$ derivatives gave analogous structural changes within the primary coordination sphere, relative to $_H\mathbf{L^{Cy}}$. The N$_{afa}$···O bond distances were then examined to compare the relative strength of hydrogen bonding interactions for the two capping groups. Both cyclohexyl derivatives $_X\mathbf{L^{Cy}Fe^{III}O}$ showed longer N$_{afa}$···O distances (X=H, 2.6531(16) Å; X=Br, 2.710(5) Å) than the phenyl complex (2.594(2) Å). This trend is in agreement with the Fe(II)-OH complexes and is consistent with the phenyl capping group acting as a stronger hydrogen bond donor, as would be expected for a weaker electron donor to the amino groups.

[N($_{Br}$afa^{Cy})$_3$Fe(III)O]OTf
$_{Br}\mathbf{L^{Cy}Fe^{III}O}$

[N(afa^{Ph})$_3$Fe(III)O]BArF$_{24}$
$[_H\mathbf{L^{Ph}Fe^{III}O}]\mathbf{BArF}$
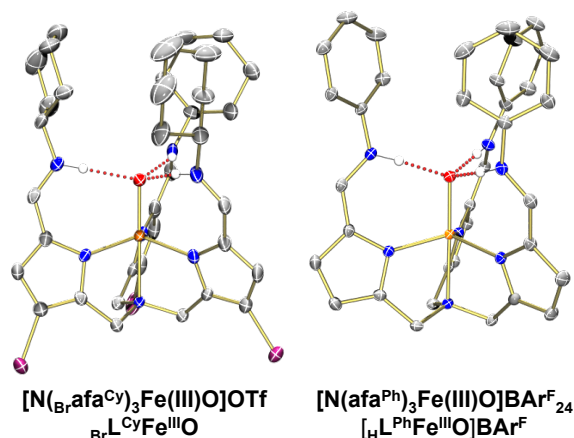
Figure 3.3 Molecular structures of $_{Br}\mathbf{L^{Cy}Fe^{III}O}$ and $[_H\mathbf{L^{Ph}Fe^{III}O}]\mathbf{BArF}$ shown with 50% probability ellipsoids. For clarity, only the major component of disordered groups is shown; counter ions and protons other than the amino groups are omitted.

While the overall trends in N···O distances suggest the phenyl capping group may tune the electronic properties of the iron center by reducing the anionic character of the oxygen donor, similarities in the primary coordination sphere bond lengths for both the Fe(II)-OH and Fe(III)-O complexes of $_{Br}\mathbf{L^{Cy}}$ and $_H\mathbf{L^{Ph}}$ likely indicate that these differences are not the only factor. The minimal differentiation between electron-withdrawing groups in the ligand's primary and secondary coordination spheres suggests delocalization of electron density across the platform. Accordingly, the possibility of the phenyl group extending the ligand's π-system was examined. If the phenyl rings are oriented coplanar with the rest of the ligand arm, π-conjugation could be further extended (Figure 3.22), resulting in an inductive effect analo-

41

gous to bromination. To test this theory, all four ligands and their Fe(II)-hydroxo complexes were characterized by electronic absorption spectroscopy.

The π-conjugation throughout the pyrrole-imine moiety of the ligand architecture results in a prominent π-π* transition in the UV region of the UV-visible absorption spectrum. This spectroscopic feature was used to examine the impact of the ligand modification on the extent of π-conjugation (Figure 3.4, Table 3.2). For the $_H L^{Cy}$ ligand this transition has an absorption maximum (λ_{max}) at 284 nm. Bromination of the pyrrole results in a minimal red shift of 2 nm, while changing the R-group from cyclohexyl to phenyl gives a more pronounced red shift of 45 nm, consistent with the expected increase in the π-conjugation
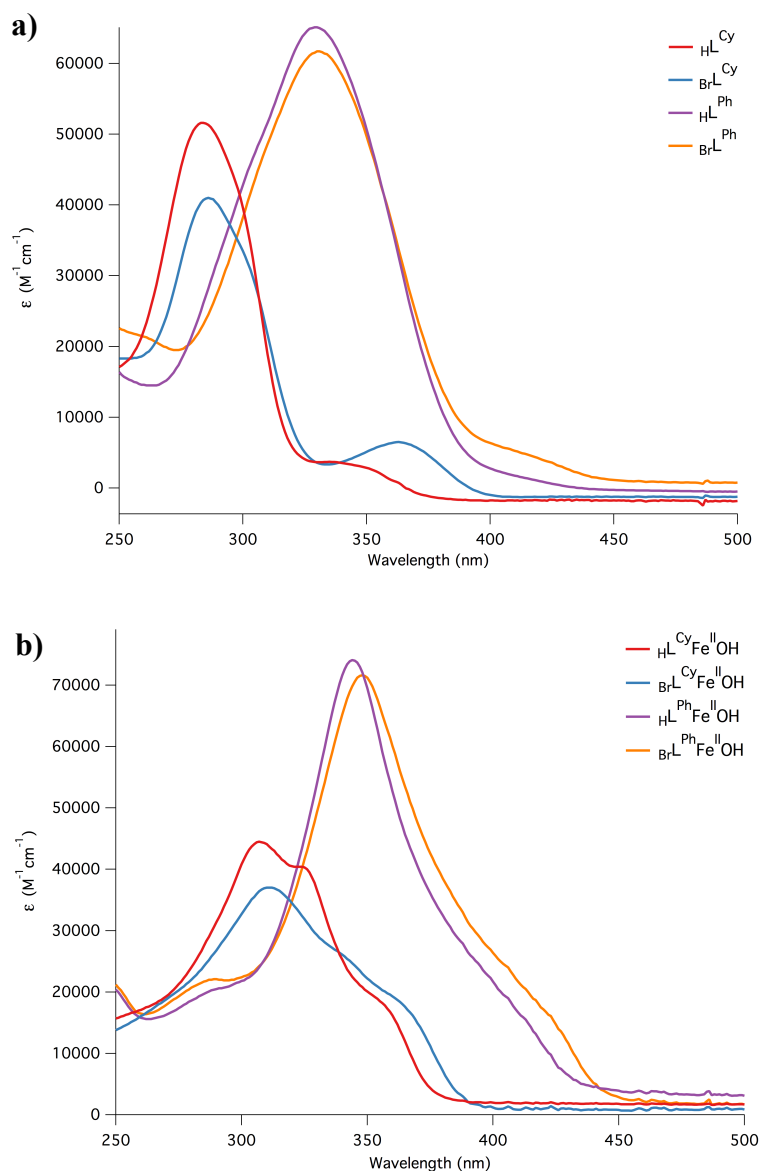
Figure 3.4 UV-visible spectra for the full series of a) ligands (top) and b) iron(II) complexes (bottom). All spectra were obtained at room temperature in dichloromethane.

(Figure 3.4a). Analogous shifts are observed for the Fe(II)-hydroxo complexes, suggesting the extended π-conjugation present in the phenyl ligands may be partially maintained upon metallation (Figure 3.4b).

3.6 DFT analysis

Density functional theory (DFT) was employed to develop a deeper understanding of the role each ligand modification plays in tuning the

Table 3.2 Absorption maxima (λ_{max}) for the series of ligands and iron(II) complexes.[a]

	Ligand		Fe(II) Complex	
	λ_{max}	$\Delta\lambda_{max}$[b]	λ_{max}	$\Delta\lambda_{max}$[b]
$_H L^{Cy}$	284		307	
$_{Br} L^{Cy}$	286	2	311	4
$_H L^{Ph}$	329	45	344	37
$_{Br} L^{Ph}$	331	47	348	41

[a]All values are reported in nanometers and correspond to the transition with the highest molar absorptivity. [b]Change in λ_{max} relative to $_H L^{Cy}$ derivative.

electronic properties of the corresponding metal complexes (B3LYP/6-311G(d,p);[48-52] see Experimental Section for computational details). The iron(II)-hydroxo ($_x L^R Fe^{II}OH$) and iron(III)-oxo ($_x L^R Fe^{III}O$) structures were optimized and are in good agreement with the experimental data obtained from X-ray diffraction experiments. Prior to analyzing the influence of the ligand modifications, the predicted shift in the redox potential of the Fe(II/III) couple was calculated for each derivative (as an average of the MeCN and THF potentials to imitate the mixed solvent system used experimentally), as a means of benchmarking the computational system against experimental results. While DFT analysis overestimated the magnitude of the potential shift in each case, possibly due to the crude approximation of the mixed solvent, these calculations successfully reproduced the trends observed in the cyclic voltammetry experiments. Both the experimental and computational data showed that bromination of the pyrrole backbone or changing the capping group from cyclohexyl to phenyl gave similar shifts in the redox potential, and that these effects were additive (Table 3.3).

Satisfied with the ability of DFT to reproduce the electronic differences created by these ligand modifications, we next examined the molecular orbitals involved in tuning these properties. Initial calculations were carried out using ligand

Table 3.3 Experimental and calculated potentials for the Fe(II/III) redox couple.[a]

	$E_{1/2} Fe^{II/III}$	$\Delta E_{1/2} exp$[b]	$\Delta E_{1/2} calc$[b]	Difference[c]
$_H L^{Cy}$	-0.69			
$_H L^{Ph}$	-0.51	0.18	0.24	0.06
$_{Br} L^{Cy}$	-0.49	0.20	0.27	0.07
$_{Br} L^{Ph}$	-0.29	0.40	0.48	0.08

[a]All values are reported in volts (V) for the corresponding Fe(II)-hydroxo complex. [b]Change in $E_{1/2}$ relative to $_H L^{Cy}$ derivative. [c]Difference in calculated and experimental potentials.

arm models (truncated as the corresponding pyrrole-imine) to probe the differences in the π-system, specifically examining the molecular orbitals (MOs) involved in the π-π* transition (see below) observed by UV-visible spectroscopy. Bromination of the pyrrole backbone stabilized both the HOMO and the LUMO by ~200 meV, through inductive electron-withdrawing effects, resulting in a minimal change in energy of the π-π* transition (Figure 3.5). This result was consistent with the minimal shift in λ_{max} observed in the experimental spectra for the corresponding ligands (Figure 3.4). Changing the imino R-group from cyclohexyl to phenyl resulted in the expected extension of the π-system. The imine nitrogen

and the ipso carbon of the phenyl ring form an anti-bonding interaction in the HOMO, destablizing it relative to the cyclohexyl variant. In the LUMO, those atoms form a bonding interaction, lowering it in energy. Taken together these differences give a lower energy π-π* transition, consistent with the experimentally observed red-shift for the phenyl capping group.

To establish whether these differences in π-conjugation were maintained upon metallation, the iron complexes' electronic absorption spectra were computationally determined (see Supporting Information). The simulated spectra were in good agreement with experimental results for both the Fe(II)-hydroxo and Fe(III)-oxo compounds (Figure 3.23). Importantly, the minimal change in absorption maxima observed
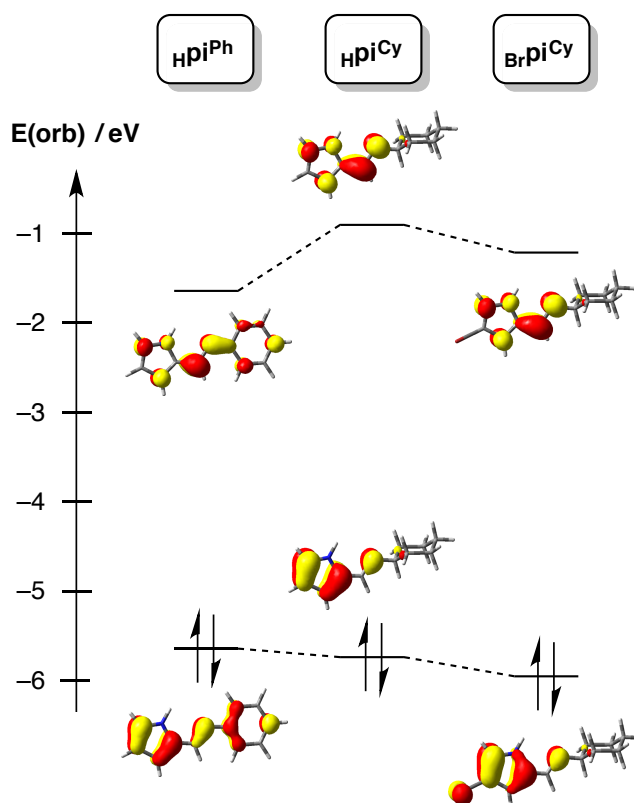
Figure 3.5 HOMO-LUMO gap calculated for truncated ligand arm models, demonstrating the differences in ligand π-π* transitions for each modification.

upon bromination, and the significant red shift observed upon changing the capping group from cyclo-hexyl to phenyl, were both reproduced in the computational data. The most significant individual transitions responsible for each peak were identified (Tables 3.5-3.8). Given the minimal shift in absorption maxima observed upon bromination, molecular orbitals were only analyzed for the proteo derivatives. The cyclohexyl variant, $_{H}L^{Cy}Fe^{II}OH$, gave two major transitions of different intensities, consistent with the experimental spectrum; the lower energy transition is a ligand π-π* transition in the protonated arms, while the higher energy band corresponds to the ligand π-π* transition in the deprotonated arm (Table 3.5). For the phenyl variant, $_{H}L^{Ph}Fe^{II}OH$, the extended π-conjugation through the capping group lowers both π-π* transitions in energy, resulting in the observed red shift of the absorption maxima (Table 3.6).

Although these alterations in π-conjugation explain the differences observed in the UV-visible spectra, they do not directly explain the shift in the Fe(II/III) redox potentials upon changing the capping group. To better understand the role of the capping group in determining the metal complexes' redox properties, their respective d-orbital manifolds were examined. DFT analysis of the high-spin, *S*=2, Fe(II)-hydroxo complexes ($_H$L^{Cy}Fe^{II}OH and $_H$L^{Ph}Fe^{II}OH) predicted a significant difference in the energy of the metal-based HOMO and SOMOs for the two different capping groups (Figure 3.6). The HOMO, which contains the electron removed upon chemical oxidation, was determined to be a metal-based d-orbital in both derivatives. While there was no direct ligand contribution to this redox-active orbital, the inductive effect of switching from a cyclohexyl to phenyl capping group lowered the metal d-orbitals in energy, thus shifting the Fe(II/III) redox couple to a more positive potential for the phenyl derivatives. This inductive electron-withdrawing effect is also evident in the increased ligand contribution to the SOMOs in $_H$L^{Ph}Fe^{II}OH, though these molecular orbitals are still primarily metal-centered.

In sum, the DFT analysis further highlighted the delocalization of the phenyl groups' electron-withdrawing effects across the extended π-system. These results were in strong agreement with the experimental data, where the $_{Br}$L^{Cy} and $_H$L^{Ph} derivatives gave analogous structural changes and similar shifts in the Fe(II/III) redox potential, relative to the $_H$L^{Cy} complex. Orbital analysis demonstrated both ligand modifications tune the redox properties of the metal complexes through inductive electron-withdrawing effects that are delocalized throughout the ligand framework.
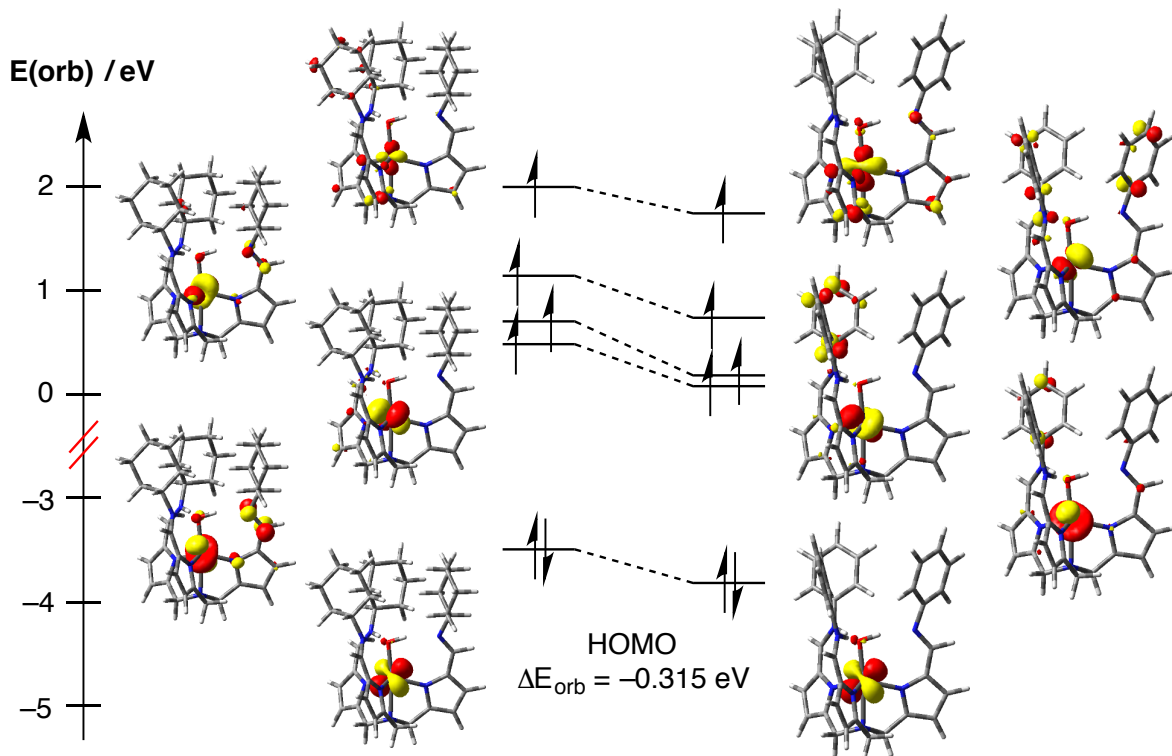
Figure 3.6 Comparison of the HOMO and SOMOs calculated for $_H$L^{Cy}Fe^{II}OH (left) and $_H$L^{Ph}Fe^{II}OH (right).

3.7 Conclusion

Derivatization of the imino-functionalized tris(pyrrolylmethyl)amine ligand, $N(_Xpi^R)_3$, has been described. Electron withdrawing derivatives have been developed by modification of the primary and secondary coordination spheres. The corresponding iron(II)-hydroxo complexes were synthesized to examine the impact of these alterations. Cyclic voltammetry experiments demonstrated that either brominating the pyrrole backbone in the primary coordination sphere, or changing the capping group from cyclohexyl to phenyl in the secondary sphere, resulted in a positive shift of the Fe(II/III) redox couple by ~200 mV.

The origins of these shifts in redox potential were examined to determine the role of each coordination sphere in modulating the electronic properties at the metal center. Electronic absorption spectroscopy demonstrated that the phenyl capping group extends the ligand π-system, which may attenuate the donor strength of the coordinating nitrogens. However, theoretical studies suggested the π-system was not solely responsible for the shift in redox potential observed with aryl capping groups, as these models showed minimal ligand contribution to the HOMO and SOMOs in $_HL^{Ph}Fe^{II}OH$, despite the extended π-conjugation. While the similarities between $_HL^{Ph}$ and $_{Br}L^{Cy}$ derivatives made it difficult to separate primary and secondary coordination sphere effects, comparison of the N···O distances in the Fe(II)-OH and Fe(III)-O complexes displayed shorter contacts for the phenyl capping group. These data are consistent with the phenyl derivatives' amino groups acting as stronger hydrogen bond donors than in the cyclohexyl analogs, which likely plays a role in determining the electronics of the iron center by tuning the donor strength of the bound hydroxo/oxo ligand.

Furthermore, this work establishes that facile ligand modifications at either site can be used to tune the electronic properties of the iron center and shift the Fe(II/III) redox couple by up to 400 mV. Given the importance of these types of modifications in dictating the reactivity of metalloenzymes, future work will examine the impact of these ligand derivatives on small molecule reactivity for our system. Ongoing studies are also targeting additional ligand modifications to electronically decouple the secondary coordination sphere and thereby enable a more direct investigation into the impact of tuning the hydrogen bonding interactions.

3.8 Experimental section

General considerations. All manipulations of air- and moisture-sensitive metal compounds were carried out in the absence of water and dioxygen using standard Schlenk techniques or in an MBraun inert atmosphere drybox under a dinitrogen atmosphere, except where specified otherwise. All glassware was oven dried for a minimum of 8 h and cooled in an evacuated antechamber prior to use in the drybox. Solvents were dried and deoxygenated on a Glass Contour System (SG Water USA, Nashua, NH) and stored over 4 Å molecular sieves purchased from Strem prior to use. Chloroform-d_1, dichloromethane-d_2, and dimethylsulfoxide-d_6 were purchased from Cambridge Isotope Labs and stored over 4 Å molecular sieves

prior to use. N-bromosuccinimide was purchased from Sigma Aldrich and recrystallized from boiling water prior to use. Cyclohexylamine (Sigma Aldrich), aniline (Acros), silver triflate (Strem), and formic acid (88% in water, Macron) were purchased from the listed vendor and used as received. $Fe(OTf)_2 \cdot 2$ $MeCN^{53}$ and ferrocenium triflate[54] were prepared according to a modified literature procedures. NaB-ArF$_{24}$,[55] Fe$_2$(Mes)$_4$,[56] tpa^{CO},[38] and N(pi^{Cy})(afa^{Cy})$_2$Fe(II)OH (**$_H$L^{Cy}Fe^{II}OH**)[38] were all prepared according to literature procedures. KC$_8$ was prepared by heating potassium metal with graphite, in a 1:8 ratio, at 80 ºC for 4 hours. *CAUTION:* potassium metal and its intercalation compound (KC$_8$) are both pyrophoric and should be handled with extra care; both the synthesis and use of the reagent were cared out under a nitrogen atmosphere. Celite® 545 (J. T. Baker) and Tetrabutylammonium hexafluorophosphate ([^{n}Bu$_4$N][PF$_6$]) (Sigma Aldrich) were dried in Schlenk flasks for 24 h under dynamic vacuum while heating to at least 150 ºC, prior to use in a drybox. NMR spectra were recorded on a Varian spectrometer operating at 500 MHz (^{1}H NMR), 377 MHz (^{19}F NMR), or 126 MHz (^{13}C NMR). All ^{1}H and ^{13}C chemical shifts (ppm) are reported relative to the resonance of the residual solvent as a standard; ^{19}F chemical shifts are reported relative to an external standard of 1% CFCl$_3$ in CDCl$_3$ as a reference. Solid-state infrared spectra were recorded using a PerkinElmer Frontier FT-IR spectrophotometer equipped with a KRS5 thallium bromide/iodide universal attenuated total reflectance accessory. UV/visible spectra were recorded on an Agilent 8453 UV/visible spectrophotometer. Elemental analyses were performed by the University of Illinois at Urbana-Champaign School of Chemical Sciences Microanalysis Laboratory in Urbana, IL. Samples submitted for elemental analyses were dried under vacuum for a minimum of 12 hours; solvates were confirmed by ^{1}H NMR.

Cyclic voltammetry. Electrochemical experiments were carried out using a CH Instruments CHI410C Electrochemical Workstation. The supporting electrolyte was 0.1 M [^{n}Bu$_4$N][PF$_6$] in a 1:1 acetonitrile/tetrahydrofuran mixture. A glassy carbon working electrode, a platinum wire counter electrode, and a silver wire pseudo reference electrode were used. The concentration of each analyte was 1 mM. Experiments were performed at a scan rate of 100 mV/s, unless otherwise specified. Each scan was referenced to internal Fc$^{0/+}$.

Magnetism. Most of the compounds reported herein were analyzed by Evan's Method to determine their solution magnetic moment.[57,58] Given the rarity of terminal iron(III)-oxo complexes, **$_H$L^{Cy}Fe^{III}O** was examined in the solid state to obtain a more precise, temperature dependent magnetic moment. Magnetic data for **$_H$L^{Cy}Fe^{III}O** were collected on a Quantum Design Multi-Property Measurement System (MPMS-7) with a Reciprocating Sample Option. Temperature dependence measurements were performed under applied 1 T DC fields from 2 to 300 K while field dependence measurements were performed at 2 K with varying applied magnetic field strengths ranging from 0 to 7 T. Corrections for the

intrinsic diamagnetism of the samples were made using Pascal's constants.[59] Data were collected on two independently prepared samples to ensure reproducibility.

Each magnetism sample was prepared in the glove box and placed in a heat-sealed compartment of a plastic drinking straw. The plastic drinking straws were evacuated overnight prior to use. These straws were then sealed at one end (~9.5 cm from the top) by heating a pair of forceps and crimping the sides of the straw until both sides were fused together. Microcrystalline compound (~10 – 20 mg) was loaded into the straw and capped with ~10 mg of Quartz wool (dried at 250 °C prior to use) and packed in tightly using a Q-tip. The other end of the plastic drinking straw was then sealed directly above the quartz wool, forming a small compartment (<1 cm). The sample and wool were massed four times each to the nearest 0.1 mg and the values used were the averages of these mass measurements.
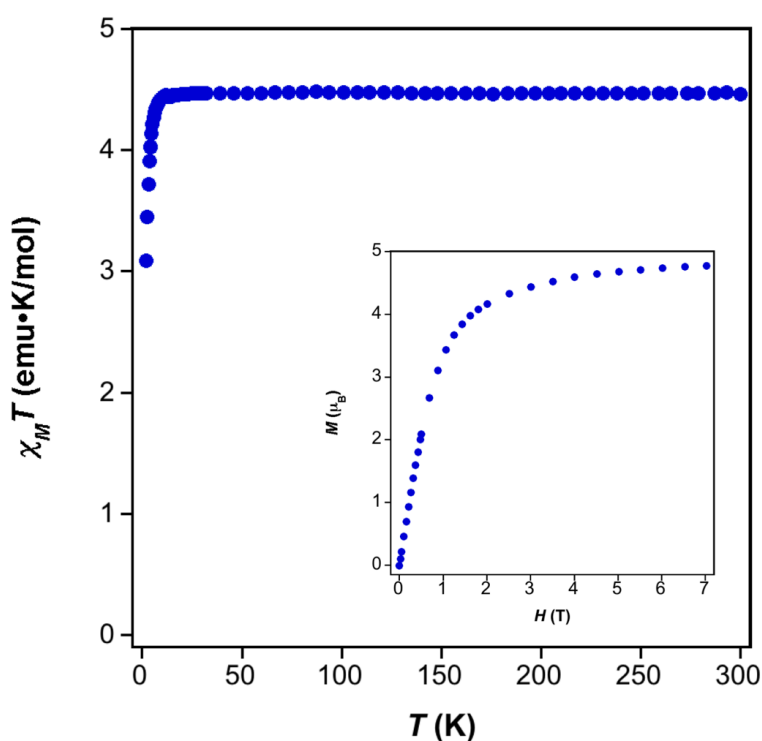
Figure 3.7 Temperature dependence of the χT product measured using a 1.0 T field and field dependence at 2 K (inset) for $[N(afa^{Cy})_3Fe(III)O]OTf$ ($_HL^{Cy}Fe^{III}O$).

Computational details. Electronic structure calculations were carried out using B3LYP/6-311G(d,p),[48-52] as implemented in Gaussian09.[60] The optimized structures were confirmed to be stable minima through analysis of the harmonic frequencies,[61-62] and the wavefunction at each minimum was confirmed to be stable.[63-64] When we attempted to optimize the iron(II)-hydroxo species, $_HL^RFe^{II}OH$, from the oxidized species, $_HL^RFe^{III}O$, the geometry optimized instead to an aquo species $_HL^RFe^{II}OH_2$ with two ligand arms bound in the pyrrole-imine tautomer for both $_HL^{Cy}$ and $_HL^{Ph}$. These aquo species are computed to be slightly more stable than the hydroxo species at –0.78 and –2.21 kcal/mol, respectively,

48

but those values are well within the error of our computational method. Since there was no experimental evidence for these isomers in the derivatives that were modeled, we focus on the isoenergetic hydroxo species in the manuscript. Follow-up single point calculations simulating solvent effects were performed using the implicit SMD[65] solvation model for acetonitrile and THF. For comparison with the experimental mixed-solvent, we averaged these two solvation energies. Table 3.4 summarizes relevant thermodynamic values. Tables containing the Cartesian coordinates and frequencies for the optimized species are provided in the Supporting Information of the published manuscript.[66]

Preparation of $_{Br}$tpa^{CO}. A 100 mL round bottom flask was charged with tpa^{CO} (1.047 g, 3.10 mmol) and 20 mL tetrahydrofuran. The resulting brown slurry was cooled to 0 ºC in an ice bath. N-bromosuccinimide (1.709 g, 9.60 mmol) was slowly added to the mixture as a solid, resulting in a deep red-brown solution. The reaction was stirred in the melting ice bath until it reached room temperature, then for an additional 2 h at room temperature. Product was precipitated from solution with 150 mL cold deionized water and collected over a fritted funnel. This material was washed with fresh DI water (2 x 50 mL) to ensure full removal of the water-soluble succinimide byproduct. The product, $_{Br}$tpa^{CO}, was collected as a tan powder and dried under vacuum overnight (1.492 g, 2.59 mmol, 84%). Analysis for $C_{18}H_{15}Br_3N_4O_3 \cdot 0.2\ C_4H_8O$: Calcd. C, 38.31; H, 2.84; N, 9.50. Found C, 38.68; H, 2.37; N, 9.30. ^{1}H NMR (DMSO-d$_6$, 500 MHz, 21 °C): δ = 3.59 (s, 6H, methylene-CH_2), 7.06 (d, J = 2.6 Hz, 3H, pyr-CH), 9.38 (s, 3H, aldehyde-CH), 12.14 (s, 3H, pyr-NH). ^{13}C NMR (DMSO-d$_6$, 126 MHz, 21 ºC): 49.12, 97.70, 122.46, 132.05, 135.40, 178.90. IR ν_{max} = 1644 cm^{-1} (C=O).

Preparation of N($_{Br}$pi^{Cy})$_3$ · H$_2$O ($_{Br}$L^{Cy}). A 100 mL round bottom flask was charged with $_{Br}$tpa^{CO} (1.712 g, 2.98 mmol) and acetonitrile 25 mL, giving a tan suspension. Cyclohexylamine (0.8964 g, 9.04 mmol, 3 equiv) was added dropwise to this suspension. The reaction was stirred at room temperature overnight to ensure complete conversion. The insoluble product was collected over a fritted funnel, washed with fresh acetonitrile (20 mL), then collected and dried under vacuum. N($_{Br}$pi^{Cy})$_3$ · H$_2$O was isolated as a tan powder (2.267 g, 2.71 mmol, 91%). Analysis for $C_{36}H_{48}Br_3N_7 \cdot 1.2\ H_2O$: Calcd. C, 51.47; H, 6.05; N, 11.67. Found C, 51.23; H, 5.74; N, 11.36. ^{1}H NMR (CDCl$_3$, 500 MHz, 21 °C): δ= 1.21 – 1.81 (m, 30H, Cy-CH), 3.11 (tt, J = 10.7, 4.0 Hz, 3H, Cy-CH), 3.61 (s, 6H, methylene-CH_2), 6.41 (s, 3H, pyr-CH), 7.94 (s, 3H, imine-CH), 9.33 (br, 3H, pyr-NH). ^{13}C NMR (CDCl$_3$, 126 MHz, 21 ºC): δ= 25.04, 25.75, 34.87, 49.39, 68.82, 97.30, 115.94, 129.80, 131.29, 148.92. UV-vis (DCM, 25 ºC) λ_{max} nm (ε M^{-1} cm^{-1}) = 286 (41000). IR ν_{max} = 1634 cm^{-1} (C=N).

General procedure for aniline condensations. A 100 mL round bottom flask was charged with the desired formylated tpa derivative (tpa^{CO} or $_{Br}$tpa^{CO}) and ethanol (25 mL), giving a tan suspension. A slight excess of aniline (3.1 equiv) was added dropwise to this suspension, followed by a catalytic amount of formic acid (3-6 drops, 88% in H$_2$O). The reaction was stirred at room temperature overnight to ensure

complete conversion, as both the formylated starting material and the imine ligand product are minimally soluble in ethanol. The crude material was collected over a fritted funnel and washed with diethylether to remove residual aniline. This crude product was dissolved in a 1:1 mixture of dichloromethane and chloroform (40 mL), then washed with a saturated aqueous solution of sodium bicarbonate (40 mL) to neutralize the residual formic acid. The organic layer was washed with brine (40 mL) then collected, dried over Na_2SO_4, and evaporated to yield the water adduct of the desired ligand, $_xL^{Ph} \cdot H_2O$, as a tan powder. See below for characterization details.

N(pi^{Ph})$_3$ · H$_2$O ($_HL^{Ph}$). 1.057 g tpa^{CO} (3.12 mmol), 0.890 g aniline (9.56 mmol, 3.1 equiv), 6 drops formic acid. 1.228 g N(pi^{Ph})$_3$ · H$_2$O collected (2.11 mmol, 68%). Analysis for $C_{36}H_{33}N_7 \cdot 1.25\ H_2O$: Calcd. C, 73.76; H, 6.10; N, 16.73. Found C, 73.62; H, 5.81; N, 16.37. ^1H NMR (CD$_2$Cl$_2$, 500 MHz, 21 °C): δ= 3.74 (s, 6H, methylene-C*H$_2$*), 6.18 (d, J = 3.6 Hz, 3H, pyr-C*H*), 6.65 (d, J = 3.6 Hz, 3H, pyr-C*H*), 7.16 (m, 9H, Ph-C*H*), 7.26 (m, 6H, Ph-C*H*), 8.26 (s, 3H, imine-C*H*), 11.06 (br, 3H, pyr-N*H*). ^{13}C NMR (CD$_2$Cl$_2$, 126 MHz, 21 °C): δ= 51.54, 109.94, 117.93, 121.29, 125.80, 129.53, 130.90, 136.65, 149.96, 151.21. UV-vis (DCM, 25 °C) λ_{max} nm (ε M^{-1} cm^{-1}) = 329 (65100). IR ν_{max} = 1615 cm^{-1} (C=N).

N($_{Br}$pi^{Ph})$_3$ · H$_2$O ($_{Br}L^{Ph}$). 1.016 g $_{Br}$tpa^{CO} (1.77 mmol), 0.514 g aniline (5.52 mmol, 3.1 equiv), 3 drops formic acid. 1.191 g N($_{Br}$pi^{Ph})$_3$ • H$_2$O collected (1.45 mmol, 82%). Analysis for $C_{36}H_{30}Br_3N_7 \cdot H_2O$: Calcd. C, 52.83; H, 3.94; N, 11.98. Found C, 52.68; H, 3.49; N, 11.66. ^1H NMR (CDCl$_3$, 500 MHz, 21 °C): δ= 3.79 (s, 6H, methylene-C*H$_2$*), 6.63 (s, 3H, pyr-C*H*), 7.07 (m, 6H, Ph-C*H*), 7.17 (m, 3H, Ph-C*H*), 7.20 (m, 6H, Ph-C*H*), 8.15 (s, 3H, imine-C*H*). ^{13}C NMR (CDCl$_3$, 126 MHz, 21 °C): δ= 50.30, 97.84, 118.76, 121.06, 126.07, 129.33, 130.16, 132.88, 148.82, 150.19. UV-vis (DCM, 25 °C) λ_{max} nm (ε M^{-1} cm^{-1}) = 331 (61700). IR ν_{max} = 1618 cm^{-1} (C=N).

General procedure for metallation. Fe$_2$Mes$_4$ was dissolved in tetrahydrofuran (5 mL) and cooled to -35 °C. Ligand was weighed by difference and added as a solid to the pale yellow solution, giving an immediate color change to dark red-orange. The reaction was stirred at room temperature for 24 h then dried in vacuo. Analytically pure product was isolated via crystallization from the crude material. Crystallization conditions and characterization data for each of the iron(II)-hydroxo products ($_xL^RFe^{II}OH$) are given below.

N($_{Br}$pi^{Cy})($_{Br}$afa^{Cy})$_2$Fe(II)OH ($_{Br}L^{Cy}Fe^{II}OH$). 0.051 g Fe$_2$Mes$_4$ (0.087 mmol), 0.146 g N($_{Br}$pi^{Cy})$_3$ · H$_2$O (0.175 mmol, 1 equiv per Fe center). Crystals suitable for X-ray diffraction were grown from a solution of $_{Br}L^{Cy}Fe^{II}OH$ dissolved in benzene and layered with hexanes. The compound was crystallized under the same initial conditions for bulk purification; a second crop was isolated by dissolving the residual solid in THF and layering the solution with hexanes. $_{Br}L^{Cy}Fe^{II}OH$ was collected as a tan powder (0.129 g, 0.145 mmol, 84% crystalline yield). Analysis for $C_{36}H_{48}Br_3FeN_7O \cdot 0.75\ C_6H_6$: Calcd. C, 51.26; H, 5.58; N, 10.33. Found C, 51.13; H, 5.52; N, 10.19. ^1H NMR (CD$_2$Cl$_2$, 500 MHz, 21 °C): δ = -4.03 (s, 3H,

imine-CH), 5.10 (s, 3H, Cy-CH), 5.27 (s, 6H, Cy-CH), 5.94 (s, 6H, Cy-CH), 6.39 (s, 3H, Cy-CH), 7.13 (s, 3H, Cy-CH), 7.55 (s, 6H, Cy-CH), 14.32 (s, 6H, Cy-CH), 41.29 (s, 3H, pyr-CH), 124.18 (br, 6H, methylene-CH_2), 190.62 (br, 3H, amino-NH/hydroxo-OH). UV-vis (DCM, 25 °C) λ_{max} nm (ε M^{-1} cm^{-1}) = 311 (37000). IR ν_{max} = 1627, 1653 cm^{-1} (C=N). μ_{eff} = 5.14(1) μ_B.
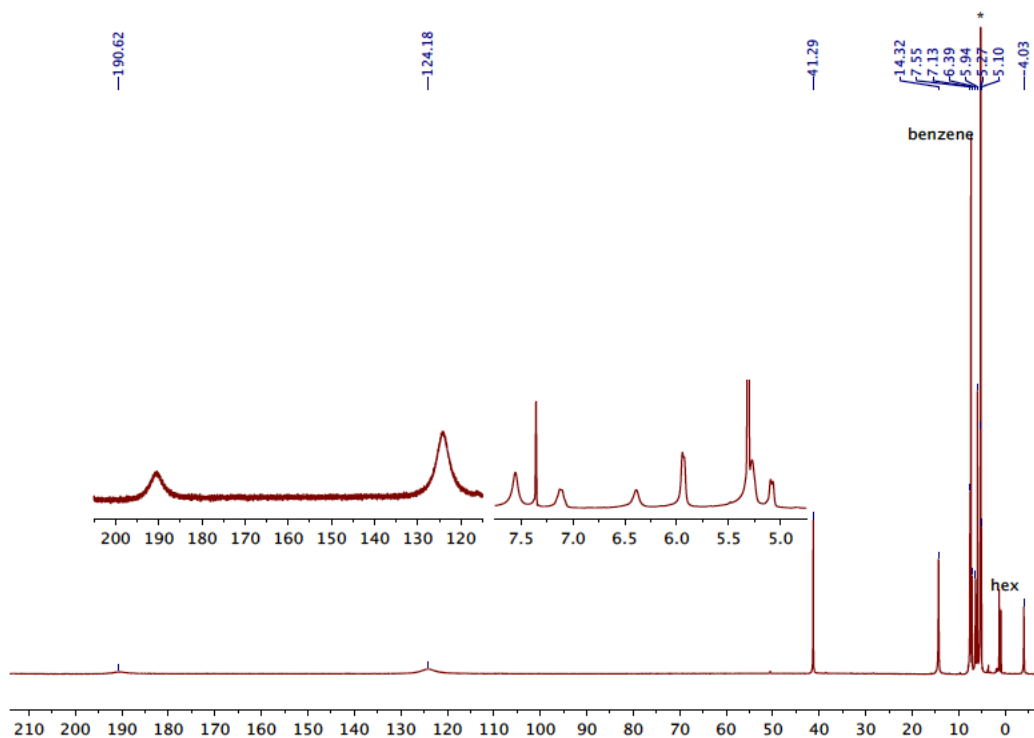
Figure 3.8 ^{1}H NMR spectrum of N$(_{Br}pi^{Cy})(_{Br}afa^{Cy})_2$Fe(II)OH (**$_{Br}$L^{Cy}Fe^{II}OH**) (500 MHz, CD$_2$Cl$_2$, *residual solvent).

N(pi^{Ph})(afa^{Ph})$_2$Fe(II)OH ($_H$L^{Ph}Fe^{II}OH). 0.055 g Fe$_2$Mes$_4$ (0.093 mmol), 0.110 g N(pi^{Ph})$_3$ · H$_2$O (0.189 mmol, 1 equiv per Fe center). Crystals suitable for X-ray diffraction were grown from a solution of **$_H$L^{Ph}Fe^{II}OH** dissolved in THF and layered with pentane. For bulk purification, the compound was crystallized from a THF solution of the complex layered with hexanes. **$_H$L^{Ph}Fe^{II}OH** was collected as a yellow-brown powder (0.088 g, 0.138 mmol, 74% crystalline yield). Analysis for C$_{36}$H$_{33}$FeN$_7$O: Calcd. C, 68.03; H, 5.23; N, 15.43. Found C, 67.56; H, 5.15; N, 15.08. ^{1}H NMR (CD$_2$Cl$_2$, 500 MHz, 21 °C): δ = -2.98 (s, 3H, imine-CH), 11.52 (s, 3H, Ph-CH), 11.66 (s, 6H, Ph-CH), 19.57 (s, 6H, Ph-CH), 26.94 (s, 3H, pyr-CH), 31.24 (s, 3H, pyr-CH), 138.73 (br, 6H, methylene-CH_2), 200.48 (br, 3H, amino-NH/hydroxo-OH). UV-vis (DCM, 25 °C) λ_{max} nm (ε M^{-1} cm^{-1}) = 344 (74100). IR ν_{max} = 1619, 1650 cm^{-1} (C=N). μ_{eff} = 5.35(11) μ_B.
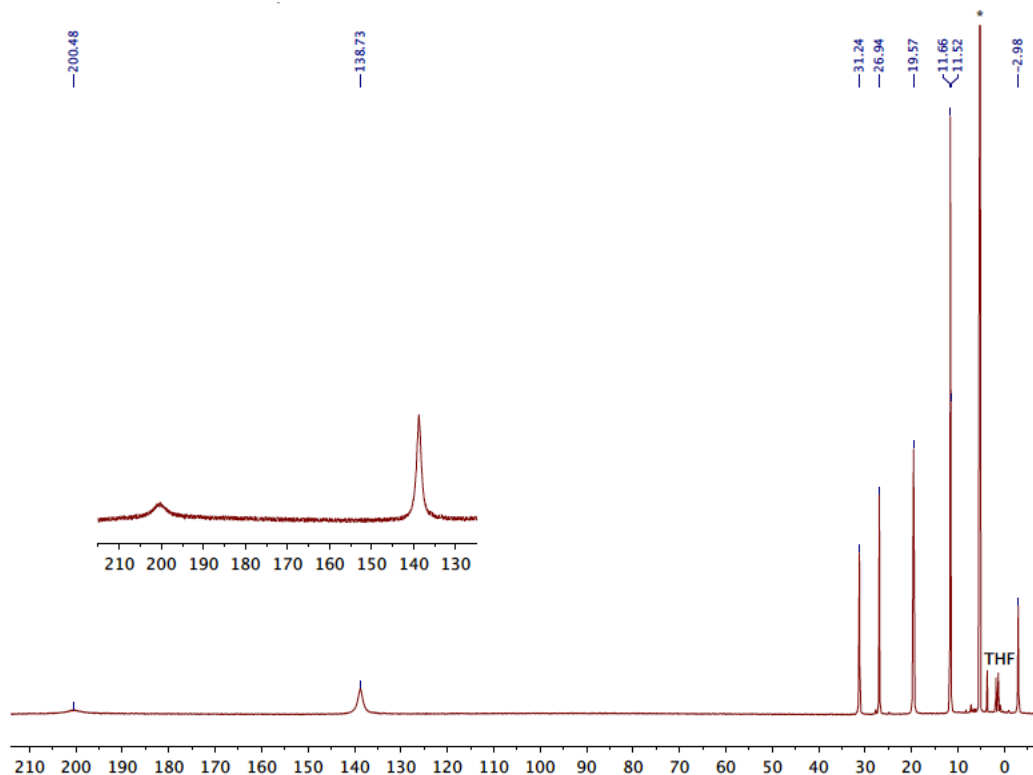
Figure 3.9 ^{1}H NMR spectrum of N(pi^{Ph})(afa^{Ph})$_2$Fe(II)OH ($_H$L^{Ph}Fe^{II}OH) (500 MHz, CD$_2$Cl$_2$, *residual solvent).

N($_{Br}$pi^{Ph})($_{Br}$afa^{Ph})$_2$Fe(II)OH ($_{Br}$L^{Ph}Fe^{II}OH). 0.054 g Fe$_2$Mes$_4$ (0.092 mmol), 0.152 g N($_{Br}$pi^{Ph})$_3$ · H$_2$O (0.186 mmol, 1 equiv per Fe center). Crystals suitable for X-ray diffraction were grown from a solution of $_{Br}$L^{Ph}Fe^{II}OH dissolved in tetrahydrofuran and layered with hexanes. For bulk purification, the compound was crystallized by dissolving in a benzene/tetrahydrofuran (~2:1) mixture layered with hexanes; a second crop was isolated by dissolving the residual solid in THF, and layering with hexanes. $_{Br}$L^{Ph}Fe^{II}-OH was collected as a yellow-brown powder (0.112 g, 0.128 mmol, 70% crystalline yield). Analysis for C$_{36}$H$_{30}$Br$_3$FeN$_7$O: Calcd. C, 49.57; H, 3.47; N, 11.24. Found C, 49.69; H, 3.38; N, 10.91. ^{1}H NMR (CD$_2$Cl$_2$, 500 MHz, 21 °C): δ = -3.52 (s, 3H, imine-CH), 11.21 (s, 3H, Ph-CH), 11.53 (s, 6H, Ph-CH), 18.74 (s, 6H, Ph-CH), 38.00 (s, 3H, pyr-CH), 131.07 (br, 6H, methylene-CH_2), 199.75 (br, 3H, amino-NH/hydroxo-OH). UV-vis (DCM, 25 °C) λ_{max} nm (ϵ M^{-1} cm^{-1}) = 348 (71600). IR ν_{max} = 1618, 1646 cm^{-1} (C=N). μ_{eff} = 5.58(10) μ_B.
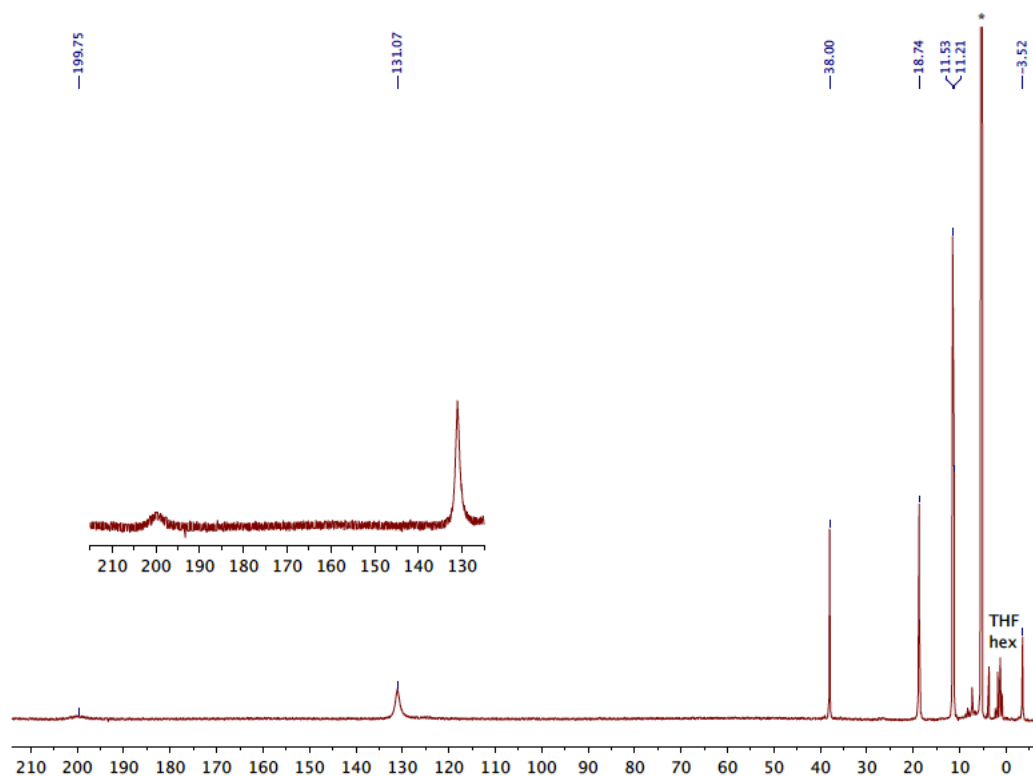
Figure 3.10 ^{1}H NMR spectrum of N($_{Br}$pi^{Ph})($_{Br}$afa^{Ph})$_2$Fe(II)OH ($_{Br}$L^{Ph}Fe^{II}OH) (500 MHz, CD$_2$Cl$_2$, *residual solvent).

Oxidation of N(pi^{Cy})(afa^{Cy})$_2$Fe(II)OH ($_{H}$L^{Cy}Fe^{II}OH) with FcOTf. *a) Preparative scale*: A 20 mL scintillation vial was charged with N(pi^{Cy})(afa^{Cy})$_2$Fe(II)OH (0.043 g, 0.066 mmol) and approximately 5 mL of DCM. FcOTf (0.022 g, 0.066 mmol) was weighed by difference and added as a solid to the brown solution, resulting in a darker brown solution. After stirring for 1 h, solvent was removed in vacuo. The resulting powder was washed with Et$_2$O to remove the ferrocene byproduct. After decanting the Et$_2$O, the purified material was dried in vacuo, yielding the product as a brown powder (0.047 g, 0.058 mmol, 88%). The product was confirmed to be the previously reported iron(III)-oxo complex,[39] [N(afa^{Cy})$_3$Fe(III)O]OTf ($_{H}$L^{Cy}Fe^{III}O), by ^{1}H NMR spectroscopy.

b) NMR Spectroscopy scale: A standard NMR tube was charged with $_{H}$L^{Cy}Fe^{II}OH (0.007 g, 0.011 mmol), FcOTf (0.004 g, 0.012 mmol), and approximately 1 mL of CD$_2$Cl$_2$. The tube was inverted multiple times, resulting in a dark brown solution. Analysis by ^{1}H NMR spectroscopy revealed quantitative conversion to $_{H}$L^{Cy}Fe^{III}O with concomitant formation of ferrocene (4.11 ppm).
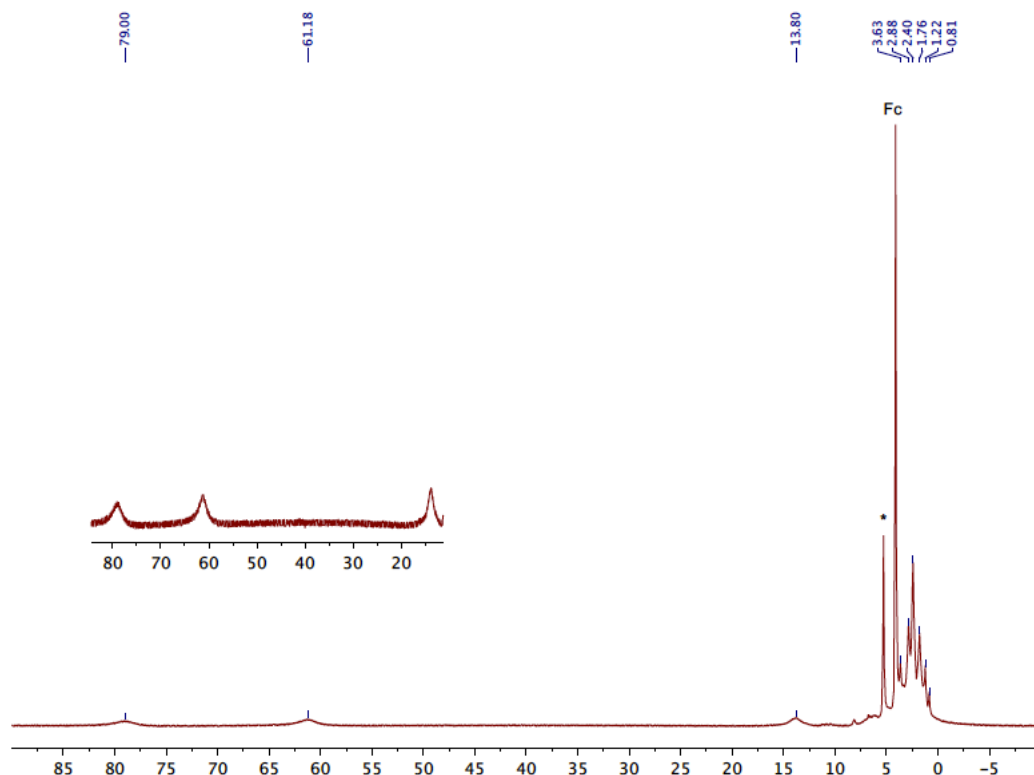
Figure 3.11 ^{1}H NMR spectrum of the crude mixture obtained from oxidation of N(pi^{Cy})(afa^{Cy})$_2$Fe(II)OH (**$_H$L^{Cy}Fe^{II}OH**) by FcOTf (500 MHz, CD$_2$Cl$_2$, *denotes residual solvent).

Oxidation of N(pi^{Cy})(afa^{Cy})$_2$Fe(II)OH ($_H$L^{Cy}Fe^{II}OH**) with AgOTf.** A 20 mL scintillation vial was charged with N(pi^{Cy})(afa^{Cy})$_2$Fe(II)OH (0.058 g, 0.097 mmol) and approximately 5 mL of DCM. The light brown solution was cooled to -35 °C. Silver triflate, AgOTf (0.025 g, 0.097 mmol), was then added as a solid, resulting in a change to a darker brown suspension. After stirring for one hour, the reaction mixture was filtered to remove Ag^0 as a black powder. The dark brown filtrate was dried in vacuo to yield the oxidized complex as a brown powder (0.061 g, 0.076 mmol, 78%). The product was confirmed to be [N(afa^{Cy})$_3$Fe(III)O]OTf (**$_H$L^{Cy}Fe^{III}O**) by ^{1}H NMR spectroscopy.

Reduction of [N(afa^{Cy})$_3$Fe(III)O]OTf ($_H$L^{Cy}Fe^{III}O**).** A 20 mL scintillation vial was charged with **$_H$L^{Cy}Fe^{III}O** (0.079 g, 0.098 mmol) and approximately 5 mL of THF. The dark brown solution was cooled to -35 °C. A slight excess of KC$_8$ (0.015 g, 0.111 mmol 1.1 equiv) was weighed by difference and added to the solution. *CAUTION*: KC$_8$ is pyrophoric; this compound should be handled with care under an inert atmosphere. The reaction was stirred at room temperature overnight, then filtered over Celite® to remove the insoluble graphite byproduct. The brown filtrate was dried under reduced pressure, then washed with Et$_2$O. The purified complex was isolated as a brown powder (0.053 g, 0.081 mmol, 83%). The product was confirmed to be the previously reported iron(II)-hydroxo complex,[38] N(pi^{Cy})(afa^{Cy})$_2$Fe(II)OH (**$_H$L^{Cy}Fe^{II}OH**), by ^{1}H NMR spectroscopy.

54
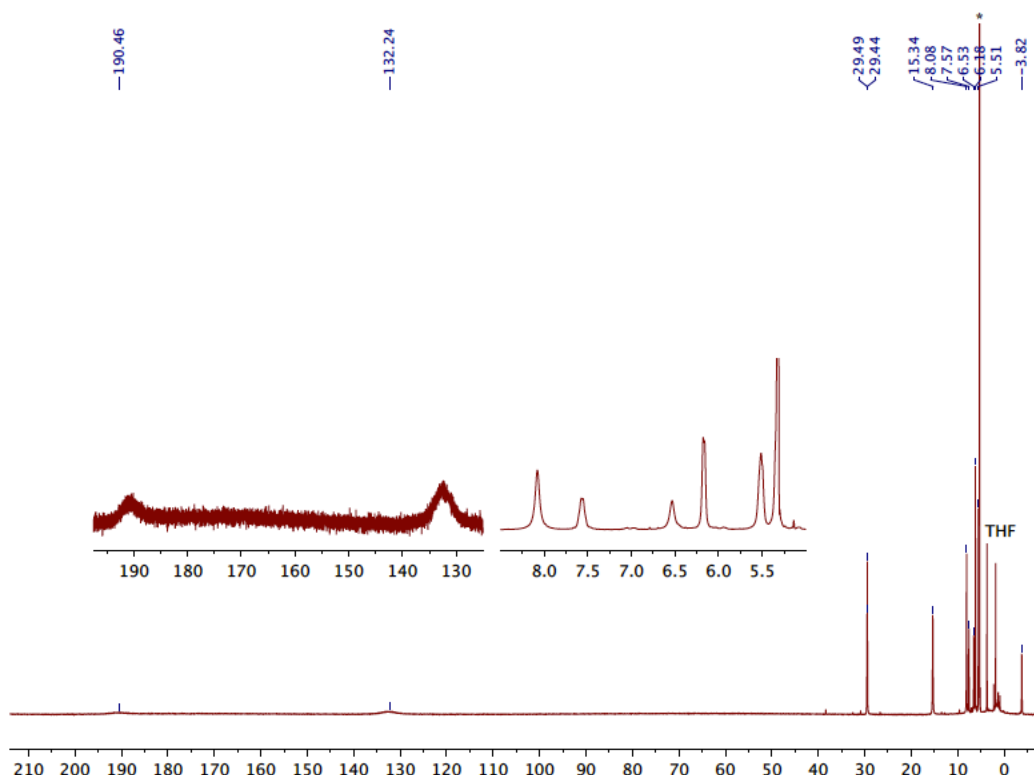
Figure 3.12 ^{1}H NMR spectrum of N(pi^{Cy})(afa^{Cy})$_2$Fe(II)OH (**$_H$L^{Cy}Fe^{II}OH**) (500 MHz, CD$_2$Cl$_2$, *residual solvent).

General procedure for AgOTf oxidation of Fe(II)-hydroxo complexes. A 20 mL scintillation vial was charged with the desired iron(II)-hydroxo complex and approximately 5 mL of DCM. The vial was covered with black electrical tape, to exclude light throughout the reaction, and then cooled to -35 ºC. AgOTf was weighed by difference and added as a solid, resulting in a color change from orange-brown to a darker brown suspension. After stirring for one hour, the reaction mixture was filtered over a pad of Celite® to remove Ag^0 as a black powder. The dark brown filtrate was dried in vacuo to yield the oxidized complex as a brown powder. Crystallization conditions and characterization data for each of the iron(III)-oxo products (**$_X$L^{R}Fe^{III}O**) are given below.

[N($_{Br}$afa^{Cy})$_3$Fe(III)O]OTf ($_{Br}$L^{Cy}Fe^{III}O).   0.062 g N($_{Br}$pi^{Cy})($_{Br}$afa^{Cy})$_2$Fe(II)OH (0.070 mmol), 0.019 g AgOTf (0.075 mmol). Crystals suitable for X-ray diffraction were grown from vapor diffusion of diethylether into a solution of **$_{Br}$L^{Cy}Fe^{III}O** dissolved in acetonitrile. For bulk purification, the compound was crystallized by vapor diffusion of diethylether into a dichloromethane solution of the complex. **$_{Br}$L-^{Cy}Fe^{III}O** was collected as a brown powder (0.057 g, 0.055 mmol, 79% crystalline yield). Analysis for C$_{37}$H$_{48}$Br$_3$F$_3$FeN$_7$O$_4$S · 0.25 CH$_2$Cl$_2$: Calcd. C, 42.18; H, 4.61; N, 9.24. Found C, 42.12; H, 4.53; N, 9.06. ^{1}H NMR (CD$_2$Cl$_2$, 500 MHz, 21 °C): δ = 1.69, 2.02, 2.38, 2.63, 2.85, 9.96, 16.27, 71.51. IR ν_{max} = 1670 cm^{-1} (C=N). μ_{eff} = 6.21(3) μ_B.

55
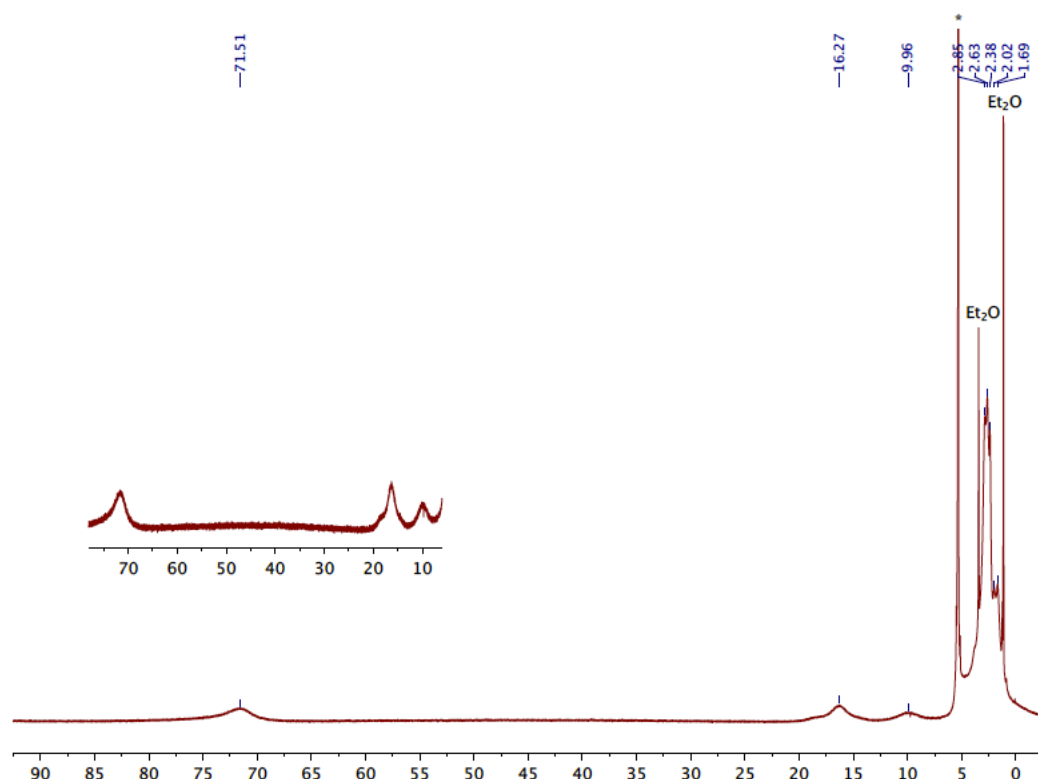
Figure 3.13 ^{1}H NMR spectrum of [N($_{Br}$afa^{Cy})$_3$Fe(III)O]OTf ($_{Br}$**L**^{Cy}**Fe**^{III}**O**) (500 MHz, CD$_2$Cl$_2$, *residual solvent).

[N(afa^{Ph})$_3$Fe(III)O]OTf ($_H$L^{Ph}Fe^{III}O). 0.045 g N(pi^{Ph})(afa^{Ph})$_2$Fe(II)OH (0.071 mmol), 0.020 g AgOTf (0.078 mmol). For bulk purification, the compound was crystallized by vapor diffusion of diethylether into a dichloromethane solution of the complex. $_H$**L**^{Ph}**Fe**^{III}**O** was collected as a yellow-brown powder (0.043 g, 0.055 mmol, 77% crystalline yield). Analysis for C$_{37}$H$_{33}$F$_3$FeN$_7$O$_4$S · 0.5 CH$_2$Cl$_2$: Calcd. C, 54.46; H, 4.14; N, 11.85. Found C, 54.53; H, 3.95; N, 11.89. ^{1}H NMR (CD$_2$Cl$_2$, 500 MHz, 21 °C): δ = 4.07, 8.17, 9.59, 11.74, 61.19, 78.77. IR ν_{max} = 1667 cm^{-1} (C=N). μ_{eff} = 6.01(8) μ_B.

Anion exchange procedure for [N(afa^{Ph})$_3$Fe(III)O]BArF$_{24}$ ([$_H$L^{Ph}Fe^{III}O]BArF). [N(afa^{Ph})$_3$Fe(III)O]OTf (0.027 g, 0.034 mmol) was suspended in approximately 5 mL Et$_2$O. NaBArF$_{24}$ (0.030 g, 0.034 mmol) was weighed by difference and added to the mixture, resulting in the immediate solvation of the complex to give a dark brown solution. The reaction was stirred at room temperature for one hour, then filtered over a pad of Celite® to remove the NaOTf byproduct. The resulting filtrate was dried to yield [N(afa^{Ph})$_3$Fe(III)O]BArF$_{24}$ ([$_H$**L**^{Ph}**Fe**^{III}**O]BArF**) as a brown powder (0.051 g, 0.034 mmol, quantitative). Crystals suitable for X-ray diffraction were grown by layering a solution of [$_H$**L**^{Ph}**Fe**^{III}**O]BArF** dissolved in ben-zene with hexamethyldisiloxane. Analysis for C$_{68}$H$_{45}$BF$_{24}$FeN$_7$O: Calcd. C, 54.49; H, 3.03; N, 6.54. Found C, 54.51; H, 2.91; N, 6.47. ^{1}H NMR (CD$_2$Cl$_2$, 500 MHz, 21 °C): δ = 7.56, 7.73,

8.15, 9.53, 11.50, 60.83, 79.07. ^{19}F NMR (CD$_2$Cl$_2$, 377 MHz, 21 °C): δ = -62.37. IR ν_{max} = 1670 cm^{-1} (C=N). μ_{eff} = 6.25(4) μ_B.
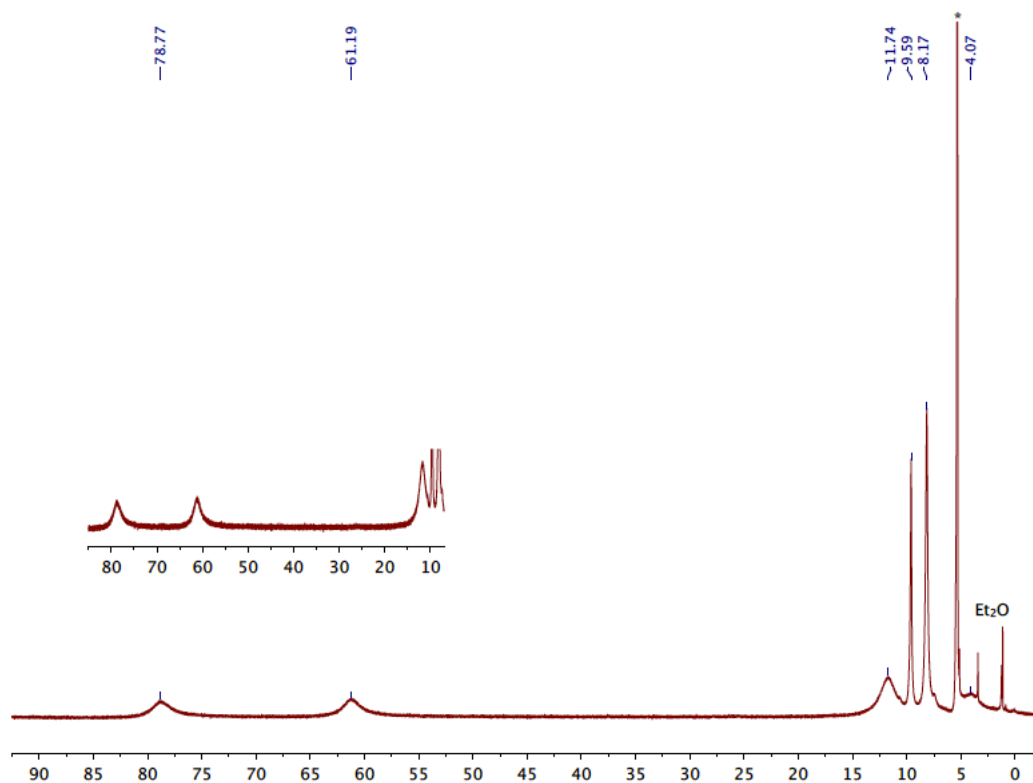
Figure 3.14 ^{1}H NMR spectrum of [N(afa^{Ph})$_3$Fe(III)O]OTf ($_H$L^{Ph}Fe^{III}O) (500 MHz, CD$_2$Cl$_2$, *residual solvent).
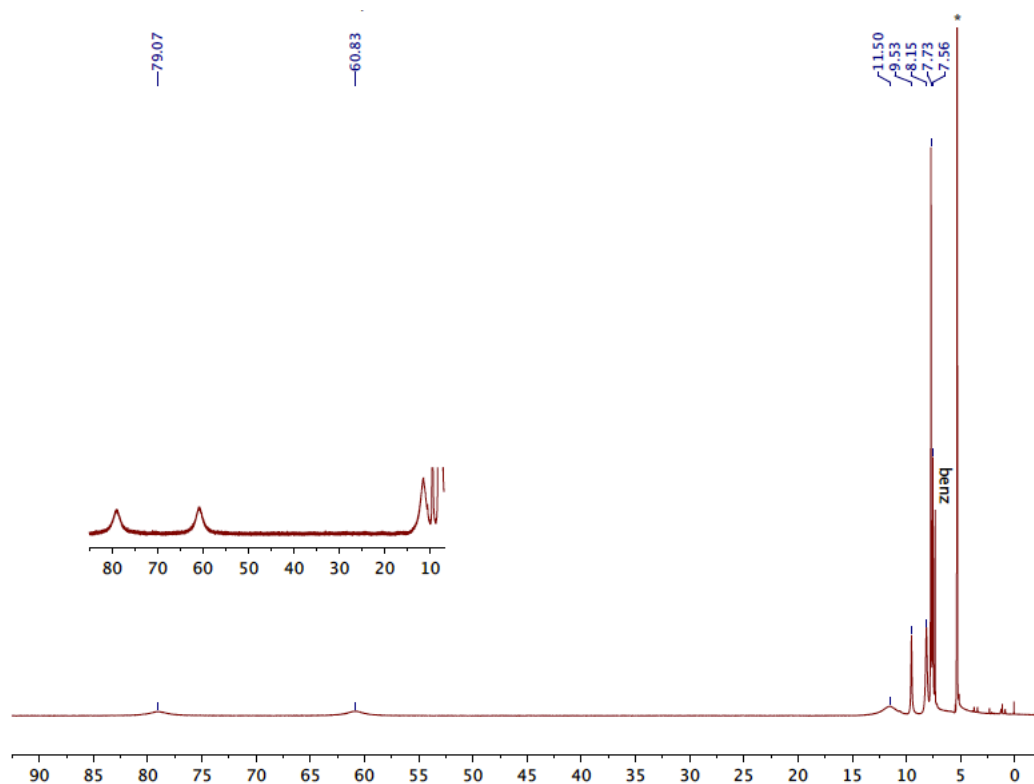
Figure 3.15 ^{1}H NMR spectrum of [N(afa^{Ph})$_3$Fe(III)O]BArF$_{24}$ (**[$_H$L^{Ph}Fe^{III}O]BArF**) (500 MHz, CD$_2$Cl$_2$, *residual solvent).
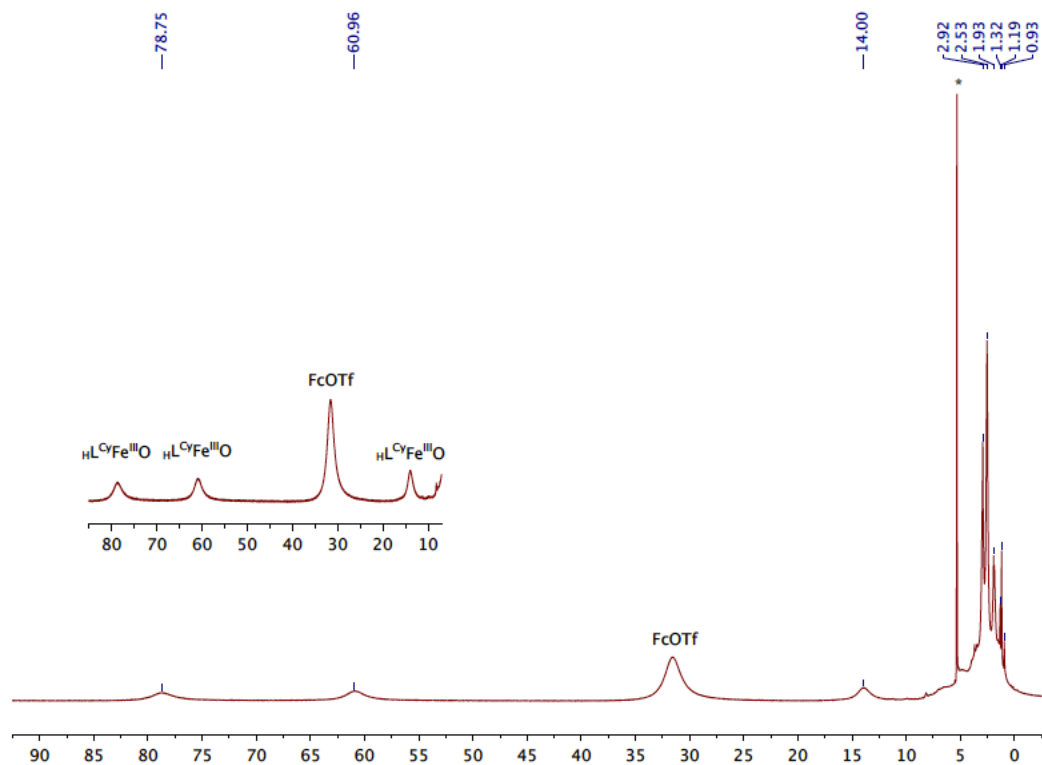
Figure 3.16 ^{1}H NMR spectrum showing no reaction occurs between [N(afa^{Cy})$_3$Fe(III)O]OTf (**$_H$L^{Cy}Fe^{III}O**) and FcOTf (500 MHz, CD$_2$Cl$_2$, *residual solvent).

3.9 Additional figures and tables
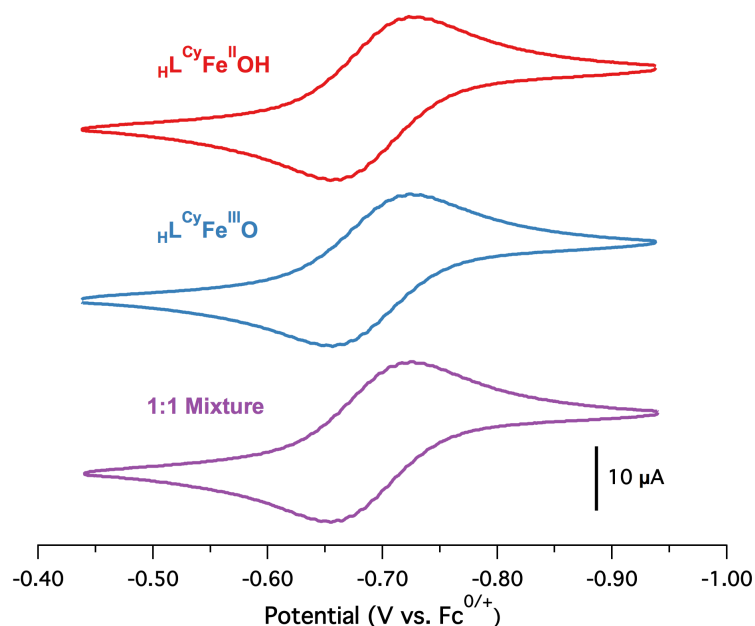
Figure 3.17 Cyclic voltammograms for $_H L^{Cy} Fe^{II} OH$ (ocp -.866 V), $_H L^{Cy} Fe^{III} O$ (ocp -.276 V), and a 1:1 mixture of both compounds (ocp -.694 V) obtained for 1 mM solutions of the complex (0.5 mM in each compound for the mixture) in a 1:1 THF/MeCN mixture with 0.1 M [$^n Bu_4 N$][PF_6] as supporting electrolyte (scan rate 0.1 V/sec).

Scan Rate	ΔE_p
12	65
25	66
50	68
100	70
250	78
500	90
1000	96
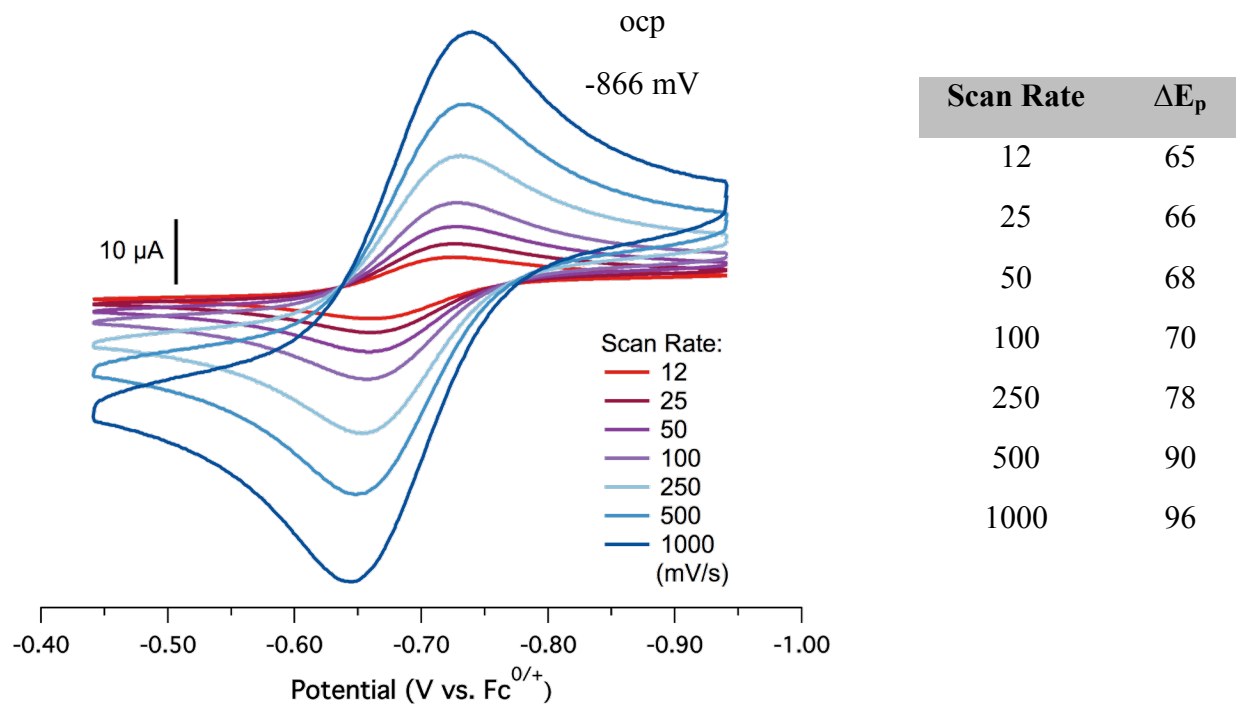
Figure 3.18 Cyclic voltammograms showing the Fe(II/III) redox couple of $_H L^{Cy} Fe^{II} OH$ obtained for a 1 mM solution of the complex in a 1:1 THF/MeCN mixture with 0.1 M [$^n Bu_4 N$][PF_6] as supporting electrolyte (left); peak-to-peak separations (mV) (right).
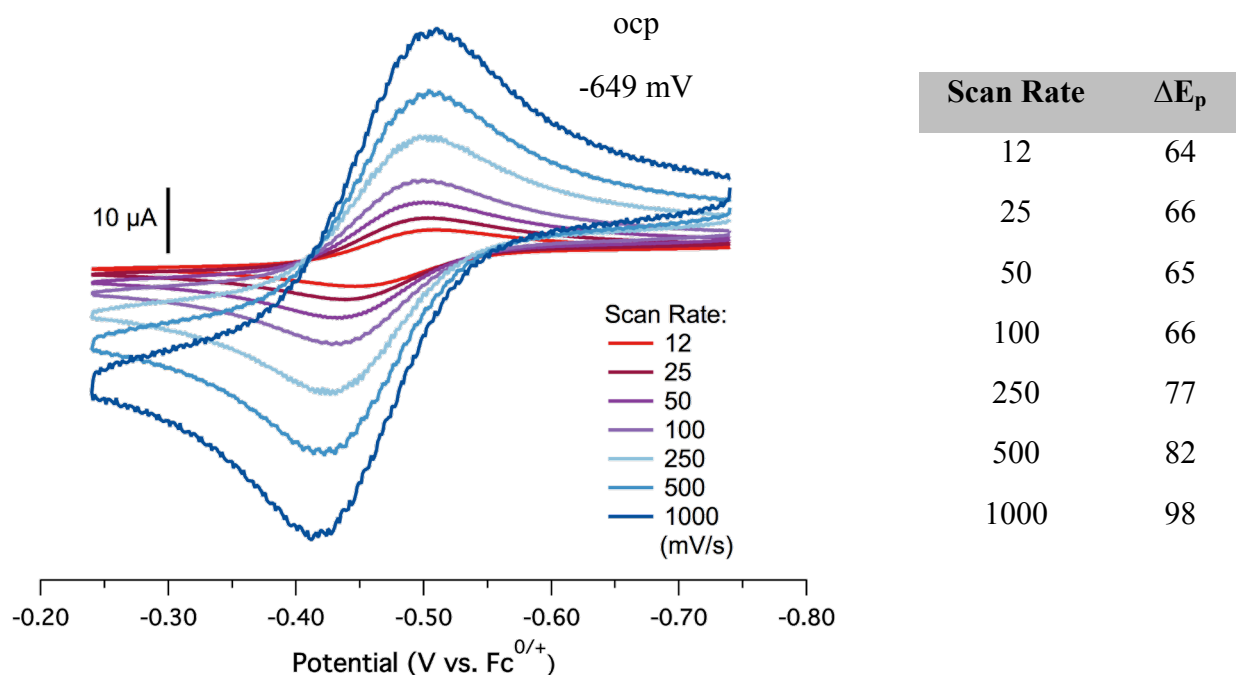
Figure 3.19 Cyclic voltammograms showing the Fe(II/III) redox couple of $_{Br}L^{Cy}Fe^{II}OH$ obtained for a 1 mM solution of the complex in a 1:1 THF/MeCN mixture with 0.1 M [$^nBu_4N$][PF_6] as supporting electrolyte (left); peak-to-peak separations (mV) (right).

Scan Rate	ΔE_p
12	64
25	66
50	65
100	66
250	77
500	82
1000	98
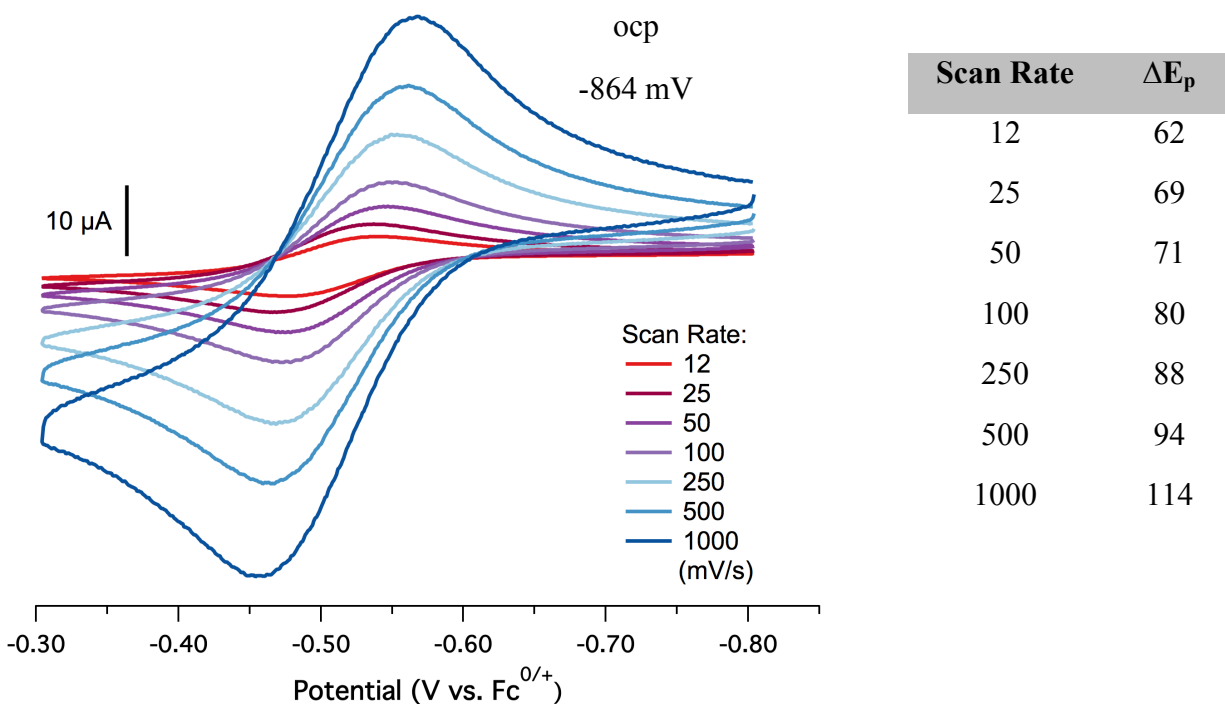
Figure 3.20 Cyclic voltammograms showing the Fe(II/III) redox couple of $_HL^{Ph}Fe^{II}OH$ obtained for a 1 mM solution of the complex in a 1:1 THF/MeCN mixture with 0.1 M [$^nBu_4N$][PF_6] as supporting electrolyte (left); peak-to-peak separations (mV) (right).

Scan Rate	ΔE_p
12	62
25	69
50	71
100	80
250	88
500	94
1000	114

ocp

-746 mV

5 µA

Scan Rate:
— 12
— 25
— 50
— 100
— 250
— 500
— 1000
(mV/s)

Scan Rate	ΔE_p
12	66
25	70
50	71
100	75
250	76
500	94
1000	117

Potential (V vs. $Fc^{0/+}$)
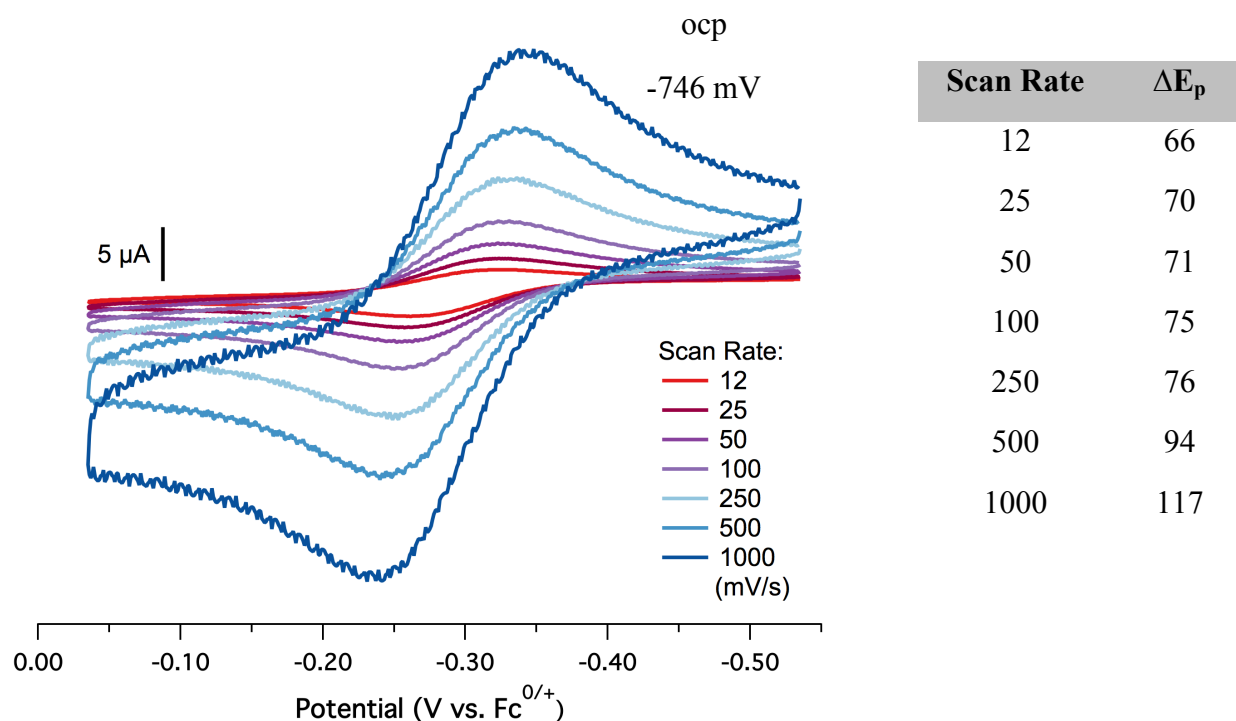
Figure 3.21 Cyclic voltammograms showing the Fe(II/III) redox couple of $_{Br}L^{Ph}Fe^{II}OH$ obtained for a 1 mM solution of the complex in a 1:1 THF/MeCN mixture with 0.1 M $[^nBu_4N][PF_6]$ as supporting electrolyte (left); peak-to-peak separations (mV) (right).

$N(pi^{Ph})(afa^{Ph})_2Fe(II)OH$
$_HL^{Ph}Fe^{II}OH$

$N(_{Br}pi^{Ph})(_{Br}afa^{Ph})_2Fe(II)OH$
$_{Br}L^{Ph}Fe^{II}OH$
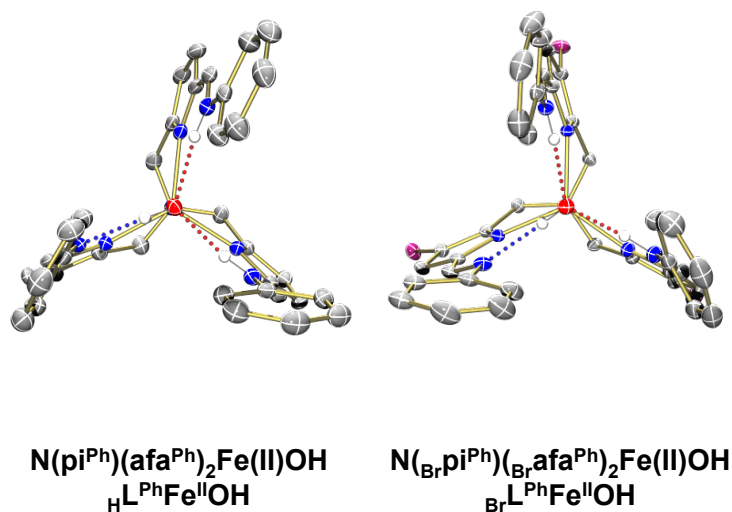
Figure 3.22 Top down view (along the Fe–O axis) for molecular structures of $_HL^{Ph}Fe^{II}OH$, $_{Br}L^{Ph}Fe^{II}OH$, and $_HL^{DIPP}Fe^{II}OH_2$, illustrating the orientation of the aromatic capping group relative to the rest of the ligand arm. In the $_HL^{Ph}Fe^{II}OH$ and $_{Br}L^{Ph}Fe^{II}OH$ structures, the phenyl rings show moderate displacement from co-planarity (average twist angle ~28º).

62

Table 3.4 Thermodynamics (E_h) for full model systems.

Species	E(SCF)	E(SCF)$_{MeCN}$	E(SCF)$_{THF}$	G(gas)
$_HL^{Cy}Fe^{III}O$	-3125.144022	-3125.226805	-3125.235547	-3124.386842
$_HL^{Ph}Fe^{III}O$	-3114.244869	-3114.330193	-3114.340103	-3113.693093
$_{Br}L^{Cy}Fe^{III}O$	-10845.758544	-10845.852045	-10845.861386	-10845.039868
$_{Br}L^{Ph}Fe^{III}O$	-10834.858025	-10834.952462	-10834.963264	-10834.346914
$_HL^{Cy}Fe^{II}OH$	-3125.327083	-3125.371003	-3125.376052	-3124.574032
$_HL^{Cy}Fe^{II}OH_2$	-3125.329920	-3125.378153	-3125.373626	-3124.575754
$_HL^{Ph}Fe^{II}OH$	-3114.437482	-3114.482547	-3114.488760	-3113.890305
$_HL^{Ph}Fe^{II}OH_2$	-3114.440381	-3114.492371	-3114.485912	-3113.893243
$_{Br}L^{Cy}Fe^{II}OH$	-10845.955158	-10846.005332	-10846.009780	-10845.241894
$_{Br}L^{Ph}Fe^{II}OH$	-10835.063151	-10835.113753	-10835.119255	-10834.556103

$G(solv) \approx G(gas) - E(SCF) + E(SCF)_{solv}$
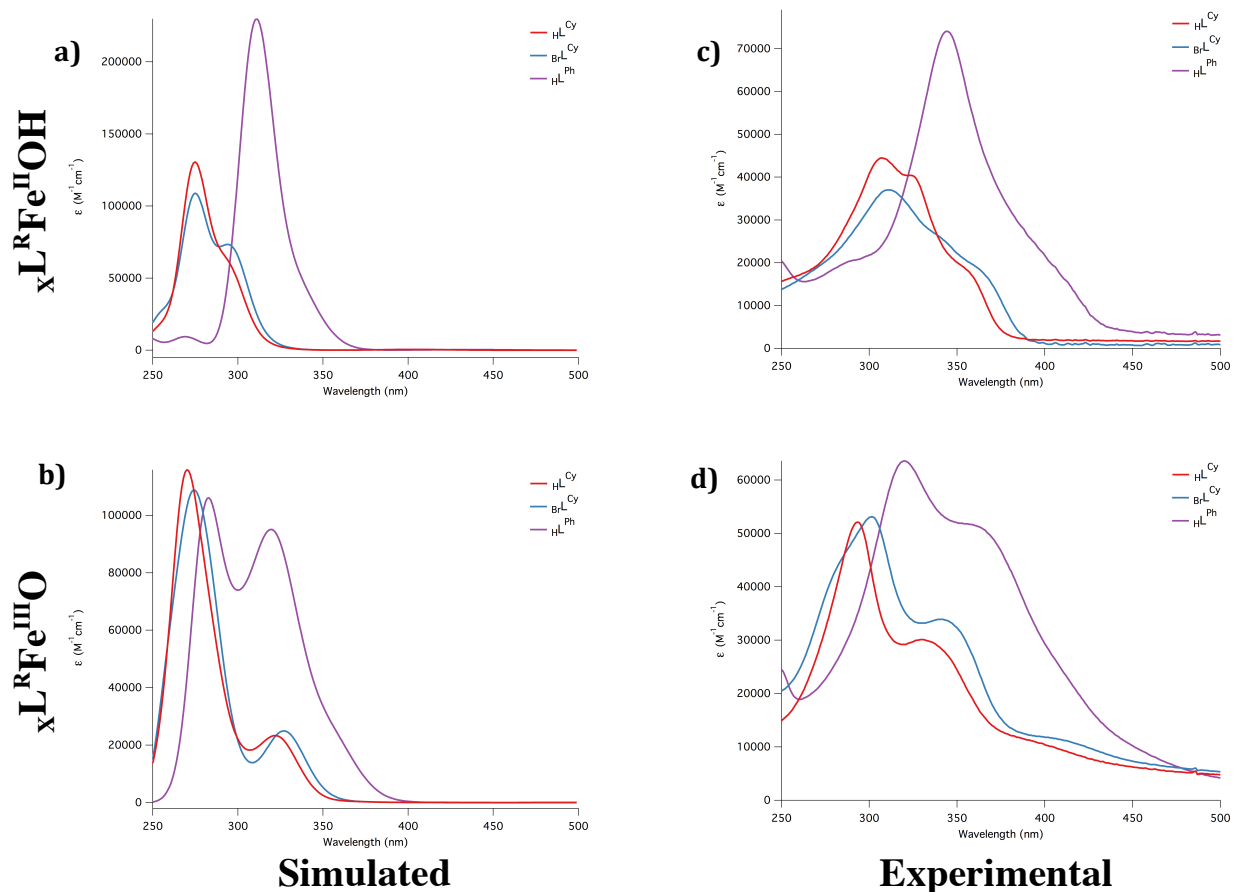
Figure 3.23 Simulated electronic absorption spectra for a) selected $_XL^RFe^{II}OH$ (top left) and b) $_XL^RFe^{III}O$ (bottom left) derivatives. Spectra were calculated at the TD-ωB97X-D/6-311G(d,p) level of theory[67,68] from ~250-500 nm (first 50 excited states). Individual transitions were fit with Gaussians having a FWHM = 0.15 eV in GaussView.[69] Experimental c) $_XL^RFe^{II}OH$ (top right) and d) $_XL^RFe^{III}O$ (bottom left) spectra are included for comparison.

Table 3.5 Electron excitations contributing to the predominant peaks for $_H\text{L}^{Cy}\text{Fe}^{II}\text{OH}$.
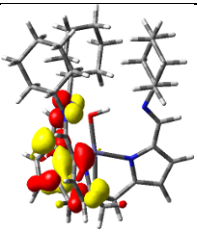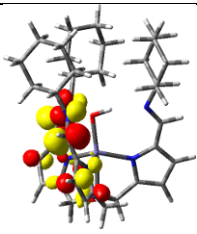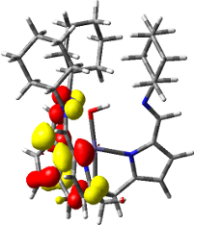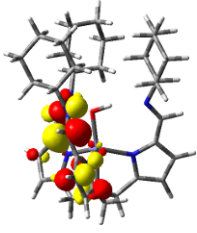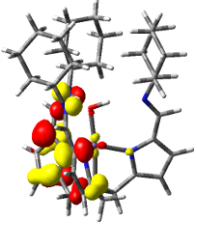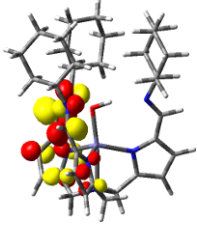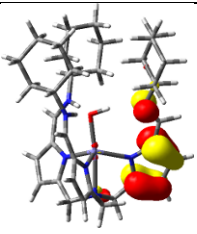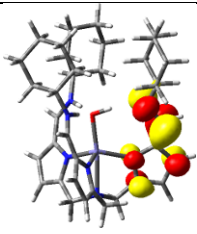
Wavelength (nm)	Occupied Orbital	Unoccupied Orbital
293.76		
274.36		

Table 3.6 Electron excitations contributing to the predominant peaks for $_H L^{Ph} Fe^{II} OH$.
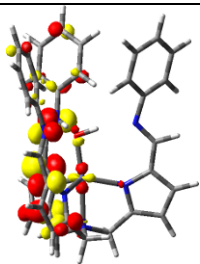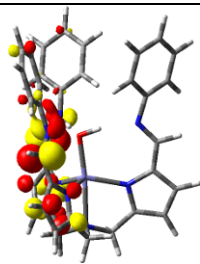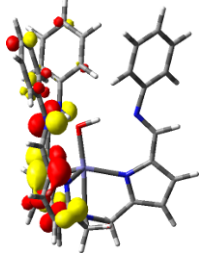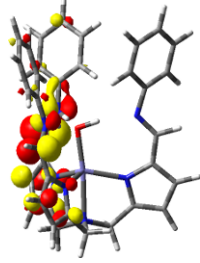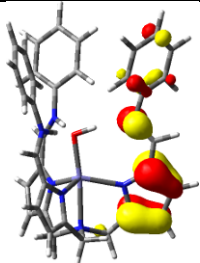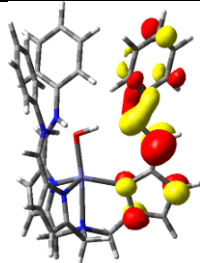
Wavelength (nm)	Occupied Orbital	Unoccupied Orbital
332.96		
310.63		

Table 3.7 Electron excitations contributing to the predominant peaks for $_HL^{Cy}Fe^{III}O$.
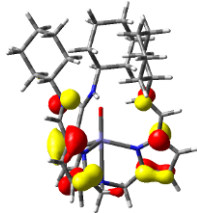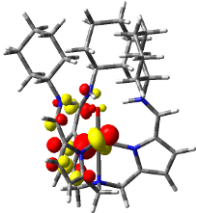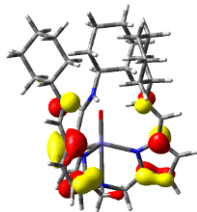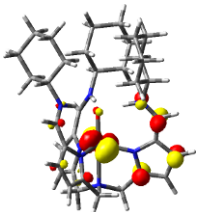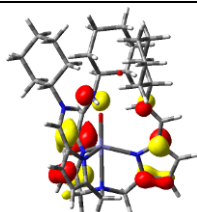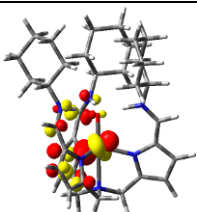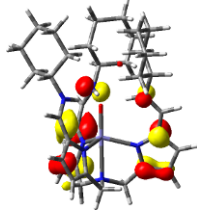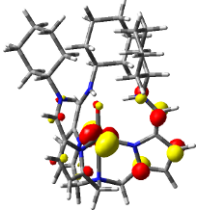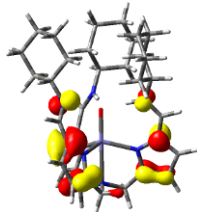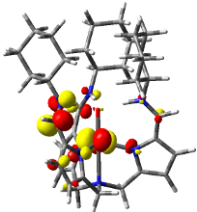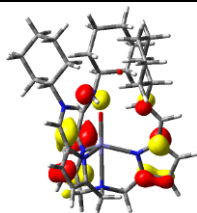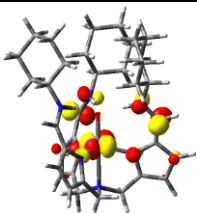
Wavelength (nm)	Occupied Orbital	Unoccupied Orbital
323.18		
282.35		
269.23		

Table 3.8 Electron excitations contributing to the predominant peaks for $_H L^{Ph} Fe^{III} O$.
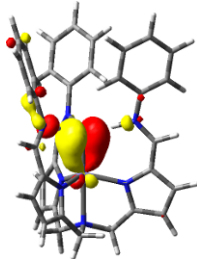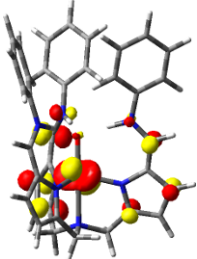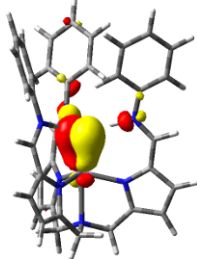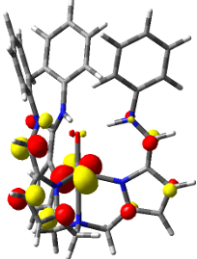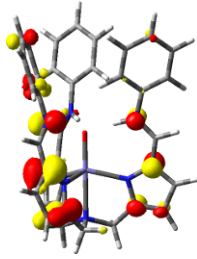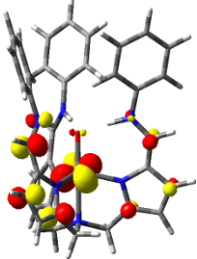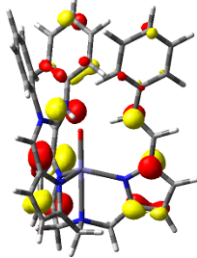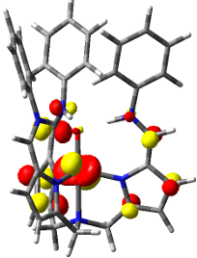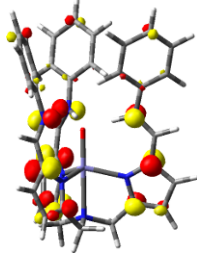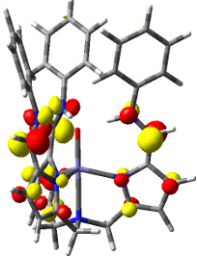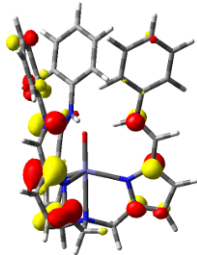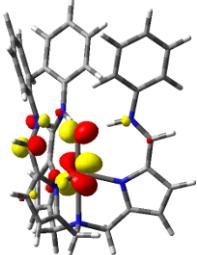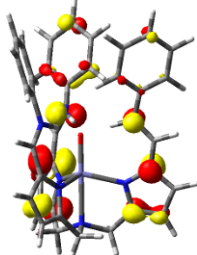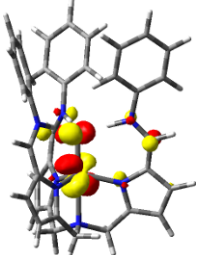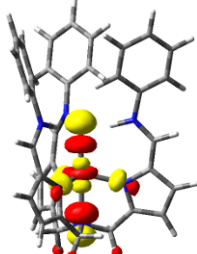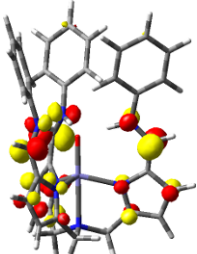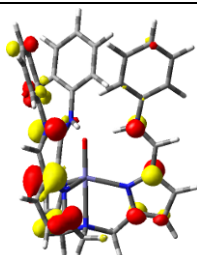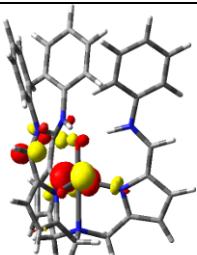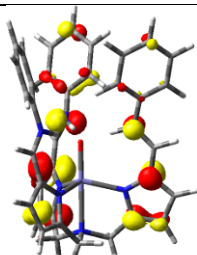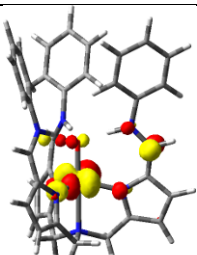
Wavelength (nm)	Occupied Orbital	Unoccupied Orbital
359.39		
316.15		

Table 3.8 (cont.)

Wavelength (nm)	Occupied Orbital	Unoccupied Orbital
316.15		
281.63		

3.10 References

(1)   Perutz, M. F. Regulation of Oxygen Affinity of Hemoglobin: Influence of Structure of the Globin on the Heme Iron. *Annu. Rev. Biochem.* **1979**, *48* (1), 327–386.

(2)   Shaanan, B. The Iron-Oxygen Bond in Human Oxyhaemoglobin. *Nature* **1982**, *296* (5858), 683–684.

(3)   Springer, B. A.; Sligar, S. G.; Olson, J. S.; Phillips, G. N., Jr. Mechanisms of Ligand Recognition in Myoglobin. *Chem. Rev.* **1994**, *94* (3), 699–714.

(4)   Michel, H.; Behr, J.; Harrenga, A.; Kannt, A. Cytochrome *C* Oxidase: Structure and Spectroscopy. *Annu. Rev. Biophys. Biomol. Struct.* **1998**, *27* (1), 329–356.

(5)   Yoshikawa, S.; Shimada, A. Reaction Mechanism of Cytochrome *C* Oxidase. *Chem. Rev.* **2015**, *115* (4), 1936–1989.

(6)   Meunier, B.; de Visser, S. P.; Shaik, S. Mechanism of Oxidation Reactions Catalyzed by Cytochrome P450 Enzymes. *Chem. Rev.* **2004**, *104* (9), 3947–3980.

(7)   Denisov, I. G.; Makris, T. M.; Sligar, S. G.; Schlichting, I. Structure and Chemistry of Cytochrome P450. *Chem. Rev.* **2005**, *105* (6), 2253–2278.

(8)   Goodin, D. B.; McRee, D. E. The Asp-His-Fe Triad of Cytochrome *C* Peroxidase Controls the Reduction Potential, Electronic Structure, and Coupling of the Tryptophan Free Radical to the Heme. *Biochemistry* **1993**, *32* (13), 3313–3324.

(9)   Nonaka, D.; Wariishi, H.; Fujii, H. Paramagnetic ^{13}C and ^{15}N NMR Analyses of Cyanide-(^{13}C^{15}N-) Ligated Ferric Peroxidases: the Push Effect, Not Pull Effect, Modulates the Compound I Formation Rate. *Biochemistry* **2009**, *48* (5), 898–905.

(10)   Nonaka, D.; Wariishi, H.; Welinder, K. G.; Fujii, H. Paramagnetic ^{13}C and ^{15}N NMR Analyses of the Push and Pull Effects in Cytochrome *C* Peroxidase and *Coprinus Cinereus* Peroxidase Variants: Functional Roles of Highly Conserved Amino Acids Around Heme. *Biochemistry* **2010**, *49* (1), 49–57.

(11)   Bowman, S. E. J.; Bren, K. L. Variation and Analysis of Second-Sphere Interactions and Axial Histidinate Character in *C*-Type Cytochromes. *Inorg. Chem.* **2010**, *49* (17), 7890–7897.

(12)   Krest, C. M.; Silakov, A.; Rittle, J.; Yosca, T. H.; Onderko, E. L.; Calixto, J. C.; Green, M. T. Significantly Shorter Fe-S Bond in Cytochrome P450-I Is Consistent with Greater Reactivity Relative to Chloroperoxidase. *Nat. Chem.* **2015**, 1–7.

(13)   Yikilmaz, E.; Rodgers, D. W.; Miller, A.-F. The Crucial Importance of Chemistry in the Structure−Function Link: Manipulating Hydrogen Bonding in Iron-Containing Superoxide Dismutase. *Biochemistry* **2006**, *45* (4), 1151–1161.

(14)   Miller, A.-F. Redox Tuning Over Almost 1 V in a Structurally Conserved Active Site: Lessons From Fe-Containing Superoxide Dismutase. *Acc. Chem. Res.* **2008**, *41* (4), 501–510.

(15)   Marshall, N. M.; Garner, D. K.; Wilson, T. D.; Gao, Y.-G.; Robinson, H.; Nilges, M. J.; Lu, Y. Rationally Tuning the Reduction Potential of a Single Cupredoxin Beyond the Natural Range. *Nature* **2009**, *462* (7269), 113–116.

(16)   Sastri, C. V.; Park, M. J.; Ohta, T.; Jackson, T. A.; Stubna, A.; Seo, M.-S.; Lee, J.; Kim, J.; Kitagawa, T.; Münck, E.; Que, L., Jr.; Nam, W. Axial Ligand Substituted Nonheme Fe^{IV}=O Complexes: Observation of Near-UV LMCT Bands and Fe=O Raman Vibrations. *J. Am. Chem. Soc.* **2005**, *127* (36), 12494–12495.

(17)   Sastri, C. V.; Lee, J.; Oh, K.; Lee, Y. J.; Lee, J.; Jackson, T. A.; Ray, K.; Hirao, H.; Shin, W.; Halfen, J. A.; Kim, J.; Que, L., Jr.; Shaik, S.; Nam, W. Axial Ligand Tuning of a Nonheme Iron(IV)-Oxo Unit for Hydrogen Atom Abstraction. *Proc. Natl. Acad. Sci. U.S.A.* **2007**, *104* (49), 19181–19186.

(18)   Jackson, T. A.; Rohde, J.-U.; Seo, M.-S.; Sastri, C. V.; DeHont, R.; Stubna, A.; Ohta, T.; Kitagawa, T.; Münck, E.; Nam, W.; Que, L., Jr. Axial Ligand Effects on the Geometric and Electronic Structures of Nonheme Oxoiron(IV) Complexes. *J. Am. Chem. Soc.* **2008**, *130* (37), 12394–12407.

(19)   Fukuzumi, S.; Kotani, H.; Suenobu, T.; Hong, S.; Lee, Y.-M.; Nam, W. Contrasting Effects of Axial Ligands on Electron-Transfer Versus Proton-Coupled Electron-Transfer Reactions of Nonheme Oxoiron(IV) Complexes. *Chem. Eur. J.* **2010**, *16* (1), 354–361.

(20)   Chantarojsiri, T.; Sun, Y.; Long, J. R.; Chang, C. J. Water-Soluble Iron(IV)-Oxo Complexes Supported by Pentapyridine Ligands: Axial Ligand Effects on Hydrogen Atom and Oxygen Atom Transfer Reactivity. *Inorg. Chem.* **2015**, *54* (12), 5879–5887.

(21)   Moore, C. M.; Szymczak, N. K. Redox-Induced Fluoride Ligand Dissociation Stabilized by Intramolecular Hydrogen Bonding. *Chem. Commun.* **2015**, *51* (25), 5490–5492.

(22)   Moore, C. M.; Szymczak, N. K. Nitrite Reduction by Copper Through Ligand-Mediated Proton and Electron Transfer. *Chem. Sci.* **2015**, *6* (6), 3373–3377.

(23)   Dahl, E. W.; Szymczak, N. K. Hydrogen Bonds Dictate the Coordination Geometry of Copper: Characterization of a Square-Planar Copper(I) Complex. *Angew. Chem. Int. Ed.* **2016**, *55* (9), 3101–3105.

(24)   Yamagishi, H.; Nabeya, S.; Ikariya, T.; Kuwata, S. Protic Ruthenium Tris(Pyrazol-3-Ylmethyl)Amine Complexes Featuring a Hydrogen-Bonding Network in the Second Coordination Sphere. *Inorg. Chem.* **2015**, *54* (24), 11584–11586.

(25)   Delgado, M.; Sommer, S. K.; Swanson, S. P.; Berger, R. F.; Seda, T.; Zakharov, L. N.; Gilbertson, J. D. Probing the Protonation State and the Redox-Active Sites of Pendant Base Iron(II) and Zinc(II) Pyridinediimine Complexes. *Inorg. Chem.* **2015**, *54* (15), 7239–7248.

(26)   Hartle, M. D.; Delgado, M.; Gilbertson, J. D.; Pluth, M. D. Stabilization of a Zn(II) Hydrosulfido Complex Utilizing a Hydrogen-Bond Accepting Ligand. *Chem. Commun.* **2016**, *52*, 7680–7682.

(27)   Kwon, Y. M.; Delgado, M.; Zakharov, L. N.; Seda, T.; Gilbertson, J. D. Nitrite Reduction by a Pyridinediimine Complex with a Proton-Responsive Secondary Coordination Sphere. *Chem. Commun.* **2016**, *52*, 11016–11019.

(28)   Reid, S. D.; Wilson, C.; Blake, A. J.; Love, J. B. Tautomerisation and Hydrogen-Bonding Interactions in Four-Coordinate Metal Halide and Azide Complexes of N-Donor-Extended Dipyrromethanes. *Dalton Trans.* **2010**, *39* (2), 418–425.

(29)   Hart, J. S.; White, F. J.; Love, J. B. Donor-Extended Tripodal Pyrroles: Encapsulation, Metallation, and H-Bonded Tautomers. *Chem. Commun.* **2011**, *47* (20), 5711–5713.

(30)   Mareque-Rivas, J. C.; Prabaharan, R.; Parsons, S. Quantifying the Relative Contribution of Hydrogen Bonding and Hydrophobic Environments, and Coordinating Groups, in the Zinc(II)–Water Acidity by Synthetic Modelling Chemistry. *Dalton Trans.* **2004**, No. 10, 1648–1655.

(31)   Rivas, J. C. M.; Prabaharan, R.; de Rosales, R. T. M.; Metteau, L.; Parsons, S. LZnX Complexes of Tripodal Ligands with Intramolecular RN–H Hydrogen Bonding Groups: Structural Implications of a Hydrogen Bonding Cavity, and of X/R in the Hydrogen Bonding Geometry/Strength. *Dalton Trans.* **2004**, *17*, 2800–2807.

(32)   Rivas, J. C. M.; Hinchley, S. L.; Metteau, L.; Parsons, S. The Strength of Hydrogen Bonding to Metal-Bound Ligands Can Contribute to Changes in the Redox Behaviour of Metal Centres. *Dalton Trans.* **2006**, *19*, 2316–2322.

(33)   Lucas, R. L.; Zart, M. K.; Mukherjee, J.; Sorrell, T. N.; Powell, D. R.; Borovik, A. S. A Modular Approach Toward Regulating the Secondary Coordination Sphere of Metal Ions: Differential Dioxygen Activation Assisted by Intramolecular Hydrogen Bonds. *J. Am. Chem. Soc.* **2006**, *128* (48), 15476–15489.

(34)   Mukherjee, J.; Lucas, R. L.; Zart, M. K.; Powell, D. R.; Day, V. W.; Borovik, A. S. Synthesis, Structure, and Physical Properties for a Series of Monomeric Iron(III) Hydroxo Complexes with Varying Hydrogen-Bond Networks. *Inorg. Chem.* **2008**, *47* (13), 5780–5786.

(35)   Shook, R. L.; Borovik, A. S. The Effects of Hydrogen Bonds on Metal-Mediated O_2 Activation and Related Processes. *Chem. Commun.* **2008**, *46*, 6095–6107.

(36)   Lau, N.; Ziller, J. W.; Borovik, A. S. Sulfonamido Tripods: Tuning Redox Potentials via Ligand Modifications. *Polyhedron* **2015**, *85*, 777–782.

(37)   Jones, J. R.; Ziller, J. W.; Borovik, A. S. Modulating the Primary and Secondary Coordination

Spheres Within a Series of Co(II)-OH Complexes. *Inorg. Chem.* **2017**, acs.inorgchem.6b01956.

(38) Matson, E. M.; Bertke, J. A.; Fout, A. R. Isolation of Iron(II) Aqua and Hydroxyl Complexes Featuring a Tripodal H-Bond Donor and Acceptor Ligand. *Inorg. Chem.* **2014**, *53* (9), 4450–4458.

(39) Matson, E. M.; Park, Y. J.; Fout, A. R. Facile Nitrite Reduction in a Non-Heme Iron System: Formation of an Iron(III)-Oxo. *J. Am. Chem. Soc.* **2014**, *136* (50), 17398–17401.

(40) Park, Y. J.; Matson, E. M.; Nilges, M. J.; Fout, A. R. Exploring Mn-O Bonding in the Context of an Electronically Flexible Secondary Coordination Sphere: Synthesis of a Mn(III)-Oxo. *Chem. Commun.* **2015**, *51* (25), 5310–5313.

(41) Scharf, A. B.; Betley, T. A. Electronic Perturbations of Iron Dipyrrinato Complexes via Ligand *B*-Halogenation and *Meso*-Fluoroarylation. *Inorg. Chem.* **2011**, *50* (14), 6837–6845.

(42) Harman, W. H.; Harris, T. D.; Freedman, D. E.; Fong, H.; Chang, A.; Rinehart, J. D.; Ozarowski, A.; Sougrati, M. T.; Grandjean, F.; Long, G. J.; Long, J. R.; Chang, C. J. Slow Magnetic Relaxation in a Family of Trigonal Pyramidal Iron(II) Pyrrolide Complexes. *J. Am. Chem. Soc.* **2010**, *132* (51), 18115–18126.

(43) Bigi, J. P.; Harman, W. H.; Lassalle-Kaiser, B.; Robles, D. M.; Stich, T. A.; Yano, J.; Britt, R. D.; Chang, C. J. A High-Spin Iron(IV)–Oxo Complex Supported by a Trigonal Nonheme Pyrrolide Platform. *J. Am. Chem. Soc.* **2012**, *134* (3), 1536–1542.

(44) MacBeth, C. E.; Golombek, A. P.; Young, V. G.; Yang, C.; Kuczera, K.; Hendrich, M. P.; Borovik, A. S. O_2 Activation by Nonheme Iron Complexes: a Monomeric Fe(III)-Oxo Complex Derived From O_2. *Science* **2000**, *289* (5481), 938–941.

(45) England, J.; Martinho, M.; Farquhar, E. R.; Frisch, J. R.; Bominaar, E. L.; Münck, E.; Que, L., Jr. A Synthetic High-Spin Oxoiron(IV) Complex: Generation, Spectroscopic Characterization, and Reactivity. *Angew. Chem. Int. Ed.* **2009**, *48* (20), 3622–3626.

(46) Lacy, D. C.; Gupta, R.; Stone, K. L.; Greaves, J.; Ziller, J. W.; Hendrich, M. P.; Borovik, A. S. Formation, Structure, and EPR Detection of a High Spin Fe^{IV}-Oxo Species Derived From Either an Fe^{III}-Oxo or Fe^{III}-OH Complex. *J. Am. Chem. Soc.* **2010**, *132* (35), 12188–12190.

(47) Ford, C. L.; Park, Y. J.; Matson, E. M.; Gordon, Z.; Fout, A. R. A Bioinspired Iron Catalyst for Nitrate and Perchlorate Reduction. *Science* **2016**, *354* (6313), 741–743.

(48) Vosko, S. H.; Wilk, L.; Nusair, M. Accurate Spin-Dependent Electron Liquid Correlation Energies for Local Spin Density Calculations: a Critical Analysis. *Can. J. Phys.* **1980**, *58* (8), 1200–1211.

(49) Lee, C.; Yang, W.; Parr, R. G. Development of the Colle-Salvetti Correlation-Energy Formula Into a Functional of the Electron Density. *Phys. Rev. B* **1988**, *37* (2), 785–789.

(50) Becke, A. D. Density-Functional Exchange-Energy Approximation with Correct Asymptotic Behavior. *Phys. Rev. A* **1988**, *38* (6), 3098–3100.

(51) Becke, A. D. A New Mixing of Hartree–Fock and Local Density-Functional Theories. *J. Chem. Phys.* **1993**, *98* (2), 1372–1377.

(52) Stephens, P. J.; Devlin, F. J.; Chabalowski, C. F.; Frisch, M. J. *Ab Initio* Calculation of Vibrational Absorption and Circular Dichroism Spectra Using Density Functional Force Fields. *J. Phys. Chem.* **1994**, *98* (45), 11623–11627.

(53) Hagadorn, J. R.; Que, L., Jr.; Tolman, W. B. N-Donor Effects on Carboxylate Binding in Mononuclear Iron(II) Complexes of a Sterically Hindered Benzoate Ligand. *Inorg. Chem.* **2000**, *39* (26), 6086–6090.

(54) Curley, J. J.; Bergman, R. G.; Tilley, T. D. Preparation and Physical Properties of Early-Late Heterobimetallic Compounds Featuring Ir–M Bonds (M = Ti, Zr, Hf). *Dalton Trans.* **2012**, *41* (1), 192–200.

(55) Brookhart, M.; Grant, B.; Volpe, A. F., Jr. [(3,5-(CF$_3$)$_2$C$_6$H$_3$)$_4$B]⁻[H(OEt$_2$)$_2$]⁺: A Convenient Reagent for Generation and Stabilization of Cationic, Highly Electrophilic Organometallic Complexes. *Organometallics* **1992**, *11* (11), 3920–3922.

(56)   Klose, A.; Solari, E.; Floriani, C.; Chiesi-Villa, A.; Rizzoli, C.; Re, N. Magnetic Properties Diagnostic for the Existence of Iron(II)-Iron(II) Bonds in Dinuclear Complexes Which Derive From Stepwise Insertion Reactions on Unsupported Iron-Aryl Bonds. *J. Am. Chem. Soc.* **1994**, *116* (20), 9123–9135.

(57)   Evans, D. F. The Determination of the Paramagnetic Susceptibility of Substances in Solution by Nuclear Magnetic Resonance. *J. Chem. Soc.* **1959**, 2003–2005.

(58)   Sur, S. K. Measurement of Magnetic Susceptibility and Magnetic Moment of Paramagnetic Molecules in Solution by High-Field Fourier Transform NMR Spectroscopy. *J. Magn. Reson.* **1989**, *82* (1), 169–173.

(59)   Bain, G. A.; Berry, J. F. Diamagnetic Corrections and Pascal's Constants. *J. Chem. Educ.* **2008**, *85* (4), 532–536.

(60)   Gaussian 09, Revision D.01, M. J. Frisch, G. W. Trucks, H. B. Schlegel, G. E. Scuseria, M. A. Robb, J. R. Cheeseman, G. Scalmani, V. Barone, B. Menucci, G. A. Petersson, H. Nakatsuji, M. Caricato, X. Li, H. P. Hratchian, A. F. Izmaylov, J. Bloino, G. Zheng, J. L. Sonnenberg, M. Hada, M. Ehara, K. Toyota, R. Fukuda, J. Hasegawa, M. Ishida, T. Nakajima, Y. Honda, O. Kitao, H. Nakai, T. Vreven, J. A. Montgomery, Jr., J. E. Peralta, F. Ogliaro, M. Bearpark, J. J. Heyd, E. Brothers, K. N. Kudin, V. N. Staroverov, T. Keith, R. Kobayashi, J. Normand, K. Raghavachari, A. Rendell, J. C. Burant, S. S. Iyengar, J. Tomasi, M. Cossi, N. Rega, J. M. Millam, M. Klene, J. E. Knox, J. B. Cross, V. Bakken, C. Adamo, J. Jaramillo, R. Gomperts, R. E. Stratmann, O. Yazyev, A. J. Austin, R. Cammi, C. Pomelli, J. W. Ochterski, R. L. Martin, K. Morokuma, V. G. Zakrzewski, G. A. Voth, P. Salvador, J. J. Dannenberg, S. Dapprich, A. D. Daniels, O. Farkas, J. B. Foresman, J. V. Ortiz, J. Cioslowski, and D. J. Fox, Gaussian, Inc., Wallingford CT, 2010.

(61)   Schlegel, H. B. Optimization of equilibrium geometries and transition structures. *J. Comput. Chem.* **1982**, *3*, 214-218.

(62)   Schlegel, H. B. Geometry Optimization. *WIREs Comput. Mol. Sci.* **2011**, *1*, 790-809.

(63)   Schlegel, H. B.; McDouall, J. J. In *Computational Advances in Organic Chemistry*; Oegretir, C.; Csizmadia, I.G., Eds.; Kluwer Academic: Amsterdam, The Netherlands, 1991.

(64)   Baurenschmitt, R.; Ahlrichs, R. Stability analysis for solutions of the closed shell Kohn−Sham equation. *J. Chem. Phys.* **1996**, *104*, 9047-9052.

(65)   Marenich, A. V.; Cramer, C. J.; Truhlar, D. G. Universal Solvation Model Based on Solute Electron Density and on a Continuum Model of the Solvent Defined by the Bulk Dielectric Constant and Atomic Surface Tensions. *J. Phys. Chem. B* **2009**, *113*, 6378-6396.

(66)   Gordon, Z.; Drummond, M. J.; Matson, E. M.; Bogart, J. A.; Schelter, E. J.; Lord, R. L.; Fout, A. R. Tuning the Fe(II/III) Redox Potential in Nonheme Fe(II)−Hydroxo Complexes through Primary and Secondary Coordination Sphere Modifications. *Inorg. Chem.*, **2017**, *56* (9), 4852.4863.

(67)   Chai J. D.; Head-Gordon, M. Systematic optimization of long-range corrected hybrid density functionals. *J. Chem. Phys.* **2008**, *128*, 084106.

(68)   Chai, J. D.; Head-Gordon, M. Long-range corrected hybrid density functionals with damped atom-atom dispersion corrections. *Phys. Chem. Chem. Phys.* **2008**, *10*, 6615.

(69)   GaussView,Version 5.0.9, Dennington, Roy; Keith, Todd; Millam, John. *Semichem Inc.*, ShawneeMission, KS, 2009

CHAPTER 4: DIFFERENTIATING BETWEEN STERIC AND ELECTRONIC EFFECTS IN HYDRATION OF NON-HEME IRON COMPLEXES WITH PENDANT HYDROGEN BONDING GROUPS

4.1 Introduction

Hydrogen bonding often plays a vital role in dictating the reactivity of metalloenzymes.[1-3] To gain a better understanding of how these non-covalent interactions influence reactivity at the metal center, numerous synthetic systems have been developed featuring hydrogen bonding groups in the secondary coordination sphere.[4,5] Significant progress has been made in applying this design principle to small molecule activation, particularly with respect to H_2 oxidation and O_2 reduction. Pioneering work by researchers at Pacific Northwest National Laboratory (DuBois, Bullock, et al.) demonstrated the benefits of a biomimetic approach to ligand design. Their systems featuring secondary sphere proton relays, inspired by the active site of [FeFe]-hydrogenase, have proven to be exceptionally active electrocatalysts for H_2 oxidation.[6-8] Borovik has demonstrated the utility of hydrogen bonding in O_2 reduction at non-heme iron centers, both in stabilizing reactive intermediates and studying how changes in the second sphere impact metal complexes' reactivity.[9-11] Design of non-heme ligand frameworks with dynamic hydrogen bonding groups, however, remains an outstanding challenge.[12]

Drawing on the importance of proton relays in promoting selective O_2 reduction in biological and synthetic heme systems,[13-20] our research group has developed a tripodal ligand platform capable of tautomerizing between hydrogen bond donating and accepting groups in the secondary coordination sphere, $N(pi^{Cy})_3$. We have previously demonstrated that the pyrrole-imine arms of the ligand can tautomerize independently to the azafulvene-amine form, affording access to a variety of manganese(II), iron(II), and cobalt(II) complexes.[21-23] Interested in further studying these ligand dynamics, we synthesized a series of electronic variants of the ligand, $N(_xpi^R)_3$, using both primary and secondary sphere modification. Having established the effects of these modifications on the electronic properties of the iron(II)-hydroxo and iron(III)-oxo complexes,[24] we next turned our attention to studying how changes to the ligand capping group (R = cyclohexyl, 4-fluoroaryl) impact the reactivity of the iron(II) complexes formed under a variety of conditions. This report describes the metallation chemistry of the 4-fluoroaryl capped ligand derivative, $N(pi^{PhF})_3$, including its ability to access binding motifs previously unobserved for the cyclohexyl variants. The influence of steric and electronic effects on the reactivity of this derivative's iron(II) complexes is established through several control reactions using the brominated cyclohexyl ligand, $N(_{Br}pi^{Cy})_3$. These studies highlight the importance of the capping group's identity in determining the binding mode of the ligand and subsequent reactivity of the iron(II) complexes towards water.

74

4.2 Metallation studies with N(pi^{PhF})$_3$

The 4-fluoroaryl ligand variant (N(pi^{PhF})$_3$, $_H$L^{PhF}) was used for these experiments, instead of the previously published phenyl derivative (N(pi^{Ph})$_3$, $_H$L^{Ph}),[24] so that products could be characterized by ^{19}F NMR spectroscopy. This additional spectroscopic feature would aid in the interpretation of ^{1}H NMR spectra containing resonances for one or more paramagnetic iron complexes. Preliminary metallation reactions were carried out in analogy to the method established for the phenyl derivative, $_H$L^{Ph}Fe^{II}OH. The ligand hydrate, N(pi^{PhF})$_3$ · H$_2$O, was added to a cold (-35 °C) solution of dimesityliron(II) (Fe$_2$Mes$_4$) in THF, giving a red-orange solution. After the reaction mixture was stirred at room temperature for one hour, volatiles were removed *in vacuo*. The crude material was analyzed by ^{1}H and ^{19}F NMR spectroscopy. The ^{1}H NMR spectrum was consistent with formation of $_H$L^{PhF}Fe^{II}OH, as determined by comparison with the phenyl analog, however additional paramagnetic resonances were present, indicating a mixture of multiple high-spin iron species. Furthermore, the ^{19}F NMR spectrum showed two resonances at –107 and –117 ppm, confirming the formation of two different products. Given that the hydroxo ligand in this complex is likely derived from the reaction of a transiently formed iron complex with an equivalent of water, the reaction with dimesityliron(II) was repeated using the dried form of the ligand to determine if the second species observed was a dehydrated precursor to the iron(II)-hydroxo complex. ^{1}H and ^{19}F NMR spectra of the crude material once again showed a mixture of $_H$L^{PhF}Fe^{II}OH and the second paramagnetic species previously observed. Intriguingly, the ratio of the two products formed was the same for metallation of the hydrated and dried ligands, as determined by integration of ^{19}F NMR spectra collected for reaction aliquots.

The second paramagnetic species formed in these reaction was structurally characterized by X-ray crystallography to determine the binding mode of the ligand. Crystals suitable for X-ray diffraction were grown by vapor diffusion of hexanes into a toluene solution of the iron species. Refinement of the data

monomer   **[N($_H$pi^{PhF})$_3$Fe(II)]$_2$**   **dimer**

asymmetric unit cell   **[$_H$L^{PhF}Fe^{II}]$_2$**   **symmetry generated**
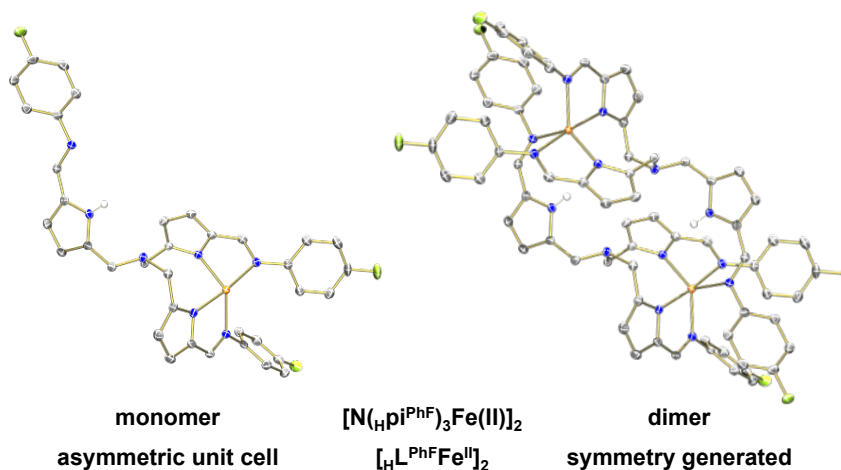
Figure 4.1 Molecular structure of **[$_H$L^{PhF}Fe^{II}]$_2$** shown with 50% probability ellipsoids. For clarity, only the pyrrole protons are shown.

75

showed that the iron center was not bound in the desired binding pocket formed by the pyrrole donors (Figure 4.1). Instead, the iron atom was bound to both the pyrrole and imine nitrogens of the two deprotonated arms of the ligand, while the third arm remained protonated. No bonding was observed between the iron center and the protonated arm or the apical nitrogen of the ligand. Interestingly, this species crystallized as a dimer, $[N(pi^{PhF})_3Fe(II)]_2$ ($[_HL^{PhF}Fe^{II}]_2$), where the imine nitrogen of the protonated ligand arm was bound to a second, symmetry-generated iron center (Figure 4.1). This dimerization resulted in two iron centers that are bound in a trigonal bipyramidal geometry by the five nitrogen donors described. Love and coworkers have previously reported similar binding modes in complexes featuring related tripodal pyrrole-imine ligands; however, these frameworks lack an apical nitrogen donor, resulting in geometric differences that likely favor binding to both nitrogen atoms in the ligand arm (pyrrole and imine).[25,26] In contrast, our previous work with imine-functionalized tris(pyrrolyl-α-methyl)amine ligand derivatives, $N(pi^R)_3$, has only resulted in one neutral iron(III) complex where the metal center binds to both nitrogen donors within the same ligand arm in an octahedral geometry.[22]

Further analysis of this dimeric complex, $[_HL^{PhF}Fe^{II}]_2$, was pursued to explore the influences that resulted in this previously unobserved binding mode of the ligand. Initial efforts were focused on determining the relationship between $[_HL^{PhF}Fe^{II}]_2$ and $_HL^{PhF}Fe^{II}OH$. Although the presence of stoichiometric water, from the ligand hydrate, gave a mixture of the two iron complexes, injection of two drops of water into an NMR sample of crystalline $[_HL^{PhF}Fe^{II}]_2$ (containing a minor but intractable $_HL^{PhF}Fe^{II}OH$ impurity) resulted in complete conversion to $_HL^{PhF}Fe^{II}OH$. Taken together with the product mixtures observed in the metallation reactions, this result indicated stoichiometric water does not promote full conversion of $[_HL^{PhF}Fe^{II}]_2$ to $_HL^{PhF}Fe^{II}OH$, however addition of excess water can be used to force complete hydration and yield the monomeric iron(II)-hydroxo complex (Figure 4.2).

Figure 4.2 ^{19}F NMR spectra for (A) $L^{PhF} \cdot H_2O$ + 0.5 Fe_2Mes_4; (B) $[_HL^{PhF}Fe^{II}]_2$ crystallized from L^{PhF} + 0.5 Fe_2Mes_4; (C) $_HL^{PhF}Fe^{II}OH$ isolated from 1. L^{PhF} + 0.5 Fe_2Mes_4, 2. excess H_2O.

Accordingly, a new synthetic procedure was adopted, whereby dry ligand was metallated with dimesityliron(II) to yield the dimeric intermediate, then treated with excess water in deoxygenated tetrahydrofuran (see Experimental Section, Method A). This method yielded pure samples of $_HL^{PhF}Fe^{II}OH$ in near quantitative yield (98%). It was later determined that pure product could also be isolated from the previous reaction conditions starting with the ligand hydrate, following the reaction of $[_HL^{PhF}Fe^{II}]_2$ and

adventitious water in the crystallization solvents (Method B, 78% crystalline yield). However, the latter route required significant optimization, as $[_HL^{PhF}Fe^{II}]_2$ and $_HL^{PhF}Fe^{II}OH$ were found to co-crystallize in all other solvent mixtures screened. Mixed tautomer binding of the ligand in $_HL^{PhF}Fe^{II}OH$ was confirmed by IR spectroscopy, which displayed two prominent C=N stretches at 1610 cm^{-1} (pyrrole-imine) and 1658 cm^{-1} (azafulvene-amine). X-ray diffraction studies were carried out to structurally characterize $_HL^{PhF}Fe^{II}OH$. The structural parameters obtained were statistically equivalent to those found for $_HL^{Ph}Fe^{II}OH$.[24]
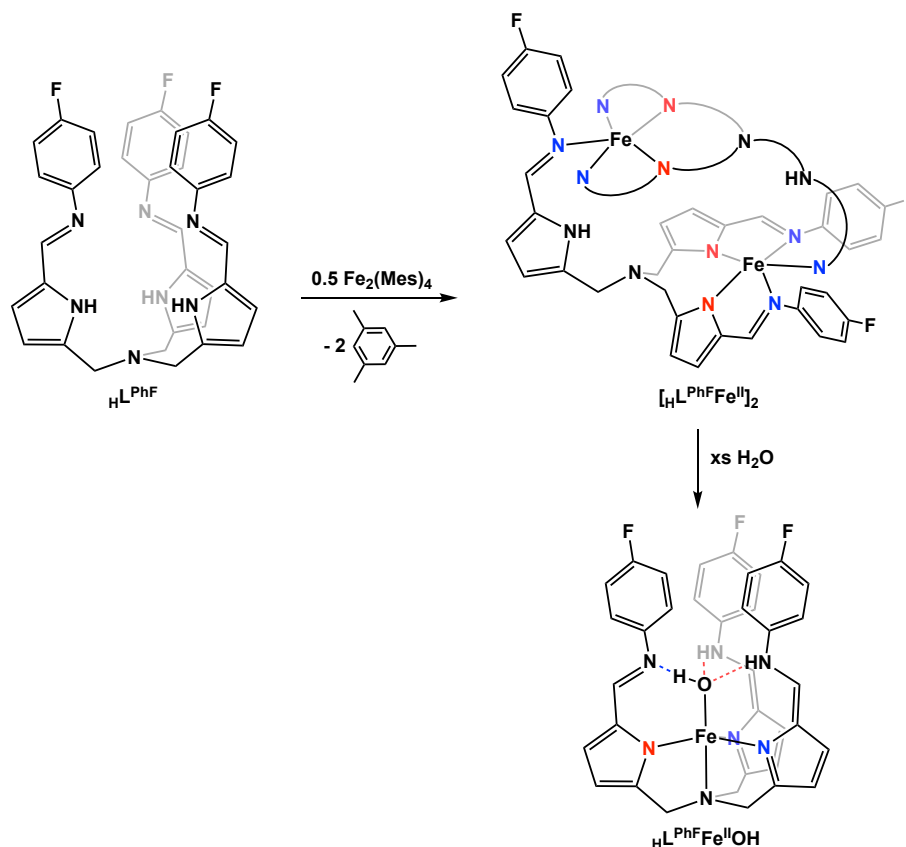
Scheme 4.1 Metallation of $_HL^{PhF}$ to form $[_HL^{PhF}Fe^{II}]_2$ and its subsequent hydration to yield $_HL^{PhF}Fe^{II}OH$.

4.3 Comparison of electronic and steric contributions to the formation of $[_HL^{PhF}Fe^{II}]_2$

Following characterization of $[_HL^{PhF}Fe^{II}]_2$ and $_HL^{PhF}Fe^{II}OH$, additional experiments were targeted to separate the electronic and steric contributions to the observed reactivity with stoichiometric amounts of water. Previous work with the iron(II)-hydroxo complex of bromo-cyclohexyl ligand, $_BrL^{Cy}Fe^{II}OH$, demonstrated this derivative could be used as a point of comparison to control for the impact of electronic differences in the $_HL^{PhF}$ and $_HL^{Cy}$ ligands.[24] This complex possesses a reversible Fe(II/III) redox couple centered at -0.49 V vs Fc$^{0/+}$, which compares well with the value obtained for $_HL^{PhF}Fe^{II}OH$ ($E_{1/2}$ = -0.47 V) and is significantly closer than $_HL^{Cy}Fe^{II}OH$ ($E_{1/2}$ = -0.69 V). Accordingly, further reactivity studies were benchmarked against the analogous $_BrL^{Cy}$ complexes. It should be noted that reaction of N$_{(Br}$pi$^{Cy})_3 \cdot$

H_2O with 0.5 Fe_2Mes_4, yields only the iron(II)-hydroxo complex, with no other major paramagnetic species observed in the ^1H NMR spectrum of the crude reaction mixture, providing an early indication that the decreased steric demand of the aryl capping group may be responsible for the disparities in reactivity.

To further examine these differences, deprotonation of the secondary coordination sphere was pursued. The first reaction targeted was treatment of the datively coordinated triflate complex, $N(afa^{PhF})_3Fe(OTf)_2$ ($_HL^{PhF}FeOTf_2$), with lithium oxide (Li_2O). In the case of $_HL^{Cy}FeOTf_2$ this reaction results in effective deprotonation of the secondary coordination sphere, generating a stoichiometric amount of water as a by-product. This water molecule is ultimately bound at the iron center, generating the iron(II)-hydroxo complex, $_HL^{Cy}Fe^{II}OH$.[22] While the exact mechanism of this reaction is unknown, it results in clean conversion without any observed intermediates. Given the monomeric nature of the starting complex for this reaction, this pathway was examined to test whether formation of the dimeric species, $[_HL^{PhF}Fe^{II}]_2$, was dependent on the metallation route or if the properties of the ligand inherently favored the dehydrated complex.

For this reaction $_HL^{PhF}FeOTf_2$ was treated with two equivalents of Li_2O and stirred overnight, the crude reaction mixture was then analyzed by ^1H and ^{19}F NMR spectroscopy. The reactions resulted in full consumption of the starting complex, $_HL^{PhF}FeOTf_2$, however minimal conversion to $_HL^{PhF}Fe^{II}OH$ was observed. Interestingly, the major product was determined to be the dimeric species $[_HL^{PhF}Fe^{II}]_2$, with relatively minor $_HL^{PhF}Fe^{II}OH$ formation. Given that the conversion of $_HL^{PhF}FeOTf_2$ to $[_HL^{PhF}Fe^{II}]_2$ requires the release of a stoichiometric amount of water following deprotonation, this result clearly indicates that
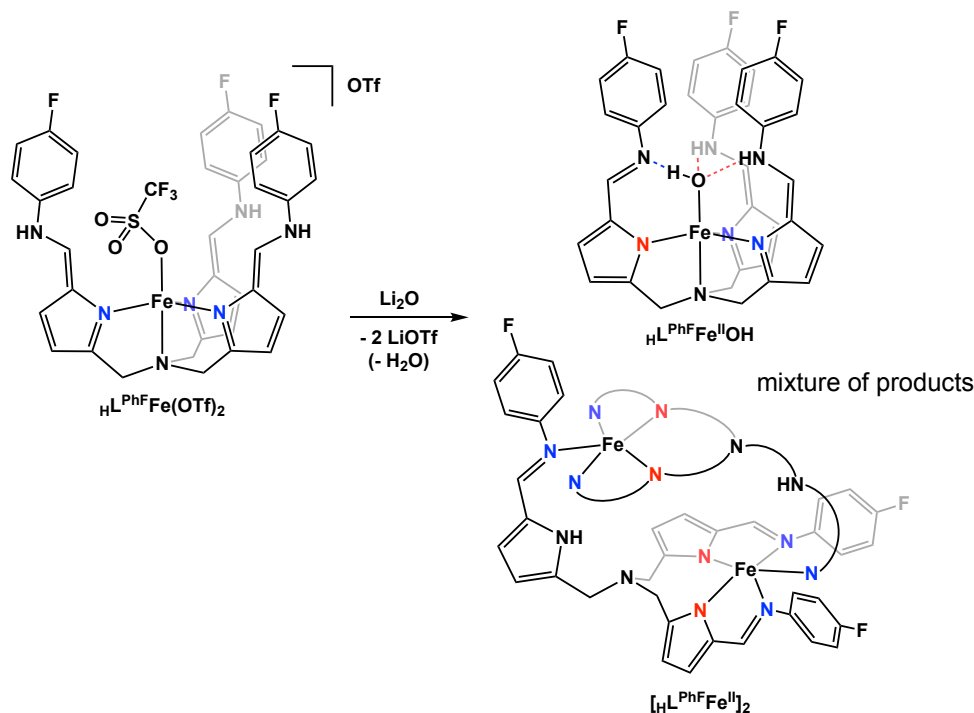
Scheme 4.2 Deprotonation of $_HL^{PhF}FeOTf_2$ by Li_2O yielding a mixture of $[_HL^{PhF}Fe^{II}]_2$ and $_HL^{PhF}Fe^{II}OH$.

formation of the dehydrated dimer is a thermodynamically favorable process, even when starting from a monomeric species where the iron center is bound in the desired pocket. When this reaction was carried out with $_{Br}L^{Cy}FeOTf_2$ the iron(II)-hydroxo complex was formed in high yield (94%), again consistent with differences in the steric demand of the capping groups causing the disparities in reactivity.

One final deprotonation reaction was examined to more directly investigate differences in the hydrogen bonding properties of the ligands. Previous analysis of the $_HL^{Ph}$ and $_{Br}L^{Cy}$ ligand variants suggested that the electronic difference between the two capping groups alters the strength of the hydrogen bonds in the secondary coordination sphere, with the phenyl variants acting as stronger hydrogen bond donors in the amino form.[24] Conversely, it would be expected that the aryl variants would act as weaker hydrogen bond acceptors in the imino tautomer, which may contribute towards their decreased reactivity towards water. The iron(II)-aquo complexes were targeted to assess this possibility. Prior work with $_HL^{Cy}$ demonstrated that deprotonation of $N(pi^{Cy})(afa^{Cy})_2Fe(II)OH$ ($_HL^{Cy}Fe^{II}OH$) results in the formation of an iron(II)-aquo complex, $K[N(pi^{Cy})_3Fe(II)OH_2]$ ($_HL^{Cy}Fe^{II}OH_2$) following tautomerization of the ligand.[22] If the differences in hydrogen bonding for the aryl capping group play a significant role in accessing the dehydrated dimer with $_HL^{PhF}$, then deprotonation of the iron(II)-hydroxo complex would be expected to yield a related dehydrated complex, given the weaker hydrogen bond accepting ability of the aryl capped imino groups.

Treatment of $_HL^{PhF}Fe^{II}OH$ with an equivalent of potassium hydride (KH) resulted in clean formation of a new paramagnetic species, as judged by ^1H and ^{19}F NMR spectroscopy. The ^1H NMR spectrum compared favorably with the previously characterized $_HL^{Cy}Fe^{II}OH_2$ complex, suggesting an analogous iron(II)-aquo species, $K[N(pi^{PhF})_3Fe(II)OH_2]$ ($_HL^{PhF}Fe^{II}OH_2$), was formed. Anionic binding of the ligand was confirmed by IR spectroscopy, indicating tautomerization of the ligand following deprotonation. Treatment of $_{Br}L^{Cy}Fe^{II}OH$ with KH proceeded similarly, resulting in the corresponding complex, $K[N(_{Br}pi^{Cy})_3Fe(II)OH_2]$ ($_{Br}L^{Cy}Fe^{II}OH_2$). These results suggest that the weaker hydrogen bond accepting abilities of the aryl capped ligand do not contribute significantly to the decreased reactivity of the L^{PhF} complexes towards water. The isolation of the monomeric iron(II)-aquo complex demonstrates the com-
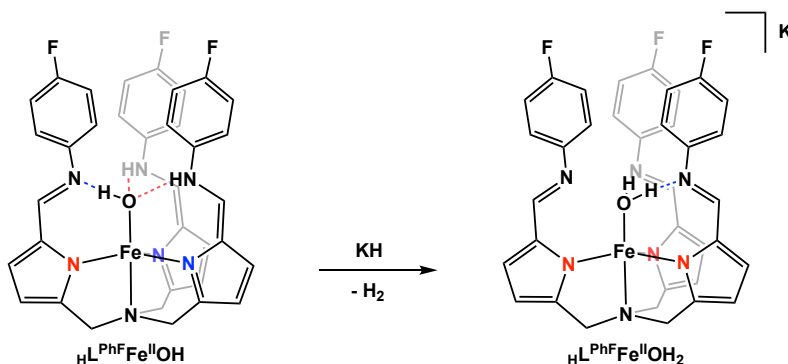
Scheme 4.3 Deprotonation of $_HL^{PhF}Fe^{II}OH$ by KH to form $_HL^{PhF}Fe^{II}OH_2$ upon tautomerization of the ligand.

79

petence of the secondary sphere imino groups in hydrogen bonding with water, providing additional evidence that the decreased steric demands of the aryl capping group are responsible for the formation of the dimeric iron(II) species, $[_H\mathbf{L}^{PhF}\mathbf{Fe}^{II}]_2$.

4.4 Conclusion

Metallation of the 4-fluoroaryl capped ligand, $N(pi^{PhF})_3$, has been described. Initial reactions of Fe_2Mes_4 with either the dried ligand or its hydrate gave a mixture of two paramagnetic species. The products were determined to be an iron(II)-hydroxo complex, $_H\mathbf{L}^{PhF}\mathbf{Fe}^{II}\mathbf{OH}$, analogous to other derivatives of the ligand, and a dehydrated iron(II) dimer, $[_H\mathbf{L}^{PhF}\mathbf{Fe}^{II}]_2$, which displayed a binding mode not previously observed for this family of ligands. Although it was converted to $_H\mathbf{L}^{PhF}\mathbf{Fe}^{II}\mathbf{OH}$ in the presence of excess water, the dimer was formed in reactions where stoichiometric water was present, including metallation of the ligand hydrate and deprotonation of $\mathbf{L}^{PhF}\mathbf{FeOTf_2}$ by Li_2O.

These results were compared to the electronically similar $_{Br}\mathbf{L}^{Cy}$ complexes to analyze the role of the aryl capping group in controlling the reactivity towards water. Given that no analogous dehydrated species was observed for the $_{Br}\mathbf{L}^{Cy}$ ligand under any of these conditions, the difference in reactivity is attributed to the decreased steric demand of the aryl capping groups, allowing two ligands to bind closely enough to form the dimeric complex. It is also worth noting that a similar dimeric binding motif was previously observed with the related dipodal framework, $^{Me}N(pi^{Cy})_2$, where the steric demands of the ligand are further decreased by removing the third pyrrole-imine arm.[27] The importance of sterics in this reactivity was also supported by isolation of the monomeric iron(II)-aquo complex, $K[N(pi^{PhF})_3Fe(II)OH_2]$ ($_H\mathbf{L}^{PhF}\mathbf{Fe}^{II}\mathbf{OH_2}$), which suggested that the weaker hydrogen bond accepting ability of the aryl imino groups does not contribute significantly to the reduced reactivity towards water. This work demonstrates the role of steric interactions in dictating the binding mode and subsequent reactivity of ligands featuring hydrogen-bonding groups in the secondary coordination sphere. Although the use of pendant imino groups as hydrogen bond acceptors can result in undesirable binding modes of the ligand, this report highlights the utility of dynamic secondary coordination sphere interactions in destabilizing dimeric species when potential hydrogen bonding substrates are present.

4.5 Experimental section

General Considerations. All manipulations of air- and moisture-sensitive metal compounds were carried out in the absence of water and dioxygen using standard Schlenk techniques or in an MBraun inert atmosphere drybox under a dinitrogen atmosphere, except where specified otherwise. All glassware was oven dried for a minimum of 8 h and cooled in an evacuated antechamber prior to use in the drybox. Solvents were dried and deoxygenated on a Glass Contour System (SG Water USA, Nashua, NH) and stored over 4 Å molecular sieves purchased from Strem prior to use. Chloroform-d_1, dichloromethane-d_2, and acetonitrile-d_3 were purchased from Cambridge Isotope Labs and stored over 4 Å molecular sieves prior

to use. 4-fluoroaniline (Sigma Aldrich), lithium oxide (Sigma Aldrich), and formic acid (88% in water, Macron) were purchased from the listed vendor and used as received. $Fe(OTf)_2 \cdot 2\ MeCN$[28] was prepared according to a modified literature procedure. $Fe_2(Mes)_4$,[29] tpa^{CO},[22] $N(_{Br}pi^{Cy})_3 \cdot H_2O$ ($_{Br}L^{Cy}$),[24] and $N(_{Br}pi^{Cy})(_{Br}afa^{Cy})_2Fe(II)OH$ ($_{Br}L^{Cy}Fe^{II}OH$)[24] were all prepared according to literature procedures. KH (suspension in mineral oil, Sigma Aldrich) was collected over a fritted funnel and washed with hexanes to remove mineral oil prior to use. Celite® 545 (J. T. Baker) and Tetrabutylammonium hexafluorophosphate ($[^nBu_4N][PF_6]$) (Sigma Aldrich) were dried in Schlenk flasks for 24 h under dynamic vacuum while heating to at least 150 °C, prior to use in a drybox. NMR spectra were recorded on a Varian spectrometer operating at 500/400 MHz (^1H NMR), 471/377 MHz (^{19}F NMR), or 126 MHz (^{13}C NMR). All ^1H and ^{13}C chemical shifts (ppm) are reported relative to the resonance of the residual solvent as a standard; ^{19}F chemical shifts (ppm) are reported relative to an external standard of 1% $CFCl_3$ in $CDCl_3$ as a reference. Solid-state infrared spectra were recorded using a PerkinElmer Frontier FT-IR spectrophotometer equipped with a KRS5 thallium bromide/iodide universal attenuated total reflectance (ATR) accessory. Elemental analyses were performed by the University of Illinois at Urbana-Champaign School of Chemical Sciences Microanalysis Laboratory in Urbana, IL. Samples submitted for elemental analyses were dried under vacuum for a minimum of 12 hours; solvates were confirmed by ^1H NMR.

Cyclic Voltammetry. Electrochemical experiments were carried out using a CH Instruments CHI410C Electrochemical Workstation. The supporting electrolyte was 0.1 M $[^nBu_4N][PF_6]$ in a 1:1 acetonitrile/tetrahydrofuran mixture. A glassy carbon working electrode, a platinum wire counter electrode, and a silver wire pseudo reference electrode were used. The concentration of each analyte was 1 mM. Experiments were performed at a scan rate of 100 mV/s, unless otherwise specified. Each scan was referenced to internal $Fc^{0/+}$.

Preparation of $N(pi^{PhF})_3 \cdot H_2O$. A 100 mL round bottom flask was charged with 488 mg of tpa^{CO} (1.44 mmol) and ethanol (25 mL), giving a tan suspension. A slight excess of 4-fluoroaniline (497 mg, 4.47 mmol, 3.1 equiv) was added to this suspension, followed by a catalytic amount of formic acid (4 drops, 88% in H_2O). The reaction was stirred at room temperature overnight to ensure complete conversion, as both the formylated starting material and the imine ligand product are minimally soluble in ethanol. The crude material was collected over a fritted funnel and washed with fresh ethanol (2 x 10 mL) then diethylether (2 x 10 mL) to remove residual aniline. $N(pi^{PhF})_3 \cdot H_2O$ was collected as a tan powder (674 mg, 1.06 mmol, 73%). ^1H NMR ($CDCl_3$, 400 MHz): δ= 3.72 (s, 6H, methylene-CH_2), 6.16 (d, $J = 3.6$ Hz, 3H, pyr-CH), 6.63 (d, $J = 3.6$ Hz, 3H, pyr-CH), 6.95 (m, 6H, Ar-CH), 7.09 (m, 6H, Ar-CH), 8.16 (s, 3H, imine-CH). ^{13}C NMR (DMSO-d_6, 126 MHz): δ= 49.98, 109.74, 115.77 (d, $J = 22.2$ Hz), 118.00, 122.31 (d, $J = 8.5$ Hz), 130.46, 135.97, 148.69, 150.72, 159.80 (d, $J = 240.9$ Hz). ^{19}F NMR ($CDCl_3$, 377 MHz): δ= -118.04.

The ligand was dehydrated by drying a solution of the ligand hydrate (531 mg, 0.835 mmol) in DCM (~ 30 mL) over 4 Å molecular sieves for at least 12 h. Volatiles were then removed under vacuum. The off-white powder was triturated with hexanes to aid in drying. 403 mg of N(pi^{PhF})$_3$ ($_H$L^{PhF}) were collected (0.652 mmol, 78%). Analysis for C$_{36}$H$_{30}$N$_7$F$_3$: Calcd. C, 70.00; H, 4.90; N, 15.87. Found C, 69.71; H, 4.79; N, 15.65. ^{1}H NMR (CD$_3$CN, 500 MHz): δ= 3.66 (s, 6H, methylene-CH_2), 6.17 (d, J = 3.1 Hz, 3H, pyr-CH), 6.62 (d, J = 3.4 Hz, 3H, pyr-CH), 7.06 (m, 6H, Ar-CH), 7.15 (m, 6H, Ar-CH), 8.23 (s, 3H, imine-CH), 9.93 (br, 3H, pyr-NH). ^{13}C NMR (CDCl$_3$, 126 MHz): δ= 50.26, 110.84, 115.96 (d, J = 22.5 Hz), 116.95, 122.28 (d, J = 8.1 Hz), 131.00, 133.83, 147.85, 149.11, 160.94 (d, J = 244.1 Hz). ^{19}F NMR (CD$_2$Cl$_2$, 471 MHz): δ= -120.79. IR ν$_{max}$ = 1615 cm^{-1} (C=N).

Formation of the dehydrated iron(II) dimer [N(pi^{PhF})$_3$Fe(II)]$_2$ ([$_H$L^{PhF}Fe^{II}]$_2$). *Attempted synthesis of N(pi^{PhF})(afa^{PhF})$_2$Fe^{II}OH ($_H$L^{PhF}Fe^{II}OH) from the ligand hydrate.* 25 mg of Fe$_2$Mes$_4$ (0.042 mmol) was dissolved in tetrahydrofuran (5 mL) and cooled to -35 °C. 54 mg of N(pi^F)$_3$ · H$_2$O (0.085 mmol, 1 equiv per Fe center) was weighed by difference and added as a solid to the pale yellow solution. The reaction was stirred at room temperature for 1 h, volatiles were then removed in vacuo. The crude material was analyzed by ^{1}H and ^{19}F NMR spectroscopy, revealing a mixture of two species (Figure 4.3 top) that were later identified as [$_H$L^{PhF}Fe^{II}]$_2$ and $_H$L^{PhF}Fe^{II}OH (see below).
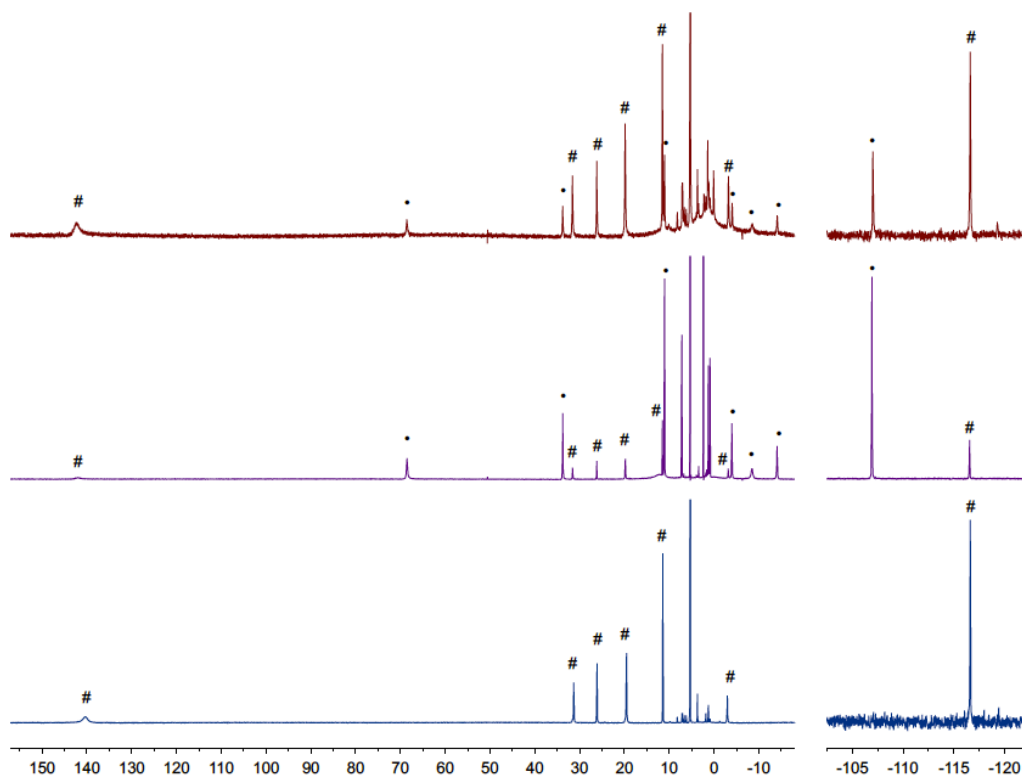
Figure 4.3 ^{1}H (right) and ^{19}F (left) NMR spectra for (A) a representative mixture of $_H$L^{PhF}Fe^{II}OH and [$_H$L^{PhF}Fe^{II}]$_2$ showing the crude material obtained from reaction of L^{PhF} · H$_2$O with 0.5 Fe$_2$Mes$_4$; (B) [$_H$L^{PhF}Fe^{II}]$_2$ crystallized from metallation of L^{PhF} with 0.5 Fe$_2$Mes$_4$; and (C) $_H$L^{PhF}Fe^{II}OH crystallized from reaction L^{PhF} · H$_2$O with 0.5 Fe$_2$Mes$_4$. Resonances marked with • correspond to [$_H$L^{PhF}Fe^{II}]$_2$; # correspond to $_H$L^{PhF}Fe^{II}OH.

Identification of the dehydrated iron(II) dimer $[N(pi^{PhF})_3Fe(II)]_2$ ($[_HL^{PhF}Fe^{II}]_2$). 33 mg of Fe₂Mes₄ (0.056 mmol) was dissolved in tetrahydrofuran (5 mL) and cooled to -35 °C. 70 mg of $N(pi^{PhF})_3$ (0.11 mmol, 1 equiv per Fe center) was weighed by difference and added as a solid to the pale yellow solution, giving an immediate color change to orange. The reaction was stirred at room temperature for 1 h then solvent was removed in vacuo. Crystals suitable for X-ray diffraction were grown from vapor diffusion of hexanes into a solution of $[_HL^{PhF}Fe^{II}]_2$ dissolved in toluene. ¹H NMR (CD₂Cl₂, 500 MHz): δ = -14.07 (s, 3H), -8.50 (br, 3H), -3.98 (s, 3H), 11.06 (s, 6H), 33.77 (s, 3H), 68.53 (s, 3H). ¹⁹F NMR (CD₂Cl₂, 471 MHz): δ= -106.93. This dehydrated complex was found to co-crystallize with the monomeric iron(II)-hydroxo, $N(pi^{PhF})(afa^{PhF})_2Fe(II)OH$ ($_HL^{PhF}Fe^{II}OH$, synthesis and characterization of this complex are reported below), under a variety of conditions, giving an intractable mixture of the two species and preventing isolation of the dimeric complex. The formation of $_HL^{PhF}Fe^{II}OH$ is attributed to reaction of the dimeric complex with two equivalents of adventitious water from the crystallization solvents. Injection of DI water (2 drops) into a NMR sample of the $[_HL^{PhF}Fe^{II}]_2$ dimer confirmed conversion to $_HL^{PhF}Fe^{II}OH$ occurs upon hydration; this reaction was tracked by both ¹H and ¹⁹F NMR spectroscopy (Figure 4.4/4.5).
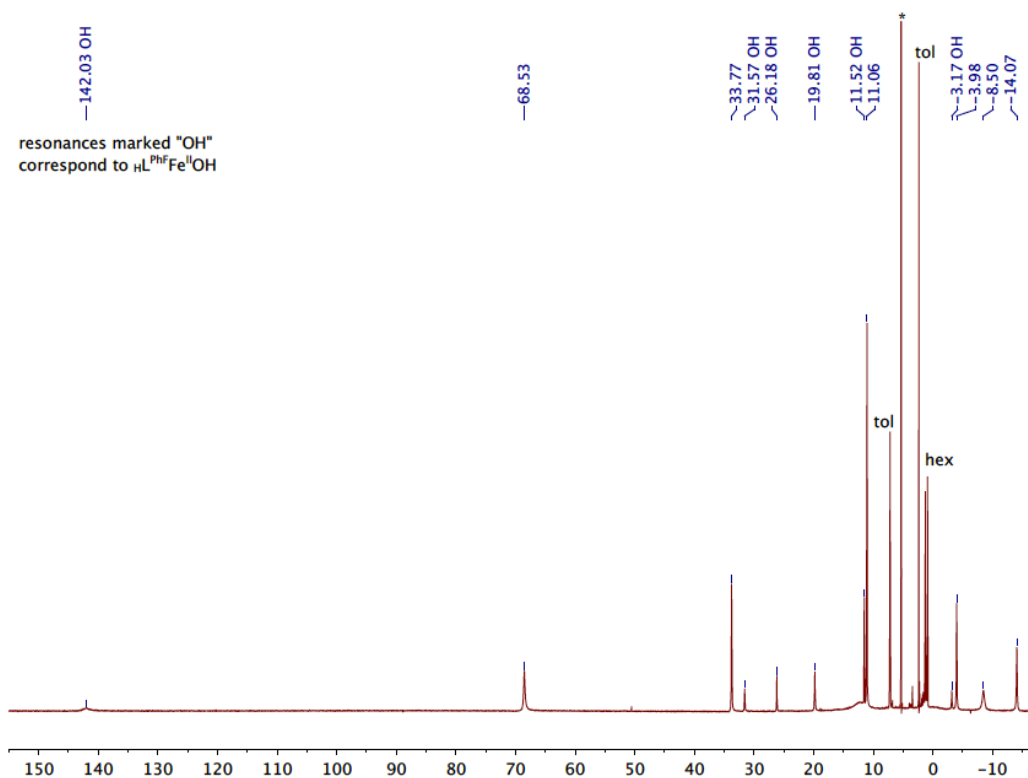
Figure 4.4 ¹H NMR spectrum of $[N(pi^{PhF})_3Fe(II)]_2$ ($[_HL^{PhF}Fe^{II}]_2$), resonances corresponding to the minor, but intractable, $_HL^{PhF}Fe^{II}OH$ impurity are marked accordingly (500 MHz, CD₂Cl₂,*residual solvent).
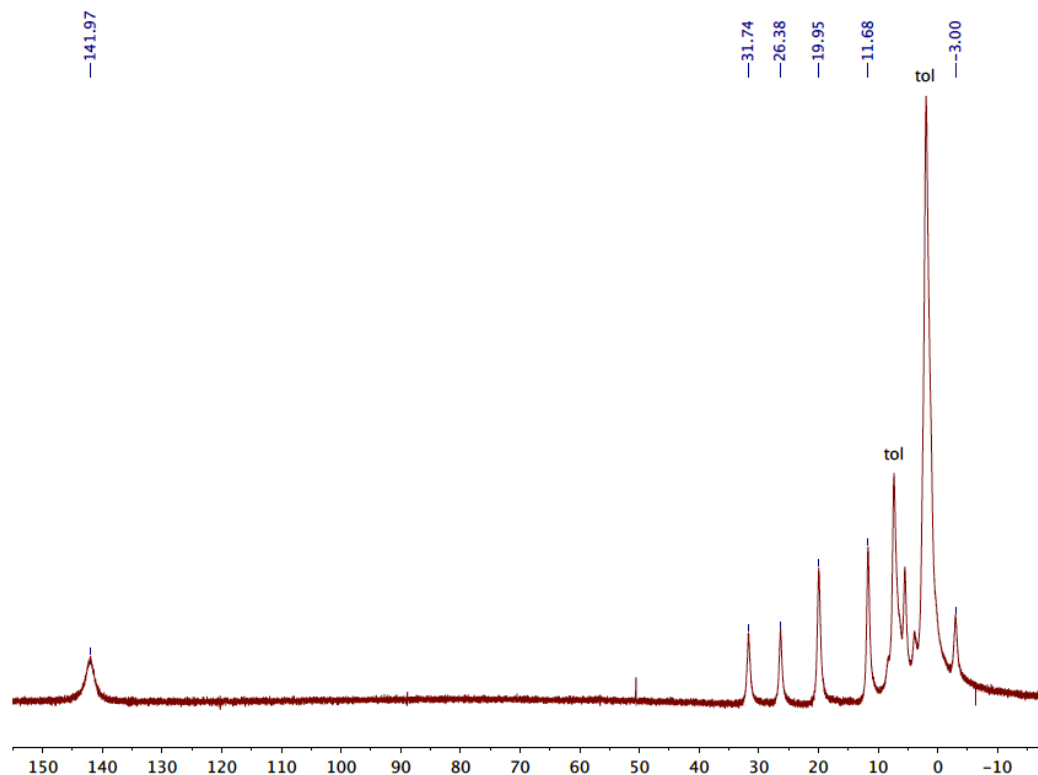
Figure 4.5 ^{1}H NMR spectrum collected following the addition of H$_2$O to a sample of [$_H$L^{PhF}Fe^{II}]$_2$, which initially gave the spectrum shown in Figure 4.4 above, demonstrating complete conversion to $_H$L^{PhF}Fe^{II}OH (500 MHz, CD$_2$Cl$_2$).

Preparation of N(pi^{PhF})(afa^{PhF})$_2$Fe(II)OH ($_H$L^{PhF}Fe^{II}OH). *Method A (using the dried ligand).* Fe$_2$Mes$_4$ (123 mg, 0.209 mmol) was dissolved in tetrahydrofuran (5 mL) and cooled to -35 ºC. N(pi^{PhF})$_3$ ($_H$L^{PhF}; 259 mg, 0.419 mmol, 1 equiv per Fe center) was weighed by difference and added as a solid to the pale yellow solution, giving an immediate color change to orange. The reaction was stirred at room temperature for 1 h then solvent was removed in vacuo. The crude material was washed with hexanes to remove the mesitylene byproduct (3 x 5 mL). Washed material was redissolved in minimal tetrahydrofuran and transferred to a Schlenk flask. Solvent was removed in vacuo to give a yellow-brown residue. The flask containing this residue was sealed with a septum then removed from the glovebox and transferred to the Schlenk line. Separately, a drop of DI water was diluted in wet tetrahydrofuran (15 mL). This solution was deoxygenated by several freeze-pump-thaw cycles, and then transferred to the Schlenk flask containing the metal complex via cannulation. Following cannulation, the reaction mixture was stirred for 30 minutes. Volatiles were removed in vacuo. The powdered product was then returned to the glovebox, transferred to a tared vial as a slurry in dichloromethane, and dried under vaccum to yield the final product, N(pi^{PhF})(afa^{PhF})$_2$Fe(II)OH ($_H$L^{PhF}Fe^{II}OH), without further purification (283 mg, 0.410 mmol, 98%). Analysis for C$_{36}$H$_{30}$F$_3$N$_7$OFe · 0.5 CH$_2$Cl$_2$: Calcd. C, 59.89; H, 4.27; N, 13.39. Found C,

60.07; H, 4.39; N, 13.03. ^{1}H NMR (CD$_2$Cl$_2$, 500 MHz, 21 °C): δ = -2.98 (s, 3H, imine-CH), 11.42 (s, 6H, Ph-CH), 19.54 (s, 6H, Ph-CH), 26.12 (s, 3H, pyr-CH), 31.32 (s, 3H, pyr-CH), 140.33 (br, 6H, methylene-CH_2), 199.89 (br, 3H, amino-NH/hydroxo-OH). ^{19}F NMR (CD$_2$Cl$_2$, 377 MHz): δ= -116.61. IR ν$_{max}$ = 1610, 1658 cm^{-1} (C=N).
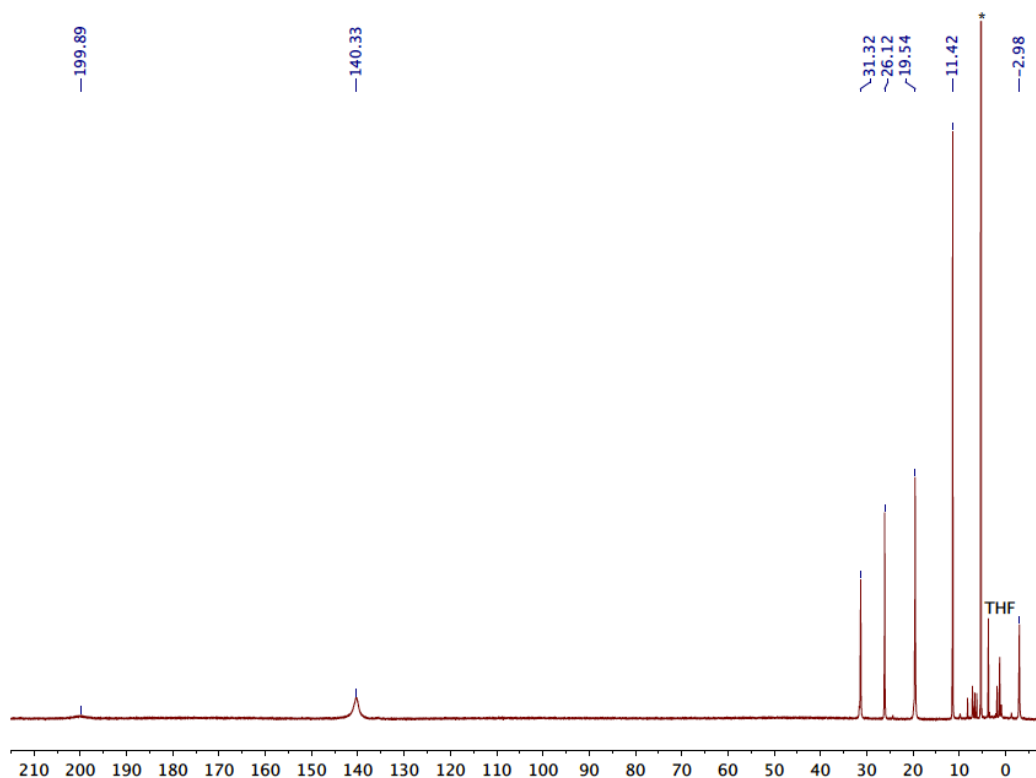
Figure 4.6 ^{1}H NMR spectra of N(pi^{PhF})(afa^{PhF})$_2$Fe(II)OH $_H$L^{PhF}Fe^{II}OH (500 MHz, CD$_2$Cl$_2$,*residual solvent).

Method B (using the ligand hydrate). Fe$_2$Mes$_4$ (27 mg, 0.046 mmol) was dissolved in tetrahydrofuran (5 mL) and cooled to -35 ºC. N(pi^{PhF})$_3$ · H$_2$O ($_H$L^{PhF}; 55 mg, 0.087 mmol, 1 equiv per Fe center) was weighed by difference and added as a solid to the pale yellow solution, giving an immediate color change to dark red-orange. The reaction was stirred at room temperature for 1 h, then filtered to remove any solids and layered with hexanes to crystallize. N(pi^{PhF})(afa^{PhF})$_2$Fe(II)OH ($_H$L^{PhF}Fe^{II}OH) was collected as an yellow-brown powder (47 mg, 0.068 mmol, 78% crystalline yield). Crystals suitable for X-ray diffraction were grown by slow evaporation of a solution of $_H$L^{PhF}Fe^{II}OH dissolved in a toluene-tetrahydrofuran mixture (~1:1).

Preparation of N(afa^PhF)₃Fe(OTf)₂ (HL^PhFFeOTf₂). Fe(OTf)₂ · 2 MeCN (24 mg, 0.055 mmol) and N(pi^PhF)₃ (34 mg, 0.055 mmol) were combined in acetonitrile (5 mL) and stirred at room temperature. After stirring for 1 h, volatiles were removed in vacuo. The crude material was washed with dichloromethane, filtered, and re-collected with tetrahydrofuran. The purified filtrate was dried under vacuum to yield the final product, **N(afa^PhF)₃Fe(OTf)₂**, as an orange powder (43 mg, 0.044 mmol, 80 %). Analysis for $C_{38}H_{30}F_9FeN_7O_6S_2 \cdot 0.5\ C_4H_8O$: Calcd. C, 47.68; H, 3.40; N, 9.73. Found C, 47.68; H, 3.55; N, 9.45. ^{19}F NMR (CD₃CN, 471 MHz): δ= -75.32 (OTf), -97.41, -115.56. IR ν_{max} = 1641 cm^{-1} (C=N). μ_{eff} = 5.49(13) μ_B.
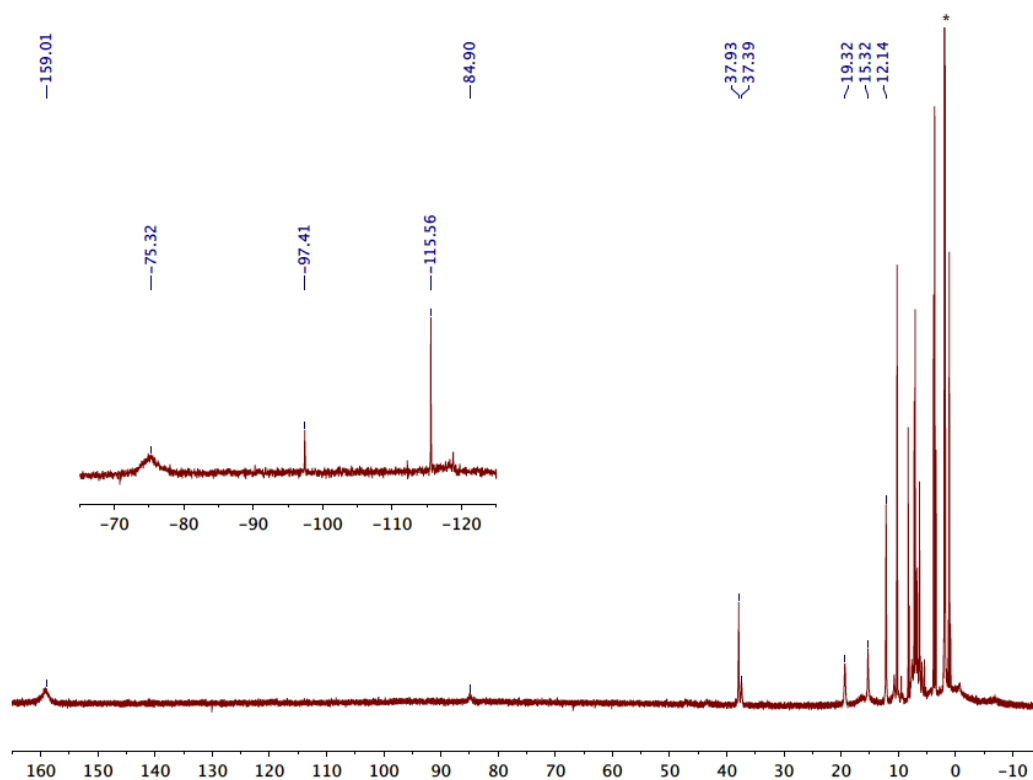
Figure 4.7 ^1H & ^{19}F (inset) NMR spectra of N(afa^PhF)₃Fe(II)(OTf)₂ **HL^PhFFeOTf₂** (500 MHz (^1H), 471 MHz (^{19}F), CD₃CN, *residual solvent).

Preparation of N($_{Br}$afa^{Cy})$_3$Fe(OTf)$_2$ ($_{Br}$L^{Cy}FeOTf$_2$). Fe(OTf)$_2$ · 2 MeCN (23 mg, 0.053 mmol) and N($_{Br}$pi^{Cy})$_3$ (43 mg, 0.053 mmol) were combined in acetonitrile (5 mL) and stirred at room temperature. After stirring for 1 h, volatiles were removed in vacuo. The crude material was washed with dichloro-methane, filtered, and re-collected with tetrahydrofuran. The purified filtrate was dried under vacuum to yield the final product, **N($_{Br}$afa^{Cy})$_3$Fe(OTf)$_2$**, as a brown powder (50 mg, 0.043 mmol, 81 %). Analysis for C$_{38}$H$_{30}$F$_9$FeN$_7$O$_6$S$_2$ · 0.5 C$_4$H$_8$O: Calcd. C, 47.68; H, 3.40; N, 9.73. Found C, 47.68; H, 3.55; N, 9.45. IR ν_{max} = 1642 cm^{-1} (C=N). μ_{eff} = 5.68(2) μ_B.
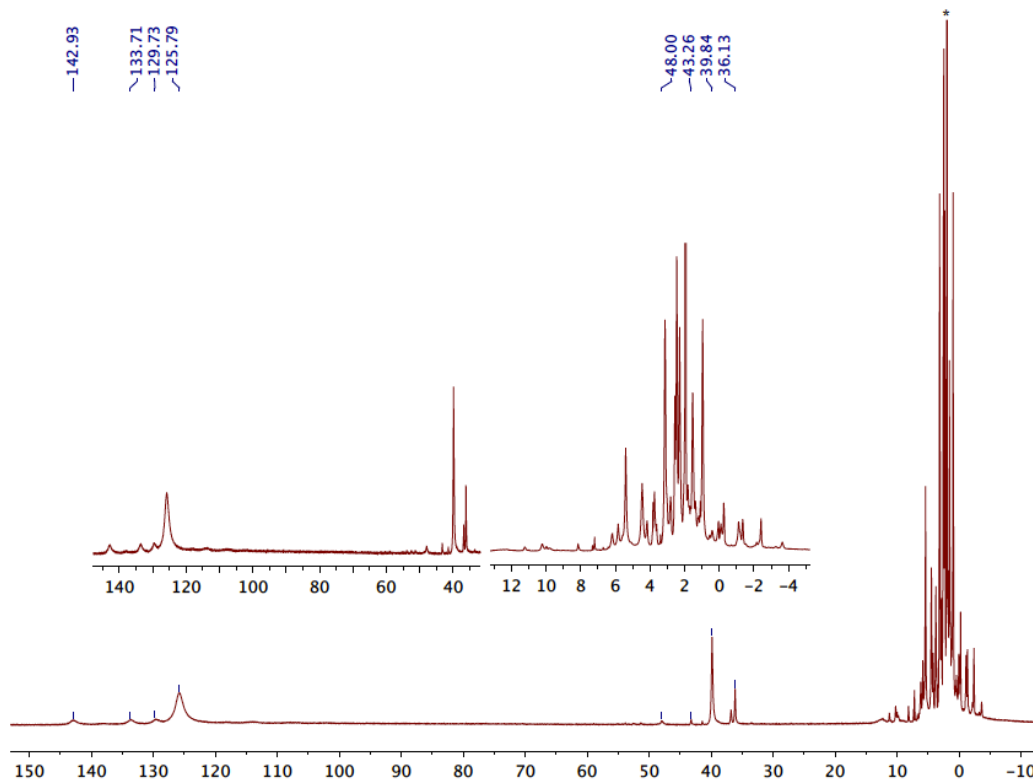
Figure 4.8 ^{1}H NMR spectrum of N($_{Br}$afa^{Cy})$_3$Fe(II)(OTf)$_2$ $_{Br}$L^{Cy}FeOTf$_2$ (500 MHz, CD$_3$CN, *residual solvent).

Deprotonation of $_H$L^{PhF}FeOTf$_2$ with Li$_2$O. N(afa^{PhF})$_3$Fe(OTf)$_2$ ($_H$L^{PhF}**FeOTf$_2$**) was generated in situ by combining Fe(OTf)$_2$ · 2 MeCN (21 mg, 0.048 mmol) and N(pi^{PhF})$_3$ (30 mg, 0.049 mmol) in tetrahydrofuran (5 mL). The mixture was stirred at room temperature for 1 h. Li$_2$O (3mg, 0.10 mmol, 2 equiv) was weighed by difference and added to the orange solution. The reaction was then stirred at room temperature overnight. The crude mixture was filtered to remove excess Li$_2$O and then dried under vacuum to remove solvent. The crude material was analyzed by ^{1}H and ^{19}F NMR spectroscopy in CD$_2$Cl$_2$, revealing a mixture of **[$_H$L^{PhF}Fe^{II}]$_2$** and $_H$L^{PhF}**Fe^{II}OH** with minor unidentified impurities.
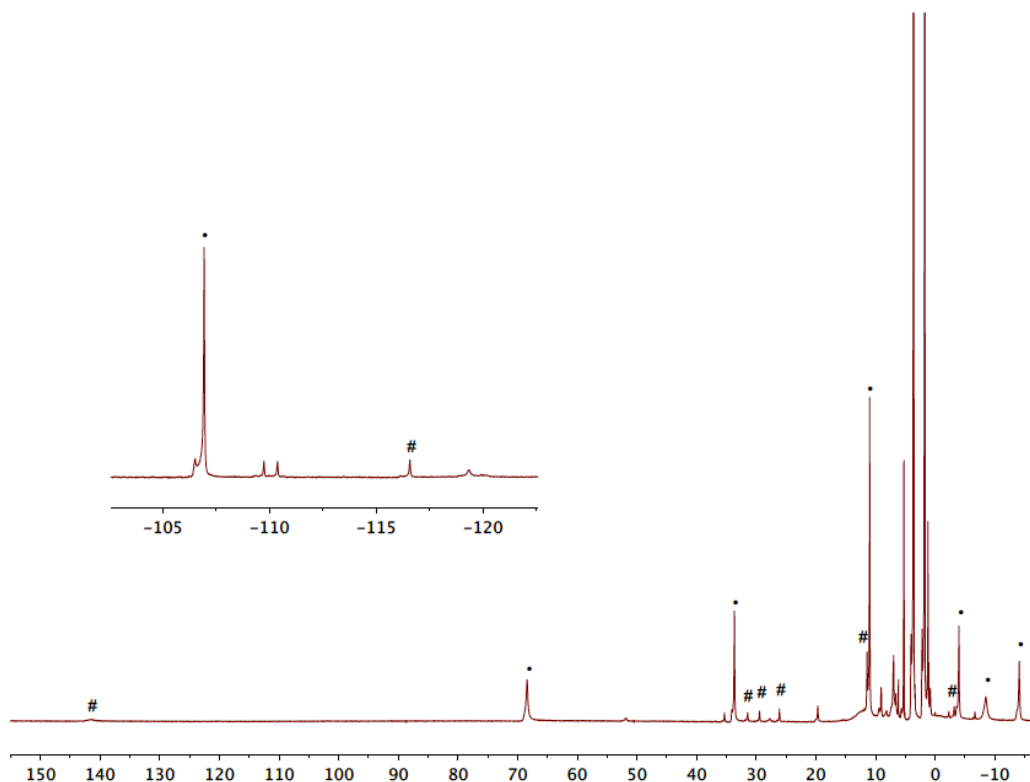
Figure 4.9 ^{1}H & ^{19}F (inset) NMR spectra of the crude product from reaction of $_H$L^{PhF}**FeOTf$_2$** with Li$_2$O (500 MHz (^{1}H), 471 MHz (^{19}F), CD$_3$CN, *residual solvent). Resonances marked with • correspond to **[$_H$L^{PhF}Fe^{II}]$_2$**; # correspond to $_H$L^{PhF}**Fe^{II}OH.**

88

Deprotonation of $_{Br}L^{Cy}FeOTf_2$ with Li$_2$O. N($_{Br}$afa^{Cy})$_3$Fe(OTf)$_2$ ($_{Br}L^{Cy}FeOTf_2$; 20 mg, 0.017 mmol) was dissolved in tetrahydrofuran (5 mL). Li$_2$O (1 mg, 0.033 mmol, 1.9 equiv) was weighed by difference and added to the biege solution. The reaction was then stirred at room temperature for overnight. The crude mixture was filtered to remove excess Li$_2$O and then dried under vacuum to remove solvent. The dried material was then redissolved in dichloromethane and filtered over a pad of Celite® to remove the LiOTf byproduct. Volatiles were removed in vacuo to yield $_{Br}L^{Cy}Fe^{II}OH$ (14 mg, 0.016 mmol, 94%). The product was confirmed to be the previously reported iron(II)-hydroxo complex,[24] N($_{Br}$pi^{Cy})($_{Br}$afa^{Cy})$_2$Fe(II)OH ($_{Br}L^{Cy}Fe^{II}OH$), by ^{1}H NMR spectroscopy.
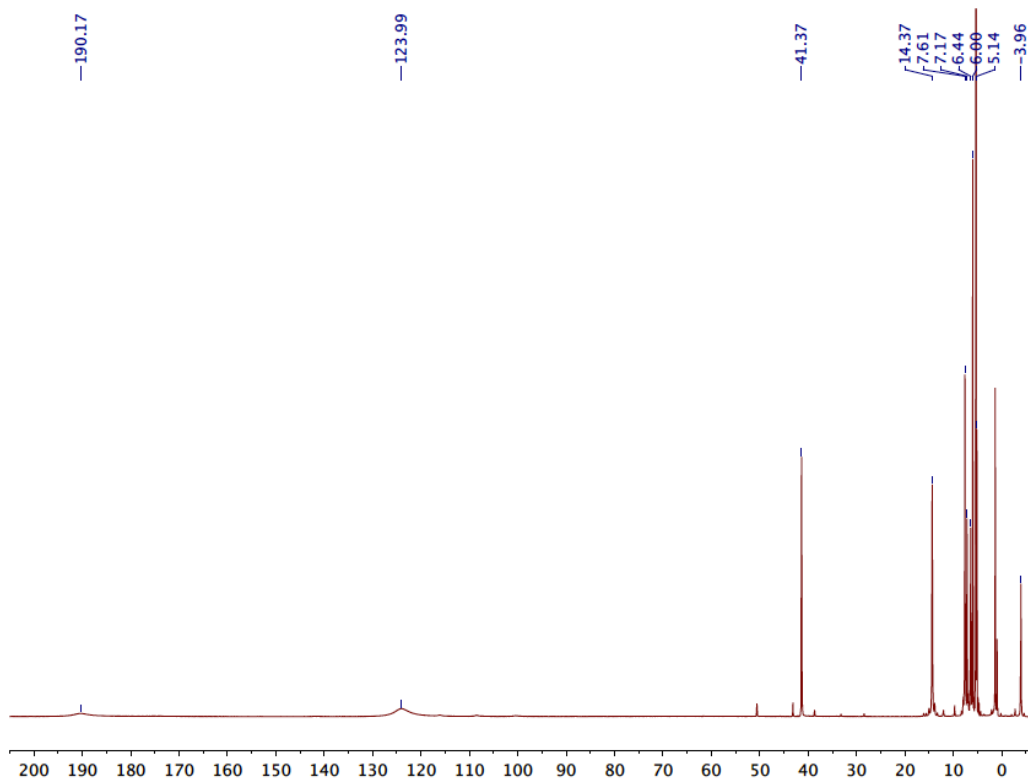
Figure 4.10 ^{1}H NMR spectrum of the crude product from reaction of $_{Br}L^{Cy}FeOTf_2$ with Li$_2$O (500 MHz, CD$_3$CN, *residual solvent). Selected resonances correspond to $_{Br}L^{Cy}Fe^{II}OH$.

Deprotonation of $_H$L^{PhF}Fe^{II}OH with potassium hydride. N(pi^{PhF})(afa^{PhF})$_2$Fe(II)OH ($_H$L^{PhF}Fe^{II}OH; 71 mg, 0.076 mmol), was suspended in acetonitrile (5 mL) and cooled to -35 ºC. Potassium hydride (KH; 3 mg, 0.076 mmol) was weighed by difference and added as a solid. The reaction was stirred at room temperature for 1 h, resulting in a gradual change from a brown-yellow suspension to a yellow-orange solution upon consumption of the insoluble base. After 1 h, the mixture was filtered over a pad of Celite® to remove any unreacted starting materials present. Volatiles were removed from the filtrate in vacuo to yield the aquo complex, K[N(pi^{PhF})$_3$Fe(II)OH$_2$] ($_H$L^{PhF}Fe^{II}OH$_2$; 51 mg, 0.070 mmol, 92%). Analysis for C$_{36}$H$_{29}$F$_3$FeKN$_7$O: Calcd. C, 59.43; H, 4.02; N, 13.48. Found C, 59.09; H, 3.91; N, 13.23. ^{1}H NMR (CD$_3$CN, 500 MHz): 10.07 (9H), 14.21 (6H), 29.41 (6H), 124.32 (6H), 185.79 (2H). ^{19}F NMR (CD$_3$CN, 471 MHz): δ= -118.55. IR ν_{max} = 1609 cm^{-1} (C=N). μ_{eff} = 5.18(6) μ_B.
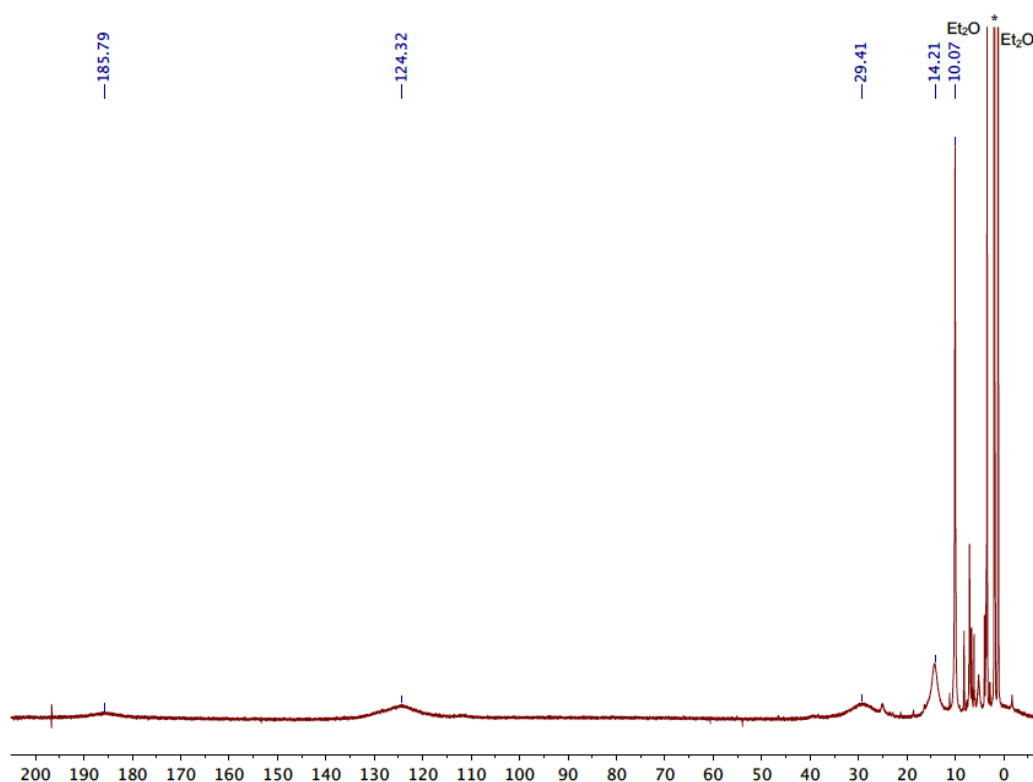
Figure 4.11 ^{1}H NMR spectra of K[N(pi^{PhF})$_3$Fe(II)OH$_2$] ($_H$L^{PhF}Fe^{II}OH$_2$) (500 MHz (^{1}H), 471 MHz (^{19}F), CD$_3$CN, *residual solvent).

Deprotonation of $_{Br}L^{Cy}Fe^{II}OH$ with potassium hydride. $N(_{Br}pi^{Cy})(_{Br}afa^{Cy})_2Fe(II)OH$ ($_{Br}L^{Cy}Fe^{II}OH$; 20 mg, 0.022 mmol), was suspended in acetonitrile (5 mL) and cooled to -35 °C. Potassium hydride (KH; 1 mg, 0.025 mmol) was weighed by difference and added as a solid. The reaction was stirred at room temperature for 1 h, resulting in a gradual change from a brown suspension to an orange solution upon consumption of the insoluble base. After 1 h, the mixture was filtered over a pad of Celite® to remove any unreacted starting materials present. Volatiles were removed from the filtrate in vacuo to yield the aquo complex, $K[N(_{Br}pi^{Cy})_3Fe(II)OH_2]$ ($_{Br}L^{Cy}Fe^{II}OH_2$; 19 mg, 0.020 mmol, 91%). Analysis for $C_{36}H_{47}Br_3FeKN_7O \cdot 0.5\ C_2H_3N$: Calcd. C, 46.83; H, 5.15; N, 11.07. Found C, 46.63; H, 4.99; N, 11.11. ^1H NMR (CD$_3$CN, 500 MHz, 21 °C): δ = -1.66 (3H), 4.36 (3H), 4.49 (6H), 5.14 (6H), 5.35 (6H), 5.68 (6H), 10.91 (6H), 44.57 (3H), 110.95 (6H), 207.80 (3H). IR v_{max} = 1611 cm^{-1} (C=N). μ_{eff} = 5.01(6) μ_B.
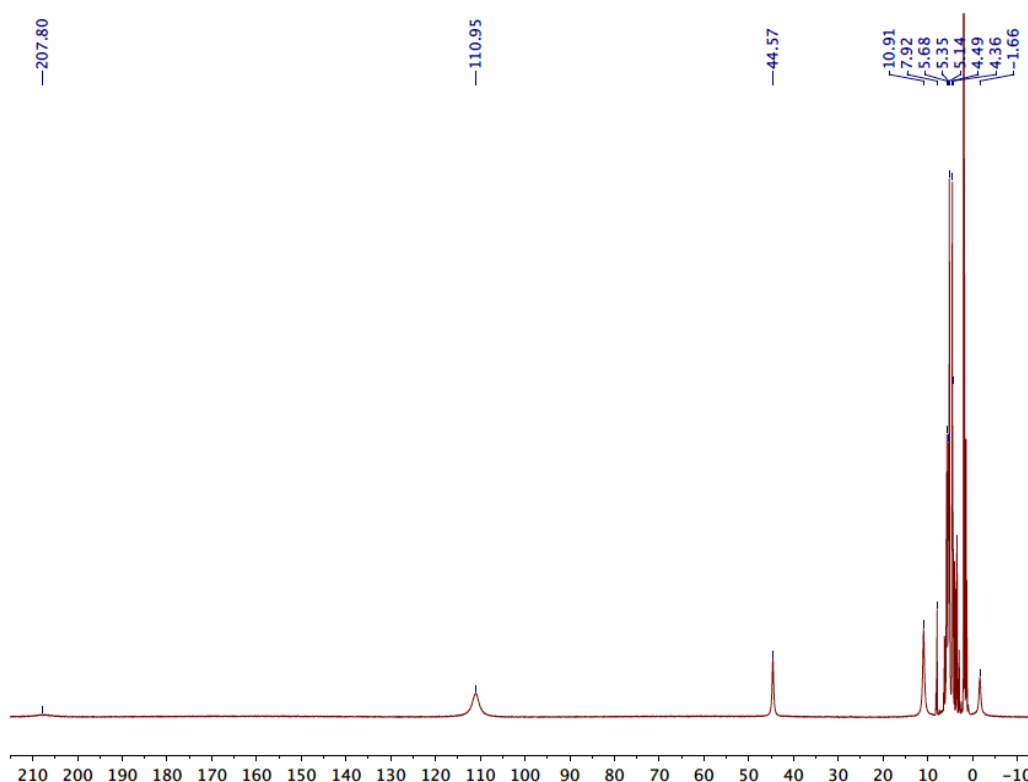
Figure 4.12 ^1H NMR spectrum of $K[N(_{Br}pi^{Cy})_3Fe(II)OH_2]$ ($_{Br}L^{Cy}Fe^{II}OH_2$) (500 MHz, CD$_3$CN, *residual solvent).

4.6 Additional figures and tables
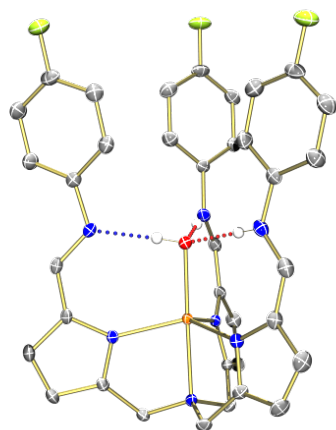
	$_HL^{Ph}Fe^{II}OH$	$_HL^{PhF}Fe^{II}OH$
Fe-O	2.0701(16)	2.0752(12)
Fe-N	2.235(2)	2.2405(17)
Fe-N$_{afa}$	2.0959(19)	2.0956(17)
Fe-N$_{pi}$	2.0845(18)	2.0815(17)
N$_{afa}$···O	2.671(3)	2.676(2)
N$_{pi}$···O	2.623(2)	2.632(2)
N$_{ave}$···O	2.655(3)	2.661(2)

Figure 4.13 Molecular structure of $_HL^{PhF}Fe^{II}OH$ shown with 50% probability ellipsoids (left). For clarity, only the amino and hydroxo protons are shown. Selected structural parameters for $_HL^{Ph}Fe^{II}OH$ (reproduced from Chapter 3) and $_HL^{PhF}Fe^{II}OH$ (right); bond lengths and distances are all listed in Å.
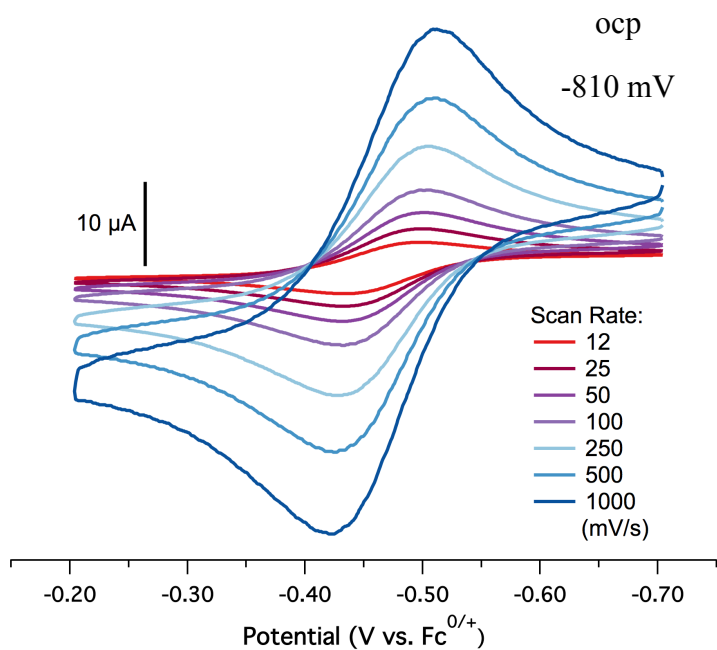
Scan Rate	ΔE_p
12	68
25	67
50	68
100	72
250	78
500	85
1000	85

Figure 4.14 Cyclic voltammograms showing the Fe(II/III) redox couple of $_HL^{PhF}Fe^{II}OH$ obtained for a 1 mM solution of the complex in a 1:1 THF/MeCN mixture with 0.1 M [$^nBu_4N$][PF_6] as supporting electrolyte (left); peak-to-peak separations (mV) (right).

4.7 References

(1)   Dawson, J. H. Probing Structure-Function Relations in Heme-Containing Oxygenases and Peroxidases. *Science* **1988**, *240* (4851), 433–439.

(2)   Jain, R.; Chan, M. Mechanisms of Ligand Discrimination by Heme Proteins. *J. Biol. Inorg. Chem.* **2003**, *8* (1-2), 1–11.

(3)   Fontecilla-Camps, J. C.; Volbeda, A.; Cavazza, C.; Nicolet, Y. Structure/Function Relationships of [NiFe]- and [FeFe]-Hydrogenases. *Chem. Rev.* **2007**, *107* (10), 4273–4303.

(4)   Natale, D.; Mareque-Rivas, J. C. The Combination of Transition Metal Ions and Hydrogen-Bonding Interactions. *Chem. Commun.* **2008**, *43* (4), 425–437.

(5)   Cook, S. A.; Hill, E. A.; Borovik, A. S. Lessons From Nature: a Bio-Inspired Approach to Molecular Design. *Biochemistry* **2015**, *54* (27), 4167–4180.

(6)   Rakowski DuBois, M.; DuBois, D. L. The Roles of the First and Second Coordination Spheres in the Design of Molecular Catalysts for H 2production and Oxidation. *Chem. Soc. Rev.* **2009**, *38* (1), 62–72.

(7)   Bullock, R. M.; Helm, M. L. Molecular Electrocatalysts for Oxidation of Hydrogen Using Earth-Abundant Metals: Shoving Protons Around with Proton Relays. *Acc. Chem. Res.* **2015**, 150616163350004–150616163350010.

(8)   Stolley, R. M.; Darmon, J. M.; Das, P.; Helm, M. L. Nickel Bis-Diphosphine Complexes: Controlling the Binding and Heterolysis of H 2. *Organometallics* **2016**, *35* (17), 2965–2974.

(9)   Borovik, A. S. Bioinspired Hydrogen Bond Motifs in Ligand Design: the Role of Noncovalent Interactions in Metal Ion Mediated Activation of Dioxygen. *Acc. Chem. Res.* **2005**, *38* (1), 54–61.

(10)   Shook, R. L.; Borovik, A. S. The Effects of Hydrogen Bonds on Metal-Mediated O_2 Activation and Related Processes. *Chem. Commun.* **2008**, *46*, 6095–6107.

(11)   Cook, S. A.; Borovik, A. S. Molecular Designs for Controlling the Local Environments Around Metal Ions. *Acc. Chem. Res.* **2015**, *48* (8), 2407–2414.

(12)   Blacquiere, J. M.; Pegis, M. L.; Raugei, S.; Kaminsky, W.; Forget, A.; Cook, S. A.; Taguchi, T.; Mayer, J. M. Synthesis and Reactivity of Tripodal Complexes Containing Pendant Bases. *Inorg. Chem.* **2014**, *53* (17), 9242–9253.

(13)   Meunier, B.; de Visser, S. P.; Shaik, S. Mechanism of Oxidation Reactions Catalyzed by Cytochrome P450 Enzymes. *Chem. Rev.* **2004**, *104* (9), 3947–3980.

(14)   Denisov, I. G.; Makris, T. M.; Sligar, S. G.; Schlichting, I. Structure and Chemistry of Cytochrome P450. *Chem. Rev.* **2005**, *105* (6), 2253–2278.

(15)   Rosenthal, J.; Nocera, D. G. Role of Proton-Coupled Electron Transfer in O–O Bond Activation. *Acc. Chem. Res.* **2007**, *40* (7), 543–553.

(16)   Soper, J. D.; Kryatov, S. V.; Rybak-Akimova, E. V.; Nocera, D. G. Proton-Directed Redox Control of O−O Bond Activation by Heme Hydroperoxidase Models. *J. Am. Chem. Soc.* **2007**, *129* (16), 5069–5075.

(17)   McGuire, R., Jr; Dogutan, D. K.; Teets, T. S.; Suntivich, J.; Shao-Horn, Y.; Nocera, D. G. Oxygen Reduction Reactivity of Cobalt(II) Hangman Porphyrins. *Chem. Sci.* **2010**, *1* (3), 411–414.

(18)   Carver, C. T.; Matson, B. D.; Mayer, J. M. Electrocatalytic Oxygen Reduction by Iron Tetra-Arylporphyrins Bearing Pendant Proton Relays. *J. Am. Chem. Soc.* **2012**, *134* (12), 5444–5447.

(19)   Matson, B. D.; Carver, C. T.; Ruden, Von, A.; Yang, J. Y.; Raugei, S.; Mayer, J. M. Distant Protonated Pyridine Groups in Water-Soluble Iron Porphyrin Electrocatalysts Promote Selective Oxygen Reduction to Water. *Chem. Commun.* **2012**, *48* (90), 11100–11103.

(20)   Rigsby, M. L.; Wasylenko, D. J.; Pegis, M. L.; Mayer, J. M. Medium Effects Are as Important as Catalyst Design for Selectivity in Electrocatalytic Oxygen Reduction by Iron-Porphyrin Complexes. *J. Am. Chem. Soc.* **2015**, *137* (13), 4296–4299.

(21)   Park, Y. J.; Matson, E. M.; Nilges, M. J.; Fout, A. R. Exploring Mn-O Bonding in the Context of an Electronically Flexible Secondary Coordination Sphere: Synthesis of a Mn(III)-Oxo. *Chem.*

Commun. **2015**, *51* (25), 5310–5313.

(22)   Matson, E. M.; Bertke, J. A.; Fout, A. R. Isolation of Iron(II) Aqua and Hydroxyl Complexes Featuring a Tripodal H-Bond Donor and Acceptor Ligand. *Inorg. Chem.* **2014**, *53* (9), 4450–4458.

(23)   Matson, E. M.; Park, Y. J.; Bertke, J. A.; Fout, A. R. Synthesis and Characterization of M(Ii) (M = Mn, Fe and Co) Azafulvene Complexes and Their X 3−Derivatives. *Dalton Trans.* **2015**, *44* (22), 10377–10384.

(24)   Gordon, Z.; Drummond, M. J.; Matson, E. M.; Bogart, J. A.; Schelter, E. J.; Lord, R. L.; Fout, A. R. Tuning the Fe(II/III) Redox Potential in Nonheme Fe(II)–Hydroxo Complexes Through Primary and Secondary Coordination Sphere Modifications. *Inorg. Chem.* **2017**, *56* (9), 4852–4863.

(25)   Hart, J. S.; White, F. J.; Love, J. B. Donor-Extended Tripodal Pyrroles: Encapsulation, Metallation, and H-Bonded Tautomers. *Chem. Commun.* **2011**, *47* (20), 5711–5713.

(26)   Hart, J. S.; Nichol, G. S.; Love, J. B. Directed Secondary Interactions in Transition Metal Complexes of Tripodal Pyrrole Imine and Amide Ligands. *Dalton Trans.* **2012**, *41* (19), 5785–4.

(27)   Matson, E. M.; Gordon, Z.; Lin, B.; Nilges, M. J.; Fout, A. R. Meridional vs. Facial Coordination Geometries of a Dipodal Ligand Framework Featuring a Secondary Coordination Sphere. *Dalton Trans.* **2014**, *43* (45), 16992–16995.

(28)   Hagadorn, J. R.; Que, L., Jr.; Tolman, W. B. N-Donor Effects on Carboxylate Binding in Mononuclear Iron(II) Complexes of a Sterically Hindered Benzoate Ligand. *Inorg. Chem.* **2000**, *39* (26), 6086–6090.

(29)   Klose, A.; Solari, E.; Floriani, C.; Chiesi-Villa, A.; Rizzoli, C.; Re, N. Magnetic Properties Diagnostic for the Existence of Iron(II)-Iron(II) Bonds in Dinuclear Complexes Which Derive From Stepwise Insertion Reactions on Unsupported Iron-Aryl Bonds. *J. Am. Chem. Soc.* **1994**, *116* (20), 9123–9135.

CHAPTER 5: CHARACTERIZATION OF TERMINAL IRON(III)-OXO AND IRON(III)-HYDROXO COMPLEXES DERIVED FROM O$_2$ ACTIVATION

5.1 Introduction

Activation of O$_2$ plays a critical role in biology, with dioxygen serving as a terminal electron acceptor or oxygen atom source in a wide array of oxidation processes. While many different enzymes are responsible for carrying out these types of reactions, a large number of them are iron-containing species that proceed through a common set of iron-oxygen intermediates.[1,2] Extensive work in the bio-mimetic subfield of inorganic chemistry has resulted in the development of a variety of synthetic systems, which have been used to successfully model iron-superoxo, iron-(hydro)peroxo, and iron-oxo intermediates.[3] In many of the enzymatic reactions, a high-valent iron-oxo intermediate serves as the active species in substrate oxidation. Thus the generation of reactive iron-oxo complexes has garnered significant attention. While these complexes have contributed greatly to the understanding of enzymatic processes, they are often synthesized using oxidants other than O$_2$, such as *m*-chloroperoxybenzoic acid (mCPBA), hydrogen peroxide (H$_2$O$_2$), alkyl hydroperoxides (ROOH), iodosobenzene (PhIO), or sodium hypochlorite (NaOCl).[4] Accordingly, the development of new systems capable of activating O$_2$ itself remains an area of interest. Goldberg has recently reviewed advances in the field, covering iron and manganese complexes with both heme and nonheme ligand architectures capable of activating dioxygen.[3]

In Nature, enzymes often rely on hydrogen-bonding interactions in the secondary coordination sphere and the extended protein superstructure to promote dioxygen activation.[5] The second sphere has been shown to contribute to enzymatic activity in multiple ways, including supporting reactive intermediates (See Chapter 1 for more detail). Borovik and coworkers demonstrated that incorporating hydrogen bonding in synthetic systems could have a similar effect, providing access to rare examples of high spin iron(III)- and iron(IV)-oxo complexes derived from O$_2$ activation.[6,7] Another important role of hydrogen bonding networks in biological O$_2$ activation is to facilitate the rapid and controlled delivery of protons to the active site. While this function has been observed for both heme[8,9] and nonheme[10] enzymes, the development of nonheme model systems that include proton relays in the second sphere remains an outstanding challenge.[11]

Drawing on these principles, we have designed a ligand that 1) contains hydrogen-bonds to mediate O$_2$ binding and activation; 2) acts as an intramolecular proton donor/acceptor to substrates; and 3) switches between two tautomeric forms, enabling proton transfers to and from the secondary coordination sphere without generating charged residues. We have previously demonstrated the ability of our tripodal ligand platform, tris(5-cyclohexyliminopyrrol-2-ylmethyl)amine (H$_3$[N(pi^{Cy})$_3$]), to tautomerize from the pyrrole-imine tautomer to the azafulvene-amine analog (H$_3$[N(afa^{Cy})$_3$]), depending on the substrate bound to and

oxidation state of the metal center.[12-16] We have also demonstrated that each arm of the ligand platform is capable of tautomerizing independently[12,14,16] and that the hydrogen-bonding in the secondary coordination sphere can facilitate the reduction of inorganic oxyanions, resulting in formation of an Fe(III)-oxo complex.[17,18] To expand on the previously observed reactivity and further explore the utility of the ligand framework in promoting small molecule activation, we investigated our system's ability to reduce dioxygen. Herein, we describe the chemical and electrochemical investigation into O_2 reduction by our previously reported $N(afa^{Cy})_3Fe(II)(OTf)_2$ complex.[12] Synthesis and characterization of terminal iron(III)-oxo and iron(III)-hydroxo complexes derived from O_2 activation are reported.

5.2 Synthesis of terminal Fe(III)-oxo and Fe(III)-hydroxo complexes from O_2 activation

Interested in exploring small molecule reactivity with our system, O_2 activation was investigated. In initial oxidation reactions, the iron(II)-triflate complex, $N(afa^{Cy})_3Fe(II)(OTf)_2$ (**1**), was exposed to an atmosphere of O_2. ^1H NMR spectroscopy of the crude material revealed a mixture of products including the Fe(III)-oxo, $[N(afa^{Cy})_3Fe(III)O]OTf$ (**2**), as well as multiple additional paramagnetic species and moderate amounts of diamagnetic material. The loss of a triflate counteranion from **2** to **1**, suggested that the diamagnetic species was potentially related to decomposition of an intermediate via protodemetallation. To assess the validity of this theory the free ligand, $N(pi^{Cy})_3$, was protonated with varying equivalents of triflic acid. The ^1H NMR spectrum for the triply protonated species, $N(pi^{Cy})_3 \cdot 3$ HOTf, matched well with the diamagnetic impurity present in the mixture of oxidation products (Scheme 5.1). After identifying this protodemetallation pathway, the reaction conditions were modified to suppress acid-induced decomposition. Addition of stoichiometric triethylamine prior to oxidation resulted in a clean reaction to give **2** in high yields (94%) with concomitant formation of triethylammonium triflate. Notably, both the protonated ligand and the additional paramagnetic species observed under the initial base-
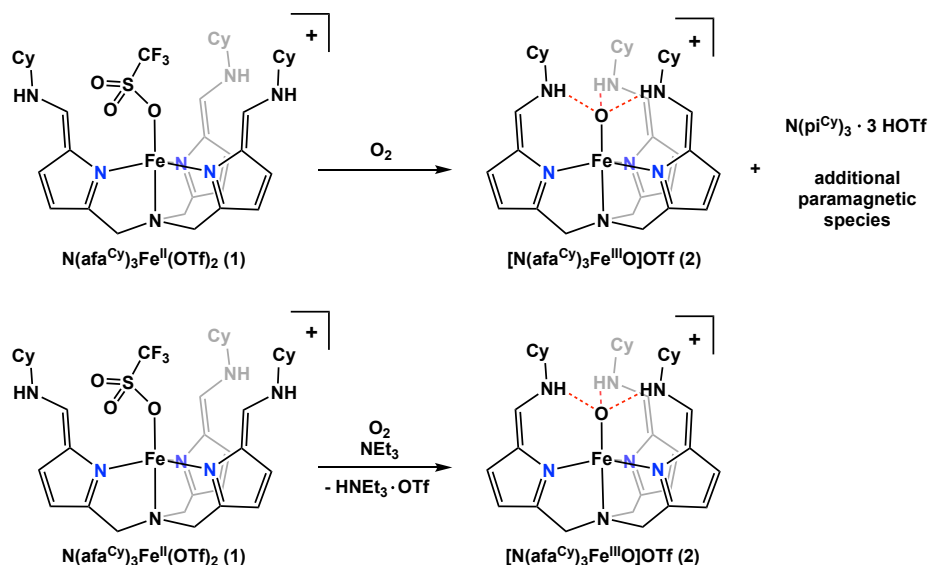
Scheme 5.1 O_2 activation by **1** under initial (base-free) and modified reaction conditions.

free conditions were no longer present, suggesting these other iron-containing products were related to the formation of triflic acid in solution.

Based on these results, independent synthesis of an Fe(III)-hydroxo complex was attempted to assess the relevance of such a species to the O_2 activation pathway that yields **2**. Treatment of the iron(III)-oxo with one equivalent of triflic acid resulted in the formation of one of the paramagnetic species previously observed under base-free oxidation conditions, as confirmed by ^{1}H NMR spectroscopy (See Figure 5.3 below). This protonated species is distinctly lower symmetry than **2**, based on the increased number of characteristic paramagnetic resonances in the downfield region of the ^{1}H NMR spectrum (four resonances are observed, compared to only two resonances for the C_3-symmetric Fe(III)-oxo complex (**2**)). Further characterization of the proposed Fe(III)-hydroxo by infrared spectroscopy was also consistent with a lower symmetry product, as indicated by the presence of two distinct C=N stretching modes ($\nu_{C=N}$ = 1640, 1667 cm^{-1}). Additionally, the increased intensity of the N–H stretching modes suggested at least one amino group in the secondary coordination sphere was no longer engaging in hydrogen-bonding with the iron-bound oxygen ligand, based on the similar behavior observed for the iron(II)-triflate complex (**1**) (Figure 5.1).
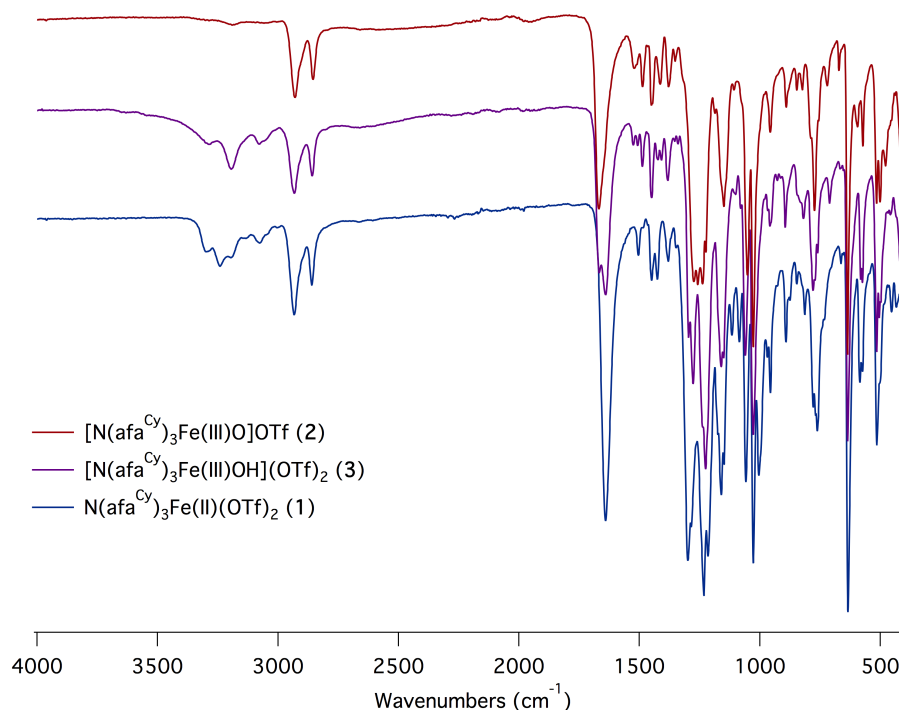
Figure 5.1 IR spectra for complexes **1-3**, demonstrating the lower symmetry and decreased hydrogen bonding in **3**.

To confirm the identity of this species, crystals suitable for X-ray analysis were grown from a concentrated solution of acetonitrile layered with diethyl ether. Structural refinement revealed distorted trigonal bipyramindal geometry about the iron center, comprised of the tripodal ligand framework with an axial

hydroxo bound trans to the apical nitrogen (Figure 5.2). Additionally, two outer-sphere triflate counter anions were present in the unit cell, one of which is hydrogen bonding to the metal bound hydroxide. Two arms of the ligand platform are oriented away from the pocket of the iron center (similar to the bind-

ing mode observed in **1**), as determined by the orientation of the N−H bonds, with one arm engaging in hydrogen bonding with the second outer-sphere triflate anion. The third arm is rotated inward towards the bound hydroxo, oriented so that the amino group serves as a hydrogen bond donor to the hydroxo (N5...O10: 2.671(5) Å) to stabilize the Fe(III)−OH species. The complex, $[N(afa^{Cy})_3Fe(III)OH](OTf)_2$ (**3**), has an Fe1−O10 bond distance of 1.840(3) Å, which is slightly elongated from **2** (Fe1−O10 1.8079(9))[17] and within the range of related terminal Fe(III)-OH species reported in the literature (1.831 – 1.926 Å).[19-22] We attrib-

ute the relatively short Fe1-O10 bond distance to the hydrogen-bonding between the hydroxo proton with an outer sphere triflate anion.[22]
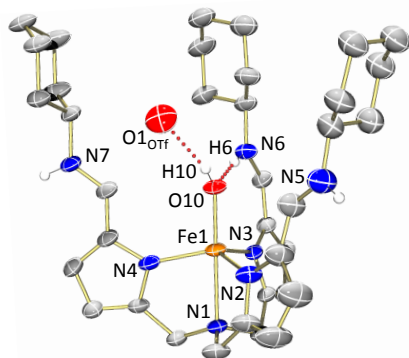
Figure 5.2 Molecular structure of **3** shown with 50% probability ellipsoids. For clarity, only the hydroxo and amino protons are shown; the outer sphere triflate hydrogen bonding to the hydroxo proton is abbreviated its relevant oxygen atom.

5.3 Deprotonation and acid-induced decomposition of $[N(afa^{Cy})_3Fe(III)OH](OTf)_2$ (3)

Given the well-established propensity of iron(IV)-oxo complexes to perform hydrogen atom abstraction,[23] we hypothesized that this iron(III)-hydroxo complex (**3**) may be formed through abstraction of a solvent H-atom by a higher valent intermediate during O_2 activation. **3** could then be converted to the final iron(III)-oxo product (**2**) by loss of an equivalent of triflic acid. Borovik previously reported the formation of a related Fe(III)-oxo complex from O_2 via an analogous mechanism, invoking H-atom abstraction by a transient Fe(IV)-oxo, resulting in the Fe(III) product.[6] To further assess the likelihood of this possible activation pathway deprotonation of **3** was pursued.

Treatment of **3** with triethylamine resulted in clean deprotonation of the complex to form **2**, as determined by ^{1}H NMR spectroscopy (Scheme 5.2). It is worth noting, however, that the Fe(III)-hydroxo complex is unstable in solution, slowly decomposing to give mixtures containing the protodemetallated ligand when no other base is present. Given the likely relevance of this decomposition process to the base-free oxidation reaction, a sample of **3** was heated to 50 ºC in a J Young tube and monitored by ^{1}H NMR spectroscopy to
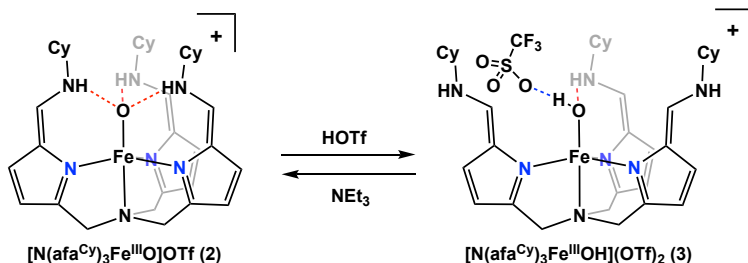
Scheme 5.2 Protonation of **2** to form **3** and the corresponding deprotonation to reform **2**.

aid in understanding the role of the acid. After 8 h, the sample showed partial conversion to a mixture of products including protodemetallated ligand, however no iron(III)-oxo formation was observed. Instead, the only apparent metal-containing product was the final paramagnetic species observed in the base-free oxidation reaction (Figure 5.3). Analysis of the isolated iron complex by IR spectroscopy gave a remarkably similar spectrum to the terminal Fe(III)-O complex, with the ligand bound in the azafulvene tautomer ($\nu_{C=N}$ = 1667 cm^{-1}). The main difference from **2** was an increase in the intensity of the N–H stretching modes, suggestive of fewer hydrogen bonding interactions.
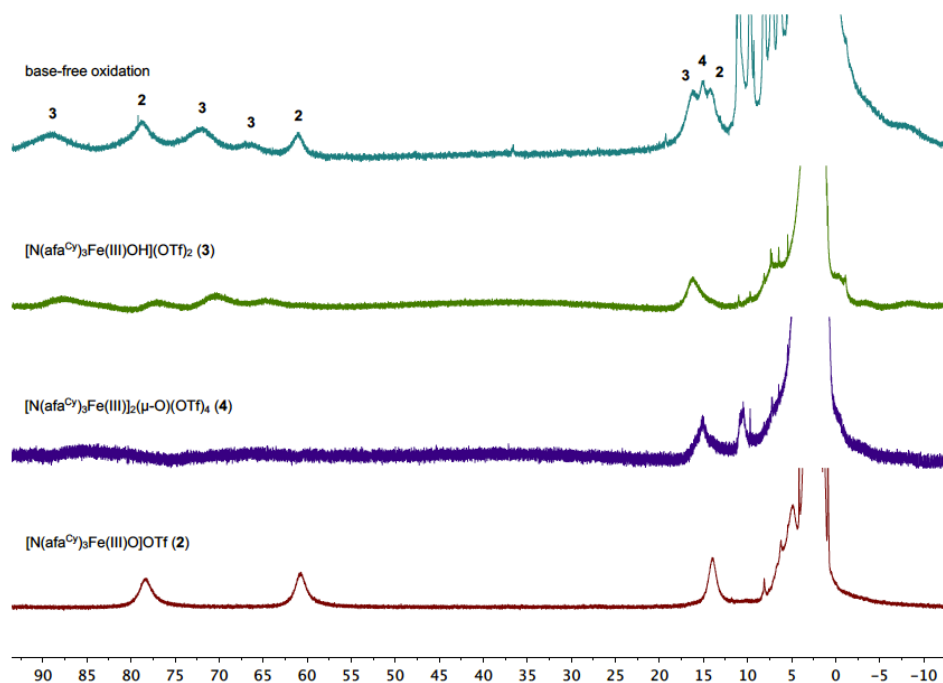
Figure 5.3 ^{1}H NMR spectra for the product mixture obtained from oxidation of **1** under base-free conditions (teal) and the independently synthesized components of the mixture: **3** (green), **4** (purple), **2** (red); (500 MHz, CD$_3$CN).

Further insights were gained from structural analysis of this complex. Vapor diffusion of diethyl ether into the CD$_3$CN solution provided crystals suitable for X-ray diffraction analysis. Refinement of the structural data revealed the decomposition product to be a bridged Fe(III)-oxo species, [N(afa^{Cy})$_3$Fe(III)]$_2$(μ-O)(OTf)$_4$ **(4)** (Figure 5.4). All three of the arms are bound in the azafulvene-amine tautomer for each ligand, however the amino groups in the secondary coordination sphere are all pointed away from the central oxo, con-
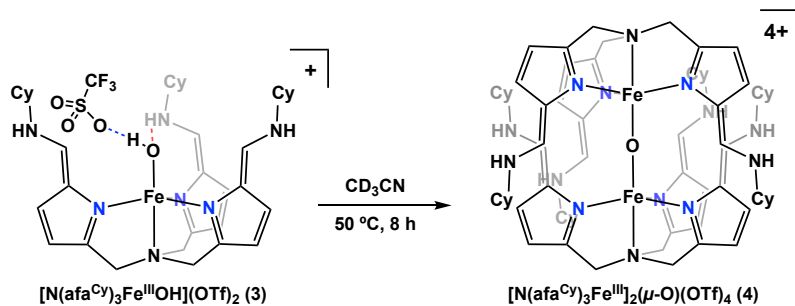
Scheme 5.3 Decomposition of **3** to yield **4**.

sistent with the interpretation of the IR spectrum. While we have not previously observed such a species with our ligand framework, the propensity of iron complexes to form [LFe(III)]$_2$(μ-O) dimers during O$_2$ activation is well established.[24]

5.4 Determining the role of the triflate anion in protodemetallation of the ligand

After characterizing the final species observed under base-free oxidation conditions (**4**), we sought to establish the relevance of these decomposition products to the productive O$_2$ activation pathway. Based on the hydrogen bond observed between the hydroxo ligand and one of the triflates in the structure of complex **3**, the role of the anion was examined. We reasoned that the hydrogen bonding could contribute heavily to the acid-induced decomposition observed by acting as a source of masked triflic acid. In an attempt to suppress this loss of acid, the triflate anions were exchanged in complex **1** for tetrakis[3,5-bis(trifluoromethyl)phenyl]borate (BArF$_{24}$). The increased steric bulk and relatively shielded negative charge of the BArF$_{24}$ anion was targeted to prevent hydrogen-bonding interactions that may promote loss of acid. The BArF$_{24}$ complex was synthesized by treating a suspension of **1** in diethyl ether with two equivalents of NaBArF$_{24}$, resulting in an immediate dissolution of the complex upon anion exchange. Analysis of the purified material by ^{19}F NMR spectroscopy confirmed complete anion exchange, showing only the expected BArF$_{24}$ resonance at -62.7 ppm.

Oxidation of [N(afa^{Cy})$_3$Fe(II)](BArF$_{24}$)$_2$ (**1-BArF**), was carried out by stirring an acetonitrile solution of the complex in air for 30 minutes. A ^{1}H NMR spectrum of the crude material showed the reaction formed primarily the terminal Fe(III)-oxo with minor Fe(III)-hydroxo and no bridged Fe(III)-oxo species present. These differences are consistent with the desired suppression of the acid-induced decomposition observed for the triflate complexes, indicating the triflate anion is largely responsible for the ligand protodemetallation and formation of the off-pathway bridged oxo species (**4**). Aside from preventing the formation of these decomposition products, the change in anion has no effect on the iron complex's reactivity towards O$_2$, suggesting it is not involved in the productive activation pathway.

Further evidence for this role of masked triflic acid in decomposition processes was provided by analysis of the BArF$_{24}$ analog of **3**. Treatment of the anion exchanged iron(III)-oxo complex, [N(afa^{Cy})$_3$Fe(III)O]BArF$_{24}$ (**2-BArF**), with an equivalent of Brookhart's acid yielded the analogous Fe(III)-OH species, [N(afa^{Cy})$_3$Fe(III)OH](BArF$_{24}$)$_2$ (**3-BArF**), as confirmed by ^{1}H NMR spectroscopy. This complex showed dramatically increased stability in a CD$_3$CN solution, with no signs of decomposition in the ^{1}H NMR spectrum after 24 h at room temperature and only minor protodemetallation after heating at 50 ºC for 8 h. Having established the role of the triflate anion in off-pathway decomposition processes, we returned to further analysis of the iron(III)-oxo complex.

5.5 Electrochemical oxidation of [N(afa^{Cy})$_3$Fe(III)O]OTf (2)

The redox properties of **2** were examined electrochemically to determine the accessibility of an iron(IV)-oxo complex with this ligand framework. Oxidation of **2** was first explored via cyclic voltammetry in a 1:1 THF/MeCN mixture, matching conditions used in the previous analysis of the reversible Fe(II)/(III) redox couple (E$_{1/2}$ = -0.69 V vs. Fc$^{0/+}$).[16] Sweeping the oxidative region of the voltammogram revealed an irreversible event at E$_{pa}$ = 0.70 V vs. Fc$^{0/+}$ (Figure 5.4). This oxidation occurs at a substantially more positive potential than Borovik's Fe(III)-oxo (E$_{1/2}$ = -0.90 V);[7] the disparity is attributed to the electronic differences in the ligand binding modes (neutral vs. trianionic). The irreversible nature of the oxidation event for complex **2** suggests that an Fe(IV)-oxo species may be transiently accessible, but undergoes a chemical change upon oxidation.

To aid in the assignment of this oxidation event, several control complexes were synthesized and electrochemically analyzed to explore the role of both oxygen ligand basicity and the redox-active metal center in the oxidation observed for complex **2**: [N(afa^{Cy})$_3$Fe(II)F]BF$_4$ (**5**), [N(afa^{Cy})$_3$Zn(II)F]BF$_4$ (**6**), N(pi^{Cy})(afa^{Cy})$_2$Zn(II)OH (**7**) (see Experimental section for synthetic details). Cyclic voltammetry for the iron(II)-fluoride complex (**5**) showed a single pseudo-reversible redox event, which was assigned as the Fe(II)/(III) couple. The zinc(II)-fluoride complex (**6**) show no events in its cyclic voltammogram, as would be expected for the redox inactive metal center. Intriguingly, analysis of the zinc(II)-hydroxo complex (**7**) shows two irreversible oxidation events (E$_{pa1}$ = 0.27 V and E$_{pa2}$ = 0.71 V vs. Fc$^{0/+}$). The second of which aligns well with the oxidation potential of **2** (E$_{pa}$ = 0.70 V). These results suggest that the oxo ligand (or the hydroxo ligand in the case of **7**) plays an important role in facilitating the oxidation process, while the metal center may be less involved.

Figure 5.4 Cyclic voltammograms for the iron(III)-oxo (**2**) and a series of control complexes **5**-**7** obtained for 1 mM solutions of the complex in a 1:1 THF/MeCN mixture with 0.1 M [^{n}Bu$_4$N][PF$_6$] as supporting electrolyte (scan rate 0.1 V/sec).

The iron(III)-hydroxo complex, [N(afa^{Cy})$_3$Fe(III)OH](OTf)$_2$ (**3**), was analyzed as a last point of comparison (Figure 5.5). The cyclic voltammogram for **3** showed a reversible Fe(II)/(III) couple centered at E$_{1/2}$ = -0.37 V, a positive shift of 0.32 V from the iron(III)-oxo (**2**). Interestingly, continuing to scan in the negative direction resulted in a second event at E$_{pc}$ = -0.71 V, which is well aligned with the reduction potential for **2**, suggesting **3** may be partially deprotonated upon reduction. Sweeping the oxidative region of the voltammogram revealed a baseline feature, which again aligned well with the analogous oxi-

Figure 5.5 Cyclic voltammograms for the iron(III)-hydroxo (**3**) and iron(III)-oxo (**2**) complexes obtained for 1 mM solutions of the complex in a 1:1 THF/MeCN mixture with 0.1 M [$^nBu_4N$][PF_6] as supporting electrolyte (scan rate 0.1 V/sec).

dation event in **2**. Given the minimal current of this feature, relative to the Fe(II)/(III) redox couple, it is assigned to a minor amount of **2** present following reduction. To confirm this assignment, the experiment was repeated with an initial scan in the positive direction. The oxidation feature is absent on the first scan, confirming that it is formed following reduction and does not represent an iron(III)-oxo impurity present in the bulk solution. It is also worth noting that the iron(III)-oxo (**2**) shows similar behavior, where a minor pre-feature matching the reduction potential of the iron(III)-hydroxo (**3**) is observed prior to the Fe(III)/(II) couple on the second scan, after sweeping the oxidation event. Taken together with the controls described for complexes **5-7**, the electrochemical analysis of **3** once again highlights the importance of proton (or hydrogen atom) transfer to the bound oxo substrate in facilitating the oxidation of **2**. In cases where the central ligand cannot accept a proton from the secondary coordination sphere no oxidation event was observed (complexes **3**, **5**, **6**). Furthermore, the comparison of the iron(III)-oxo (**2**) and iron(III)-hydroxo (**3**) complexes was consistent with the hypothesis that **3** results from H-atom abstraction by a higher valent intermediate in the O_2 activation process.

As a final point of analysis, oxidation of **2** was examined using spectroelectrochemical methods. If electrochemical one-electron oxidation of **2** resulted in the formation of a meta-stable iron(IV)-oxo complex, then the UV-visible absorption spectrum would be expected to contain a near-IR feature (λ_{max} = ~700-900 nm) characteristic of such species.[4] Although analysis of the oxidized species showed no observable feature in the near-IR region, there were significant differences in the UV absorption features, consistent with formation of a new species at potentials above the observed oxidation event (E_{pa} = 0.70 V).

Borovik and coworkers have recently demonstrated that hydrogen bonding interactions can result in the absence of a near-IR absorption for an iron(IV)-oxo complex.[25] Accordingly, DFT analysis was used to simulate the UV-visible spectrum of the iron(IV)-oxo complex, [N(afa^{Cy})$_3$Fe(IV)O]$^{2+}$. Previous work has demonstrated the ability of this computational method to successfully reproduce the absorption spectra of the iron(II)-hydroxo and iron(III)-oxo complexes in our system.[16] Spectra were computed for the optimized iron(IV)-oxo model, as well as complexes with constrained Fe–O bond lengths of 1.60 Å and 1.80 Å. All three of these species are predicted to give prominent features in the visible range, as would be

expected for an iron(IV)-oxo complex. While it is difficult to prove the absence of these near-IR absorptions in the spectroelectrochemical data, given their low molar absorptivity, significant deviations were also noted in the UV features, suggesting that an alternative oxidation product is accessed electrochemically.

Based on our proposed mechanism for the O_2 activation reaction, we hypothesized that the species observed may be the iron(III)-hydroxo complex, resulting from hydrogen-atom abstraction by a transient iron(IV)-oxo. Analysis of $[N(afa^{Cy})_3Fe(III)OH](OTf)_2$ (**3**) by UV-visible absorption spectrometry revealed a good match

Figure 5.6 UV-visible spectra related to the electrochemical oxidation of the iron(III)-oxo complex (**2**). The black trace corresponds to **2** prior to oxidation; the purple trace was collected while applying a potential held beyond the oxidation event; the green trace shows a normalized spectrum for the iron(III)-hydroxo complex (**3**) collected independently. All spectra were collected in MeCN.

to the electrochemically oxidized species (Figure 5.6). Chemical oxidation of the iron(III)-oxo complex (**2**) provided further support for this assignment. Treating a cold acetonitrile solution of **2** with a stock solution of $NOBF_4$ resulted in conversion to the iron(III)-hydroxo complex ($[N(afa^{Cy})_3Fe(III)OH]X_2$, X =
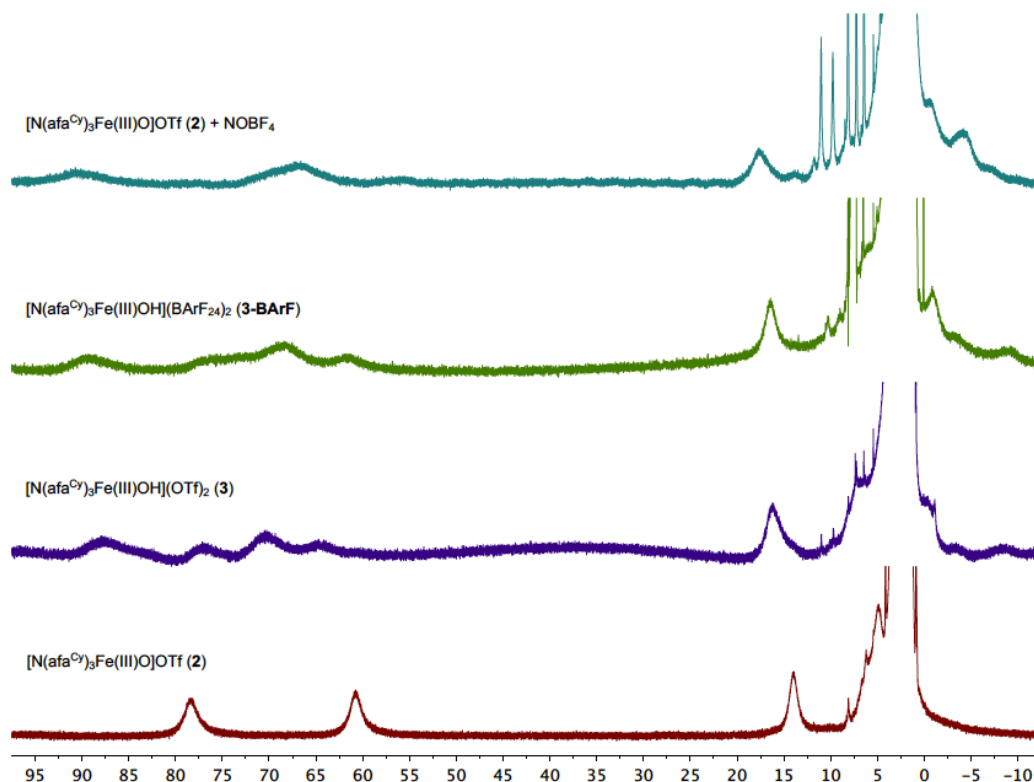
Figure 5.7 ^{1}H NMR spectra for the crude product of $NOBF_4$ oxidation of **2** (teal) and the isolated iron(III) species **3-BArF** (green), **3** (purple), **2** (red); (500 MHz, CD$_3$CN).

OTf/BF$_4$, **3-X**), as determined by ^{1}H NMR spectroscopy (Figure 5.7). The lack of any observed intermediates in these oxidation processes precluded further analysis of the putative iron(IV)-oxo intermediate, however, the formation of **3-X** following one-electron oxidation of **2** is once again consistent with the proposed hydrogen atom abstraction step in the O$_2$ activation pathway.

5.6 Conclusion

O$_2$ activation by an iron(II)-triflate, N(afa^{Cy})$_3$Fe(OTf)$_2$ (**1**), has been described. Initial reaction conditions lead to a mixture of oxidized species that were identified as the terminal iron(III)-oxo ([N(afa^{Cy})$_3$Fe(III)O]OTf, **2**), terminal iron(III)-hydroxo ([N(afa^{Cy})$_3$Fe(III)OH](OTf)$_2$, **3**), and bridging iron(III)-oxo complexes ([N(afa^{Cy})$_3$Fe(III)]$_2$(μ-O)(OTf)$_4$, **4**), following independent synthesis of each species. Formation of the bridging oxo complex (**4**) was determined to result from an off-pathway decomposition process following the loss of acid from **3**, which also produced protodemetallated ligand. This acid-induced decomposition was attributed to hydrogen bonding between the hydroxo proton and a triflate anion in complex **3**, providing a source of masked triflic acid. Replacing the OTf anions with BArF$_{24}$ was confirmed to suppress the decomposition pathway by preventing this hydrogen bonding interaction in the oxidized species.

Electrochemical analysis of the iron(III)-oxo (**2**) and iron(III)-hydroxo (**3**) complexes suggested that **3** resulted from H-atom abstraction by an iron(IV)-oxo intermediate formed immediately following O–O bond cleavage. Further evidence for this proposal came from investigation of a series of control compounds, which demonstrated the importance of proton transfer to the bound oxo in facilitating one-electron oxidation of these species.

Attempts to access the one-electron
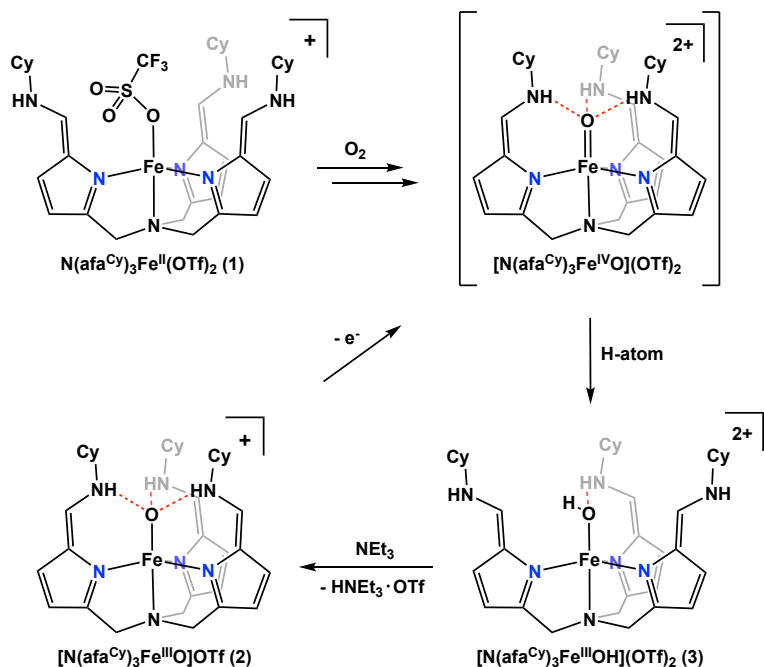
Scheme 5.4 Proposed pathway to yield complexes **2** and **3** following O$_2$ activation by **1**.

oxidized species resulted instead in the formation of the iron(III)-hydroxo complex (**3**). While these results precluded detailed analysis of the oxidized species, tentatively assigned as an iron(IV)-oxo, it provided further support for the proposed role of hydrogen atom abstraction in the formation of **3**. These experiments offer insight into the potential role of the secondary coordination sphere in facilitating O$_2$

activation, suggesting ligand dynamics play a key role in accessing high-valent intermediates with this framework.

5.7 Experimental section

General Considerations. All manipulations were carried out in the absence of water and dioxygen using standard Schlenk techniques, or in an MBraun inert atmosphere drybox under a dinitrogen atmosphere except where specified otherwise. All glassware was oven dried for a minimum of 8 h and cooled in an evacuated antechamber prior to use in the drybox. Solvents were dried and deoxygenated on a Glass Contour System (SG Water USA, Nashua, NH) and stored over 4 Å molecular sieves purchased from Strem following literature procedure prior to use. Acetonitrile-d_3 and dichloromethane-d_2 were purchased from Cambridge Isotope Labs and stored over 4 Å molecular sieves prior to use. Trifluoromethylsulfonic acid (triflic acid) was purchased from Sigma Aldrich and used as received. Triethylamine was purchased from Sigma Aldrich, degassed by three freeze-pump-thaw cycles, and stored over 4 Å molecular sieves prior to use. Oxygen gas was purchased from Airgas and used as received. $[N(afa^{Cy})_3FeOTf]OTf$ was prepared according to literature procedure.[2] Celite® 545 (J. T. Baker) and Tetrabutylammonium hexafluorophosphate (Sigma Aldrich) were dried in Schlenk flasks for 24 h under dynamic vacuum while heating to at least 150℃, prior to use in a drybox. NMR spectra were recorded on a Varian spectrometer operating at 500 MHz (^{1}H NMR), 471/377 MHz (^{19}F NMR), or 126 MHz (^{13}C NMR). All ^{1}H and ^{13}C chemical shifts (ppm) are reported relative to the resonance of the residual solvent as a standard; ^{19}F chemical shifts are reported relative to an external standard of 1% $CFCl_3$ in $CDCl_3$ as a reference. Solid-state infrared spectra were recorded using a PerkinElmer Frontier FT-IR spectrophotometer equipped with a KRS5 thallium bromide/iodide universal attenuated total reflectance accessory. Elemental analyses were performed by the University of Illinois at Urbana-Champaign School of Chemical Sciences Microanalysis Laboratory in Urbana, IL. Electrospray ionization mass spectrometry (MS-ESI) was recorded on a Water Q-TOF Ultima ESI instrument.

Cyclic Voltammetry. Electrochemical experiments were carried out using a CH Instruments CHI410C Electrochemical Workstation. The supporting electrolyte was 0.1 M [^{n}Bu$_4$N][PF$_6$] in a 1:1 acetonitrile/tetrahydrofuran mixture. A glassy carbon working electrode, a platinum wire counter electrode, and a silver wire pseudo reference electrode were used. The concentration of each analyte was ~1 mM. Experiments were performed at a scan rate of 100 mV/s. Each scan was referenced to internal Fc$^{0/+}$.

Spectroelectrochemistry. *Equipment.* All spectroelectrochemical experiments were performed using a CH Instruments (Austin, TX) 1201B mini-potentiostat. A Pt mesh working electrode and Pt wire counter electrode were both flame cleaned prior to use. All potentials are listed versus a 0.1 M Ag/Ag$^+$ reference electrode. UV-vis spectra during electrochemical measurements were collected using a SEC2000 spectrometer (ALS Co., Japan) equipped with a 1 mm path length quartz spectro-electrochemical cuvette.

105

Method. The quartz cuvette was filled with a blank electrolyte solution that contained only acetonitrile and supporting salt (0.1 M [^{n}Bu$_4$N][PF$_6$]), for purposes of collecting a background UV-vis spectra between 215-900nm. Subsequently, the blank electrolyte solution was removed and replaced with an acetonitrile solution containing supporting electrolyte (0.1 M [^{n}Bu$_4$N][PF$_6$]) and the iron(III)-oxo complex, [N(afa^{Cy})$_3$Fe(III)O]OTf (**2**; 0.2 mM). Solutions were prepared in an inert atmosphere glovebox to minimize amounts of moisture and any dissolved oxygen. A UV-vis spectrum of the samples were taken before initiating any electrochemical measurements in order to capture spectral qualities of only the reduced state. After identifying a potential region of interest, cyclic voltammetry was employed at a slow scan rate of 2 mV/s in order to give time for the sample to completely convert between oxidation states during electrolysis in the small volume of the spectro-electrochemical cell. Complete UV-vis spectra were collected every 60 seconds, which after accounting for the potential scan rate corresponds to spectral data points at 120 mV intervals in the voltammogram. Post experiment data analysis is used to identify specific spectral qualities that only appear in the oxidized or reduced states of the material. A UV-vis spectrum of the oxidized species was obtained by applying a potential just beyond the oxidation event for 60 seconds prior to collecting the spectrum. The degree of electrochemical reversibility is also inferred by comparing the initial and final UV-vis spectra.

Oxidation of [N(afa^{Cy})$_3$Fe(II)OTf]OTf (1) under base-free conditions. [N(afa^{Cy})$_3$Fe(II)OTf]OTf (**1**) (0.015 g, 0.034 mmol) was dissolved in 5 mL MeCN giving a golden yellow solution. The vial was sealed with a 14/20 septum and tape, and then removed from the glovebox. A standard balloon attached to a syringe barrel was filled with O$_2$ and injected through the septum with a needle. The atmosphere was purged with O$_2$, resulting in a gradual color change to dark brown with solvation of the suspended material. The mixture was stirred at room temperature for one hour to ensure completion. The reaction was degassed and dried under vacuum on a Schlenk line. The resulting residue was returned to the glovebox and analyzed by ^{1}H NMR spectroscopy without further purification.

Preparation of [N(afa^{Cy})$_3$Fe(III)O]OTf (2) via O$_2$ activation. *a) Using O$_2$ gas as the oxidant*: A 20 mL scintillation vial was charged with [N(afa^{Cy})$_3$Fe(II)OTf]OTf (**1**) (0.034 g, 0.036 mmol), triethylamine (0.004 g, 0.040 mmol), and approximately 5 mL of dichloromethane, giving a yellow slurry. The vial was sealed with a 14/20 septum and tape, and then removed from the glovebox. A standard balloon attached to a syringe barrel was filled with O$_2$ and injected through the septum with a needle. The atmosphere was purged with O$_2$, resulting in a gradual color change to dark brown with solvation of the suspended material. The mixture was stirred at room temperature for one hour to ensure completion. The reaction was degassed and dried under vacuum on a Schlenk line. The resulting residue was returned to the glovebox for purification. Crude material was redissolved in minimal dichloromethane; product was precipitated with diethyl ether (~10 mL), filtered to remove the triethylammonium triflate byproduct, and

washed with fresh diethyl ether (~10 mL). The precipitate was collected with dichloromethane and dried in vacuo to yield the final product (0.027 g, 0.034 mmol, 94%). The product was confirmed to be the previously reported iron(III)-oxo complex,[9] [N(afa^{Cy})$_3$Fe(III)O]OTf (**2**), by ^{1}H NMR spectroscopy. ^{1}H NMR (reproduced from ref. 17) (CD$_3$CN, 500 MHz, 21 °C): δ = 1.41-2.96, 5.02, 14.26, 61.65, 79.52.

b) Using air as the oxidant: A 20 mL scintillation vial was charged with [N(afa^{Cy})$_3$Fe(II)OTf]OTf (**1**) (0.025 g, 0.027 mmol), triethylamine (0.003 g, 0.030 mmol), and approximately 5 mL of dichloro-methane, giving a yellow slurry. The vial was then removed from the glovebox and exposed to air, giving a gradual color change to dark brown upon solvation of the suspended material. The mixture was stirred at room temperature for one hour to ensure completion. The solution was concentrated by rotary evapora-tion to a volume of approximately 1 mL. Product was precipitated with diethyl ether (~10 mL), filtered to remove the triethylammonium triflate byproduct, and finally washed with fresh diethyl ether (~10 mL). The washed precipitate was collected with dichloromethane and dried in vacuo to yield the final product, [N(afa^{Cy})$_3$Fe(III)O]OTf (**2**) (0.020 g, 0.025 mmol, 93 %), as confirmed by ^{1}H NMR spectroscopy.

Preparation of N(pi^{Cy})$_3$ · 3 HOTf. A 20 mL scintillation vial was charged with N(pi^{Cy})$_3$ (0.011 g, 0.019 mmol) and approximately 5 mL of acetonitrile. The resulting suspension was cooled to -35 ºC. Cold triflic acid (stored at -35 ºC; 0.009 g, 0.060 mmol) was weighed by difference and added to the sus-pension. The reaction was stirred at room temperature, resulting in the gradual dissolution of the ligand upon protonation, giving a yellow solution. After stirring for 20 minutes, solvent was removed in vacuo to yield the product, N(pi^{Cy})$_3$ · 3 HOTf, as a yellow powder (0.020 g, 0.019 mmol, quantitative). Analysis for C$_{39}$H$_{54}$F$_9$N$_7$O$_9$S$_3$ · H$_2$O: Calcd. C, 44.61; H, 5.38; N, 9.34. Found C, 44.81; H, 5.11; N, 9.25. LR-MS-ESI (M$^+$) *m/z* calc. for H[N(pi^{Cy})$_3$ · 2HOTf]$^+$, 882.4, found 882.3. ^{1}H NMR (CD$_3$CN, 400 MHz, 21 °C): δ= 1.18 - 2.05 (m, 30H, Cy-C*H*), 3.65 (m, 3H, Cy-C*H*), 3.78 (s, 6H, methylene-C*H$_2$*), 6.45 (d, *J* = 4, 3H, pyr-C*H*), 7.23 (d, *J* = 4, 3H, pyr-C*H*), 8.11 (s, 3H, imine-C*H*), 9.70 (br, s, 3H, pyr-N*H*), 10.99 (br, s, 3H, imine-N$^+$*H*). ^{13}C NMR (CD$_3$CN, 126 MHz, 21 ºC): δ= 25.14, 25.56, 33.03, 52.69, 62.40, 115.57, 120.32, 122.86, 123.67, 147.15, 152.36. IR ν$_{max}$ = 1660 cm^{-1} (C=N).

Preparation of [N(afa^{Cy})$_3$Fe(III)OH](OTf)$_2$ (3). A 20 mL scintillation vial was charged with **2** (0.042 g, 0.052 mmol) and approximately 5 mL of tetrahydrofuran. The resulting suspension was frozen at -196 ºC. A slight excess of cold triflic acid (stored at -35 ºC; 0.011 g, 0.073 mmol) was weighed by difference and added to the frozen suspension. The reaction was stirred at room temperature for approximately 3 minutes, resulting in the gradual dissolution of the starting material upon protonation, giving a dark red-brown solution. After full dissolution of the solid material, solvent was removed in vacuo. Analytically pure sample was isolated by recrystallization from a concentrated acetonitrile solution of the crude mate-rial layered with diethyl ether. Both solvents were cooled to -35 ºC prior to use and the crystallization was carried out at this temperature over several days. Because of complex **3**'s instability to loss of acid,

an extra drop of triflic acid (0.005 g, 0.033 mmol) was added to the acetonitrile prior to use as the crystallization solvent. $[N(afa^{Cy})_3Fe(III)OH](OTf)_2$ (**3**) was collected as dark brown crystalline material (0.024 g, 0.025 mmol, 48%). Analysis for $C_{38}H_{52}N_7FeO_7F_6S_2$: Calcd. C, 47.90; H, 5.50; 10.29. Found C, 47.78; H, 5.69; N, 10.20. ^{1}H NMR (CD$_3$CN, 500 MHz, 21 °C): δ = -8.47, -3.49, 16.21, 64.69, 70.25, 77.15, 87.80. IR ν_{max} = 1640, 1667 cm^{-1} (C=N).

Preparation of $[N(afa^{Cy})_3Fe(III)O]OTf$ (2) by deprotonation of 3. A 20 mL scintillation vial was charged with **3** (0.017 g, 0.018 mmol) and approximately 3 mL of acetonitrile, the resulting dark brown solution was cooled to -35 °C. Triethylamine (0.002 g, 0.020 mmol) was weighed into a vial and dissolved in cold acetonitrile (~1 mL). Dropwise addition of the triethylamine solution resulted in a slight fading of the solution's color, giving a lighter brown. The reaction was stirred at room temperature for 30 minutes, and then dried in vacuo. Analysis of the crude residue by ^{1}H NMR spectroscopy revealed quantitative conversion to **2** with concurrent formation of [HNEt$_3$]OTf (δ= 1.25, 3.15, 7.01 ppm).

Preparation of $[N(afa^{Cy})_3Fe(III)]_2(\mu\text{-}O)(OTf)_4$ (4) via decomposition of 3. A J Young tube was charged with **3** (0.013 g, 0.014 mmol) and approximately 1 mL of acetonitrile-d$_3$. The sample was heated to 50 °C for 8 h while monitoring the decomposition by ^{1}H NMR spectroscopy. Although only partial conversion was observed after 8 h, further heating was found to result primarily in increased formation of $N(pi^{Cy})_3 \cdot 3$ HOTf, not the desired metal complex. The sample was taken back into the glovebox and set to crystallize by vapor diffusion of diethyl ether into the CD$_3$CN solution yielding crystals suitable for X-ray diffraction were grown under the same conditions. Analysis for $C_{76}H_{102}F_{12}Fe_2N_{14}O_{13}S_4 \cdot 2\ H_2O$: Calcd. C, 47.45; H, 5.55; 10.19. Found C, 47.56; H, 5.48; N, 9.81. IR ν_{max} = 1667 cm^{-1} (C=N).

Preparation of $[N(afa^{Cy})_3Fe(II)](BArF_{24})_2$ (1-BArF) via anion exchange of 1. A 20 mL scintillation vial was charged with **1** (0.052 g, 0.056 mmol) and approximately 5 mL of diethyl ether. The yellow suspension was treated with 2 equivalents of sodium tetrakis[3,5-bis(trifluoromethyl)phenyl]borate (NaBArF$_{24}$; 0.097 g, 0.109 mmol)**,** resulting in an immediate dissolution of the material upon successful anion exchange. After 30 min, the reaction was filtered over a small pad of Celite® to remove residual starting material, then solvent was removed in vacuo. The crude material was redissolved in dichloromethane and filtered again to remove the NaOTf byproduct. After drying the filtrate, the product was dissolved in minimal Et$_2$O and diluted with hexanes (~5 mL) to facilitate drying. The dried material was triturated with additional hexanes as necessary to yield **1-BArF** as a yellow powder (0.129 g, 0.055 mmol, 98%). Analysis for $C_{100}H_{75}B_2F_{48}FeN_7$: Calcd. C, 50.80; H, 3.20; 4.15. Found C, 50.43; H, 3.33; N, 4.16. ^{19}F NMR (CD$_3$CN, 377 MHz, 21 °C): δ = -62.68. IR ν_{max} = 1643 cm^{-1} (C=N). μ_{eff} = 5.62(5) μ_B.

Preparation of $[N(afa^{Cy})_3Fe(III)O]BArF_{24}$ (2-BArF) via anion exchange of 2. A 20 mL scintillation vial was charged with **2** (0.042 g, 0.052 mmol) and approximately 5 mL of diethyl ether. The brown suspension was treated with sodium tetrakis[3,5-bis(trifluoromethyl)phenyl]borate (NaBArF$_{24}$; 0.046 g,

0.052 mmol), resulting in an immediate dissolution of the material upon successful anion exchange. After 30 min, the reaction was filtered over a small pad of Celite® to remove residual starting material, then solvent was removed in vacuo. The crude material was redissolved in dichloromethane and filtered again to remove the NaOTf byproduct. After drying the filtrate, the product was dissolved in minimal Et_2O and diluted with hexanes (~5 mL) to facilitate drying. The dried material was triturated with additional hexanes as necessary to yield **2-BArF** as a brown powder (0.079 g, 0.052 mmol, quantitative). Analysis for $C_{68}H_{63}BF_{24}FeN_7O \cdot 0.5 \ C_4H_{10}O$: Calcd. C, 54.10; H, 4.41; 6.31. Found C, 54.05; H, 4.16; N, 6.01. ^{19}F NMR (CD_3CN, 471 MHz, 21 °C): δ = -63.45. IR ν_{max} = 1669 cm^{-1} (C=N). μ_{eff} = 6.04(6) μ_B.

Preparation of [N(afa^{Cy})$_3$Fe(III)OH](BArF$_{24}$)$_2$ (3-BArF). A 20 mL scintillation vial was charged with **2-BArF** (0.030 g, 0.020 mmol) and approximately 5 mL of diethyl ether. The resulting brown solution was cooled to -35 °C, then treated with Brookhart's acid, [H(OEt$_2$)$_2$]BArF$_{24}$, (0.020 g, 0.020 mmol). After 5 min, the reaction was diluted with hexanes, then solvent was removed in vacuo. The dried material was triturated with additional hexanes as necessary to yield **3-BArF** as a brown powder (0.046 g, 0.019 mmol, 95%). Analysis for $C_{100}H_{76}B_2F_{48}FeN_7O$: Calcd. C, 50.44; H, 3.22; 4.12. Found C, 49.94; H, 3.31; N, 4.15. ^{1}H NMR (CD_3CN, 500 MHz, 21 °C): δ = -9.14, -3.41, -0.84, 7.66, 7.69, 16.44, 61.56, 68.50, 75.55, 88.92. IR ν_{max} = 1642, 1664 cm^{-1} (C=N).

Preparation of [N(afa^{Cy})$_3$Fe(II)F]BF$_4$ (5). A 20 mL scintillation vial was charged with FeCl$_2$ (0.009 g, 0.071 mmol) and approximately 5 mL of acetonitrile. The suspension was treated with 2 equivalents of AgBF$_4$ (0.027 g, 0.14 mmol), resulting in a gradual consumption of the starting material with generation of a fluffy white precipitate (AgCl) upon anion exchange. After stirring for 30 min, the reaction was filtered over a pad of Celite® to remove the AgCl. The colorless filtrate was then cooled to -35 °C. N(pi^{Cy})$_3$ (0.038 g, 0.065 mmol) was weighed by difference and added as a solid, giving a gradual change to an orange solution. The reaction was stirred for an additional hour, then dried in vacuo. The crude material was dissolved in acetonitrile then crystallized by vapor diffusion of diethyl ether into the solution. [N(afa^{Cy})$_3$Fe(II)F]BF$_4$ (**5**) was collected as an orange crystalline solid (0.034 g, 0.046 mmol, 71%). ^{1}H NMR (CD_2Cl_2, 500 MHz, 21 °C): δ = 5.03, 5.66, 6.46, 6.78, 8.32, 13.11, 27.71, 28.39, 72.39, 138.78. IR ν_{max} = 1655 cm^{-1} (C=N).

Preparation of [N(afa^{Cy})$_3$Zn(II)F]BF$_4$ (6). A 20 mL scintillation vial was charged with ZnCl$_2$ (0.008 g, 0.059 mmol) and approximately 5 mL of acetonitrile. The suspension was treated with 2 equivalents of AgBF$_4$ (0.024 g, 0.12 mmol), resulting in a gradual consumption of the starting material with generation of a fluffy white precipitate (AgCl) upon anion exchange. After stirring for 30 min, the reaction was filtered over a pad of Celite® to remove the AgCl. The colorless filtrate was then cooled to -35 °C. N(pi^{Cy})$_3$ (0.034 g, 0.059 mmol) was weighed by difference and added as a solid, giving a gradual change to a cloudy tan solution. The reaction was stirred for an additional hour, then dried in vacuo. The crude mate-

rial was dissolved in acetonitrile then crystallized by vapor diffusion of diethyl ether into the solution. [N(afa^{Cy})$_3$Zn(II)F]BF$_4$ (**6**) was collected as a tan crystalline solid (0.036 g, 0.048 mmol, 81%). ^{1}H NMR (CD$_3$CN, 500 MHz, 21 °C): δ = 1.17 (q, 3H, J = 12.9 Hz), 1.41 (q, 6H, J = 12.9 Hz), 1.51 (q, 6H, J = 12.0 Hz), 1.80 (d, 6H, J = 13.3 Hz), 1.92 (d, 6H, J = 13.3 Hz), 2.12 (d, 6H, J = 10.6 Hz), 3.41 (m, 3H), 3.83 (s, 6H), 6.30 (d, 3H, J = 3.9 Hz), 7.13 (d, 3H, J = 3.9 Hz), 7.51 (dd, 3H, J = 14.9, 6.7 Hz), 11.13 (br d, 3H). IR v_{max} = 1650 cm^{-1} (C=N).

Preparation of N(afa^{Cy})$_3$Zn(II)OH (7). A 20 mL scintillation vial was charged with N(pi^{Cy})$_3$ · H$_2$O (0.055 g, 0.092 mmol) and approximately 5 mL of tetrahydrofuran. The resulting biege solution was cooled to -35 ºC, then treated with 2 equivalents of benzyl potassium (KBn; 0.025 g, 0.192 mmol). After stirring for 30 min, the solution was again cooled to -35 ºC. ZnCl$_2$ was then added as a solid (0.013 g, 0.095 mmol) and the reaction was allowed to stir for an additional hour. After stirring, solvent was removed in vacuo. The dried material was taken up in dichloromethane and filtered over a pad of Celite® to remove the KCl formed during the reaction. The filtrate was concentrated in vacuo, then diluted with hexanes to precipitate the product, which was collected in a pipet filter and washed with a second portion of fresh hexanes (~5 mL). Solid was collected with dichloromethane and dried to yield N(afa^{Cy})$_3$Zn(II)OH (**7**) as an off-white powder (0.055 g, 0.083 mmol, 90%). Analysis for C$_{36}$H$_{51}$N$_7$OZn · 0.3 CH$_2$Cl$_2$: Calcd. C, 63.31; H, 7.55; 14.24. Found C, 63.24; H, 7.20; N, 13.88. ^{1}H NMR (CDCl$_3$, 500 MHz, 21 ºC) δ 1.17 (qt, J = 13.0, 3.6 Hz, 3H), 1.35 (qt, J = 13.2, 3.5 Hz, 6H), 1.60 (qd, J = 12.8, 3.6 Hz, 6H), 1.74 (dddd, J = 11.7, 5.2, 3.4, 1.7 Hz, 3H), 1.85 (dt, J = 13.8, 3.4 Hz, 6H), 1.90 – 1.99 (m, 6H), 3.13 (tq, J = 11.4, 3.6 Hz, 3H), 3.77 (s, 6H), 6.07 (d, J = 3.4 Hz, 3H), 6.69 (d, J = 3.4 Hz, 3H), 7.61 (d, J = 6.3 Hz, 3H), 13.37 (dd, J = 6.3, 2.8 Hz, 3H). IR v_{max} = 1626, 1659 cm^{-1} (C=N).

5.8 References

(1)   Poulos, T. L. Heme Enzyme Structure and Function. *Chem. Rev.* **2014**, *114* (7), 3919–3962.

(2)   Solomon, E. I.; Goudarzi, S.; Sutherlin, K. D. O$_2$ Activation by Non-Heme Iron Enzymes. *Biochemistry* **2016**, *55* (46), 6363–6374.

(3)   Sahu, S.; Goldberg, D. P. Activation of Dioxygen by Iron and Manganese Complexes: a Heme and Nonheme Perspective. *J. Am. Chem. Soc.* **2016**, *138* (36), 11410–11428.

(4)   McDonald, A. R.; Que, L., Jr. High-Valent Nonheme Iron-Oxo Complexes: Synthesis, Structure, and Spectroscopy. *Coord. Chem. Rev.* **2013**, *257* (2), 414–428.

(5)   Shook, R. L.; Borovik, A. S. The Effects of Hydrogen Bonds on Metal-Mediated O$_2$ Activation and Related Processes. *Chem. Commun.* **2008**, *46*, 6095–6107.

(6)   MacBeth, C. E.; Golombek, A. P.; Young, V. G.; Yang, C.; Kuczera, K.; Hendrich, M. P.; Borovik, A. S. O$_2$ Activation by Nonheme Iron Complexes: a Monomeric Fe(III)-Oxo Complex Derived From O$_2$. *Science* **2000**, *289* (5481), 938–941.

(7)   Lacy, D. C.; Gupta, R.; Stone, K. L.; Greaves, J.; Ziller, J. W.; Hendrich, M. P.; Borovik, A. S. Formation, Structure, and EPR Detection of a High Spin Fe^{IV}-Oxo Species Derived From Either an Fe^{III}-Oxo or Fe^{III}-OH Complex. *J. Am. Chem. Soc.* **2010**, *132* (35), 12188–12190.

(8)   Meunier, B.; de Visser, S. P.; Shaik, S. Mechanism of Oxidation Reactions Catalyzed by Cytochrome P450 Enzymes. *Chem. Rev.* **2004**, *104* (9), 3947–3980.

(9)   Denisov, I. G.; Makris, T. M.; Sligar, S. G.; Schlichting, I. Structure and Chemistry of Cyto-

chrome P450. *Chem. Rev.* **2005**, *105* (6), 2253–2278.

(10)   Kovaleva, E. G.; Rogers, M. S.; Lipscomb, J. D. Structural Basis for Substrate and Oxygen Activation in Homoprotocatechuate 2,3-Dioxygenase: Roles of Conserved Active Site Histidine 200. *Biochemistry* **2015**, *54* (34), 5329–5339.

(11)   Blacquiere, J. M.; Pegis, M. L.; Raugei, S.; Kaminsky, W.; Forget, A.; Cook, S. A.; Taguchi, T.; Mayer, J. M. Synthesis and Reactivity of Tripodal Complexes Containing Pendant Bases. *Inorg. Chem.* **2014**, *53* (17), 9242–9253.

(12)   Matson, E. M.; Bertke, J. A.; Fout, A. R. Isolation of Iron(II) Aqua and Hydroxyl Complexes Featuring a Tripodal H-Bond Donor and Acceptor Ligand. *Inorg. Chem.* **2014**, *53* (9), 4450–4458.

(13)   Matson, E. M.; Park, Y. J.; Bertke, J. A.; Fout, A. R. Synthesis and Characterization of M(Ii) (M = Mn, Fe and Co) Azafulvene Complexes and Their X 3−Derivatives. *Dalton Trans.* **2015**, *44* (22), 10377–10384.

(14)   Park, Y. J.; Matson, E. M.; Nilges, M. J.; Fout, A. R. Exploring Mn-O Bonding in the Context of an Electronically Flexible Secondary Coordination Sphere: Synthesis of a Mn(III)-Oxo. *Chem. Commun.* **2015**, *51* (25), 5310–5313.

(15)   Matson, E. M.; Gordon, Z.; Lin, B.; Nilges, M. J.; Fout, A. R. Meridional vs. Facial Coordination Geometries of a Dipodal Ligand Framework Featuring a Secondary Coordination Sphere. *Dalton Trans.* **2014**, *43* (45), 16992–16995.

(16)   Gordon, Z.; Drummond, M. J.; Matson, E. M.; Bogart, J. A.; Schelter, E. J.; Lord, R. L.; Fout, A. R. Tuning the Fe(II/III) Redox Potential in Nonheme Fe(II)–Hydroxo Complexes Through Primary and Secondary Coordination Sphere Modifications. *Inorg. Chem.* **2017**, *56* (9), 4852–4863.

(17)   Matson, E. M.; Park, Y. J.; Fout, A. R. Facile Nitrite Reduction in a Non-Heme Iron System: Formation of an Iron(III)-Oxo. *J. Am. Chem. Soc.* **2014**, *136* (50), 17398–17401.

(18)   Ford, C. L.; Park, Y. J.; Matson, E. M.; Gordon, Z.; Fout, A. R. A Bioinspired Iron Catalyst for Nitrate and Perchlorate Reduction. *Science* **2016**, *354* (6313), 741–743.

(19)   MacBeth, C. E.; Gupta, R.; Mitchell-Koch, K. R.; Young, V. G.; Lushington, G. H.; Thompson, W. H.; Hendrich, M. P.; Borovik, A. S. Utilization of Hydrogen Bonds to Stabilize M−O(H) Units: Synthesis and Properties of Monomeric Iron and Manganese Complexes with Terminal Oxo and Hydroxo Ligands. *J. Am. Chem. Soc.* **2004**, *126* (8), 2556–2567.

(20)   Çelenligil-Çetin, R.; Paraskevopoulou, P.; Dinda, R.; Staples, R. J.; Sinn, E.; Rath, N. P.; Stavropoulos, P. Synthesis, Characterization, and Reactivity of Iron Trisamidoamine Complexes That Undergo Both Metal- and Ligand-Centered Oxidative Transformations. *Inorg. Chem.* **2008**, *47* (3), 1165–1172.

(21)   Mukherjee, J.; Lucas, R. L.; Zart, M. K.; Powell, D. R.; Day, V. W.; Borovik, A. S. Synthesis, Structure, and Physical Properties for a Series of Monomeric Iron(III) Hydroxo Complexes with Varying Hydrogen-Bond Networks. *Inorg. Chem.* **2008**, *47* (13), 5780–5786.

(22)   Cook, S. A.; Ziller, J. W.; Borovik, A. S. Iron(II) Complexes Supported by Sulfonamido Tripodal Ligands: Endogenous Versus Exogenous Substrate Oxidation. *Inorg. Chem.* **2014**, *53* (20), 11029–11035.

(23)   Engelmann, X.; Monte-Pérez, I.; Ray, K. Oxidation Reactions with Bioinspired Mononuclear Non-Heme Metal-Oxo Complexes. *Angew. Chem. Int. Ed.* **2016**, *55* (27), 7632–7649.

(24)   Kurtz, D. M. Oxo- and Hydroxo-Bridged Diiron Complexes: a Chemical Perspective on a Biological Unit. *Chem. Rev.* **1990**, *90* (4), 585–606.

(25)   Hill, E. A.; Weitz, A. C.; Onderko, E.; Romero-Rivera, A.; Guo, Y.; Swart, M.; Bominaar, E. L.; Green, M. T.; Hendrich, M. P.; Lacy, D. C.; Borovik, A. S. Reactivity of an Fe(IV)-Oxo Complex with Protons and Oxidants. *J. Am. Chem. Soc.* **2016**, *138* (40), 13143–13146.

CHAPTER 6: SYNTHESIS AND METALLATION OF TRIPODAL LIGANDS FEATURING PHENOXY GROUPS IN THE SECONDARY COORDINATION SPHERE

6.1 Introduction

Redox active amino acid (e.g. tyrosine and tryptophan) often play critical role in biological charge transfer reactions.[1,2] These residues are located in the secondary coordination sphere of metalloenzymes where they can facilitate metal-centered reactivity through proton-coupled electron transfer (PCET).[3,4] Such interactions are critical to a range of biological processes, including small molecule activation. For example, the generation of tyrosyl radicals has been demonstrated in O_2 reduction by cytochrome *c* oxidase as well as water oxidation by the oxygen-evolving complex of photosystem II.[5-7] In both of these enzymes, the controlled movement of four protons and four electrons to or from the active site is essential for productive reactivity. Given the success of this approach in promoting multi-proton and multi-electron reactions in biological systems, the development of synthetic model systems that incorporate similar functionalities in the ligand framework represents an attractive target.

Despite their ubiquity in Nature, synthetic complexes with secondary sphere hydroxy/phenoxy groups remain rare. A notable example is Naruta's use of binaphthol functionalized "twin coronet" porphyrin systems.[8,9] The hydroxy groups in the secondary coordination sphere have been demonstrated to contribute significantly to the properties and reactivity of these heme systems (see Chapter 1 for details). Furthermore, generation of the aryloxyl radical was demonstrated to play a role in mediating oxygenation of a 1,4-diene substrate by the heme complex.[10] Szymczak has developed a related nonheme ligand framework with second sphere hydroxy groups by incorporating a 2-pyridone motif, which tautomerizes upon metallation to give a 2-hydroxypyridine.[11,12] The hydroxy groups in this system have been shown to facilitate small molecule activation through PCET, mimicking the role of amino acid radicals in biology.[13] In an effort to develop new systems featuring similar functionalities in the secondary coordination sphere, the synthesis and metallation of nonheme ligands was pursued, based on elaboration of tris(2-aminoethyl)amine (tren). This report describes several generations of the ligand framework, detailing their syntheses and metallation with late first row transition metals.

6.2 Synthesis and metallation of tren-based ligands functionalized with hydroxybenzamide groups

The first generation of the ligand framework was developed based on a benzamide functionality appended to the commercially available tris(2-aminoethyl)amine (tren) chelate. The amide functionality was chosen to provide a rigid linker between the desired primary and secondary coordination spheres, keeping the phenoxy groups appropriately positioned to interact with substrates bound to the metal center. 3-hydroxybenzoic acid was coupled with tren to form the amide ligand, tris{2-[(3-hydroxybenzoyl)amino]ethyl}amine ($^{3OH}L_{amide}$), via activation of the acid with diisopropylcarbodiimide

(DIC). A number of metallations were attempted with this ligand, primarily using metal complexes with endogenous bases, such as $[M^{II}(N(TMS)_2)_2]_2$ species (TMS = trimethylsilyl). Unfortunately, the products yielded in these reactions were insoluble in all glove box solvents, showing minimal solubility even in high polarity solvents such as *N,N*-dimethylformamide (DMF) or *N,N*-dimethylacetamide (DMA), precluding their characterization.

In an effort to increase the solubility of the ligand framework and determine the accessibility of the desired coordination geometry, the methoxy ligand analog was synthesized tris{2-[(3-methoxybenzoyl)amino]ethyl}amine ($^{3OMe}L_{amide}$). Deprotonation of $^{3OMe}L_{amide}$ was achieved by addition of three equivalents of lithium hexamethyldisilazide (LiN(SiMe$_3$)$_2$). The trianionic lithium salt was then metallated with cobalt(II) chloride (CoCl$_2$) (Scheme 6.1). While the product still suffered from low solubility, single crystals were successfully grown from vapor diffusion of diethylether (Et$_2$O) into a DMA solution of the complex. Refinement of the X-ray diffraction data resulted in a structural model consistent with the cobalt center bound in a four-coordinate, trigonal monopyramidal geometry (Li[$^{3OMe}L_{amide}$Co], **1**). All four nitrogen donors are coordinated as desired, with a vacant coordination site trans to the apical nitrogen donor. The methoxy groups are all rotated away from the metal, however, rendering interpretation of potential hydrogen bonding interactions speculative. Although Li[$^{3OMe}L_{amide}$Co] provided evidence for the desired coordination of the metal center, it was unclear if the intended

Scheme 6.1 Metallation of $^{3OMe}L_{amide}$ to form complex **1**.

binding pocket would be accessible in ligands with protic functionalities in the secondary coordination sphere, given the use of a strong base to deprotonate the amide nitrogens.
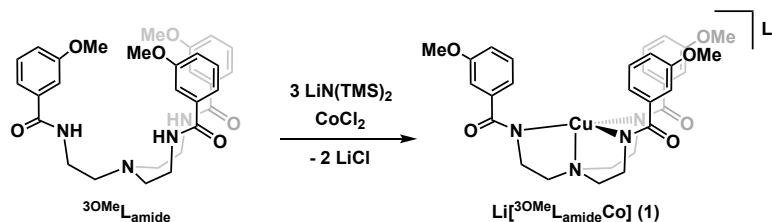
6.3 Synthesis and metallation of tren-based ligands functionalized with hydroxybenzylidene groups

In the second generation of the ligand framework, the amide linker was reduced to a more soluble imine functionality. The redesigned ligand was intended to maintain the rigid connection between primary and secondary coordination spheres, while providing neutral donors in the tren base, which could be datively coordinated to avoid deprotonation of the phenoxy groups during metallation. The imine ligand derivatives were synthesized via condensation of tren with three equivalents of the desired aldehyde (see experimental section for details).

6.3.1 Dative coordination of the 3-hydroxy ligand variant

Initial studies were carried out using the 3-hydroxy ligand variant, tris{2-[(3-hydroxybenzylidene)amino]-ethyl}amine ($^{3OH}L_{imine}$). Dative coordination of the ligand was achieved by treating the ligand with copper(I) bromide in a THF/DMA mixture (~5 : 1) (Scheme 6.2). Single crystals

of the complex were grown by vapor diffusion of Et$_2$O into a filtered reaction aliquot. The resulting molecular structure showed the desired trigonal monopyramidal coordination of the metal center, with an outer sphere bromide anion, [^{3OH}L$_{imine}$Cu]Br (**2**). While this
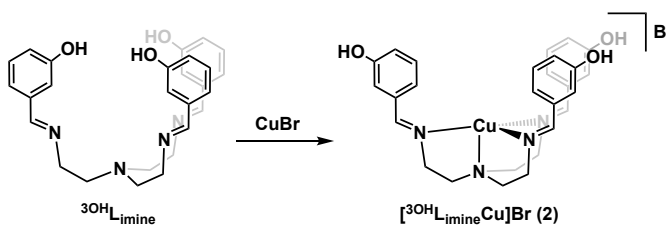

Scheme 6.2 Metallation of ^{3OH}L$_{imine}$ to form complex **2**.

complex demonstrated successful dative coordination of the nitrogen donors, it appeared that the hydroxyl groups were likely too far from the metal center to engage in hydrogen bonding with bound substrates. Additionally, this variant showed continued solubility issues. Both of these factors suggested the 2-hydroxy substituted derivative might prove more suited for the desired chemistry.

6.3.2 Dative coordination of the 2-hydroxy ligand variant

Synthesis of the 2-hydroxy ligand, tris[2-(salicylideneamino)-ethyl]amine (^{2OH}L$_{imine}$) was accomplished by condensation of tren with three equivalents of salicylaldehyde. While the synthesis of this ligand first appeared in the literature as early as 1968,[14] and its metallation has been previously described using metal(III) salts,[15,16] its coordination chemistry has not been reported under air- and moisture-free conditions using metal(II) species. Since the completion of this work, a number of additional reports have been published on the metallation of ^{2OH}L$_{imine}$ (and other closely related ligand derivatives) with first row transition metals.[17-19]
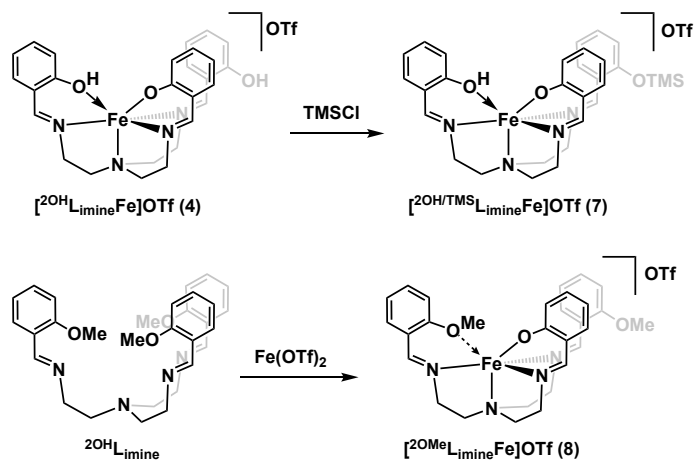
Initial metallation of ^{2OH}L$_{imine}$ with metal(II) halide salts resulted in minimally soluble products. However, reaction of metal(II) salts using the non-coordinating triflate (OTf) anion yielded more soluble species. Dative coordination of Mn(OTf)$_2$ in THF gave a yellow solution. Structural characterization via X-ray crystallography revealed that the manganese center was not coordinated in the desired fashion, instead binding to all three phenoxy groups, with the phenolic protons migrating to the imine nitrogens. The metal center was further ligated with two acetonitrile solvent molecules and one of the triflate anions, resulting in an octahedral coordination geometry, [$^{2O-}$L$_{imine}$Mn(MeCN)$_2$(OTf)]OTf (**3**). In contrast to manganese, metallation of iron, cobalt, and copper resulted in complexes where the metal center was bound in the desired pocket, coordinated by the three imines and the apical nitrogen. However, in all three cases one of the phenoxy groups was deprotonated and bound to the metal center, resulting in the loss of triflic acid during metallation, even in the absence of exogenous base ([^{2OH}L$_{imine}$Fe]OTf, **4**; [^{2OH}L$_{imine}$Co]OTf, **5**; [^{2OH}L$_{imine}$Cu]OTf, **6**). In complex **4** an additional hydroxy group is datively coordinated to the iron center, resulting in a distorted octahedral geometry. Metallations were also carried out in the presence of triphenylphosphine oxide with the goal of preventing deprotonation of the phenoxy groups by introducing an potential hydrogen bond acceptor, however the same products (**4-6**) were
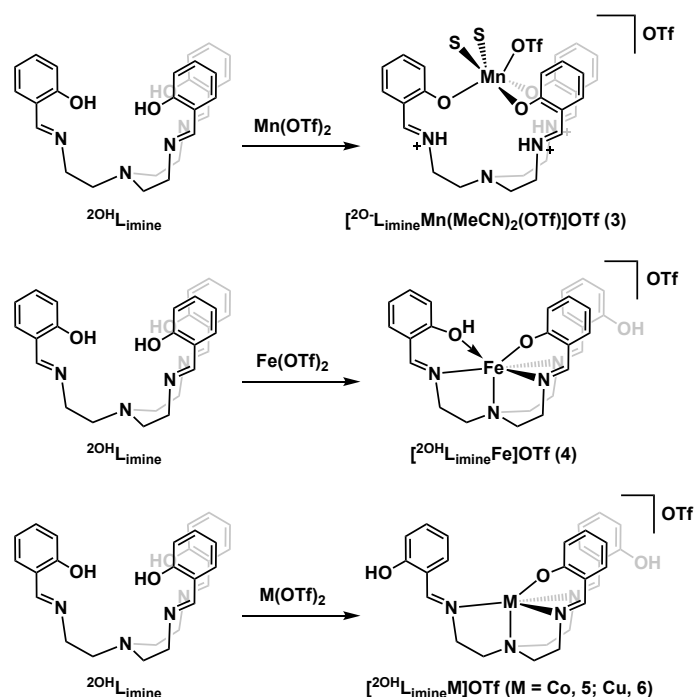
Scheme 6.3 Metallation of $^{2OH}L_{imine}$ with metal(II)-triflate salts.

formed under these conditions. Initial reactivity studies with these complexes targeted dissociation of these oxygen donors from the metal centers, focusing on the iron species.

Attempts to re-protonate the bound phenoxide by treating complex **4** with several acids resulted in minimal conversion or demetallation of the ligand. The use of protecting groups was then briefly explored. Addition of 1-3 equivalents of TMSCl to an acetonitrile solution of **4** resulted in the formation of a new paramagnetic species, as determined by ^1H NMR spectroscopy. Analysis of this product by X-ray crystallography revealed that the TMS

protecting group had reacted with the unbound phenoxy group, yielding $[^{2OH/OTMS}L_{imine}Fe]OTf$ (**7**). The two other phenoxy groups remained bound at the metal center, one anionically and one datively, as in the starting complex (**4**). As a final attempt at accessing a trigonal monopyramidal iron complex, the 2-methoxy ligand, tris{2-[(2-methoxybenzylidene)amino]-ethyl}amine ($^{2OMe}L_{imine}$), was synthesized and

metallated. Dative coordination of $^{2OMe}L_{imine}$ was attempted under conditions analogous to those used in the synthesis of **4**. Crystallographic characterization of the product revealed an intriguingly similar structure to **4**. The C–O bond of one of the methoxy groups had been cleaved, resulting in a bound phenoxide. A second methoxy group was rotated towards the metal center, with an iron-oxygen distance of 2.44 Å suggesting weak interaction. The similarities between the

Scheme 6.4 Synthesis of complexes **7** and **8**.

methoxy complex, $[^{2OMe}L_{imine}Fe]OTf$ (**8**), and the hydroxy analog (**4**) demonstrated the strong driving force behind formation of the iron-oxygen bond. In light of these results, further studies were carried out using the phenoxide-bound iron and cobalt complexes without further modification.

115

6.3.3 Redox chemistry of the iron(II) (4) and cobalt(II) (5) complexes

Oxidation of [^{2OH}L$_{imine}$Fe]OTf (**4**) and [^{2OH}L$_{imine}$Co]OTf (**5**) was explored to determine what role, if any, the pendant phenoxy groups played in facilitating the redox chemistry of the metal complexes. Addition of ferrocenium hexafluorophosphate (FcPF$_6$) to an acetonitrile solution of complex **4** resulted in a color change from orange to dark purple. Formation of a new paramagnetic species was confirmed by ^{1}H NMR spectroscopy. Structural analysis of the product revealed formation of a dimeric species, with all three phenoxy groups bound to one of the iron centers ([$^{2O\text{-}}$L$_{imine}$Fe]$_2$(OTf)$_2$, **9**). Each iron center is bound in a distorted octahedral geometry where one face is occupied by two imines and the apical amine, and the other is composed of two phenoxide groups from the same ligand and a third phenoxide donor bridging from the second ligand. The bridging arm of each ligand is protonated at nitrogen, resulting in an iminium hydrogen bonding to the adjacent phenoxide oxygen atom. This dimeric complex was found to form under a variety conditions (oxidation of **4** with FcPF$_6$, pyridine-*N*-oxide, or air; oxidation of the TMS protected analog (**7**) with FcPF$_6$ or pyridine-*N*-oxide), once again demonstrating the driving force to form iron-oxygen bonds with this ligand framework. Oxidation of the cobalt complex (**5**) with FcPF$_6$ was then carried out, resulting in a new paramagnetic species. X-ray crystallography analysis revealed the product to be a monomeric complex, however binding of a second phenoxide ligand was observed ([$^{2O\text{-}}$L$_{imine}$Co]OTf, **10**).

**Scheme 6.5** Oxidation of the iron(II) and cobalt(II) complexes.
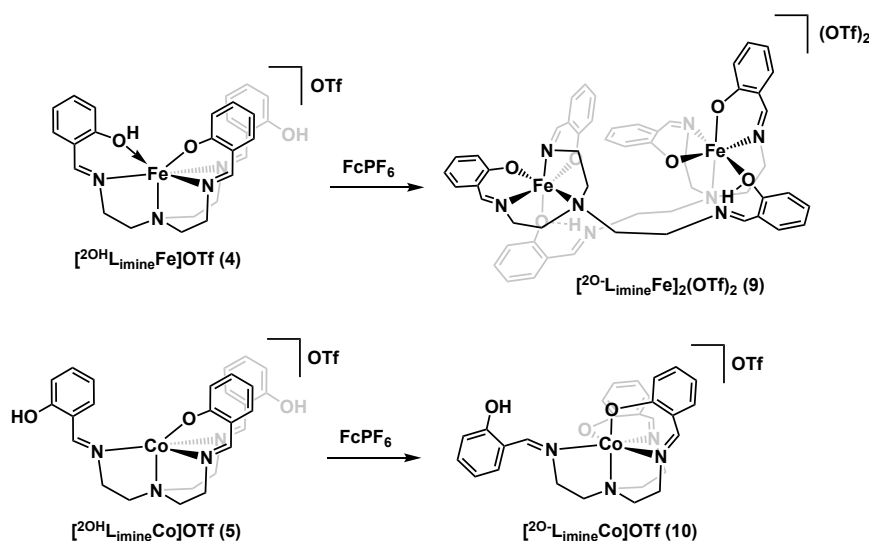
Given the binding of additional phenoxy groups upon oxidation of **4** and **5**, focus was shifted to the reduction of these complexes. Both species were treated with sodium naphthalenide, resulting in formation of new paramagnetic species, as judged by ^{1}H NMR spectroscopy. In both cases the resulting product was relatively unreactive, showing no reaction with pyridine-n-oxide or water at room temperature, with moderate decomposition observed upon heating. The only reaction that resulted in conversion of these reduced species was their oxidation with ferrocenium. Intriguingly, the products of these reactions were determined to be complexes **9** and **10** respectively, based on their ^{1}H NMR spectra. Because the same products are accessed from oxidation of complexes **4** and **5**, these results suggested that treatment with sodium naphthalenide resulted in effective deprotonation instead of the desired reduction.

These resulted further demonstrated the propensity to form oxygen-bound metal complexes, establishing that additional modification of the ligand design was needed, thus attention was shifted to a third-generation design of the framework.

6.4 Synthesis and metallation of tren-based ligands functionalized with hydroxybenzyl groups

After metallation studies demonstrated that neutral imine donors were easily displaced by binding of the phenoxy oxygen atoms, the ligand backbone was further reduced to the saturated amine linker. It was hypothesized that this modification would provide several benefits relative to the previous designs: i) an anionic binding mode would diminish the driving force behind deprotonation of the phenol groups, ii) the added flexibility of the amine linker would allow for better orientation of the hydrogen bonding network in the secondary coordination sphere, and iii) the fully saturated backbone would lead to increased solubility.

The (*tert*-butyldimethylsilyl)oxy (OTBS) protected ligand, tris[2-({2-[(*tert*-butyldimethylsilyl)oxy]benzyl}amino)ethyl]amine (²ᴼᵀᴮˢL$_{amine}$), was synthesized by reducing the corresponding imine (²ᴼᵀᴮˢL$_{imine}$) with sodium borohydride in good yields. Attempts to deprotonate the amine nitrogens with a variety of bases resulted primarily in cleavage of the TBS protecting group, as judged by the absence of the TBS resonances in the ¹H NMR spectrum of the products. Metallations with

Scheme 6.6 Metallation of ²ᴼᵀᴮˢL$_{amine}$ to yield complex **11**.
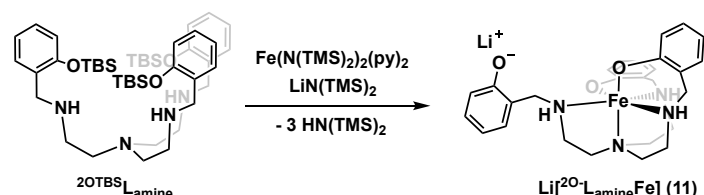
Fe(N(SiMe₃)₂)₂(py)₂ also resulted in cleavage of the protecting group, yielding an octahedral iron complex neutrally bound by the four amine donors and anionically coordinated to two of three phenoxy groups, as determined by X-ray crystallography (Li[²ᴼ⁻L$_{amine}$Fe], **11**).[20] This result once again underscored the difficulties associated with designing ligand frameworks based on nitrogen donors with pendant hydroxy groups in the secondary coordination sphere, ultimately leading us to pursue alternative design motifs.

6.5 Conclusion

The synthesis and metallation of tren-based ligands featuring phenoxy moieties in the secondary coordination sphere has been described. Initial efforts using a rigid amide linker between the two coordination spheres of the ligand resulted in the formation of a four-coordinate cobalt complex with the desired trigonal monopyramidal geometry, Li[³ᴼᴹᵉL$_{amide}$Co] (**1**). However, the minimal solubility of these ligand derivatives prevented detailed analysis of the desired protic analog (³ᴼᴴL$_{amide}$). A second generation of the ligand with an imine linker was then pursued. Although the 3-hydroxy variant was successfully metallated with CuBr, yielding [³ᴼᴴL$_{imine}$Cu]Br (**2**), its minimal solubility proved problematic once again. Switching to the 2-hydroxy derivative provided increased solubility, however, this positioning of the phenoxy groups led to phenoxide binding during metallation with late first row

117

transition metals ([$^{2O^-}$L$_{imine}$Mn(MeCN)$_2$(OTf)]OTf, **3**; [^{2OH}L$_{imine}$Fe]OTf, **4**; [^{2OH}L$_{imine}$Co]OTf, **5**; [^{2OH}L$_{imine}$Cu]OTf, **6**). Furthermore, redox chemistry with the iron and cobalt complexes resulted in the formation of additional metal-phenoxide bonds. Analogous behavior was noted for a final ligand design based on a flexible amine linker, yielding an octahedral iron(II) complex, despite the use of protecting groups during metallation (Li[$^{2O^-}$L$_{amine}$Fe], **11**).

Ultimately this work demonstrated the challenges of designing new ligands featuring hydroxy functionalities in the secondary coordination sphere. The use of aryl groups to position the pendant groups proved unsuccessful, with the 3-position likely proving too far from the metal center to engage in hydrogen bonding and the 2-position placing the second sphere groups too close to the metal center, resulting in M–O bond formation. More successful designs seeking to incorporate hydroxy groups in the secondary coordination sphere would likely require elaborate linkers between the two spheres of the ligands to more precisely position the pendant functionalities.

6.6 Experimental section

Preparation of tris{2-[(3-hydroxybenzoyl)amino]ethyl}amine (^{3OH}L$_{amide}$). 4-dimethylaminopyridine (DMAP) (139 mg, 1.14 mmol) was dissolved in 50 mL THF. Diisopropylcarbodiimide (DIC) (1.410 mL, 9.01 mmol) was added dropwise, followed by tris(2-aminoethyl)amine (tren) (0.340 mL, 2.27 mmol). This mixture was stirred at room temperature for five minutes. Separately, 3-hydroxybenzoic acid (1.009 g, 7.30 mmol) was dissolved in 10 mL THF. The benzoic acid solution was then added to the reaction mixture dropwise, resulting in the immediately formation of an off-white precipitate. The reaction was stirred at room temperature for three hours to ensure complete conversion. The ligand, tris{2-[(3-hydroxybenzoyl)amino]ethyl}amine (^{3OH}L$_{amide}$), was collected as a solid over a frit and washed with dry DCM. ^{1}H NMR (DMSO-d$_6$, 500 MHz): δ = 2.55 (br t, 6H), 2.80 (br t, 6H), 6.74 (d, 3H, J = 7.5 Hz), 7.09 (t, 3H, J = 7.7 Hz), 7.28 (d, 3H, J = 7.5 Hz), 7.32 (s, 3H). ^{13}C NMR (DMSO-d$_6$, 126 MHz): δ = 37.21, 52.81, 116.14, 116.67, 119.62, 128.26, 140.01, 157.24, 170.99.

Preparation of tris{2-[(3-methoxybenzoyl)amino]ethyl}amine (^{3OMe}L$_{amide}$). 3-methoxybenzoyl chloride (0.770 mL, 5.48 mmol) was dissolved in 20 mL THF. NEt$_3$ (0.760 mL, 5.45 mmol) was added dropwise, followed by tren (0.270 mL, 1.80 mmol). A white precipitate was formed immediately upon addition of tren. The reaction mixture was stirred at room temperature for thirty minutes. The reaction mixture was filtered over Celite to remove the triethylammonium chloride precipitate. The filtrate was dried in vacuo to yield the desired ligand, tris{2-[(3-methoxybenzoyl)amino]ethyl}amine (^{3OMe}L$_{amide}$), as a oily foam. ^{1}H NMR (DMSO-d$_6$, 500 MHz): δ = 2.55 (br t, 6H), 2.80 (br t, 6H), 6.74 (d, 3H, J = 7.5 Hz), 7.09 (t, 3H, J = 7.7 Hz), 7.28 (d, 3H, J = 7.5 Hz), 7.32 (s, 3H).

Synthesis of Li[^{3OMe}L$_{amide}$Co] (1). ^{3OMe}L$_{amide}$ (92 mg, 0.17 mmol) was dissolved in 6 mL THF and frozen in a liquid nitrogen cold well. Lithium bis(trimethylsilyl)amide (LiN(TMS)$_2$) (80 mg, 0.48 mmol)

was weighed by difference and added as a solid. The reaction mixture was slowly thawed at room temperature. A white precipitate was formed upon stirring. After thirty minutes, the solvent was removed in vacuo to yield the lithium salt of the ligand as a white powder. This salt was then added to a suspension of $CoCl_2$ (17.8 mg, 0.14 mmol) in 6 mL THF at room temperature. The solids slowly dissolved upon stirring overnight to give a cloudy blue mixture. Solvent was removed to yield the crude product. Crystals of Li[^{3OMe}L$_{amide}$Co] (**1**) suitable for x-ray diffraction were grown by vapor diffusion of Et$_2$O into a DMA solution of the complex.

Preparation of tris{2-[(3-hydroxybenzylidene)amino]-ethyl}amine (^{3OH}L$_{imine}$). 3-hydroxybenzaldehyde (1.057 g, 8.66 mmol) and tren (0.420 mL, 2.81 mmol) were combined in 30 mL dry DCM. The reaction was stirred at room temperature overnight. The ligand, tris{2-[(3-hydroxybenzylidene)amino]-ethyl}amine (^{3OH}L$_{imine}$), precipitated out of solution as an off-white solid, which was collected and dried over a frit. ^{1}H NMR (DMSO-d$_6$, 500 MHz): δ = 2.81 (t, 6H, J = 6.6 Hz), 3.58 (t, 6H, J = 6.3 Hz), 6.82 (d, 3H, J = 8.1 Hz), 6.98 (d, 3H, J = 7.6 Hz), 7.11 (s, 3H), 7.18 (t, 3H, J = 7.8 Hz), 8.13 (s, 3H).

Synthesis of [^{3OH}L$_{imine}$Cu]Br (2). ^{3OH}L$_{imine}$ (48.7 mg, 0.10 mmol) was suspended in 6 mL of a 2:1 mixture of THF and DMA. This mixture was then added dropwise to a cold suspension of CuBr (15.3 mg, 0.11 mmol) in 6 mL THF. The reaction was stirred at room temperature overnight, yielding a yellow mixture. Crystals of [^{3OH}L$_{imine}$Cu]Br (**2**) suitable for X-ray diffraction were grown by vapor diffusion of a filtered reaction aliquot with Et$_2$O.

Preparation of tris[2-(salicylideneamino)-ethyl]amine (^{2OH}L$_{imine}$). Tren (7.183 g, 49.1 mmol) was dissolved in 80 mL DCM and stirred over Na$_2$SO$_4$. Salicylaldehyde (18.007 g, 147 mmol) was added slowly, resulting in a bright yellow solution. The reaction was stirred for thirty minutes to ensure full conversion, then filtered and dried to yield the desired ligand, tris[2-(salicylideneamino)-ethyl]amine (^{2OH}L$_{imine}$), as a pale yellow powder (22.290 g, 48.6 mmol, 99%). ^{1}H NMR (CD$_3$CN, 400 MHz): δ = 2.83 (t, 6H, J = 5.5 Hz), 3.53 (t, 6H, J = 5.0 Hz), 6.43 (d, 3H, J = 6.0 Hz), 6.67 (d, 3H, J = 7.0 Hz), 7.27 (t, 3H, J = 6.7 Hz), 7.97 (s, 3H), 13.68 (s, 3H).

Synthesis of [$^{2O^-}$L$_{imine}$Mn(L)$_2$(OTf)]OTf (L = THF/MeCN, 3). Mn(OTf)$_2$(MeCN)$_2$ (53 mg, 0.12 mmol) was dissolved in THF (~10 mL) and cooled to -35ºC. ^{2OH}L$_{imine}$ (60 mg, 0.13 mmol) was weighed by difference and added as a solid, giving an immediate golden yellow precipitate. The reaction mixture was stirred at room temperature for 1 h. The precipitate was then collected over a frit, washed with benzene, then hexane, and dried under vacuum. Crystals of [$^{2O^-}$L$_{imine}$Mn(MeCN)$_2$(OTf)]OTf (**3**) suitable for X-ray diffraction were grown by vapor diffusion of Et$_2$O into a MeCN solution.

Synthesis of [^{2OH}L$_{imine}$Fe]OTf (4). Pyridine (1.263 g, 16.0 mmol) and Fe(OTf)$_2$(THF)$_2$ (3.936 g, 7.90 mmol) were combined in 125 mL THF, then cooled to -35ºC. ^{2OH}L$_{imine}$ (3.646 g, 7.95 mmol) was then

119

slowly added as a solid, resulting in immediate formation of a bright orange precipitate. The reaction was stirred at room temperature for one hour. The product, [^{2OH}L$_{imine}$Fe]OTf (**4**), was collected over a frit, washed with THF and Et$_2$O (both 2 x 15 mL), then dried (4.870 g, 7.34 mmol, 93%). Crystals suitable for X-ray diffraction were grown by vapor diffusion of Et$_2$O into a MeCN solution.

Synthesis of [^{2OH}L$_{imine}$Co]OTf (5). This complex was synthesized following an analogous procedure to complex **4**. Pyridine (724 mg, 9.15 mmol) and Co(OTf)$_2$(THF)$_2$ (2.292 g, 4.57 mmol) were combined in 80 mL MeCN, then cooled to -35 °C. ^{2OH}L$_{imine}$ (2.203 g, 4.80 mmol) was added as a solid resulting in a color change from pink to green-yellow with the formation of substantial precipitate. After stirring for one hour, the solid was collected over a frit, washed with Et$_2$O, and dried to yield the product, [^{2OH}L$_{imine}$Co]OTf (**5**), (2.746 g, 4.13 mmol, 90%). Crystals suitable for X-ray diffraction were grown by slow evaporation of a ^{1}H NMR sample in CD$_3$CN.

Synthesis of [^{2OH}L$_{imine}$Cu]OTf (6). This complex was synthesized following an analogous procedure to complex **4**. Pyridine (53 mg, 0.67 mmol) and Cu(OTf)$_2$(MeCN)$_2$ (135 mg, 0.30 mmol) were combined in ~10 mL THF, then cooled to -35ºC. ^{2OH}L$_{imine}$ (146 mg, 0.32 mmol) was added as a solid resulting in a color change from royal blue to dark blue-green. After stirring for ~3 h, volatiles were removed in vacuo to yield the crude product as an oil. The oil was washed with benzene, then hexanes, and dried to yield the product, [^{2OH}L$_{imine}$Cu]OTf (**6**). Crystals suitable for X-ray diffraction were grown by slow evaporation of a ^{1}H NMR sample in CD$_3$CN.

Silylation of 4 to form [$^{2OH/OTMS}$L$_{imine}$Fe]OTf (7). [^{2OH}L$_{imine}$Fe]OTf (**4**; 43 mg, 0.065 mmol) was dissolved in ~5 mL MeCN, then cooled to -35ºC. Excess TMSCl (23 mg, 0.21 mmol) was separately dissolved in an additional 2 mL MeCN and cooled. The TMSCl solution was added dropwise to complex **4**, resulting in an immediate color change from dark red-orange to bright orange. After stirring at room temperature for one hour, volatiles were removed in vacuo to yield the crude product. Crystals of [$^{2OH/OTMS}$L$_{imine}$Fe]OTf (**7**) suitable for X-ray diffraction were grown by vapor diffusion of a MeCN solution with Et$_2$O.

Preparation of tris{2-[(2-methoxybenzylidene)amino]-ethyl}amine (^{2OMe}L$_{imine}$). This ligand was prepared by condensation of tren (563 mg, 3.85 mmol) and *o*-anisaldehyde (1.579 g, 11.6 mmol), following the same procedure used for ^{2OH}L$_{imine}$. The product was isolated as a viscous yellow oil. ^{1}H NMR (CD$_3$CN, 500 MHz): δ = 2.87 (t, 6H, J = 6.6 Hz), 3.65 (t, 6H, J = 6.6 Hz), 3.81 (s, 9H), 6.92 (t, 3H, J = 7.5 Hz), 6.99 (d, 3H, J = 8.3 Hz), 7.37 (ddd, 3H, J = 9.1, 7.4, 1.8 Hz), 7.81 (dd, 3H, J = 7.7, 1.8 Hz), 8.62 (s, 3H).

Synthesis of [^{2OMe}L$_{imine}$Fe]OTf (8). This complex was synthesized following an analogous procedure to complex **4**. Pyridine (170 mg, 2.15 mmol) and Fe(OTf)$_2$(THF)$_2$ (513 mg, 1.03 mmol) were combined in ~10 mL MeCN, then cooled to -35ºC. ^{2OMe}L$_{imine}$ (2.2030 g, 1.05 mmol) was added as a solid resulting

in an orange solution, which was stirred at room temperature for 1 h. Crystals of [^{2OMe}L$_{imine}$Fe]OTf (**8**) suitable for X-ray diffraction were grown by layering a THF solution of the complex with hexamethyldisiloxane (TMS$_2$O).

Oxidation of 4 to form [$^{2O-}$L$_{imine}$Fe]$_2$(OTf)$_2$ (9).   [^{2OH}L$_{imine}$Fe]OTf (**4**) (138 mg, 0.21 mmol) was dissolved in ~5 mL MeCN and cooled to -35ºC. FcPF$_6$ (70 mg, 0.21 mmol) was added as a solid, resulting in a color change from dark red-orange to dark red-purple. The reaction was stirred at room temperature for ~2 h. Solvent was removed in vacuo to yield the crude product, which was washed with Et$_2$O to remove the Fc byproduct. The Et$_2$O layer was decanted and the solid was redried to yield [$^{2O-}$L$_{imine}$Fe]$_2$(OTf)$_2$ (**9**) as a powder. Crystals suitable for X-ray diffraction were grown by vapor diffusion of Et$_2$O into a dilute MeCN solution.

Oxidation of 5 to form [$^{2O-}$L$_{imine}$Co]OTf (10).   [^{2OH}L$_{imine}$Co]OTf (**5**) (248 mg, 0.37 mmol) was dissolved in ~5 mL MeCN and cooled to -35ºC. FcPF$_6$ (137 mg, 0.41 mmol) was added as a solid, resulting in a color change from dark yellow to dark yellow-green. The reaction was stirred at room temperature for ~2 h. Solvent was removed in vacuo to yield the crude product, which was washed with Et$_2$O to remove the Fc byproduct. The Et$_2$O layer was decanted and the solid was redried to yield [$^{2O-}$L$_{imine}$Co]OTf (**10**) as a powder. Crystals suitable for X-ray diffraction were grown by vapor diffusion of benzene into a MeCN solution.

Reduction of [^{2OH}L$_{imine}$Fe]OTf (4). Na[C$_{10}$H$_8$] was generated in situ by stirring naphthalene (40 mg, 0.31 mmol) over excess sodium in 6 mL THF. After stirring for four hours, the dark green mixture was filtered to remove unreacted sodium metal; the filtrate was cooled to -35ºC. Separately, [^{2OH}L$_{imine}$Fe]OTf (**4**) (206 mg, 0.28 mmol) was suspended in 4 mL THF, the mixture was then frozen in the cold well. Na[C$_{10}$H$_8$] was slowly added to the metal complex. The reaction mixture was stirred for 5 minutes while thawing, resulting in a color change from dark red-orange to dark purple. The reaction was then refrozen to prevent decomposition observed in early trials. The frozen mixture was dried in vacuo to yield the crude product as a gummy brown residue. The product was powdered with Et$_2$O, which was decanted to remove the soluble naphthalene byproduct. The solid was dried in vacuo to yield a light purple powder.

Reduction of [^{2OH}L$_{imine}$Co]OTf (5). Na[C$_{10}$H$_8$] was generated in situ from naphthalene (45 mg, 0.35 mmol) as described above. [^{2OH}L$_{imine}$Co]OTf (**5**) (209 mg, 0.31 mmol) was reduced following the procedure used for [^{2OH}L$_{imine}$Fe]OTf (**4**), resulting in a color change from yellow to dark red-brown, with a significant increase in solubility. The product was isolated as a light yellow-brown powder following the workup described above.

Preparation of tris[2-({2-[(*tert*-butyldimethylsilyl)oxy]benzyl}amino)ethyl]amine (^{2OTBS}L$_{amine}$). ^{2OH}L$_{imine}$ (1.011 g, 2.20 mmol) was dissolved in 15 mL THF and cooled to -35ºC. KH (267 mg, 6.66 mmol, 3 equiv) was added as a solid. The reaction mixture was stirred at room temperature for 1.5 h,

resulting in a thick white suspension. TBSCl (1.006 g, 6.67 mmol, 3 equiv) was added, resulting in a thinner white suspension. After stirring for another thirty minutes, solvent was removed in vacuo to yield the silyl protected imine intermediate ($^{2OTBS}L_{imine}$) as an oil. The intermediate was taken on without further purification.

Crude $^{2OTBS}L_{amine}$ was dissolved in 15 mL MeOH. NaBH$_4$ (360 mg, 9.51 mmol, 4.3 equiv) was added; the reaction was stirred at room temperature for one hour. Volatiles were removed from by rotary evaporation. The crude material was partially dissolved in DI water then extracted with EtOAc (3 x 20 mL). The combined organic layers were washed with brine (2 x 20 mL) and water (20 mL), and then dried over Na$_2$SO$_4$. Drying by rotary evaporation yielded the product, tris[2-({2-[(*tert*-butyldimethylsilyl)oxy]benzyl}amino)ethyl]amine ($^{2OTBS}L_{amine}$), as a yellow oil (1.293 g, 1.60 mmol, 73%).

Synthesis of Li[$^{2O\text{-}}$L$_{amine}$Fe] (11). Fe(N(TMS)$_2$)$_2$(py)$_2$ (33.5 mg, 0.063 mmol) and LiN(TMS)$_2$ (12.7 mg, 0.076 mmol) were combined in 4 mL THF, then cooled to -35ºC. $^{2OTBS}L_{amine}$ was separately dissolved and cooled in another 4 mL THF. The ligand solution was then added dropwise to the metal, resulting in a color change from orange to dark red. The reaction was stirred at room temperature for two hours, then dried in vacuo. Crystals of Li[$^{2O\text{-}}$L$_{amine}$Fe] (**11**) suitable for X-ray diffraction were from a MeCN solution of the complex.

6.7 References

(1)   Pesavento, R. P.; van der Donk, W. A. Tyrosyl Radical Cofactors. *Adv. Protein Chem.* **2001**, *58*, 317–385.

(2)   Himo, F.; Siegbahn, P. E. M. Quantum Chemical Studies of Radical-Containing Enzymes. *Chem. Rev.* **2003**, *103* (6), 2421–2456.

(3)   Reece, S. Y.; Nocera, D. G. Proton-Coupled Electron Transfer in Biology: Results From Synergistic Studies in Natural and Model Systems. *Annu. Rev. Biochem.* **2009**, *78* (1), 673–699.

(4)   Migliore, A.; Polizzi, N. F.; Therien, M. J.; Beratan, D. N. Biochemistry and Theory of Proton-Coupled Electron Transfer. *Chem. Rev.* **2014**, *114* (7), 3381–3465.

(5)   Yoshikawa, S.; Shimada, A. Reaction Mechanism of Cytochrome C Oxidase. *Chem. Rev.* **2015**, *115* (4), 1936–1989.

(6)   McEvoy, J. P.; Brudvig, G. W. Water-Splitting Chemistry of Photosystem II. *Chem. Rev.* **2006**, *106* (11), 4455–4483.

(7)   Vogt, L.; Vinyard, D. J.; Khan, S.; Brudvig, G. W. Oxygen-Evolving Complex of Photosystem II: an Analysis of Second-Shell Residues and Hydrogen-Bonding Networks. *Curr. Opin. Chem. Biol.* **2015**, *25*, 152–158.

(8)   Matsu-ura, M.; Tani, F.; Nakayama, S.; Nakamura, N.; Naruta, Y. Hydrogen-Bonded Dioxygen Adduct of an Iron Porphyrin with an Alkanethiolate Ligand: an Elaborate Model of Cytochrome P450. *Angew. Chem. Int. Ed.* **2000**, *39* (11), 1989–1991.

(9)   Matsu-ura, M.; Tani, F.; Naruta, Y. Formation and Characterization of Carbon Monoxide Adducts of Iron "Twin Coronet" Porphyrins. Extremely Low CO Affinity and a Strong Negative Polar Effect on Bound CO. *J. Am. Chem. Soc.* **2002**, *124* (9), 1941–1950.

(10)   Matsui, E.; Naruta, Y.; Tani, F.; Shimazaki, Y. An Active-Site Model of Prostaglandin H Synthase: an Iron "Twin-Coronet" Porphyrin with an Aryloxyl Radical Overhang and Its Catalytic Oxygenation of 1,4-Diene. *Angew. Chem. Int. Ed.* **2003**, *42* (24), 2744–2747.

(11)   Moore, C. M.; Quist, D. A.; Kampf, J. W.; Szymczak, N. K. A 3-Fold-Symmetric Ligand Based on 2-Hydroxypyridine: Regulation of Ligand Binding by Hydrogen Bonding. *Inorg. Chem.* **2014**, *53* (7), 3278–3280.

(12)   Moore, C. M.; Szymczak, N. K. Redox-Induced Fluoride Ligand Dissociation Stabilized by Intramolecular Hydrogen Bonding. *Chem. Commun.* **2015**, *51* (25), 5490–5492.

(13)   Moore, C. M.; Szymczak, N. K. Nitrite Reduction by Copper Through Ligand-Mediated Proton and Electron Transfer. *Chem. Sci.* **2015**, *6* (6), 3373–3377.

(14)   Broomhead, J. A.; Robinson, D. J. A Potential Septadentate Ligand. *Aust. J. Chem.* **1968**, *21* (5), 1365–1367.

(15)   Malek, A.; Dey, G. C.; Nasreen, A.; Chowdhury, T. A.; Alyea, E. C. Potentially Heptadentate Ligands Derived From Tris(2-Aminoethyl)Amine(Tren). *Synth. React. Inorg. Met.-Org. Chem.* **1979**, *9* (2), 145–155.

(16)   Chandra, S. K.; Chakraborty, P.; Chakravorty, A. Mono- and Tetra-Nuclear Manganese(III) Complexes of Tripodal Tris[2-(Salicylideneamino)Ethyl]Amines. *J. Chem. Soc., Dalton Trans.* **1993**, No. 6, 863–867.

(17)   Kim, K. B.; Kim, H.; Song, E. J.; Kim, S.; Noh, I.; Kim, C. A Cap-Type Schiff Base Acting as a Fluorescence Sensor for Zinc(Ii) and a Colorimetric Sensor for Iron(II), Copper(II), and Zinc(II) in Aqueous Media. *Dalton Trans.* **2013**, *42* (47), 16569–16569.

(18)   Malpaharia, P.; Pramanik, K.; Costes, J.-P.; Tuchagues, J.-P.; Moulton, B.; Zaworotko, M. J.; Das, B.; Chandra, S. K. Tetranuclear [Mn$_2$Co$_2$], [Mn$_2$Fe$_2$], And [Mn$_2$Mn$_2$] Complexes with Defective Double-Cubane Cores and Phenoxo and Oxo Bridges: Syntheses, Crystal Structures, and Electronic Properties. *Eur. J. Inorg. Chem.* **2014**, *2014* (22), 3527–3535.

(19)   Matin, S. J.; Khojasteh, R. R. Synthesis, Characterization, and Antibacterial Activities of Cr(III), Co(III), Ni(II), and Mn(III) Complexes of Heptadentate Schiff Base Ligand Derived From Tris(2-Aminoethyl)Amine. *Russ. J. Gen. Chem.* **2015**, *85* (7), 1763–1767.

(20)   The molecular structure of a closely related iron(III) complex of the ligand has been reported previously reported. Leed, M. G. D.; Wolkow, N.; Pham, D. M.; Daniel, C. L.; Dunaief, J. L.; Franz, K. J. Prochelators Triggered by Hydrogen Peroxide Provide Hexadentate Iron Coordination to Impede Oxidative Stress. *J. Inorg. Biochem.* **2011**, *105* (9), 1161–1172.